OXIDE NANOMATERIALS:

SYNTHESIS, STRUCTURE, PROPERTIES AND NOVEL DEVICES

A Dissertation
Presented to
The Academic Faculty

by

Rusen Yang

In Partial Fulfillment
of the Requirements for the Degree
Doctor of Philosophy in the
School of Materials Science and Engineering

Georgia Institute of Technology
August, 2007

OXIDE NANOMATERIALS:

SYNTHESIS, STRUCTURE, PROPERTIES AND NOVEL DEVICES

Approved by:

Dr. Zhong Lin Wang, Advisor
School of Materials Science & Engineering
Georgia Institute of Technology

Dr. Christopher Summers
School of Materials Science & Engineering
Georgia Institute of Technology

Dr. C.P. Wong
School of Materials Science & Engineering
Georgia Institute of Technology

Dr. Peter J. Hesketh
School of Mechanical Engineering
Georgia Institute of Technology

Dr. Robert L. Snyder
School of Materials Science & Engineering
Georgia Institute of Technology

Date Approved: June 19, 2007

ACKNOWLEDGEMENTS

I would like to express my deepest gratitude, respect, and admiration to my advisor, Dr Z.L. Wang. I was so much influenced by his brilliant ideas and dedicated working attitude and managed to be a researcher with confidence, persistence, and consistence, as advised by Dr Wang. In addition to guide my scholastic studies, Dr. Wang and his family have also cared for my family day to day.

My gratitude is also to my committee members: Dr. Peter Hesketh, Dr. Robert Snyder, Dr. Chris Summers, and Dr. C.P. Wong. I benefit from their earnest care and support. The members in our group have also had a great impact on my research and my life. In particular, I would like to thank my officemates, Jenny Morber, Dr. Jin Li, and Dr. Puxian Gao. Being both a friend and a teacher, Jenny helped me so much with my writing, speaking, and so on. She added “giraffe”, among others, in my vocabulary, which did make a difference when I spelled my name “Yang’ to others. Dr. Jin Li taught me many TEM techniques, which seems so obvious for an expert but is really magic for a beginner. Puxian Gao has also helped me with SEM and shaped my scientific outlook.

I ought to express my thanks to all my classmates. Especially, I need to thank Xiang Ren and Hong Ye Wang’s. Without their support I would not be able to take the TOEFL, or GRE test, not to say affording the tremendously high Pei Yang Fee and then air-fare to US for pursuing this Ph.D. degree.

I am heavily indebted to my parents for their unconditional support, understanding, and dedication. To my parents who taught me to be sparing, honest, obliging, generous, and hardworking. To my brothers who cared for me when I was

young. To my aunt's family whose support enabled me to study in school. To hospitable parents-in-law, brothers-in-law, sister-in-law, and others, who made me to feel at home when I visited them.

Last, but certainly not least, thanks to my wife. Thank you for sharing joy and sorrow with me. Thank you for encouraging me when I feel low. Thank you for finding a solution when I am in trouble. Thank you for taking care everything so that I can concentrate in school. Moreover, special thanks to my three-year-old son and the kid on the way, who let me to learn patience, circumspection, and responsibility.

TABLE OF CONTENTS

LIST OF TABLES

LIST OF FIGURES

SUMMARY

One-dimensional and hierarchical nanostructures have acquired tremendous attention in the past decades due to their possible application. In spite of the rapid emergence of new morphologies, the underlying growth mechanism is still not well understood. The lack of effective *p*-type or *n*-type doping is another obstacle for many semiconducting nanomaterials. A deeper investigation into these structures and new methods to fabricate devices are of significant impact for nanoscience and nanotechnology.

Motivated by a desire to understand the growth mechanism of nanostructures and investigate novel device fabrication method, the research described in this thesis carried out on the synthesis, characterization, and device fabrication of semiconducting nanostructures.

The main focus of the research was on ZnO, SnO_2, and Zn_3P_2 for their great capability for fundamental phenomena studying, promising applications in sensors and optoelectronics, and the potential generalization of results to other materials. Within this study the following goals have been achieved: 1) Improved understanding of polar-surface-induced growth mechanism in wurtzite-structured ZnO and generalization of this growth mechanism with the discovery and analysis of rutile –structured SnO_2, 2) observation of the significance of the transversal growth, which is usually ignored, in interpenetrative ZnO nanowires, 3) rational design and growth control over versatile nanostructures of ZnO and Zn_3P_2, and 4) conjunction of *p*-type Zn_3P_2 and *n*-type ZnO semiconducting nanostructures for device fabrications.

The framework for the research is reviewed first in chapter 1. Chapter 2 gives the detailed experimental setup, synthesis procedure, and common growth mechanism for nanostructure growth. A detailed discussion on the growth of ZnO nanostructures in chapter 3 provides more insight into the polar-surface-induced growth, transversal growth, vapor-solid growth, and vapor-liquid-solid growth during the formation of nanostructures. Polar-surface-induced growth is also confirmed in the growth of SnO_2 nanostructures, which is also included in chapter 2. Chapter 3 presents Zn_3P_2 nanostructures from the newly designed experiment setup and the device fabrication from ZnO and Zn_3P_2 crossed nanowires

CHAPTER 1

INTRODUCTION

Nanoscience and nanotechnology is a highly multidisciplinary field of applied science and technology covering a broad range of topics. The main unifying theme is the control of matter on a scale smaller than 1 micrometer, normally between 1-100 nanometers, as well as the fabrication of devices on this same length scale. At this length scale, nanomaterials have very large surface to volume ratio, and quantum confinement starts to play an important role. As a result, nanomaterials are found to possess unique or enhanced properties compared with their bulk counterparts and more and more devices continue to be fabricated to utilize these properties.

Top-down and bottom-up are two distinct strategies for fabricating nanostructures and devices. The top-down method starts from bulk materials, which are sculpted into nanosized features by carving, milling, etching and patterning. Lithography methods such as e-beam lithography, photolithography, focused ion beam lithography, dip pen lithography, etc, are getting more important to realize nanostructures in this top-down approach. Benefited by increasingly powerful computers, software, and well-developed techniques, the top-down method can usually achieve good control over the device dimension, location, and organization with high precision. However, high precision induces greater cost when the size of device is reduced, especially when the size is below 100 nanometers. In comparison, bottom-up methods construct structures or devices from the basic building blocks, atom by atom or molecule by molecule. This method utilizes the self-assembly concept, in which the building blocks, atoms or molecules, automatically arrange themselves into desired conformation. Bottom-up approaches usually are able to produce devices in parallel and much cheaper than top-down methods. However, this method could potentially be outgrown as the size and complexity of the

desired assembly increases. Sometimes scaling-up can be problematic, for bottom up methods. Because both top-down and bottom-up have their own advantages and drawbacks, hybrid methods combining both approaches should be desired techniques in the future to achieve molecular resolution and functionality on large areas.

1.1 One-Dimensional Nanomaterials

Nanomaterials can be classified into zero-dimensional, one-dimensional, and two-dimensional nanomaterials. Being confined in all three dimensions, quantum dots and nanoparticles are considered zero dimensional nanostructures and have been extensively studied. Being confined to the nanoscale in one-dimension, two-dimensional nanostructure of thin film have traditionally been studied and developed for use in fields as diverse as electronic devices and photovoltaic applications. In comparison, being confined to the nanoscale in two dimensions, the wire- or rod-like shape of one-dimensional nanostructures became the source of intensifying research over the past several years.

The category of one-dimensional nanostructures consists of a wide variety of morphologies, such as whiskers, nanowires, nanorods, fibers, nanocables, nanotubes, and nanobelts, among others. In fact, the distinguishing features between these are a little arbitrary. Whiskers and fibers mainly appeared in early literatures and are of diameters from several nanometers to several hundred microns. In contrast, nanorod and nanowire are more recent and of diameter less than 100 nanometers. Nanotubes usually take a nanowire shape with a hollow center, while nanobelts have well-defined side surface and rectangular cross-sections.

1.1.1 Nanotubes

Many materials have been used to make tubular nanostructures. Among one of the first discovered 1D nanomaterials, the carbon nanotube is the most intensively studied

nanotube structure in the areas of syntheses, property characterization, and applications. Carbon nanotubes are often referred to as the materials of the future; it has recently been demonstrated that they have existed in the global atmosphere for at least 10,000 years[1]. Murr et al.[2] presented transmission electron microscope observations of carbon nanotubes and related nanostructures generally collected in the air, and from common, domestic, clean-burning gas sources, which now appear to be major contributors to both indoor and outdoor carbon nanoparticles matter. Carbon nanotubes have also been appeared in the literature for a long time, while they might have been labeled with other names.

The first mention of the possibility of forming carbon filaments from the thermal decomposition of gaseous hydrocarbon (methane) was reported in 1889[3] in a patent that proposed the use of such filaments in the light bulbs that had just been presented by Edison at the Paris Universal Exposition. However, resolution limitations of the available microscopy tools (optical microscopes) prevented people from imaging filaments smaller than few micrometers in diameter, not to say the sub-micrometer inner cavity in carbon nanotubes. The subsequent invention of the transmission electron microscope (TEM) made the direct observation of carbon nanotubes possible. The first clear TEM images of 50 nanometer diameter carbon nanotubes was published in Russian Journal of Physical Chemistry in 1952, as presented in Figure 1.1[4, 5].

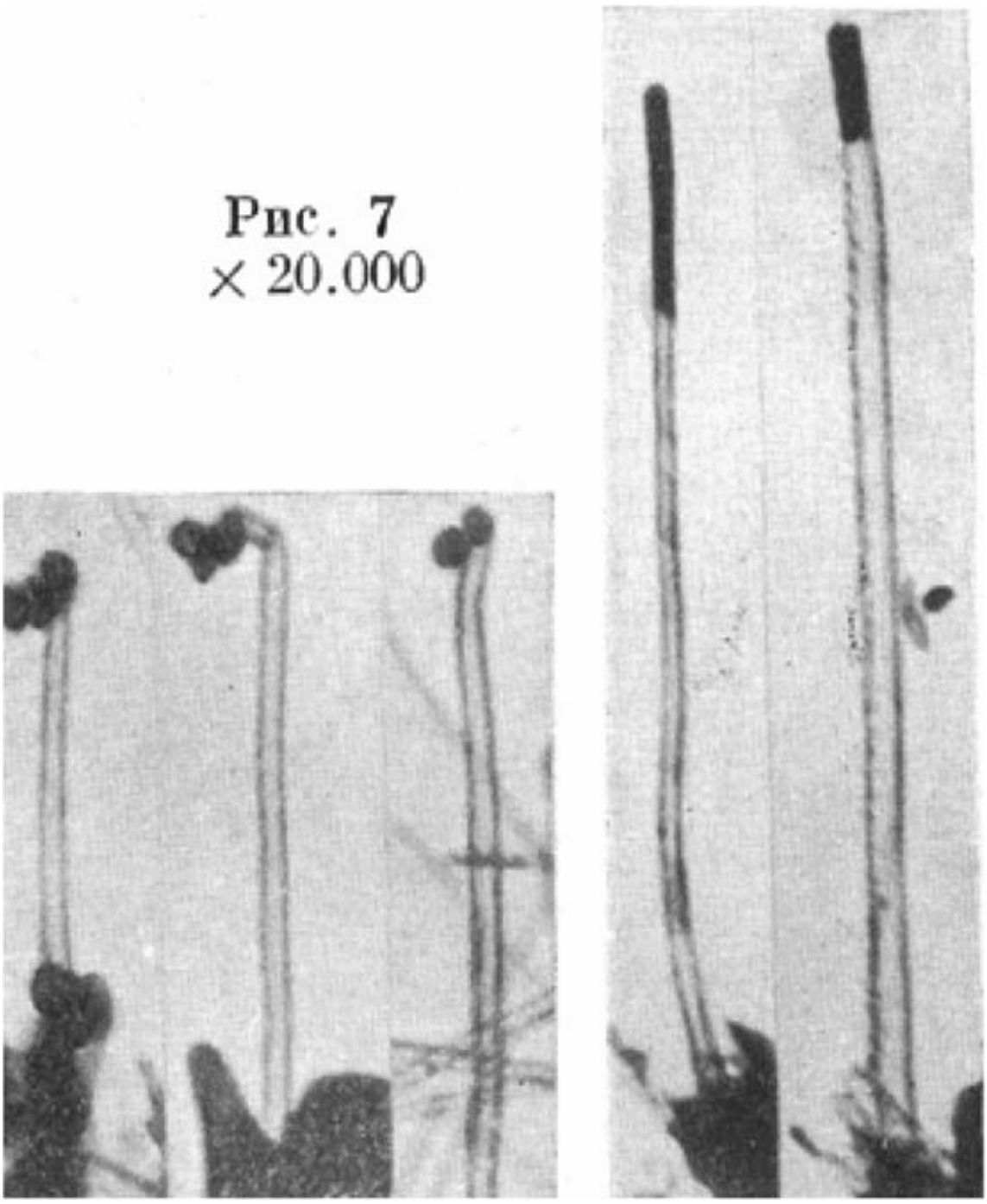

Figure 1.1 Examples of TEM images of carbon nanotubes published in 1952.[5]

However, this discovery was mainly unnoticed due to the limited access to Russian press for western scientists during the Cold War. After that, more and more observations of carbon nanotubes have been reported. In 1976 Oberlin, Endo, and

Koyama clearly showed hollow carbon fibers with nanometer-scale diameters using a vapor-growth technique and proposed a growth mechanism with catalytic effect[6]. In 1981 a group of Ukrainian scientists published the chemical and structural characterization of carbon nanoparticles produced by a thermocatalytical disproportionation of CO. Based on the TEM images and XRD patterns, the authors indicate that their "carbon multi-layer tubular crystals" were formed by rolling graphene layers into cylinders. Many different arrangements of the graphite hexagonal nets are possible for such rolling process. They pointed out two possible arrangements. One is circular arrangement, which will result in the armchair nanotubes. The other is a spiral, helical arrangement, which will result in the chiral tubes.

However, none of these discoveries of carbon filaments, carbon nanotubes, reached the impact of the 1991 Iijima paper in NATURE[7]. There are many reasons for this. One is that carbon filaments and nanotubes have long been investigated for a better understanding of the growth mechanisms so that they could be avoided in coal and steel industry processing and in the coolant channels of nuclear reactors. Another reason is related to the level of maturity of science. The available materials, related theory, investigation instruments, scientific minds, etc at that time were not ready for people to think "nano". In comparison, Iijima's paper in 1991[7] achieved significant impact, which resulted from several favorable factors, a high quality paper, a top-ranked journal read by all kinds of scientists worldwide, a boost from the its relation to the fullerenes, remarkably improved characterization instrument, and a fully mature scientific audience ready for "nano" Nanotube research accelerated greatly following the discoveries of single-walled carbon nanotubes and methods to specifically produce them by adding transition-metal catalysts to the carbon in an arc discharge[8, 9].

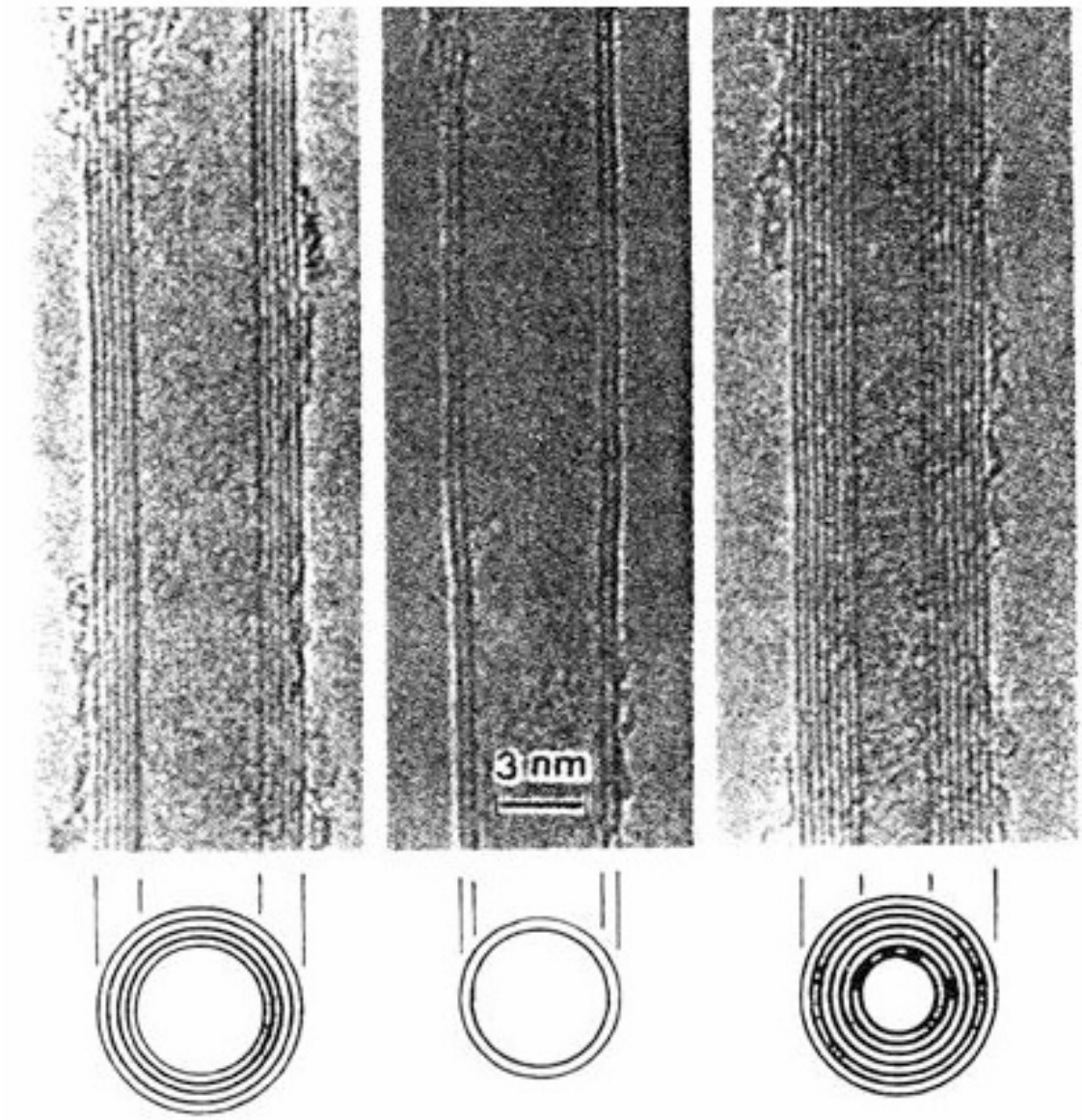

Figure 1.2: Electron micrographs of microtubes of graphitic carbon. Parallel dark lines correspond to the (002) lattice image of graphite, a cross-section of each tubes is illustrated. (a) Tube consisting of five graphitic sheets, diameter 6.7 nm. (b) Two sheet tube, diameter 5.5 nm. (c) Seven-sheet tube, diameter 6.5 nm, which has the smallest hollow diameter (2.2 nm).[7]

Figure 1.2 presents the needle-like structure of carbon nanotubes found by Iijima from the cathode-discharged by-product of graphite rod. High resolution transmission electron microscopy (HRTEM) revealed that this structure was composed by coaxial rolls of graphite sheets, where the distance between each roll was identical to the lattice

constant along the c-axis of graphite, which is ~0.34 nm. These kinds of carbon nanomaterials are called multi-walled nanotubes (MWNT), which always consist of multiple layers of graphite rolled in on themselves to form a tube shape and can be described with a Russian Doll model. In contrast, single-walled nanotube can be conceptualized by wrapping one-atom-thick layer of graphite hexagonal network, called graphene, into a seamless cylinder. The ends of carbon nanotubes are sometimes capped with half of a fullerene molecule.

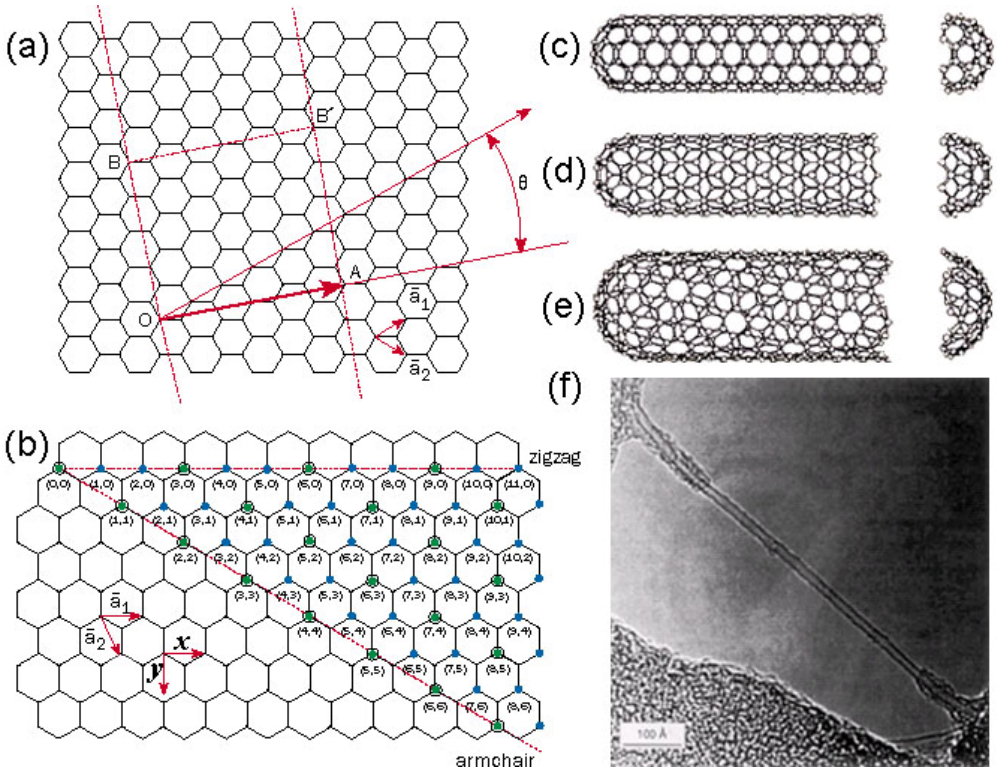

Figure 1.3: (a-b) Schematic of a graphite sheet showing different rolling directions to form carbon nanotubes. (c) Armchair carbon nanotube. (d) Zigzag carbon nanotube. (e) Chiral carbon nanotube. (f) TEM image of a SWNT.

People usually adopted Hamada's notation[10] to describe a single-walled nanotube, in which a tubule can be represented by an index (m, n), or a chiral vector,

$$\vec{C} = n\vec{a}_1 + m\vec{a}_2 = a\sqrt{3}\left[(n+\frac{m}{2})\vec{x} + \frac{\sqrt{3}}{2}m\vec{y}\right],$$

where $\vec{a}_1$ and $\vec{a}_2$ are unit vectors and n and m are integers. Figure 1.3a has been constructed for (n, m) = (4, 2), and the unit cell of this nanotube is bounded by OAB'B.

The chiral vector defines the circumferential direction of the nanotubes, thus the nanotube circumference C is given by

$$C = \left|\vec{C}\right| = a\sqrt{3(n^2 + nm + m^2)}$$

There are some other parameters commonly used for nanotubes, such as the diameter d_t, and chiral angle θ. Although the valid combination of d_t and θ could be infinite, a carbon nanotubes can only be formed with a limited number of d_t and θ set when the boundary condition and the symmetry of the carbon hexagon. The diameter d_t and chiral angel θ of a single-walled carbon nanotube can also be expressed in terms of *n* and *m*, as shown below.

$$d_t = C/\pi = a\sqrt{3(n^2 + nm + m^2)}/\pi$$
$$\theta = tg^{-1}[\sqrt{3}m/(m + 2n)]$$

The physical properties of single-walled carbon nanotubes are closely related to the chirality, or the direction the nanotubes are rolled. Three types of nanotubes have been observed based on their chirality: armchair (Figure 1.3c), zigzag (Figure 1.3d), and chiral (Figure 1.3e). The armchair nanotube has a chiral angle of 30° with *n=m* for the chiral vector. "Armchair" nanotubes correspond to the configuration with no "twist" in the rolling. In comparison, Zigzag nanotube has a chiral angle of 0° with either *n* or *m* is zero for chiral vector. As can be clearly seen in Figure 1.3d that "zigzag" should comes from the zigzag edge of this type of nanotube. When the chiral angle is between 0°and 30°, the nanotube becomes a chiral one. Chirality of the nanotube is directly related to the electrical conductivity. Armchair nanotubes have always metallic conduction. For other nanotubes, there is simple rule for the relation between the chirality and the electrical property. If $n - m = 3q$ (where *q* is an integer), the nanotube is metallic. Otherwise, the

nanotube will be semiconducting. In theory, metallic nanotubes can have an electrical current density more than 1,000 times greater than metals such as Ag and Cu. At the same time, many other carbon nanotubes have the same electronic properties as a semiconductor, where electrons must overcome a bandgap in order to enter the conduction band.

Although the chirality of the nanotubes determines whether it's metallic or semiconducting, the chemical bonding between the carbon atoms is exactly the same in both cases. The reason behind this supervising phenomenon is due to the special electronic structure of two-dimensional graphite sheet, which is a semiconductor with a zero band gap. Besides the chirality of the nanotube, the diameter can also affect the conductance as well. The band gap in a semiconducting nanotube is inversely proportional to the tube diameter. When the diameter is greater than 3 nm, the band gap is comparable to the thermal energies at room temperature.

Though carbon nanotubes have some properties for promising application, they have also some challenges to overcome before their realistic commercialization. As mentioned above, the electronic properties of carbon nanotubes depend on their chirality and vary slightly with the diameter. However, the control over the chirality is still not available for current synthesis techniques, and metallic and semiconducting nanotubes are always formed side by side. The heterogeneity of as-synthesized single-walled carbon nanotubes precludes their widespread application in electronics, optics and sensing. This forms developing attempts to separate different nanotubes post-synthesis. Recently people have investigated some sorting techniques, such as AC dielectrophoresis[11] or density-gradient ultracentrifugation[12] to separate different carbon nanotubes accordingly to their conductivity or size. However, current sorting techniques have still scale-up problems or others to overcome before the realization of the practical isolation of different carbon nanotubes according to their electrical property and size in a large yield and reasonable low cost.

While improving the uniformity and yield during the synthesis and investigating better post-synthesis sorting techniques for carbon nanotubes, people have also worked on many other materials. Various tubular forms other than carbon nanotubes have been reported so far. Notable examples are including BN[13], $B_xC_yN_z$[14], metal dichalcogenides such as WS_2[15] and MoS_2[16], V_2O_5[17], and GaN[18].

1.1.2 Nanowires

Nanotubes, especially carbon nanotubes, have achieved great success so far and inspired tremendous research interests in nanoscience and nanotechnology. The term 'nanowire' is widely used to represent one-dimensional nanostructures. Some researchers are still working on the mono-structured carbon nanotubes with the same chiral angle and diameter, while the others have started to work on another category of nanostructures, i.e. nanowires. Unlike carbon nanotubes, nanowires have been grown with well controlled structures by tailoring synthesis conditions. As a result, uniformity can be expected in crystal structure, chemical composition, electrical property, and others from nanowires.

Just like nanotubes, nanowires and nanorods are considered one-dimensional nanostructures because only their cross-sections are in the nanoscale. The cross-section of a nanowire is negligibly small compared with its extremely long length. In contrast, the cross-section and the length of nanorods are within an order of magnitude of each other. In other words, the nanorod could be considered as a "short version" of the nanowire and become a simple subgroup of this nanostructure. As such, the term "nanowire" will be referred as the large class of materials, including both the extremely long and thin nanowire and the relatively short and thick nanorod.

Nanowires have been successfully synthesized out of a wide range of materials, including elemental materials (Si[19], Ge[20], B[21], Au[22], etc), binary oxide (SiO_2[19, 23], Ga_2O_3[24], MgO[25], TiO_2[26], etc), nitride (GaN[27, 28], AlN[29], and InN[30]), boride (CeB_6[31] and LaB_6[32]), metal carbide (TiC, NbC, Fe_3C, SiC, and BC_x[33]), and

metal chalcogenide (CdS[34], CdSe[35, 36], CdTe[36], etc), and ternary materials ($BaTiO_{3[37]}$, $SrTiO_3$[37], $K_2Ti_6O_{13}$[38], etc) as well. With the improvement of present synthesis method and the developing of new techniques, more and more nanowires are expected to come. Not only did those nanowire structures provide ideal systems for studying transport processes of one-dimensionally confined objects and related fundamental phenomena, but they are also very important for developing new generation nanodevices with high performance.

Similarly to quantum dots and nanotubes, one particular nanowire material has been the focus of a large amount of research. In the late 1990's, research in nanowires was dominant by silicon, which is of remarkable importance in semiconductor industry. The main synthesis technique for the growth of Si nanowires is physical vapor deposition (PVD). In this technique, a source material, usually high purity silicon[19] or silicon dioxide[39], was sublimated with laser ablation[20] or elevated temperature evaporation[19]. The vapor was then transported to a cool zone where it deposited in the form of silicon nanowires. Chemical vapor deposition (CVD) is another technique for the synthesis of Si nanowires[40].

In most cases the growth of silicon nanowires are facilitated by metal catalyst and follows a vapor-liquid-solid (VLS) process, which will be discussed in detail later in this dissertation. This catalyst confined nanostructure growth has been proven to be a effective method for a precise size control. Figure 4 indicated clearly that the diameter of the nanowire is determined by the size of the metal catalyst particles. Taking advantage of the well-defined Au nanoclusters colloidal as catalyst, Cui et al.[40] has successfully synthesized monodisperse silicon nanowires via a VLS process. The SiNWs grown from 5, 10, 20, and 30 nm nanocluster catalysts had mean diameters of 6, 12, 20, and 31 nm, respectively, and the diameter distributions of the SiNWs mirror those of catalysts.

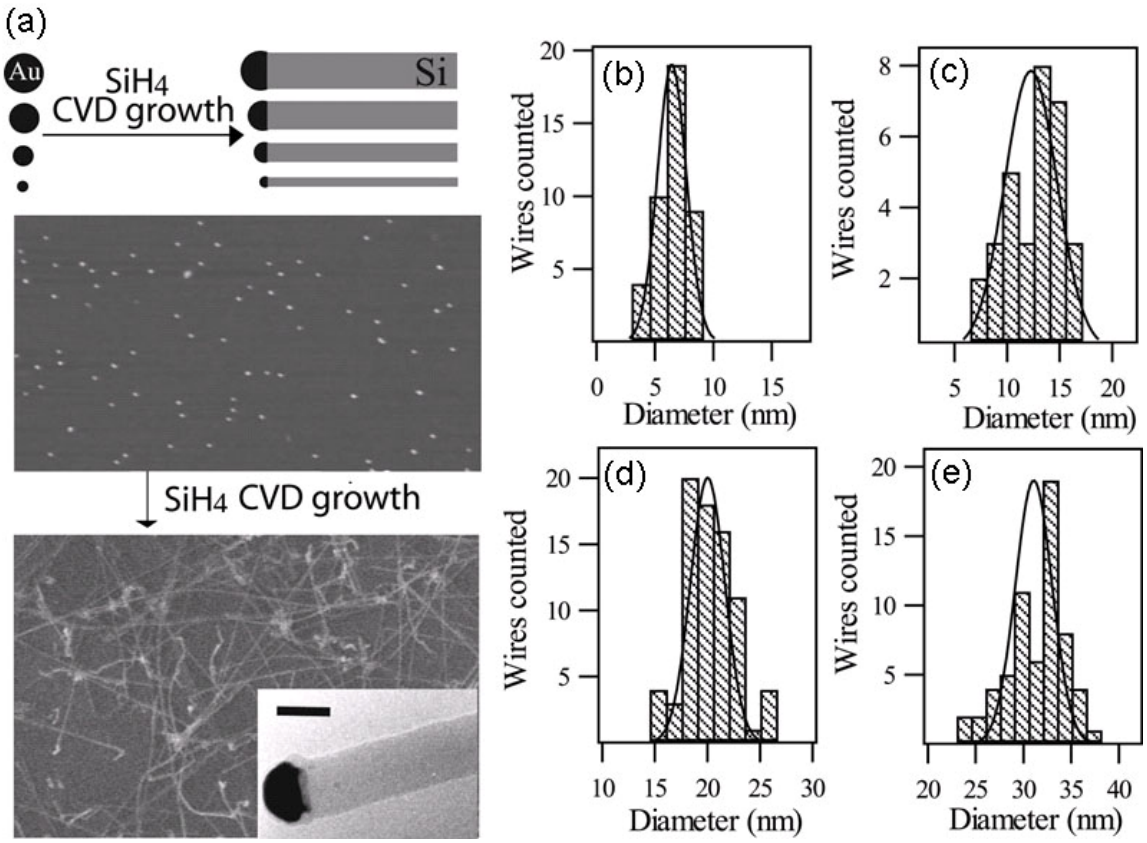

Figure 1.4: (a) Size-controlled synthesis of SiNWs from Au nanoclusters. (b-e) Histograms of SiNW diameters grown from 5-, 10-, 20-, and 30-nm-diammeter Au nanoclusters.

The well defined silicon nanowires assure the uniform property of the grown product, which is important for the commercial application. In addition, the electronic structure of silicon benefits silicon nanowires over nanotubes for certain applications. Whereas carbon nanotubes are either metallic or semiconducting and usually coexist in the grown product, silicon nanowires were always semiconducting in nature. This native property enables silicon nanowires to be directly applied to device fabrication, bypassing the hurdle that carbon nanotubes faced as there is no need for separation of different electronic types of nanowires.

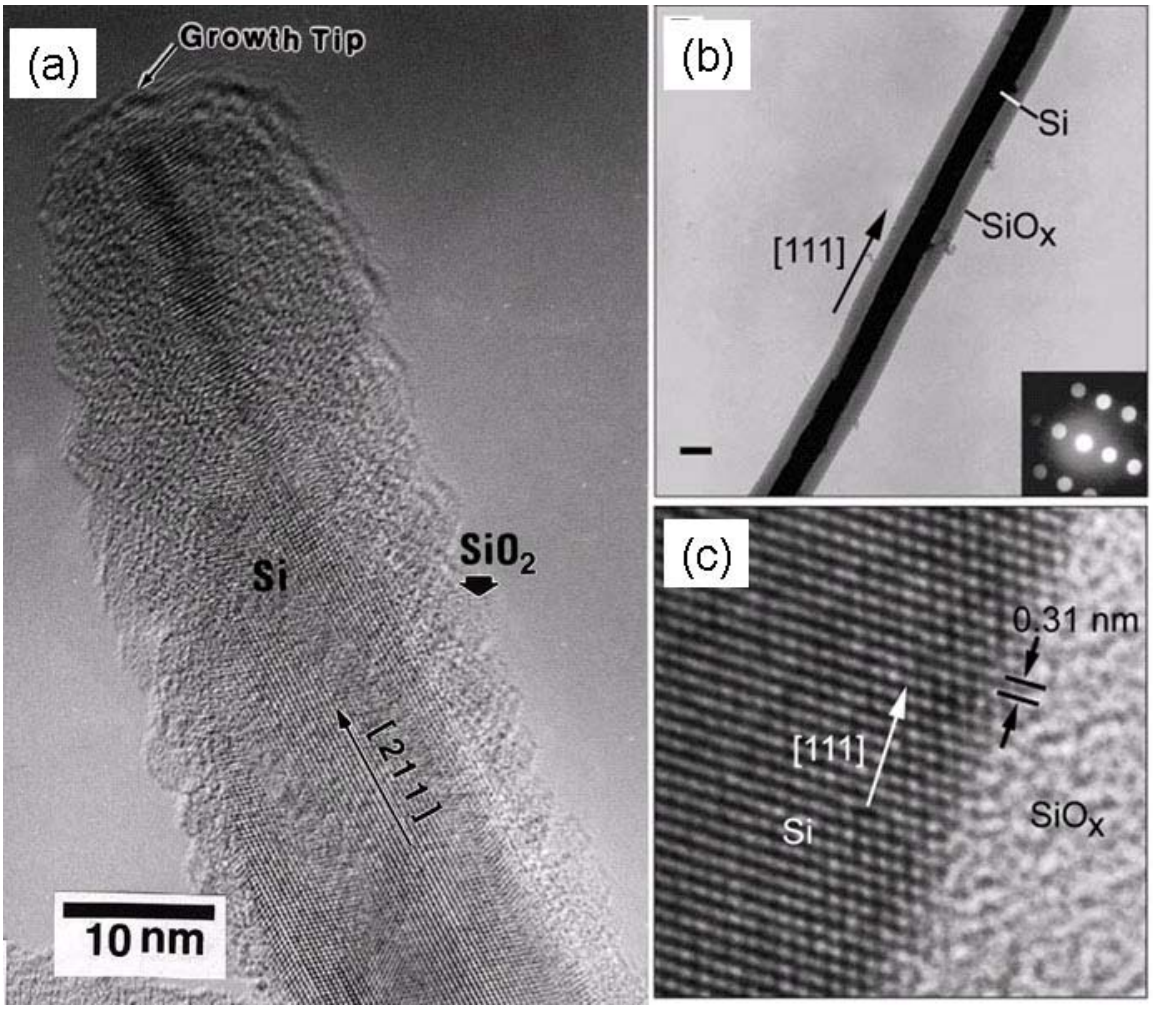

Figure 1.5: (a) High-resolution TEM image of nanowires showing a crystalline Si core and an amorphous SiO_2 sheath. (b) Diffraction contrast TEM image of a Si nanowire with lighter SiO_x sheath. (c) High-resolution TEM image of the crystalline Si core and amorphous SiO_x sheath.

Although people have achieved great success over the size control of silicon nanowires, silicon nanowires have had some problems, which retarded their wide applications. TEM analysis revealed that silicon nanowires are sometimes made of polycrystalline cores and have dislocations and defects incorporated into the nanostructures [41-43], as shown in Figure 1.5a. The growth defects can also cause bending and kinking during the growth of silicon nanowires.[41] When the diameter shrinks to the 1-3 nanometer range, silicon nanowires form cage compounds of Si_{24}-type

cluster in the core[42]. The grain boundaries in polycrystalline materials, as well as any dislocations that are present, serve as possible scattering events. Scattering events not only hinder the charging carriers, either electrons or holes, from moving through silicon nanowires, but they can also ruin a material's thermal transport properties. Thermal transport properties are very important in nanoscale electronics, partly due to the ultra-high device integration.

The ideal materials for electronic applications should be single-crystalline and defect free. Charles Lieber was the front-runner for the synthesis of single-crystalline silicon nanowires. Silicon nanowires with good crystallinity diameter of 6 to 20 nm were grown firstly with a laser ablation process in his group[20]. Later on, they adopted a chemical vapor deposition (CVD) method for the synthesis of single crystalline silicon nanowires with well defined diameters[40]. The new growth technique decreased the dislocation concentration and avoided grain boundaries within the nanowires, improving the quality drastically.

In spite of having a single-crystalline core and far fewer defects than previously grown silicon nanowires, the silicon nanowires grown either by CVD or laser ablation, still had an unavoidable passivation layer of SiO_2 sheaths surrounding them. This is also indicated in Figure 1.5b and Figure 1.5c[20]. The passivation SiO_2 is amorphous and electrically insulating, which can affect any semiconducting properties that the silicon nanowire might have.

Because of the difficulty to avoid the oxidation during the synthesis of the silicon nanowire or manipulation afterwards in air, post-synthesis treatment is necessary to deal with the issue of the SiO_2 passivation layer. Hydrofluoric acid treatment has been introduced and proven to be an effective method[44]. Not only does this treatment etch away the SiO_2 layer, it also leaves behind a hydrogen-terminated surface, which was confirmed by the atomically resolved scanning tunneling microscope (STM) image in Figure 1.6[44]. The hydrogen-terminated silicon nanowire surface seems to be more

oxidation-resistant than regular silicon wafer surface and results in a stable silicon nanowire. However, it is worth noting that hydrofluoric acid is a dangerous and toxic chemical reagent requiring special precautions for its safe handing.

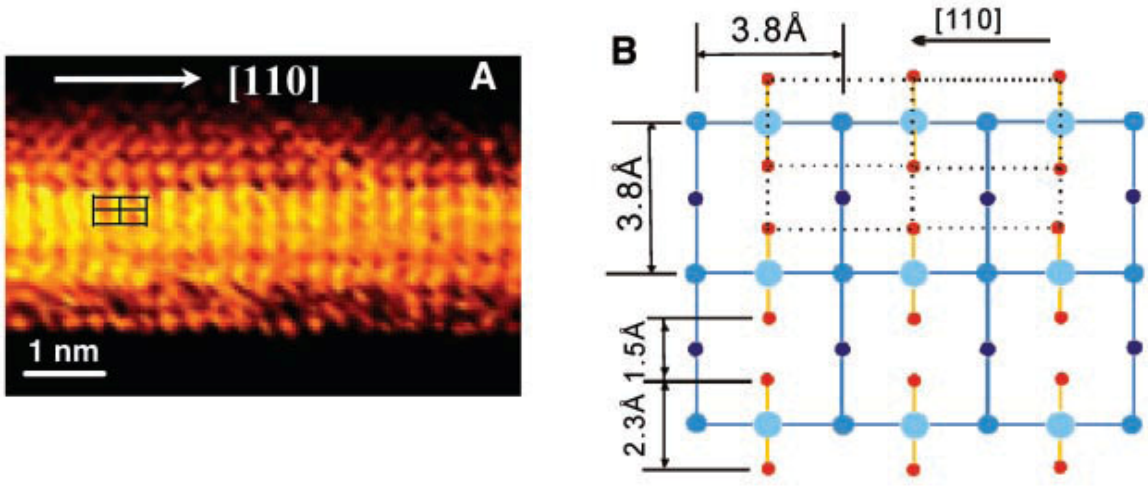

Figure 1.6: STM image and schematic view of a SiNW with a Si (001) facet after treatment with hydrofluoric acid. Crystallographic directions are shown. (a) Constant-current STM image of a SiNW on a HOPG substrate. (b) Schematic view of the dihydride phase on Si (001). Red and large blue circles represent H and Si atoms in the dihydride phase, respectively. Small blue circles correspond to Si atoms on the layers below.

While some researchers were working on the improvement of quality of silicon nanowires, others started to shift to other materials. Single-crystalline nanowires have been successfully discovered from group III-V and II-VI semiconductors [27, 45-47], which do not suffer the passivation sheath problem.

1.1.3 Nanobelts

As inspired by nanotubes and nanowires, 1D nanomaterials have become the research forefront in nanoscience and nanotechnology due to their novel electronic, optical, mechanical, and chemical properties. More and more 1D nanotubes or nanowires are discovered from different materials and proposed for different applications.

A group of transparent conducting oxides, ZnO, In_2O_3, Ga_2O_3, SnO_2, and CdO, presented a unique properties when doped with the correct constituents[48] (see Table 1). The commercial value of transparent conducting oxides has been recognized, and optoelectronic device application has been investigated, especially for tin-doped indium oxide (ITO) [49]. The transparent conducting oxides were widely used in the majority of flat panel display (FPD) applications. The market for FPDs in 2000 was estimated to be over $15 billion and was predicted to grow over $27 billion by 2005[50]. As a result, those transparent conducting oxides have the potential for more widespread applications and future funding as well. Dr. ZL Wang's group at Georgia Tech recognized the impact in nanotechnology if the transparent conducting oxides could be made into nanostructures and set up synthesis experiments through a physical vapor deposition technique. Their experiments resulted in the discovery of a new category of 1D nanostructure, which took a belt or ribbon shape with well defined side surfaces and was named nanobelt or nanoribbon[51] (Figure 1.7).

Table 1.1: Choice of transparent conductors.

Property	Material
Highest transparency	ZnO:F, Cd_2SnO_4
Highest conductivity	In_2O_3:Sn
Lowest plasma frequency	SnO_2:F, ZnO:F
Highest plasma frequency	Ag, TiN, In_2O_3:Sn
Highest work function, best contact to *p*-Si	SnO_2:F, $ZnSnO_3$
Lowest work function, best contact to *n*-Si	ZnO:F

Table 1 (continued)

Property	Material
Best thermal stability	SnO_2:F, TiN, Cd_2SnO_4
Best mechanical durability	SnO_2:F
Best chemical durability	SnO_2:F
Easiest to etch	ZnO:F, TiN
Best resistance to H plasma	ZnO:F
Lowest deposition temperature	In_2O_3:Sn, ZnO:B, Ag
Least toxic	ZnO:F, SnO_2:F
Lowest cost	SnO_2:F

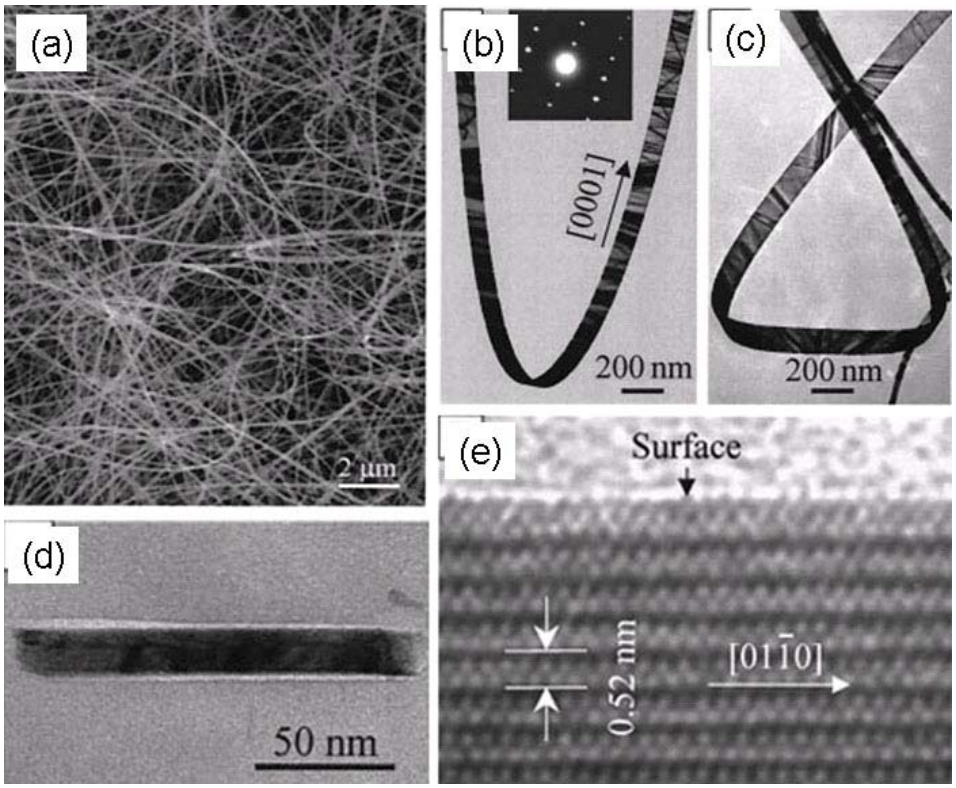

Figure 1.7: (a) Ultralong nanobelt structure of ZnO (with wurtzite crystal structure). (b-c) TEM images of several twisted ZnO nanobelts, displaying the shape characteristics of the belts. (d) Cross-sectional TEM image of a ZnO nanobelt, showing a rectangle cross section with width-to-thickness ratio of 9. (e) HRTEM image of a ZnO nanobelt.

As inspired by this discovery, belt-like nanostructures have attracted more and more attention since then and the research in functional oxide based 1D nanostructures is becoming a forefront research in nanotechnology. Although the first nanobelts were obtained from binary oxide such as, ZnO, SnO_2, In_2O_3, CdO, Ga_2O_3, and PbO_2[51], similar nanostructures have also been synthesized from elementary materials (Zn[52], Sn[53]), sulfides (ZnS [54] and CdS [55]), selenides (CdSe [56], ZnSe [57], and Bi_2Se_3[58]), Nitrides (GaN [59], AlN [60], Si_3N_4 [61], and InN [62]) and even ternary materials ($Bi_{12}O_{17}Br_2$[63], $BaCrO_4$[64], $CoFe_2O_4$[65], and $Pb_2V_2O_4$[65]).

The nanobelt is a unique group of 1D nanostructure. The increasing interests in them result from their outstanding properties. In most cases nanobelts are synthesized as single crystal. The excellent crystallinity ensures the high quality of those nanomaterials. Nanobelts usually have well-defined crystallographic planes. In other words, not only is the fastest growth direction well-defined, but the top and bottom (along the width) surfaces and the side (along the thickness) surfaces are well-defined crystallographic planes as well. The growth direction and the side surfaces are determined by the synthesis technique and growth conditions. This presents a possible way to tune the properties and catalytic surfaces of nanowires, which is of significant importance for the fundamental studying and practical application. Nanobelts are also essentially dislocation and defect free, although stacking faults have been observed in some nanobelts. Even if a stacking fault exists, it typically run through the whole length and never terminates within the nanobelts. The presence of dislocation is not energetically feasible due to the small size and extremely high surface area to volume ratio. The high quality of nanobelts in structure naturally leads to excellent optical, electrical, and mechanic properties. In addition, the belt-like geometry benefits this kind of nanomaterials to be certain building blocks or work as cantilever. The length of nanobelts can be very long and thickness is very small, while the width can be tailored in a wide range from one hundred nanometers to as small as six nanometers[66]. It is worth noting the difference between the nanobelt

and its bulk countpart. Many nanobelts are made of ceramic materials, which are very brittle and rigid in bulk. In comparison, nanobelts exhibit extreme flexibility. Because of the absence of dislocations, nanobelts should be very resistant to fatigue and failure.

Among all nanobelt materials, ZnO is most extensively studied. A great number of ZnO nanostructures based on ZnO nanobelts have been found. These unique nanostructures unambiguously demonstrate that ZnO probably has the richest family of nanostructures among all materials, both in structures and in properties. ZnO in bulk has two possible phases, including Wurtzite and Zinc blend, while ZnO nanobelts are always in wurtzite phase (hexagonal, space group P63mc).

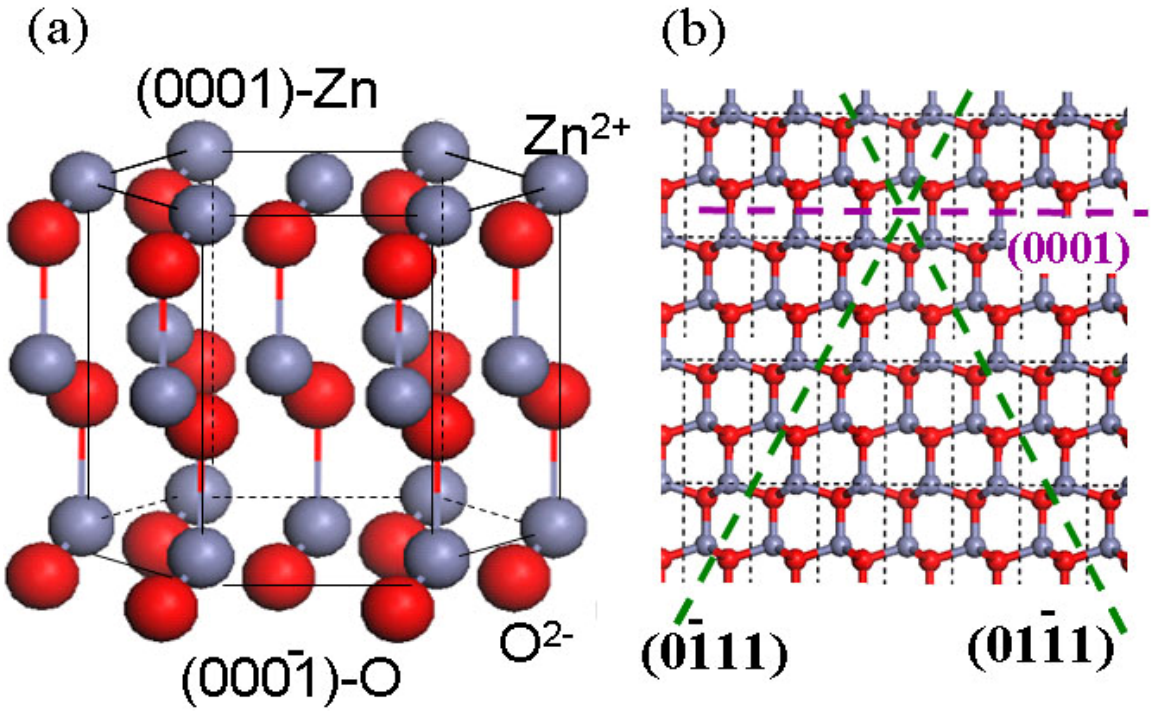

Figure 1.8: Atomic model and projection along $[2\,\bar{1}\,\bar{1}\,0]$ of wurtzite-structured ZnO.

Being a wurtzite-structured oxide with lattice parameters a=0.3296nm and c=0.52065 nm, ZnO can be simply described as a number of alternating planes composed of tetrahedrally coordinated O^{2-} and Zn^{2+} ions, stacked alternately along the c-axis(Figure 8-0 a). The non-centrosymmetric structure results in piezoelectricity and spontaneous

polarization in ZnO. The strongest polarity occurs along c-axis with positively charged Zn-(0001) polar surface and negative charged O-(000) polar surface (Figure 1.8. The polar surfaces often have facets or surface reconstruction to maintain a stable structure. On the contrary, ZnO (0001) are atomically flat, stable and without reconstruction in ZnO nanobelts.

Wurtzite-structured ZnO has three set of lowest energy surfaces within the crystal, $\{0001\}$, $\{01\bar{1}0\}$, and $\{2\bar{1}\bar{1}0\}$, and three fast growth directions, [0001], $[01\bar{1}0]$, and $[2\bar{1}\bar{1}0]$. Four possible nanobelt configurations and their crystallographic orientations with respect to one another are illustrated in Figure 1.9. The four types of nanobelts in Figure 1.9 are the most common ZnO nanobelts observed experiments, although nanobelts grown along other directions are also possible. Among all growth directions, [0001] direction is the fastest growth direction among Wurtzite crystal. As a result, ZnO nanobelt grown along [0001] with the No 1 configuration in Figure 1.9 are commonly observed in different synthesis experiment. This kind nanobelt has non-polar surfaces as its side surfaces. No 2 configuration has a growth direction of $[01\bar{1}0]$ and polar ± (0001) surface as its smaller side surfaces. A stacking fault along the whole length is always observed in this kind of nanobelt, which can reduce the barrier to growth. In comparison, No 3 and No 4 configuration have a growth direction along $[01\bar{1}0]$ and $[2\bar{1}\bar{1}0]$ respectively and have polar ± (0001) surfaces as their primary (larger) side surfaces. Thus, these nanobelts in no. 3 and no. 4 configuration are also defined as polar-surface-dominated (PSD) nanobelts. Based on their geometry and crystallographic orientation, polar-surface-dominated nanobelts have induced a great variety of novel nanostructures, which will be discussed in detail later.

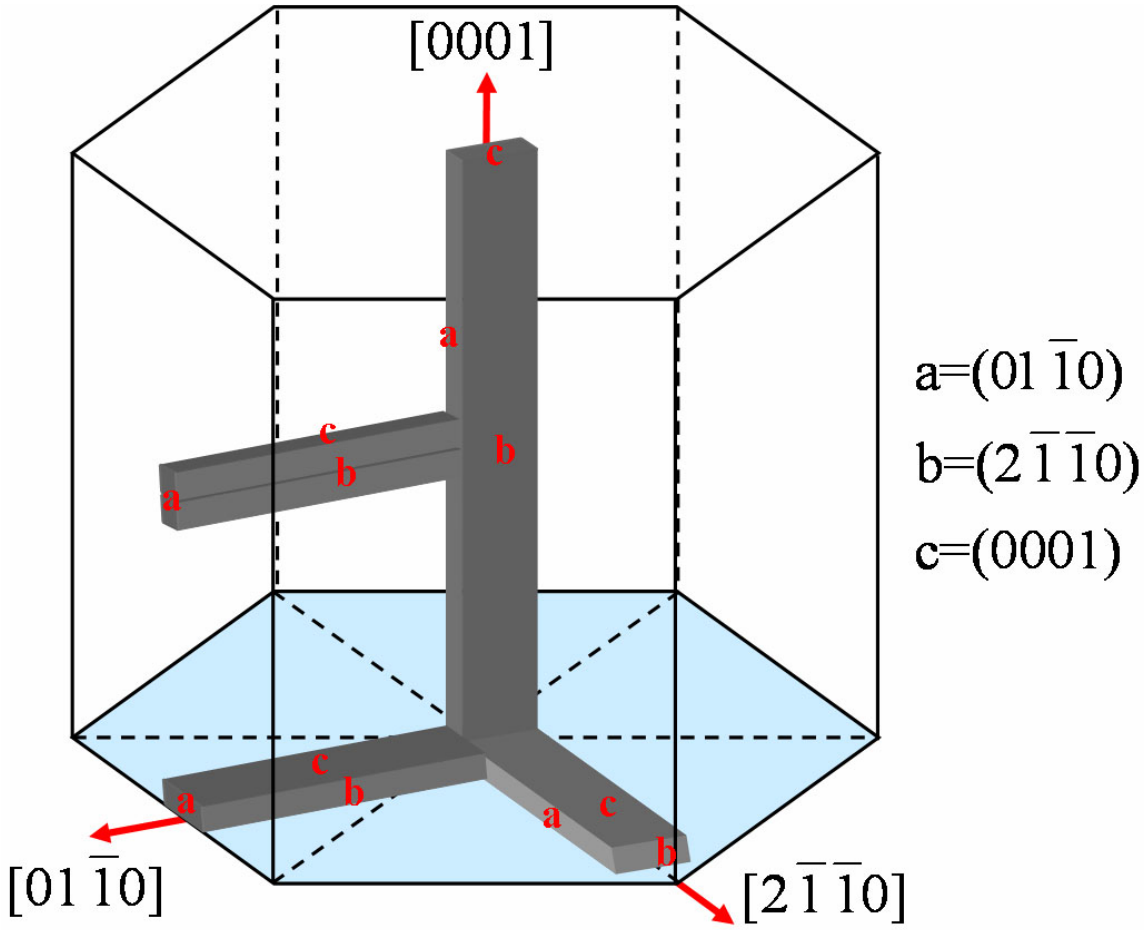

Figure 1.9 Schematic showing 4 types of ZnO belts and their crystallographic orientations with respect to one another, where a, b, c are the three defining surfaces of each belt. Configurations 3 and 4 are polar-surface-dominated (PSD) belts.

1.2 Hierarchical Nanostructures

Carbon nanotubes and silicon nanowires brought wide attention to 1D nanostructures, while the discovery of semiconducting nanobelts provided a new type of nanoscale building blocks with precisely defined size, shape, and composition. Furthermore, unique or enhanced properties have also been revealed from those nanostructures due to their high surface-to-volume ratio, size confinement effect, and high-quality crystallinity. Numerous novel applications have thus been proposed and even demonstrated in laboratories in diverse fields of optics, electronics, mechanics, and

biomedical science. The integration of nanostructure elements into variety of nanodevices for practical applications requires significant further development and breakthrough in many research respects. One step towards this goal is the growth of hierarchical nanostructures from the atomic lever via self-assembly process, which is an elegant concept for the production of the next generation miniaturized devices. Controlling growth of materials opens the way to fabricate regular highly perfect structures without any top-down tool making it far less cost intensive and widening the application range. In addition, conjunction and integration of self-assembled process and structures with lithography based nanofabrication techniques is the key of bridging “bottom-up” with “top-down” approach in nanotechnology. By combining tailored self-assembly processes (a "bottom-up" approach) with conventional lithographic processes (a "top-down" approach), the ever-present thirst of the consumer for faster, better, and cheaper devices are becoming more realistic in a very simple, yet robust, ways.

1.2.1 Self-assembly induced Hierarchical Nanostructures

Nature is a master in self-assembly of proteins. In nanoscience and nanotechnology, self-assembly is referred to as a 'bottom-up' manufacturing technique in contrast to a 'top-down' technique such as lithography where the desired final structure is carved from a larger block of matter. As inspired by the discovery of oxide nanobelts[51], research into functional 1D nanostructures is expanding rapidly and coming to the forefront of research in nanotechnology.

1.2.1.1 Novel Nanostructures of ZnO

Among numerous nanomaterials, the most typical and successful example should be ZnO, which mainly benefits from three factors, direct wide bandgap semiconduction, piezoelectricity, and biocompatibility.

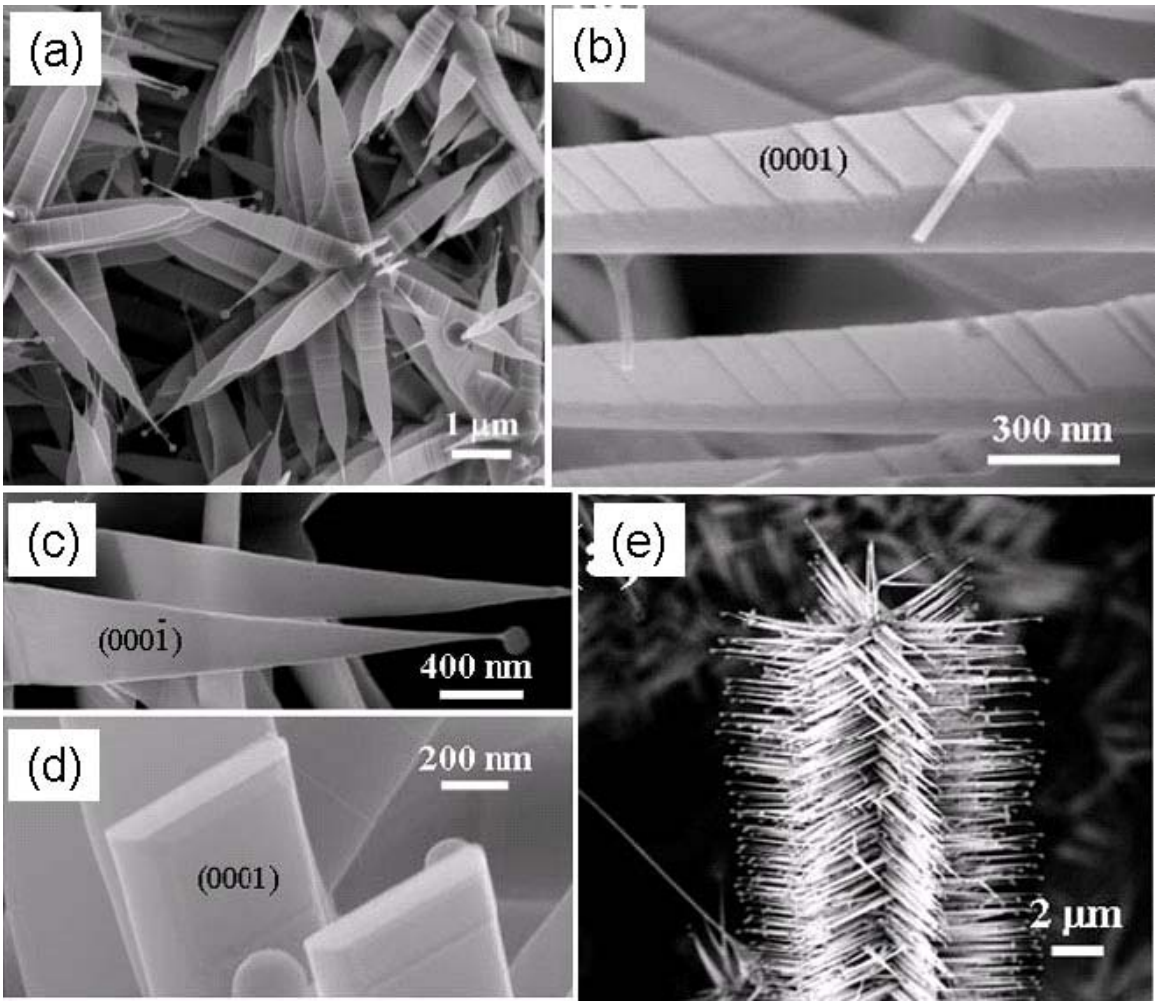

Figure 1.10 (a) SEM images of six-fold symmetrical ZnO nanopropeller arrays. (b) Front view of two individual blades, showing surface steps. (c) Back side view of the bottom surfaces of nanoblades, showing smoother surface. (d) Trapezoid cross section of nanoblades. (e) A single column of the as-synthesized ZnO nanopropeller arrays.

Wurtzite-structured ZnO has three types of fast growth directions, <0001>, <01 $\bar{1}$ 0>, and <2 $\bar{1}$ $\bar{1}$ 0>. Those fast growth directions, combing with the polar-surface-induced phenomena, resulted in a diverse group of ZnO nanostructures, and this forms probably the richest family of nanostructures among the entire family of 1D nanostructures, even including carbon nanotubes. Among many synthesis techniques, thermal evaporation is very versatile and has been used for synthesis of a variety of ZnO

nanostructures, such as nanocombs[67], nano tetralegs[68], nanopropellers[69], nanohelixes[70-72], nanorings[70, 73], and nanobows.[74]

Figure 1.10 presents ZnO nanopropellers, which were fabricated by a two-step high temperature solid-vapor deposition process. A mixture of ZnO, SnO_2, and graphite powders were placed in the middle of a tube furnace and served as source materials. The N_2 carrier gas flow through the tube at 20 sccm during the synthesis, and a polycrystalline Al_2O_3 substrate was placed downstream for collecting the nanostructures. Figure 1.10a present the top view of as-grown ZnO propellers. Each column of a nanopropeller is of a diameter ~10 μm and consists of six arrays of triangular shaped blades of 4-5 μm in length. A tiny Sn ball of a diameter ~50 nm can always be found at the tip of the blade. All the blades have a uniform isosceles triangular shape and different top and bottom surface morphology. A closer side view of the top surface in Figure 1.10b clearly shows steps across the width the blade. In comparison, the bottom surface in Figure 1.10c is flat and much smoother. A broken blade in Figure 1.10d reveals its trapezoid cross section.

Besides the closely packed columns of nanopropeller arrays in Figure 1.10a, free standing nanopropeller arrays have also been observed at a lower growth temperature region. Figure 1.10e is a side view of a separated column of ZnO nanopropeller arrays. This ZnO nanopropeller consists of hexagonal symmetrical array of ZnO triangular blades, which are about 20-500 nm in width and 4-5 μm in length and always have a tiny Sn ball on the tip as well.

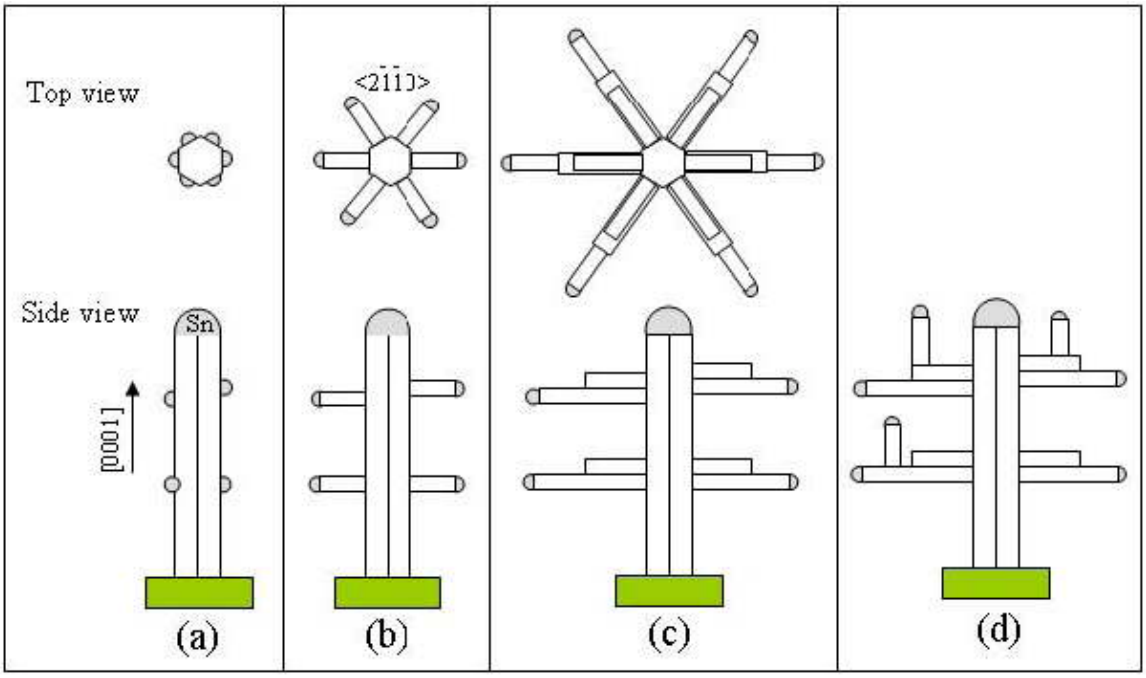

Figure 1.11 Schematic growth process of the nanoblades arrays. The diagram shows only one column of nanopropeller array for simplicity of illustration.

The Sn balls on the tips of blades indicate the growth of ZnO is dominated by the vapor-liquid-solid (VLS) process. The self-catalysis process might also play an important role, because ZnO can be self-catalytic active and ZnO nanocantilever arrays have been grown on polar surfaces without using catalyst[75]. At the elevated temperature, ZnO and SnO_2 powders in the middle of the tube are reduced by graphite and released vapor containing Zn, ZnO, Sn, and O. The entrained N_2 gas carries all vapor downstream and result in liquid Sn balls on the collecting substrate. Those Sn balls initiate the fast growth of ZnO nanowires along [0001] and enclosed by $\{2\bar{1}\bar{1}0\}$ side surfaces[76] (Figure 1.11a). Incoming Sn vapor condenses later on the side surface and initiates the epitaxial growth of ZnO nanobelts along the six equivalent radial directions, $\pm [2\bar{1}\bar{1}0]$, $\pm [11\bar{2}0]$, and $\pm [1\bar{2}10]$, forming the hexagonal symmetric nanoblades (Figure 1.11 b). The nanoblades grow also transversely as the growth proceeds along $<2\bar{1}\bar{1}0>$, resulting in the trapezoid-shaped blades with steps on the top surface (Figure 1.11 c). The later

condensed Sn droplet on the surface of the nanoblades can also lead to the secondary nanowires along c-axis (Figure 1.11d).

1.2.1.2 Nanowire Networks

Nanowires have been studied intensively not only because low dimensionality and their interesting intrinsic properties, but also due to their unique properties arising from quantum confinement effects and their capability for direct nanosystem integration. To date, nanoscale building-block assemblies for applications such as nanocomputing, nanosensors, and nanophotonics require intensive interwire communications (e.g. efficient charge transport), high surface areas, excellent accessibility, and mechanical robustness. Fabrication of 3D nanowire networks with controlled diameters and arrangements of the wire, tailored pore structures, and effective interwire connectivity is therefore paramount for new device applications. Current inverse opal networks[77] are limited by the large diameters of the wire that may preclude quantum effects. Accordingly, new techniques are needed for the growth of nanowire networks.

So far, nanowire networks have been synthesized from various materials with different techniques. Solid vapor deposition is one of the commonly used techniques for the growth of 1D and complex nanostructures. Through carefully designing the experimental setup and tuning the synthesis conditions, researchers have obtained nanowire networks form PbSe[78], In_2O_3[79, 80], tetragonal $WO_{2.9}$[81], $WO_{3-\delta}$[82], trigonal Se[83], and ZnO[84]. Solution-based chemistry is another widely studied technique for the synthesis of nanostructures and result in some nanowire networks as well, such as AuCu[85], $AuCu_3$[85], Au[86]. Based on a templated electrodeposition technique, Dr. D.Wang, et al. proposed a general synthetic rout to nanowire networks of metals or semiconductors[87], such as Pd, Pt, Co, PtNi, CdSe, CdS, and Bi_2Te_3.Some other techniques have also successfully produced nanowire networks of Cu[88], SiC[89],

Al-Si[90], HfS_2[91], and Rb[91].Figure 1.12 listed some of the nanowires have been synthesized so far[78, 79, 83-85, 87].

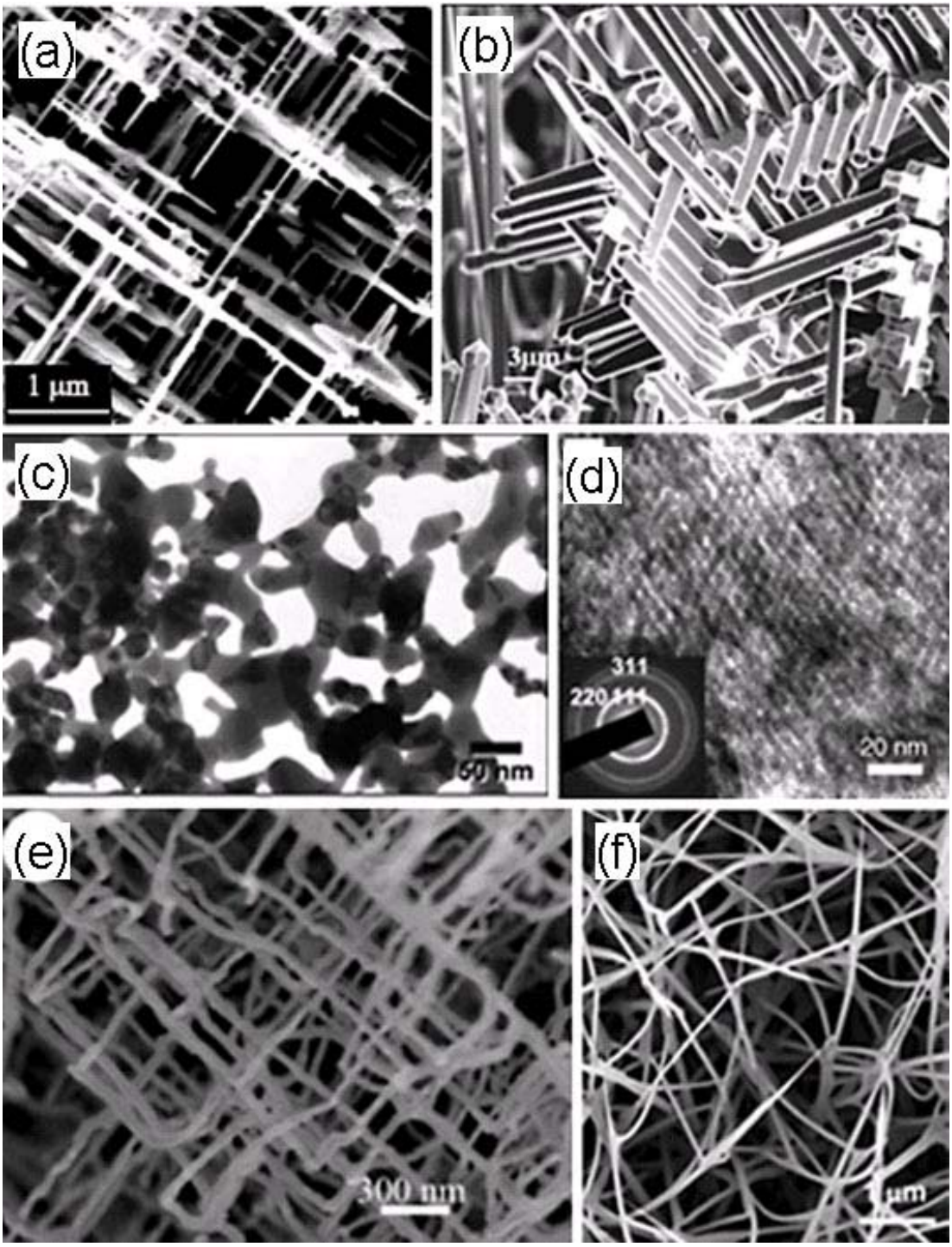

Figure 1.12 A collection of nanowire networks from different materials: (a) PbSe, (b) In_2O_3, (c) $AuCu_3$, (d) CdSe, (e) Se, and (f) ZnO.

Among functional oxides, tungsten oxides ($WO_{3-\delta}$) are of great interest and have been investigated widely due to their outstanding electrochromic, optoelectronic, and gaschromic properties. Although 1D tungsten oxide nanostructures have been developed[92], ordered superstructures or complex functional architectures will offer great opportunities for exploring their novel properties and for the fabrication of nanodevices[93] including three-dimensional nanoelectronics. Three-dimensional (3D) tungsten oxide nanowire networks were synthesized using a thermal evaporation approach, in which W powder were sprinkled on a W boat and thermal evaporated in the presence of oxygen. Figure 11a show the typical morphology of the as-synthesized products with high yield. High-magnification SEM image in Figure 11b clearly demonstrates 3D network, which are formed from intercrossed polygonal tungsten oxide nanowires. This $WO_{3-\delta}$ nanowires are of width 10-180 nm and along three perpendicular directions. No obvious stem was observed in this network. The high crystallinity was revealed in TEM analysis, as indicated in Figure 11 c-f. Figure 11c illustrated a typical TEM image of a broken $WO_{3-\delta}$ nanowire network segment. The angel between branches are nearly 90°, which is consistent with the observation in SEM. Selected-area electron diffraction (SAED) patterns in Figure 11d-f prove that the entire network is single crystal. Index of SAED indicates that the nanowires grow along six equivalent <100> directions and intersect with each other to form the 3D network.

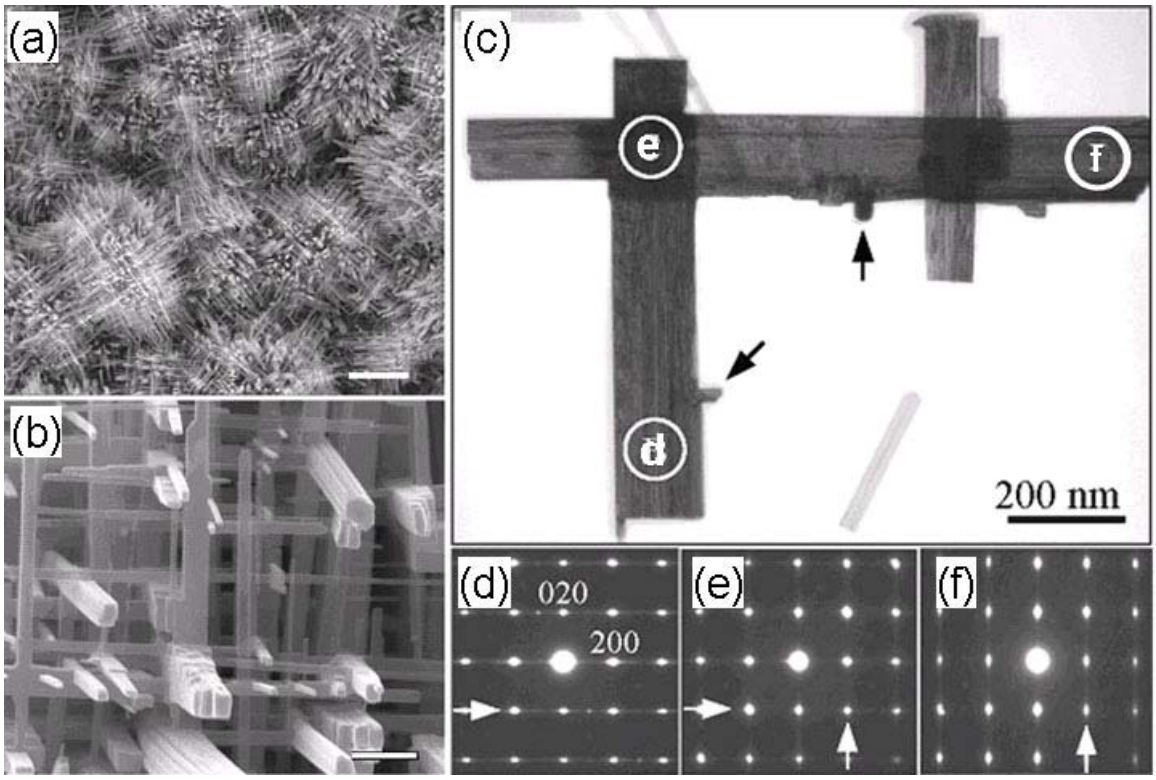

Figure 1.13 (a) Low-magnification and (b) High-magnification SEM images of the tungsten oxide nanowire networks. (c) TEM image of a network segment. (e-f) SAED patterns of regions d, e, and f in (a).

1.2.2 Lithography-assisted Hierarchical Nanostructures

The emerging nanostructures via self-assembly have provided us with building blocks of various size, shape, and composition. Based on their morphology and unique properties, a diversity of novel applications has thus been proposed and even demonstrated in laboratories. However, assembling nanostructures into devices is still challenging due to the difficulties in manipulating structures of such small size. Hybrid top-down and bottom-up nanomanufacturing can help with massive and parallel integration of nanostructures into devices.

1.2.2.1 Patterned, Aligned ZnO Nanorod Arrays

Being a functional transparent semiconducting oxide with piezoelectricity and biocompatibility, 1D ZnO nanostructures have attracted wide research interest in for variety promising application in optics, electronics, mechanics, piezotronics, and biomedical science. Integration of the nanowires into useful devices requires placing them in specific positions, orientation, and density with desired configurations reproducibly. Numerous 1D nanostructures have been grown with the initiation and guidance of catalysts via a VLS process[45], while nanosphere lithography (NSL) provides an inexpensive, inherently parallel high-throughput, and materials general nanofabrication technique[94]. Combining the two advanced techniques can lead to patterned growth of aligned ZnO nanorods for nano-optoelectronic, nanosensor, and nanogenerator applications [95, 96].

SEM images in Figure 1.14 illustrated the fabrication process for the hexagonally patterned ZnO nanorod arrays. The synthesis process involves three main steps. Using a nanosphere lithography (NSL) technique, a two-dimensional, large area, self-assembled and ordered monolayer of submicron polystyrene is firstly introduced onto the single-crystal Al_2O_3 substrate, as shown in Figure 1.14a. After that, a thin layer of Au catalyst particles is dispersed on the substrate with thermal evaporation or sputtering technique. Etching away the polystyrene sphere with toluene produces a highly ordered hexagonal gold pattern (Figure 1.14b). Finally, ZnO nanowires are grown on the patterned catalysts through a VLS process (Figure 1.14c). As can be seen from this growth process, the spatial distribution of the ZnO nanowires is determined by the catalysts pattern. Using a variety of mask technologies can produce ZnO nanowire arrays of complex configuration and well-controlled density. During the growth of ZnO nanowires, the lattice mismatch between the bottom substrate and ZnO is very important for the growth direction and alignment. Choosing the optimum match can result in the epitaxial grown of ZnO nanowires normal to the substrate. Above all, the distribution of the catalysts particles

determines the density and location of the nanowires, and the vertical alignment can be achieved with the epitaxial growth of nanowires on the substrate. A synthesis process combining those two can achieve site, density, and orientation control and result in patterned nanowire arrays in large area.

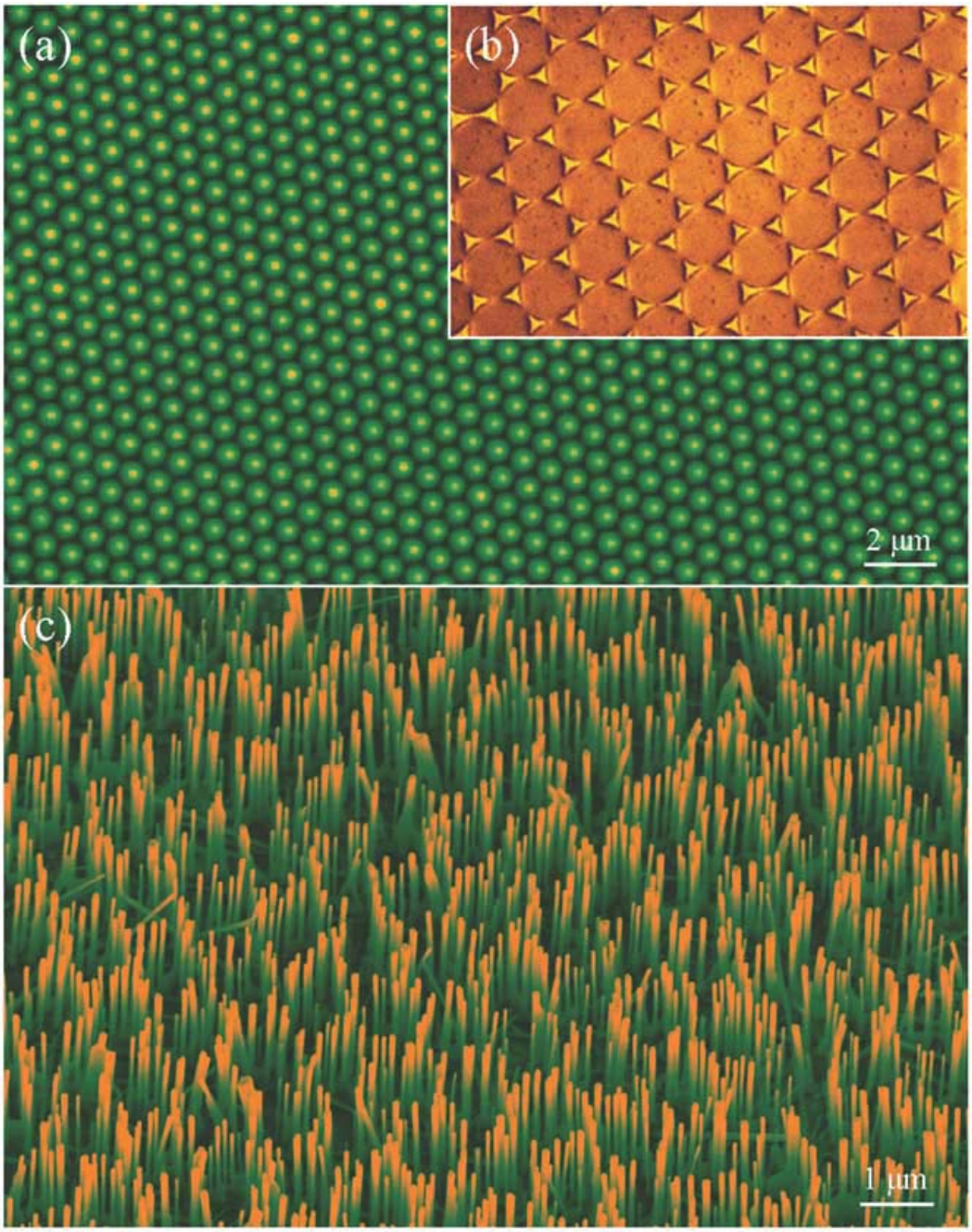

Figure 1.14 (a) SEM images of a self assembled monolayer of polystyrene (PS) spheres; (b) Gold catalyst patterns generated PS monolayer as mask. (c) A side view of the aligned ZnO nanowire arrays.

In addition, the same strategy can also be applied to other materials. For example, Using hot filament plasma-enhanced chemical vapor deposition (PECVD), Huang et al. have grown periodically arranged carbon nanotubes on NSL-induced nickel dots pattern[97].

1.2.2.2 Position-Controlled Nanowire Complex

The discoveries of increasingly complex structures open the door to more complex 3D materials and devices exploiting the unique properties of nanomaterials. However, greater control is needed in order to make commercial use of these promising structures. A combination of top-down techniques with complex nanostructures might provide a feasible way to incorporate functional nanostructures into specified positions and allow for their incorporation into more complex devices. This strategy has resulted in the production of position-controlled interconnected InAs nanowire networks[98] and ordered GaP nanotrees[99] .

These position-controlled nanowire networks are achieved by the combination of top-down lithographic processing, which defines the position of the first generation nanowire trunk, and bottom-up epitaxial growth, which results in highly crystalline nanowires of selected length, diameter, and orientation. Sequential levels of semiconductor nanowires are grown to form the interconnected nanowire networks eventually.

In comparison with the nanosphere lithography (NSL) in the previous section, e-beam lithography is used to produce initial patterned catalysts. Metal-organic vapor phase epitaxy (MOVPE) is used for the growth of nanowires. The substrates have to be carefully selected to make sure that the nanowires will grow vertically to serve as trunks. After that, more nanoparticles are introduced on the substrate by electrostatic precipitation and initiate the secondary branch to growth. Through this process, branched ‘nanotrees’ are fabricated from GaP [99], as shown in Figure 1.15a-b. In addition, if the

trunk seed particles are positioned along specific direction with lithography technique, the branches will grow toward neighboring trunks and connected them together. As a result, a large-scale interconnected nanowire network is fabricated and shown in Figure 1.15 c-d.

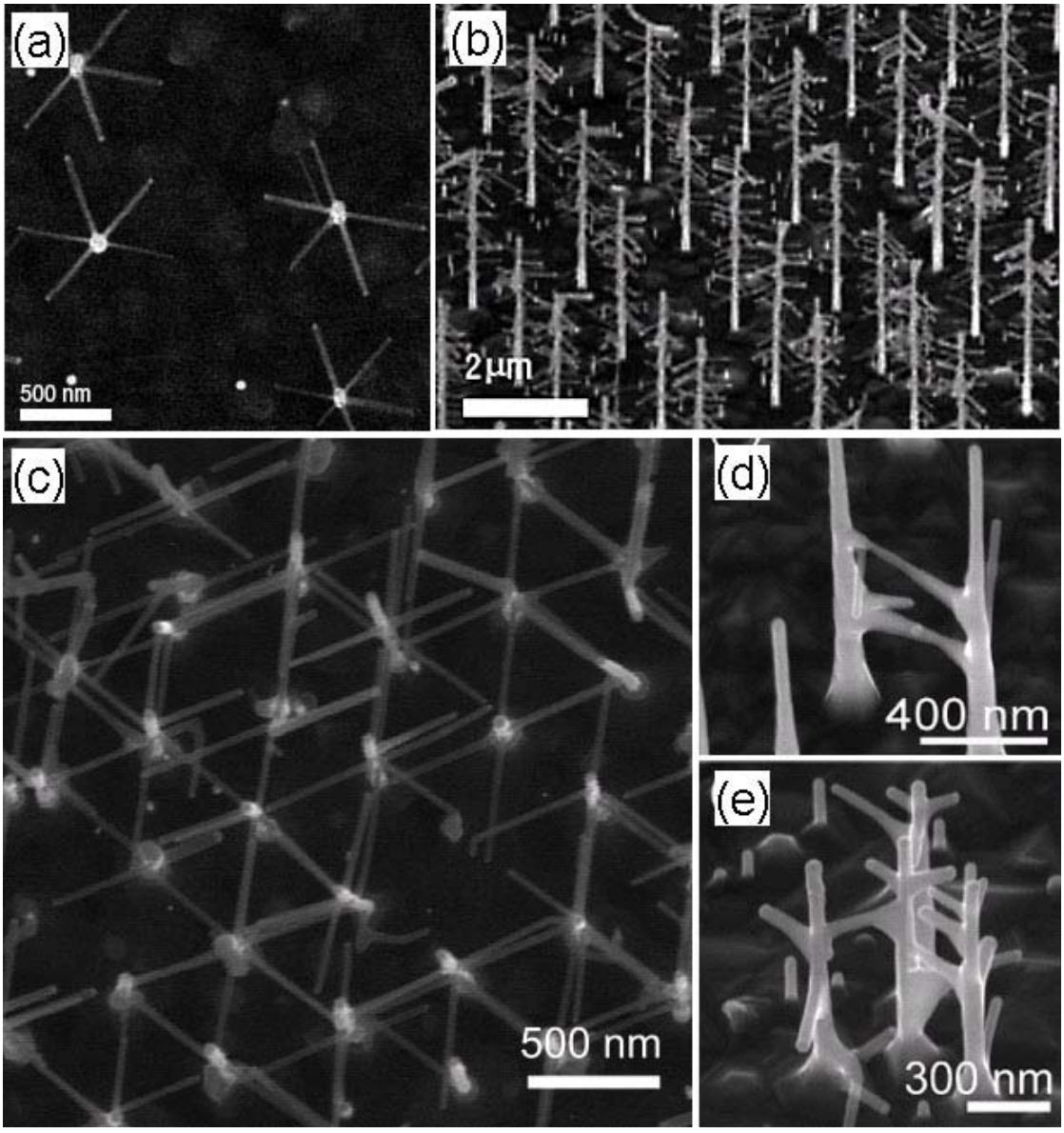

Figure 1.15 (a) Top view of GaP nanotrees. (b) Ordered array of nanotrees, viewed at 45° from normal. (c) SEM image of a large-scale position-controlled interconnected InAs nanowire network. (d-e) Two and four interconnected InAs nanotrees, viewed at an angle of 45° to the surface normal.

1.3 Properties and Applications of Nanostructures

Recently, 1D nanostructures, such as nanotubes, nanowires, nanobelts, and hierarchical derivative nanostructures have become the focus of intensive research owing to their unique properties (e.g., thermal, mechanical, field emission, electronic, optoelectronic, optical, nonlinear optical, magnetic, and piezoelectric). These nanostructures provide an ideal system to study the dependence of electrical, thermal transport, mechanical, and other properties of a material on its dimensionality, size reduction, and crystal structure and orientations. Besides their importance to fundamental understanding of properties and phenomena of materials in nanoscale, they play also an important role as both interconnect and functional units in fabricating electron, optoelectronic, electrochemical, and electromechanical devices with nanoscale dimensions.

1.3.1 Property Characterization

Functional nanostructures are splendid, diverse, and complex. Controlled synthesis and technological applications require a deep understanding of their growth and properties. Dealing with a large quantity of nanomaterials all together, conventional techniques can provide important information on nanomaterials as a whole. Investigation of the unique characteristics of individual nanomaterials is essential to fully utilize the basic and technological advantages offered by the size specificity and selectivity of the nanomaterials. Sometimes such property characterization becomes very challenging due to their small size. The extremely small size of nanostructures prohibits the application of well-established testing techniques, and the manipulation of nanomaterials is also rather difficult. Accordingly, new approaches have to be developed for measuring the properties of individual nanostructures.

There are three commonly used techniques for the characterization of individual nanostructures: transmission electron microscopy (TEM), scanning probe microscopy (SPM), and microelectromechanical systems (MEMS) or nanoelectromechanical systems

(NEMS) techniques. Some other techniques are also developed in this field. For example, a combination of an SEM and probe station can manipulate and provide measurement over a single nanostructure[78], and X-ray nanodiffraction techniques can provide structural characterization of individual nanomaterials as well[100].

1.3.1.1 Transmission Electron Microcopy for Nanotechnology

Being indispensable for nanotechnology, TEM is one of the most powerful tools used for the characterizing nanomaterials and have been used in the following areas: in-situ microscopy for study dynamic shape transformation of nanocrystals, in-situ nanoscale property measurements on the mechanical, electrical and field emission properties of nanotubes/nanowires, environmental microscopy for direct observation of surface reactions, aberration-free angstrom-resolution imaging of light elements (such as oxygen and lithium), high-angle annular-dark-field scanning transmission electron microscopy (STEM) for imaging of atom clusters with atomic resolution chemical information, electron holography of magnetic materials; and high-spatial resolution electron energy-loss spectroscopy (EELS) for nanoscale electronic and chemical analysis[101]. As a result of those tremendous capabilities, TEM becomes the foundation of nanometer-scale technology.

In the early days before the national nanotechnology initiative, scientists had started to exam “small particles’, i.e. nanoparticles, with TEM. TEM has been mainly applied for imaging, diffraction, and chemical analysis of solid materials, which has result in the discoveries of numerous nanomaterials, including carbon nanotubes [4, 5, 7]. Conventional imaging and diffraction are the two most powerful methods in studying the phase structure and phase transformation of inorganic materials. Energy dispersive X-ray spectroscopy (EDS) and electron energy-loss spectroscopy (EELS) enable transmission electron microscopy to be a versatile and comprehensive analysis tool for characterizing the chemical and electronic structure at nanoscale. TEM has been widely utilized for

determination of the shape and structure of nanomaterials and will play a critical role in this field in the future. Recently, new and novel developments to TEM have made it even more important for nanotechnology.

Utilization of nanomaterials as basic building blocks in nanotechnology requires a good understanding of the properties of individual nanostructures, such as mechanical and electrical properties. Such measurement is rather challenging or even impossible with conventional techniques. For example, the conventional tensile and creep test requires that the size of the sample should be large enough to be clamped rigidly by the sample holder without sliding. In addition, due to the small size of the nanomaterials, their manipulation is very difficult, and specialized techniques are required for picking up and mounting individual nanostructures. In practical terms, it is impossible to test nanomaterials using conventional means. Integrating the detailed structure information of nanostructure provided by TEM with properties measured in-situ from the same nanostructure provides an ideal technique for understanding the property-structure relationship.

In order to perform property measurement on nanostructures, a TEM compatible specimen holder is needed for manipulate and measurement [102, 103]. The TEM sample holder in Figure 1.16 can apply a voltage across a nanostructure and its counter electrode. The sample holder requires the translation of the nanostructure via either mechanical movement by a micrometer or axial directional piezo. The static and dynamic properties of the nanostructure can be obtained by applying a controllable static and alternating electric field. The nanostructure can be glued using silver paste onto a gold wire, through which the electric contact was made. The counter electrode can be a droplet of mercury or gallium for electric contact measurement or an Au/Pt ball for electron field-emission characterization. At the same time, the microstructure of the measured object can be fully characterized by electron imaging, diffraction, and chemical analysis technique.

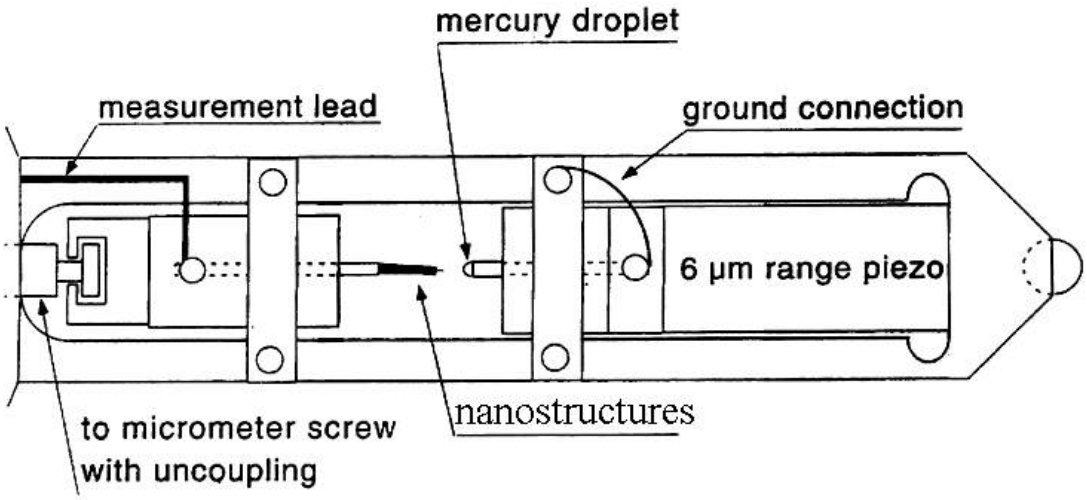

Figure 1.16 TEM specimen holder to in-situ properties measurement

The nanostructure was directly imaged under TEM, as shown in Figure 1.17a. Microanalysis and be performed in situ and electron diffraction pattern and images can be recorded from the nanostructure to reveal the surface and the intrinsic structure. This is a unique advantage over the SPM techniques.

The technique was carried out for carbon nanotubes. The conductance of an arc-produced multiwalled carbon nanotube (MWNT) was measured and quantized conductance was identified[104]. Further more, this technique has also provide in situ TEM observation of the electron field emission from individual carbon nanotubes, and field induced structure damage of multiwalled nanotubes[105], as shown in Figure 1.17.

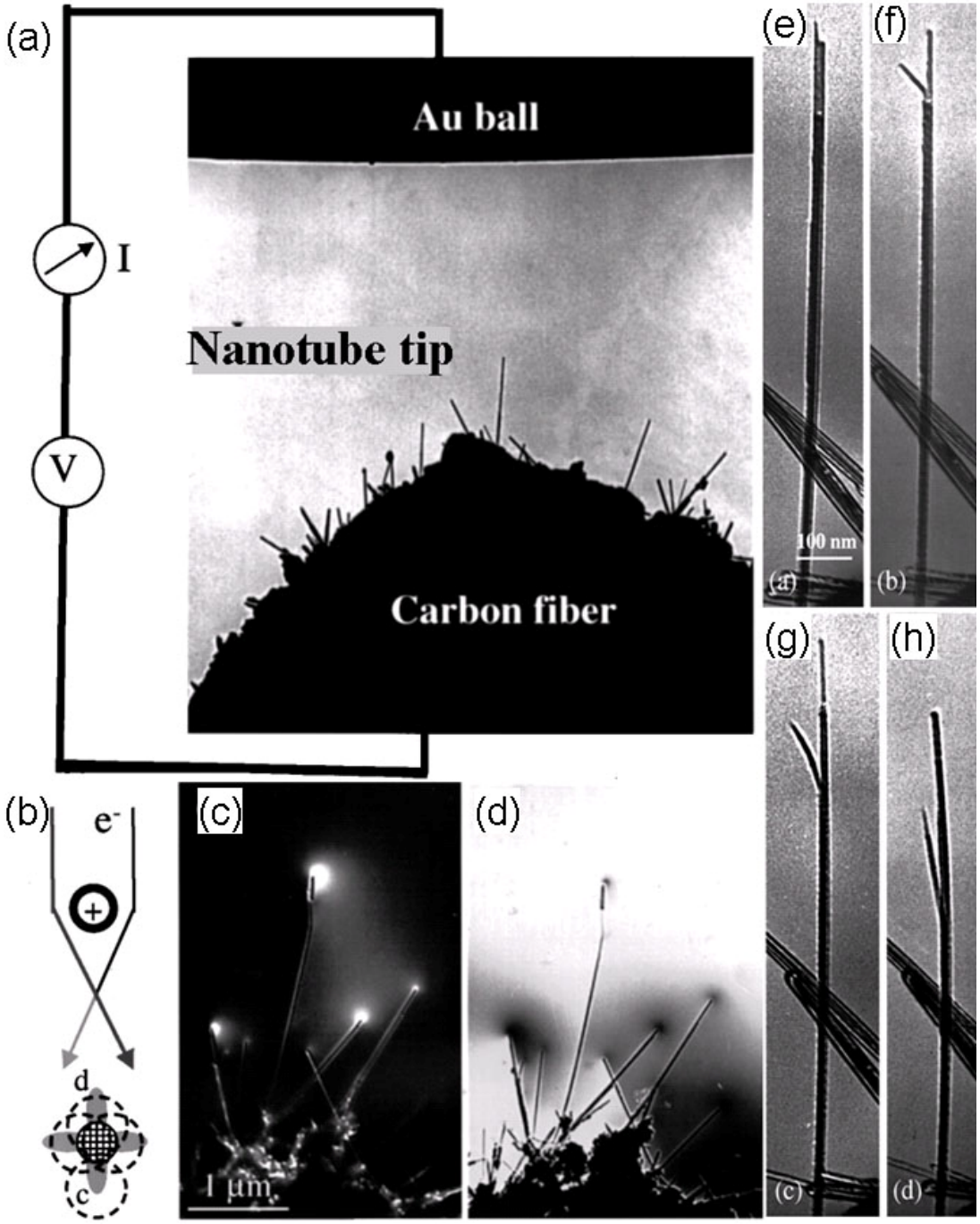

Figure 1.17 (a) TEM image of carbon nanotubes and a counterelectrode. (b) Schematic diagram showing the deflection of the electron beam passing a positively charged nanotube in TEM. (c) and (d) TEM images of carbon nanotubes produced by arc discharge by positioning the objective aperture at positions b and c, respectively. (e-h) "Splitting" process in structural damage.

The electrostatically induced beam deflection was used to observe the electrostatic field distribution. When the nanotube is positively charged (Figure 1.17b), the electrons passing through the two sides of a nanotube are deflected toward each other due to electrostatic attraction, resulting in a weak diffusion scattering in the electron diffraction pattern around the central transmission beam. The field distribution around the nanotube then can be revealed by selecting a portion of the diffusely scattered electrons using a small size objective aperture. Figure 1.17c and d are two mages of the nanotubes acquired by placing the objective aperture at the c and d position as indicated in Figure 1.17b.corresponding to the dark field (DF) and bright field (BF) images, respectively, of the nanotubes that are emitting electrons. The mostly pronounced contrast near the tips of nanotubes confirmed the emission of electrons from the tips, just as expected.

Another important phenomenon in this study is the observation of structural damage to a carbon nanotube during field emission under a higher voltage. This study is very useful in determining the structural stability of the nanotubes. Figure 1.17e-h shows a series of images of a nanotube that was damaged more apparently with the increase of an applied voltage. TEM observation of this degradation process indicates that the damage occurs in such a way that the walls of the nanotubes are split patch-by-patch and segment-by-segment. A concentrical layer-by-layer stripping process has also been observed for some damaged carbon nanotubes.

Apparently this method is not material-limited. Similar measurement can also be applied to other materials. In addition, this method can also be modified to measure other properties [102, 103, 106-108]. For example, the mechanical property of a ZnO nanobelt has been successfully studied with an alternating electric field instead of static one as in the previous case[108].

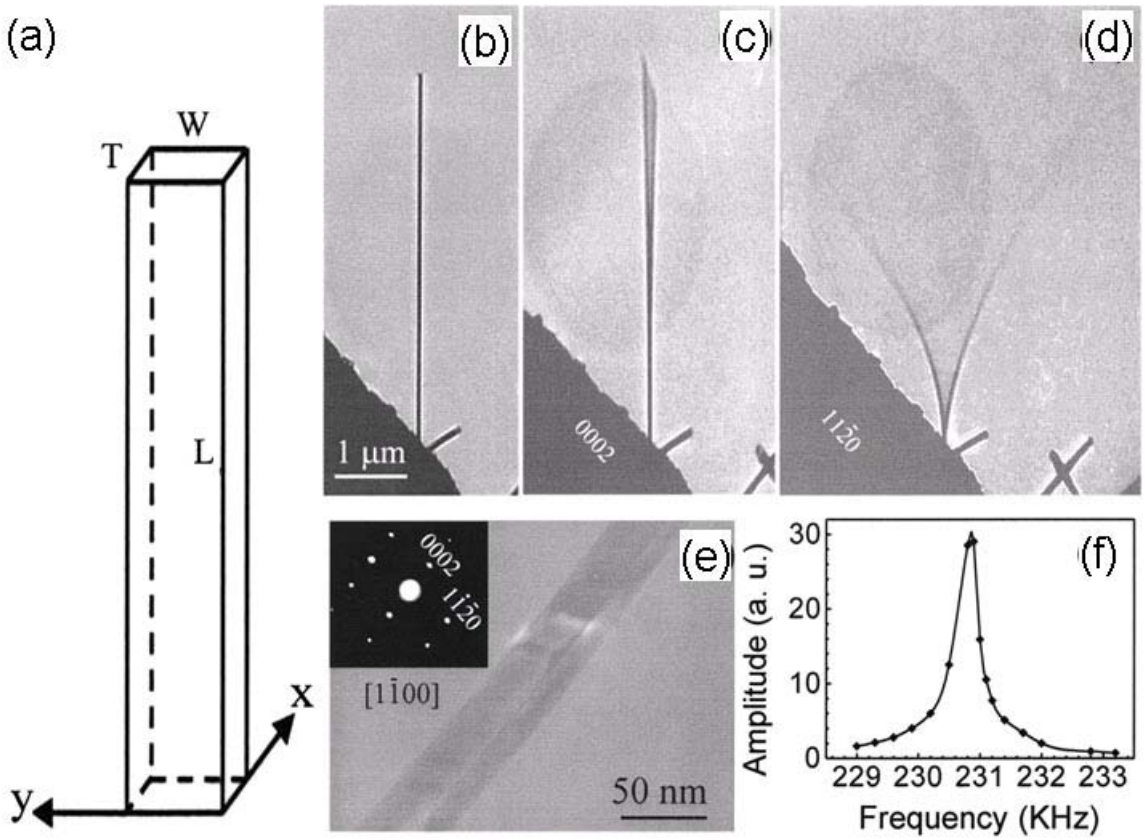

Figure 1.18 (a) Schematic geometrical shape of the nanobelt. A selected ZnO nanobelt at (b) stationary, (c) the first harmonic resonance in x direction, v_{x1}=622 kHz and (d) the first-harmonic resonance in y direction, v_{y1}=691 kHz. (e) An enlarged image of the nanobelt and its electron diffraction pattern (inset). The projected shape of the nanobelt is apparent. (f) The FWHM of the resonance peak measured from another ZnO nanobelt. The resonance occurs at 230.9 kHz.

In order to carry out the mechanical property measurements in the TEM, the nanobelts were attached to a solid gold ball electrode in the TEM sample holder in Figure 1.18. An oscillating voltage with tunable frequency was applied between the nanostructure and the counterelectrode. Since the electrically induced charge on the tip of the nanobelt oscillates at the frequency of the applied voltage, mechanical resonance is induced if the applied frequency matches the natural vibration frequency. Due to the mirror symmetry and rectangular cross-section of ZnO nanobelts (Figure 1.18a), two distinct fundamental resonance frequencies corresponding to vibration in the thickness and width directions are expected. From the classical elasticity theory for a rectangular

beam, the fundamental resonance frequency corresponding to the thickness direction (x-axis) is

$$v_x = \frac{\beta_i^2 T}{4\pi L^2}\sqrt{\frac{E_x}{3\rho}}$$

Where β_i is a constant for the i^{th} harmonic: β_1=1.875 and β_2=4.694, E_x is the bending modulus for the vibration along x-axis, and ρ, L, W, and T is the density, length, width, and thickness of the nanobelt respectively. The corresponding resonance frequency along width direction (y-axis) is

$$v_y = \frac{\beta_i^2 T}{4\pi L^2}\sqrt{\frac{E_y}{3\rho}}$$

The above two modes are decoupled and can be observed separately in experiments. By changing the frequency of the applied voltage, two fundamental resonance frequencies in two orthogonal transverse vibration directions were found by Bai et al.[108] Figure 1.18 c and d presents the harmonic resonance with the vibration planes nearly perpendicular and parallel to the view direction, respectively.

The accuracy of the experiment depends on the fundamental resonance frequency v and the dimensional sizes (L, W, and T) of the nanobelt. To measure v, the stability of resonance frequency and the resonant excitation around the half value of the observed resonance frequency has been checked carefully to ensure one end of the nanobelt is tightly fixed and the measured frequency is the fundamental frequency.

The geometrical parameters are critical for accurate derivation of the mechanical properties from the measured resonance frequencies. The real length (L) of the nanobelt can be obtained when the nanobelt is aligned perpendicular to the electron beam. Now the normal direction of the wide facet of the nanobelt can be determined to be $[2\,\bar{1}\,\bar{1}\,0]$ by the electron diffraction pattern. The nanobelt was then tilted about its axis from its normal direction. The tilting direction can be monitored from the corresponding electron diffraction pattern. Figure 1.18e presents the image of the nanobelt after the rotation, and

the corresponding electron diffraction pattern in the inset shows that the electron beam direction is [$1\,\bar{1}\,00$]. The angle between [$1\,\bar{1}\,00$] and [$2\,\bar{1}\,\bar{1}\,0$] is 30°, which means the normal direction of the wide facet of the nanobelt is 30° tilted from the direction of the electron beam. From the projected dimension measured and the tilted angle, the geometrical parameters were determined to be W=28nm and T=19nm. Based on the experimentally measured data, the bending modulus of the ZnO nanobelt is derived from above two formulas to be about ~52 GPa. Because of the convolution of shape and anisotropic structure of ZnO nanobelt in the measurement, the derived bending modulus cannot be directly compared to Young's Modulus of ZnO (C_{33}=310 GPa, C_{13}=104 GPa)[109]. However, the bending modulus measured by the resonance technique is in excellent agreement with the elastic modulus measured by nanoindentation for the same type of nanobelts[110].

1.3.1.2 Scanning Probe Microscopy for Nanotechnology

Detecting the Van Der Waals force, electron tunneling between the tip and the surface, the atomic force microscope (AFM) and the Scanning Tunneling Microscope (STM) are two early versions of scanning probes microscope (SPM) that launched nanotechnology. Now many types of scanning probe microscope, such as scanning confocal microscope, and scanning acoustic microscope, have been developed. Not only is the scanning probe microscope a powerful imaging tool with atomic resolution, it is also widely used to investigate the optical, mechanical, electrical, magnetic, and piezoelectric property of various materials.

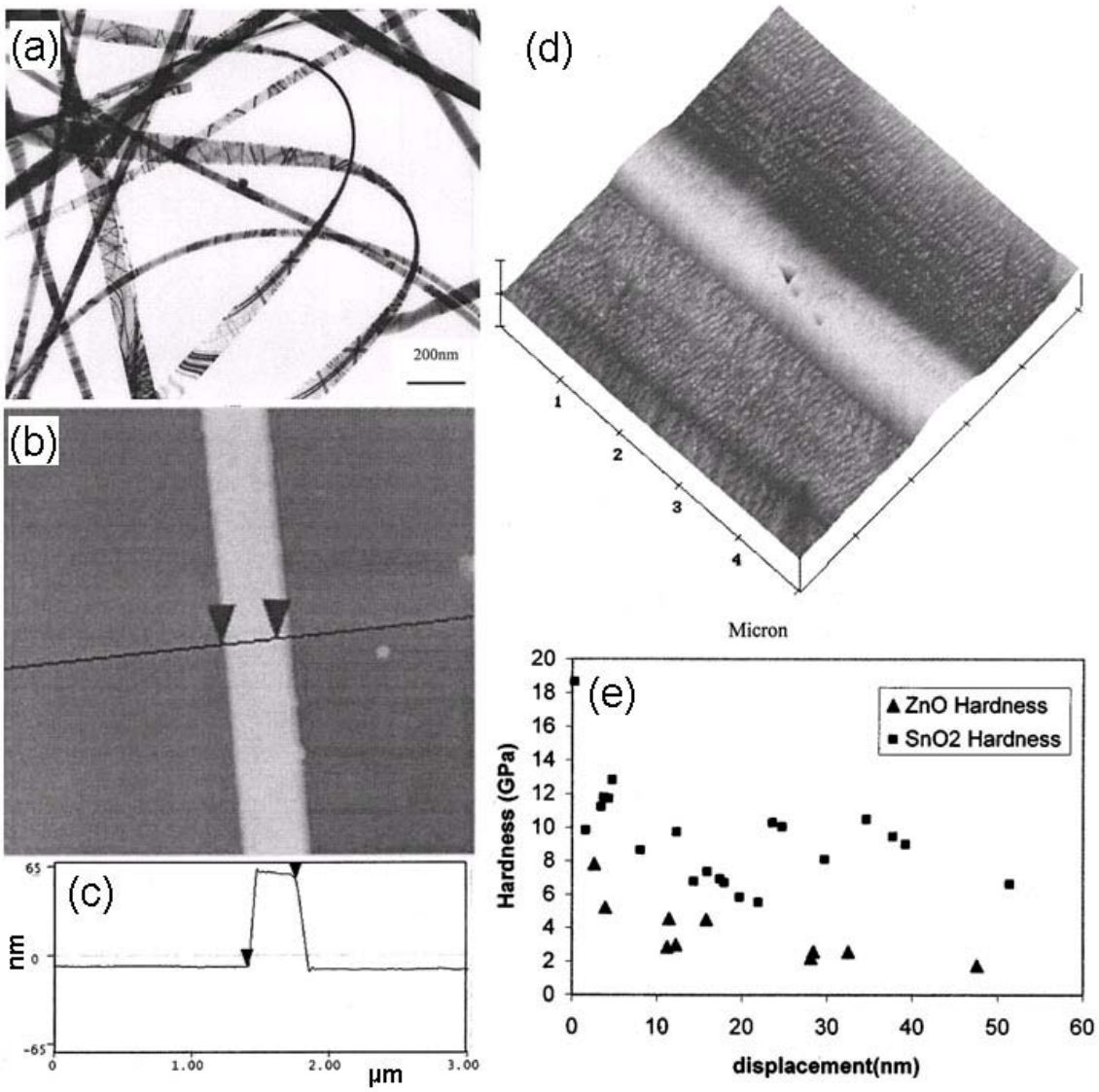

Figure 1.19 (a) TEM image of ZnO nanobelt. (b-c) Section analysis of ZnO nanobelt with AFM. (d) Indentation of a SnO_2 nanobelt by a cubic indenter. The load for large and small indents is 300 and 200 μN, respectively. (e) Hardness of ZnO and SnO_2 nanobelts as a function of penetration during nanoindentation.

The mechanical properties of nanostructures have been successfully investigated by the nano-indentation technique with SPM[110]. In this technique, SPM can monitor the repulsive force between the sharp probe and material surface as a means to detect the mechanical properties of materials. The key advantages of SPM nano-indentation are its imaging capability which allows accurate measurement of indentation geometry and precise location of indentation probe for nanomechanical measurement. This particular

study explores the areas of applicability of SPM for measuring mechanical properties such as Young's modulus of nanomaterials[111].

Figure 1.19 shows the nanoindentation measurement using an atomic force microscope (AFM) with a diamond cube corner tip. TEM image ZnO nanobelts in Figure 1.19a illustrates the geometrical shape. The nanobelt was grown along [0001] direction with $\{10\bar{1}0\}$ side surfaces. Section analysis by AFM in Figure 19b and c confirms the rectangular section and indicates that the nanobelt is about 360 nm in width and 65 nm in height. The indentation is performed with a cubic indenter under AFM with a load 0-300μN and loading rate of 10 μN/s. Based on the method of Oliver and Pharr[112], the hardness can be calculated as a function of indentation penetration. This technique is not materials-limited and was applied to ZnO and SnO_2 nanobelts in this study. The topographical image of the nanobelt after indentation is given in Figure 1.19c. The calculated result for ZnO and SnO_2 in Figure 18e show marked indentation size effect (ISE) for less than 50 nm indentation, which can be attributed to the effect of the strain gradient during nanoindentation of ceramic materials. In addition, the comparison of the ZnO nanobelt with a ZnO bulk (0001) single crystal by nanoindentation shows that ZnO nanobelt is a little softer. This is reasonable because (0001) is the most closely packed plane for hexagonal structured ZnO and the hardness along [0001] (the c-axis) may be higher than other directions.

Furthermore, the piezoelectric properties of ZnO nanobelt have also been characterized with piezoresponse force microscope (PFM), which is becoming a standard method for the study of ferroelectric and piezoelectric phenomena[113]. The schematic experimental setup is shown in Figure 1.20a. The technique is based on the detection of local vibrations of the ZnO nanobelt induced by an AC signal applied between the conductive tip of PFM and the bottom electrode. The local oscillations of the ZnO nanobelt surface are transmitted to the tip and detected using a lock-in technique. The out-of-plane piezoresponse signal is extracted from the z-deflection signal given by the

position sensitive detector (PSD) and represents the local oscillations perpendicular to the plane of the sample surface.

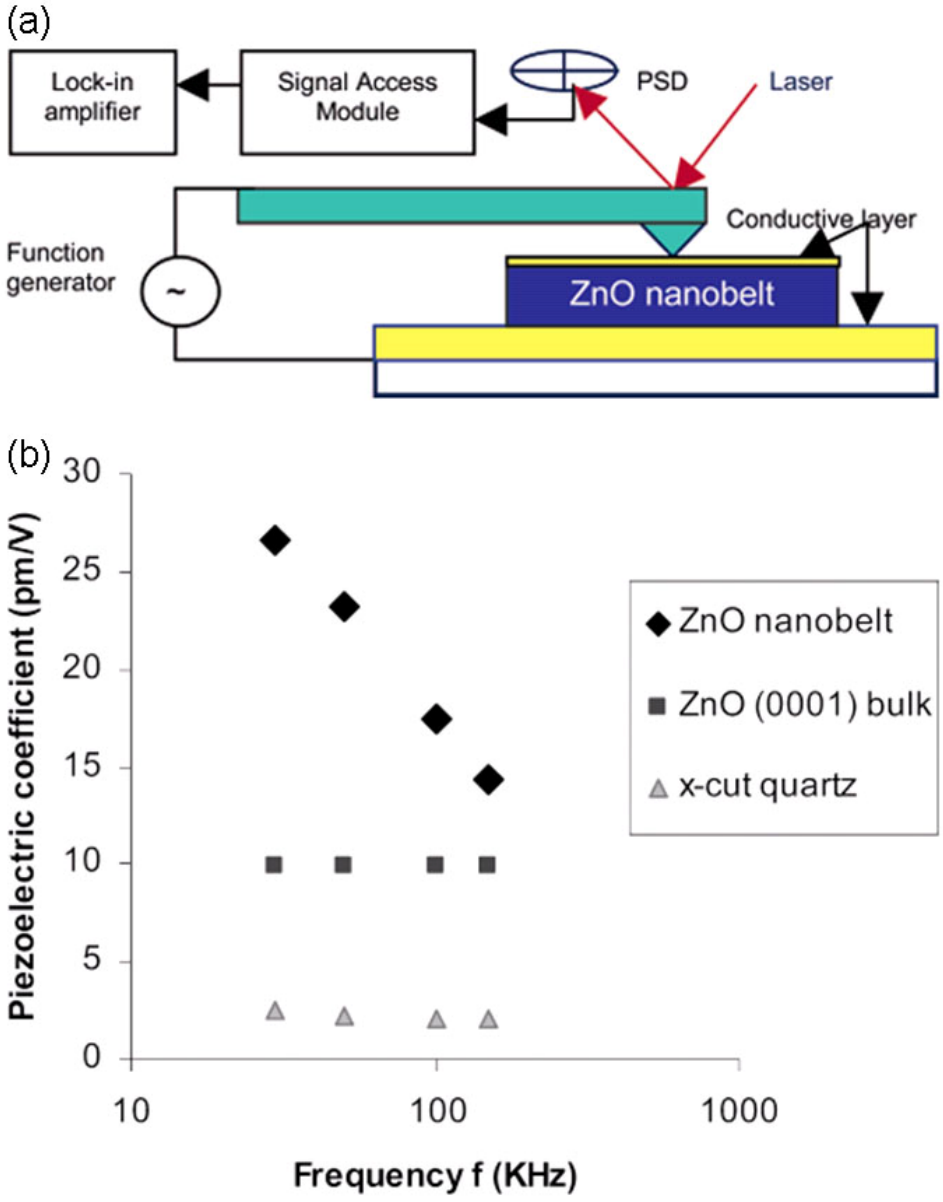

Figure 1.20 (a) Schematic of the AFM system showing the setup for piezoelectric measurement. (b) Frequency dependence of piezoelectric coefficient of ZnO nanobelt, bulk (0001) ZnO, and x-cut quartz.

To ensure the reliability and accuracy of the measurement, calibration has been performed and effective piezoelectric coefficients of (0001) bulk ZnO and x-cut quartz

(serving as a piezoelectric standard) were measured using the same PFM technique. Experimental results of piezoelectric measurements in Figure 1.20b show that the effective piezoelectric coefficients are d_{11}=2.17 pm/V for x-cut quartz and d_{33}=9.93pm/V for (0001) bulk ZnO, which are almost frequency independent. The measured values for x-cut quartz and (0001) bulk ZnO is consistent with the accepted values (d_{11}=2.3 pm/V for quartz and d_{33}=12.4pm/V for ZnO[114]), which confirms the reliability and accuracy of the measuring technique. Interestingly, the effective piezoelectric coefficient of the ZnO nanobelt is frequency dependent and varies from 14.3 to 26.7 pm/V, which is much larger than that of the bulk ZnO. As inherent reduction in the piezoelectric coefficient due to internal defects is revealed in thin PZT films (Ca. 500nm)[115], the enhanced electromechanical response for the ZnO nanobelt might benefit from its perfect single crystallinity and freedom of dislocation while a certain amount of defects are inevitable in the commercially available single-crystal bulk sample. The experimental result is very encouraging, and shows that ZnO nanobelts can be excellent candidate for nanosensors, nanoactuators, and nanogenerators.

1.3.1.3 Microfabrication

Being a manufacturing technology for making microscopic devices, microfabrication is usually based on specialized batch processing technologies developed for the semiconductor industry. Typical microfabrication processes include photolithography, deposition, and etching. Microfabrication achieved great success in integrated circuit and microelectromechanical systems (MEMS). Now it continues to play an important role in nanoscience and nanotechnology. In order to perform property measurement of nanomaterials, the investigated nanostructures are commonly integrated into desired measuring circuit, which are made through microfabrication.

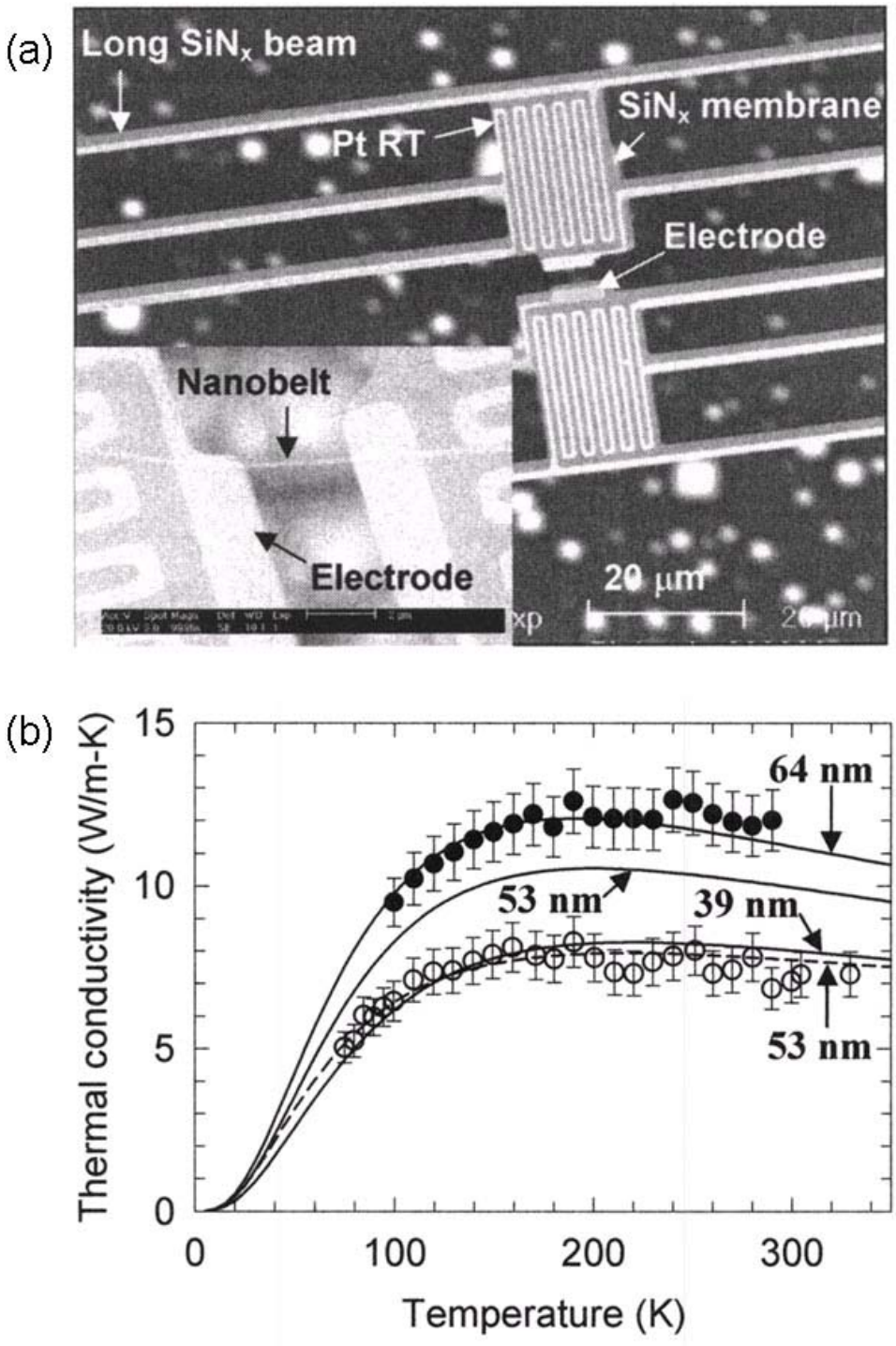

Figure 1.21 (a) A microfabricated device for measuring the thermal conductivity of a nanostructure. Inset: A 53-nm-thick SnO_2 nanobelt trapped on the two Pt electrodes of the device. (b) Thermal conductivities of a 64-nm-thick (solid circles) and a 53- nm-thick (open circles) SnO_2 nanobelt as a function of temperature.

Recently Shi et al. has used a microfabricated device for the thermal measurement of individual SnO_2 nanobelts[116]. The microdevice they used was a suspended membrane structure consisting of two suspended SiN_x membranes, as shown in Figure 1.21a. A platinum serpentine is patterned on each membrane, serving as a heater and resistance thermometer (RT) as the same time. A pair of Pt electrodes is patterned on the edge of each membrane. Using a wet deposition method a SnO_2 nanobelt is deposited on a Pt electrode pair, as shown in the inset in Figure 1.21a.

The measurement was performed in an evacuated continuous flow liquid-helium cryostat. The temperature gradient was built when a DC current was supplied to one Pt serpentine. The temperature rises in two membranes were measured by the Pt RTs. The thermal conductance (G_s) of the nanobelt is achieved as

$$G_s = \frac{Q_h + Q_L}{\Delta T_h + \Delta T_s} \frac{\Delta T_s}{\Delta T_h - \Delta T_s}$$

Where $Q_h = I^2 R_h$ is the joule heating in the heating Pt serpentine, Q_L is the joule heating in one of the two Pt leads supplying the DC current to the heating serpentine, and ΔT_h and ΔT_s are the temperature rise in the heating and sensing membranes, respectively. In addition, the thickness (t) of the nanobelt was measured using tapping mode atomic force microscope, and the length (L) and width (w) were obtained using a high-resolution scanning electron microscope. The thermal conductivity of the SnO_2 nanobelt were calculated according to

$$\kappa_n = \frac{G_s L}{wt} = \frac{L}{wt} \frac{Q_h + Q_L}{\Delta T_h + \Delta T_s} \frac{\Delta T_s}{\Delta T_h - \Delta T_s}$$

The obtained thermal conductivity in Figure 1.21b was found to be substantially lower than the bulk values[117], which are attributed to an increased phonon-boundary scattering rate.

1.3.2 Applications

Recently, 1D nanostructures such as tubes, wires, and belts, and hierarchical architectures such as nanowire arrays and networks have become the focus of intensive research owing to their unique applications in mesoscopic physics and fabrication of nanoscale devices. 1D nanostructures are of fundamental importance in providing a good system to investigate unique phenomena in the nanoscale and the dependence of electrical and thermal transport or mechanical properties on dimensionality and size reduction (or quantum confinement). At the same time, they are also expected to play an important role as both interconnects and functional units in fabricating electronic, optoelectronic, electrochemical, and electromechanical devices with nanoscale dimensions.

Among steadily increasing nanomaterials, ZnO is one of the most studied materials because of its semiconducting, piezoelectric, pyroelectric properties, biodegradability or possible biocompatibility, broad synthesis techniques, and wide range of structures.

1.3.2.1 Room Temperature Nanolaser

ZnO exhibits a direct band-gap of 3.37eV at room temperature with a large exciton binding energy of 60meV, which is much larger than that of GaN (25 meV) and the thermal energy at room temperature (26 meV). Such large exciton energy can ensure an efficient exciton emission at room temperature under low excitation energy. As a result, ZnO is recognized as promising photonic materials in the blue-UV region.

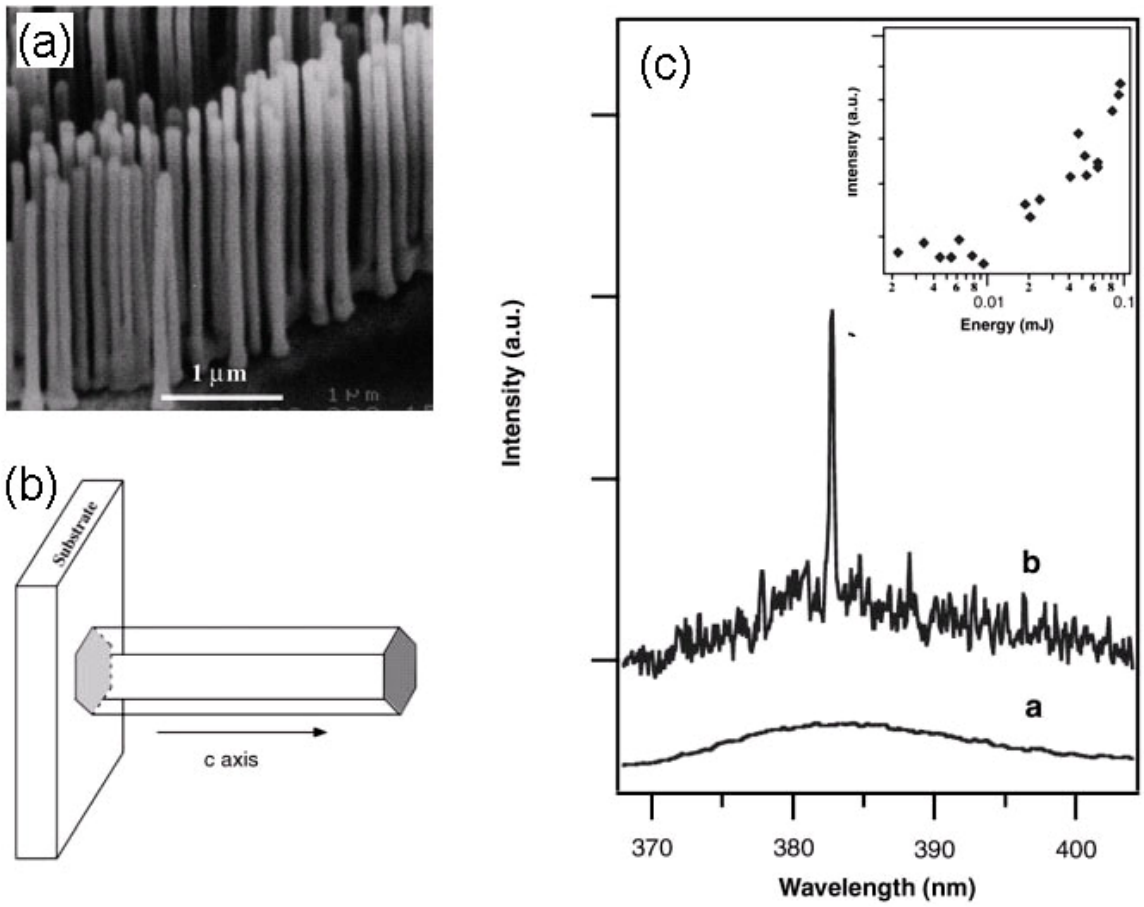

Figure 1.22 (a) SEM images of ZnO nanowire arrays grown on sapphire substrates. (b) Schematic illustration of a nanowire as a resonance cavity with two naturally faceted hexagonal end faces acting as reflecting mirrors. (c) Emission spectra from nanowire arrays below (line a) and above (line b and inset) the lasing threshold.

Room-temperature ultraviolet lasing in ZnO nanowire arrays has been demonstrated[118]. Using a simple solid-vapor deposition process, the self-organized, <0001> orientated ZnO nanowires grew from sapphire substrate (Figure 1.22a). The grown ZnO nanowires has well defined facet accordingly to electron microscope observation. In this configuration, one end of the nanowire was the epitaxial interface between sapphire and ZnO and the other end is the flat top (0001) plane of hexagonal ZnO nanocrystal. Considering the refractive indices of sapphire (1.8), ZnO (2.5), and air (1.0), both ends of the nanowires serve as good mirrors to form an optical cavity (Figure

1.22b). This nature cavity/waveguide structure provided a simple approach to the fabrication of nanoscale optical resonance cavities without cleavage and etching.

The samples were optically pumped by the fourth harmonic of Nd: YAG (yttrium-aluminum-garnet laser) (266 nm, 3-ns pulse width) at room temperature. Figure 1.22c shows the emission spectra recorded at different pumping powers. At low excitation power, a broad spontaneous luminescence peak was observed with a full width at half maximum (FWHM) of ~17 nm (the bottom curve in Figure 1.22c). This spontaneous emission is generally ascribed to the recombination of excitons through an exciton-exciton collision process. The emission peak narrows with the increase of pump power because of the preferential amplification of frequencies close to the maximum of the gain spectrum. Once the excitation power was increased above the threshold (~40 kW/cm^2), a sharp peak with much higher intensity was observed (the top curve in Figure 1.22c). The linewidths of these peaks are less than 0.3nm and more than 50 times smaller than the linewidth of the spontaneous emission peak below threshold. Above the threshold, the integrated emission intensity increases significantly with the pump power (Inset of Figure 1.22c). The narrow linewidth and the rapid increase of emission intensity are strong indications of stimulated emission in the aligned ZnO nanowire arrays.

1.3.2.2 Pico-gram Nanobalance

The most sensitive and smallest balance in world was fabricated with a carbon nanotube and demonstrated in TEM with picogram-to-femtogram resolution[119]. Further development has been made since then with carbon nanotube oscillators[120] and nanomechanical resonators[121] All these nanobalances have to work under high vacuum conditions, which might not feasible for practical applications. Using ZnO nanowires as nanoresonator for measuring tiny mass, a pico-gram balance has been demonstrated at ambient conditions[122].

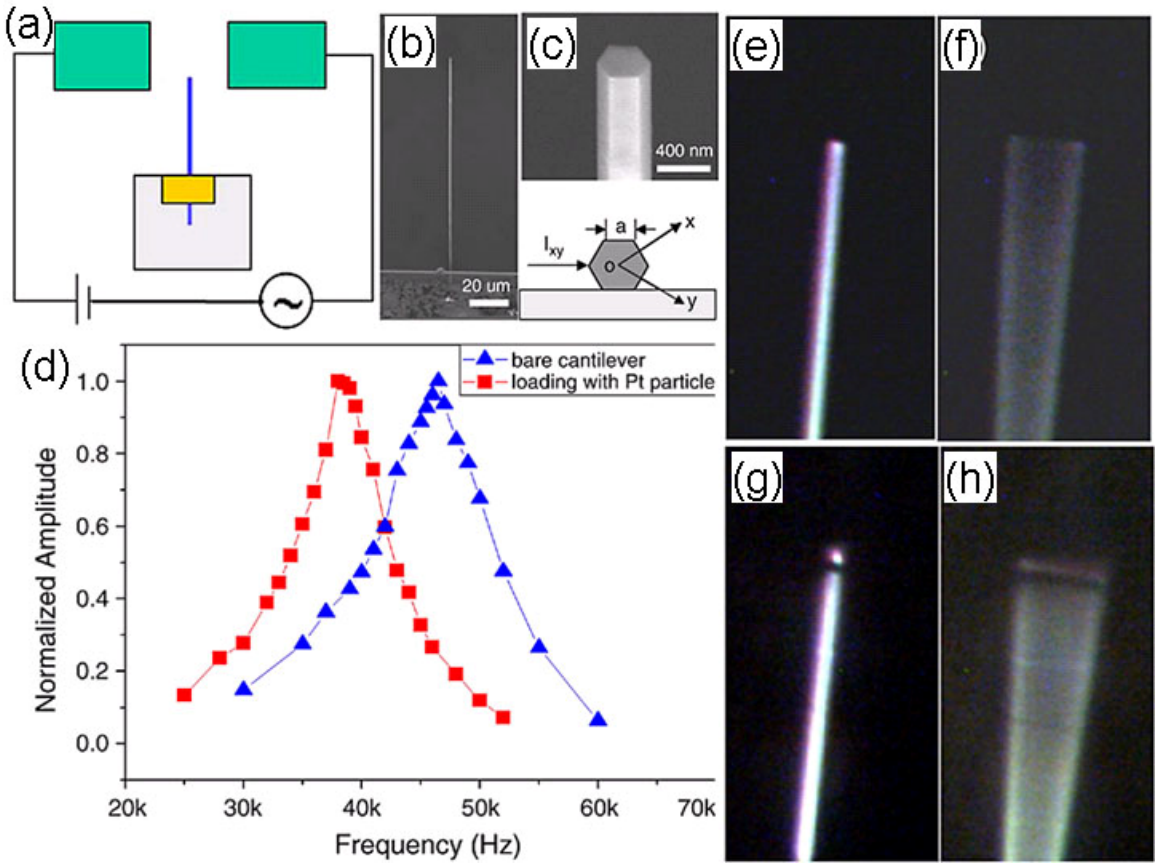

Figure 1.23 (a) Circuit diagram of the experimental setup for the ZnO nanowire based picogram balance. (b) SEM images of the ZnO nanowire cantilever. (c) Tilted cross-sectional SEM image and model for dimension measurement. (d) Frequency response plots of a cantilever before and after attaching a Pt particle at its tip, respectively. Optical microscopy images of the native ZnO nanowire cantilever at (e) stationary , (f) the first harmonic resonance, (g) stationary with Pt particle, and (h) the first harmonic resonance with Pt particle.

An individual ZnO nanowire was placed on a silicon substrate with one side fixed with silver paste and the other side in the middle position of two electrodes, as shown in Figure 1.23a and b. A constant voltage V_{dc} and an oscillating Voltage V_{ac} with tunable frequency were applied between two electrodes to stimulate the nanowire. The dimensions of the nanowire were measured with field emission scanning electron microscope (FE-SEM). The nanobalance worked at the ambient condition with the dynamic behavior monitored with an optical microscope (Figure e-h). The resonance vibration behavior of a ZnO nanowire was studied before and after placing a Pt short

segment at the very end. The frequency response was plotted in Figure 1.23d and showed a clear shift induced by the Pt particle. Then the Pt particle can be calculated by

$$M_{eff} = \frac{3M_0}{\beta^4}\left[\left(\frac{f_0}{f}\right)^2 - 1\right]$$

Where $M_{eff}=M_p(x/l)$ is the effective mass of the loading materials to the cantilever, M_P is the mass of the loading particle, which is located at a distance x from the base of the cantilever, l is the length of the cantilever, M_o is the mass of the bare cantilever, and f_o and f is the resonance frequency of the native cantilever before and after adding the particle, respectively.

The mass of the Pt particle was found to be ~ (26±1) pg, which is consistent with the calculated value from the shape of Pt particle. The sensitivity of the mass measurement was estimated to be 1.2 pg and can be improved with smaller nanowires.

1.3.2.3 Nanogenerator and Nanopiezotronics

In-situ, real-time and implantable biosensing, biomedical monitoring and biodetection require the development of novel technologies for wireless nanodevices and nanosystems. Such devices or systems still require a power source. A self-powered integrated nanosystem, which can harvest energy from its environment, will be greatly reduced in size and ideal for practical application. Recently, Wang et al. have demonstrated an innovative approach for converting nano-scale mechanical energy into electric energy by piezoelectric zinc oxide nanowire (NW) arrays[123]. By deflecting the aligned NWs using a conductive atomic force microscopy (AFM) tip in contact mode, the elastic energy that was first created by the deflection force and later converted into electricity by piezoelectric effect has been measured for demonstrating nano-scale power generator[123]. The operation mechanism of the electric generator relies on the unique coupling of piezoelectric and semiconducting dual properties of ZnO as well as the

elegant rectifying function of the Schottky barrier formed between the metal tip and the ZnO NW.

Based on this principle, piezoelectric-field effect transistor, piezoelectric gated diode, sensors and resonators have also been fabricated. These devices form the fundamental components of nanopiezotronics, a new field in nanotechnology[124, 125].

Before introducing nanopiezotronics, we first illustrate the piezoelectric behavior of a single nanowire (NW) or nanobelt (NB) of a piezoelectric material, such as ZnO[126]. The deflection of a vertical, straight ZnO NB by an external applied force F results in (tensile) stretching of its outer surface (positive stain ε) and compressing of its inner surface (negative strain, ε), as shown in Figure 1.24 (a) and (b). Because of the piezoelectric effect of ZnO, an electric field E_z along the NB (z-direction) is then created inside the NB

$$E_z=\varepsilon_z/d$$

where d is the piezoelectric coefficient along the NB axial direction, that is the normally the positive c-axis of ZnO. The PZ-field is closely parallel to the z-axis (NB direction) and pointing upwards at the tensile surface and downwards at the compressed surface (Figure 1.24c). As a result of flipping of the PZ field across the width of the NB, the electric potential distribution from the compressed to the stretched side surface is approximately between V_p^- (negative) to V_p^+ (positive) under the first-order approximation. The electrode at the base of the NB is grounded. Note V_p^- and V_p^+ are the voltages produced by the PZ effect. The potential is created by the relative displacement of the Zn^{2+} cations with respect to the O^{2-} anions because of the PZ effect in the wurtzite crystal structure. These ionic charges cannot freely move and cannot recombine without releasing the strain (Figure 1.24d). As a result, the potential difference is maintained as long as the deformation is in place and no foreign free charges (such as from the metal contacts) are injected. The process shown in Figure 1.24a–d is the fundamental principle

of piezotronics for creating functional devices such the nanogenerator, piezoelectric transistor, and piezoelectric diode.

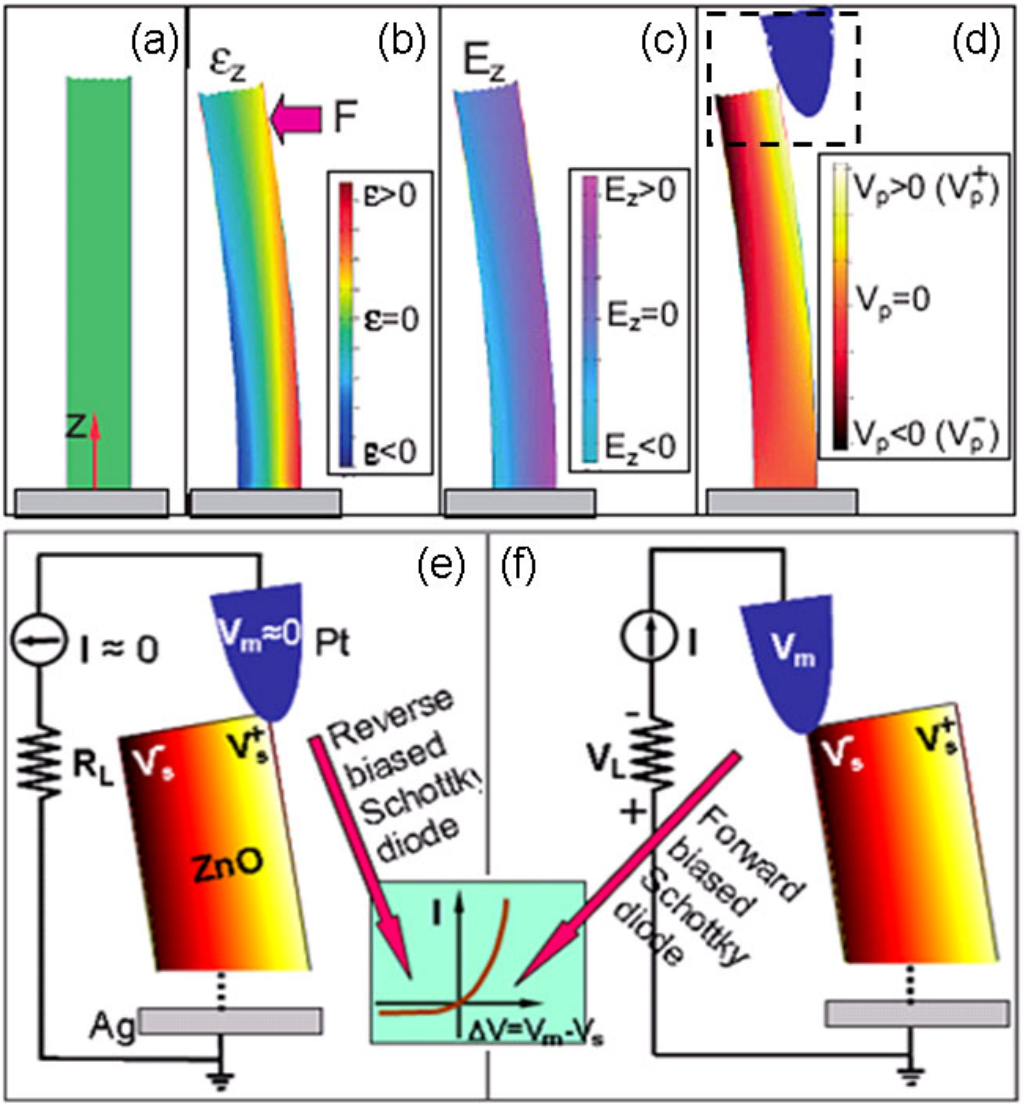

Figure 1.24 Physical principle of the observed power generation process of a piezoelectric ZnO nanowire. (a) Schematic illustration of a nanowire and the coordination system. (b) Longitudinal strain ε_z distribution, (c) corresponding longitudinal piezoelectric-induced electric field E_z, and (d) resultant potential distribution in the nanowire after being deflected from the side. Dashed box in (d) indicates the area shown in detail in (e) and (f). (e), (f) Metal and semiconductor contacts between the AFM tip and the semiconductor ZnO nanowire at two reversed local contact potentials (positive and negative), showing reverse-biased and forward-biased Schottky rectifying behavior, respectively.

Figure 1.24 a-d shows how the charge is separated. Now we will discuss the preserving and discharging process and how the energy is collected, which is illustrated in Figure 1.24c. In the first step, the atomic force microscope (AFM) conductive tip that induces the deformation force F is in contact with the stretched surface of positive potential V_p^+.(Figure 1.24 d and e) The metal tip has a potential of nearly zero, $V_m = 0$, so the metal tip/ZnO interface is negatively biased for $\Delta V = V_m - V_p^+ < 0$. Because the as synthesized ZnO NWs behave as n-type semiconductors, the Pt metal–ZnO semiconductor (M-S) interface in this case is a reverse-biased Schottky diode (figure 1.24 e), and little current flows across the interface. This is the process of preserving and accumulating charges. In the second step, when the AFM tip is in contact with the compressed side of the NB (Figure 1.24f), the metal tip/ZnO interface is positively biased for $\Delta V = V_L = V_m - V_p^- > 0$. The M/S interface in this case is a positively biased Schottky diode, and it produces a sudden increase in the output electric current. The current is the result of ΔV-driven flow of electrons from the semiconductor ZnO NB to the metal tip. The flow of the free electrons from the loop through the NB to the tip will neutralize the ionic charges distributed in the volume of the NB and thus reduce the magnitude of the potentials V_p^- and V_p^+. This is the process of outputting piezoelectric charges. The principle demonstrated in Figure 1.24 is the fundamental of nanopiezotronics.

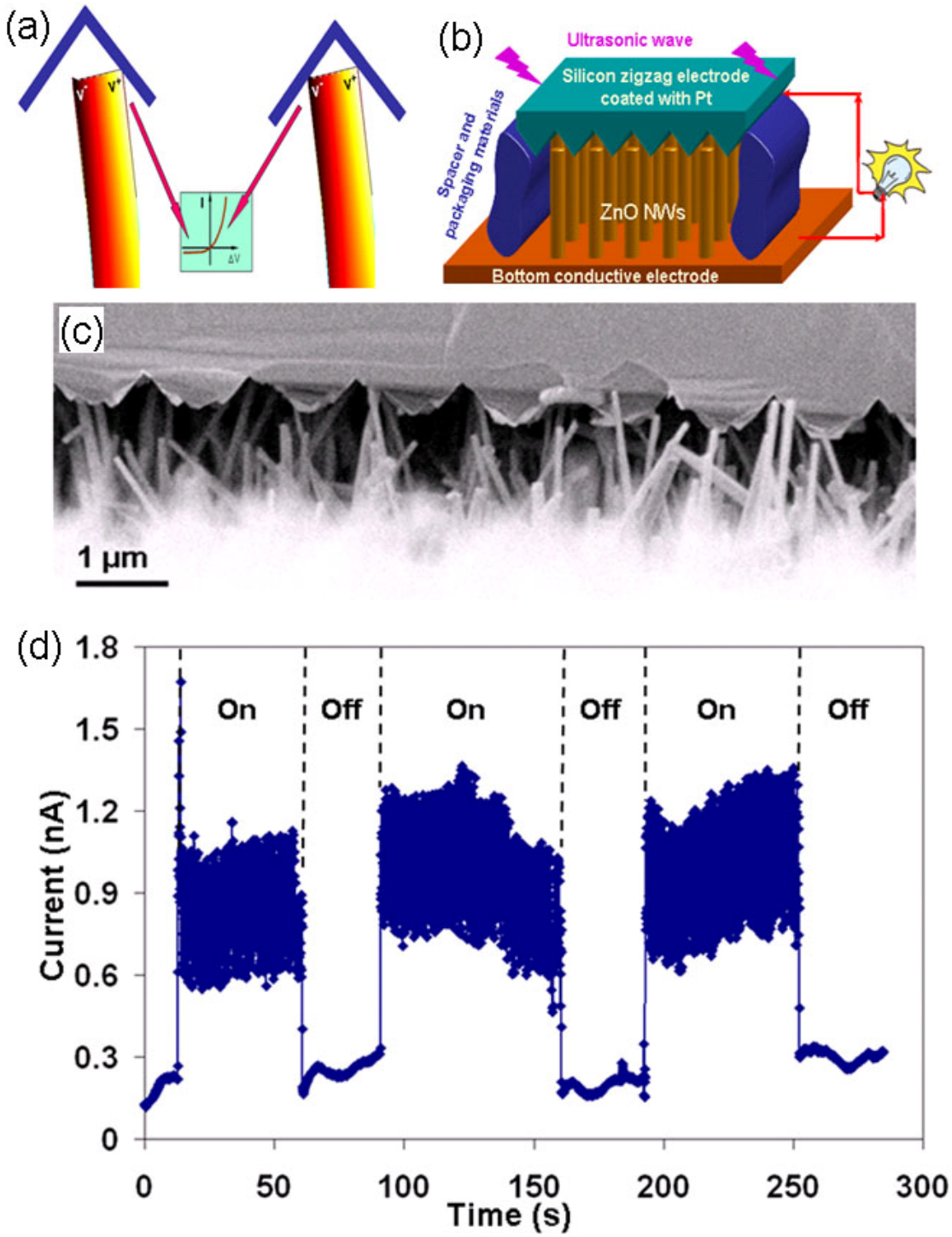

Figure 1.25 (a) Simplified top electrode model showing the working principle. (b) Schematic diagram showing the design and structure of the nanogenerator. (c) Cross-sectional SEM image of the nanogenerator, which is composed of aligned NWs and the zigzag electrode. (Inset) A typical NW that is forced by the electrode to bend.

By deflecting the aligned NWs with a conductive atomic force microscopy (AFM) tip in contact mode, the mechanical energy created by the deflection force was converted into electricity with the use of the piezoelectric properties of the NWs[123, 126]. To improve the power generation capabilities of the system, it is necessary to replace the AFM tip with a simpler source of mechanical energy that can actuate all the NWs simultaneously and continuously. These problems were solved with new designed electrodes and using ultrasonic waves to drive the motion of the NWs, leading to the production of a continuous current[96].

The principle is still the same as that described in Figure 1.24, while the AFM tip is replaced with an L-shaped electrode (Figure 1.25a). When the electrode is pushed down and starts to deform the NWs with one side, piezoelectric potential is created across NWs without the flow of the current owing to the reversely biased Schottky barrier at the electrode/NW interfaces (Figure 1.25a). With further pushing by the electrode, the other side of the electrode will contact the NWs as well. The second interface is a forward-biased Schottky barrier, which result in a sudden increase in the output electric current flowing from the top electrode into the NW. The experimental setup is schematically shown in Figure 1.25b and the section view of the real device in Figure 1.25c. The ZnO NWs arrays were covered by a zigzag Si electrode coated with Pt. The spacing was controlled by soft-polymer stripes between the electrode and NW arrays at the four sides. When the packaged device was driven with ultrasonic wave, continuous and reasonably steady DC electricity was generated, as shown in Figure 1.25c. The direct-current nanogenerator driven by ultrasonic waves presents an adaptable, mobile, and cost-effective technology for harvesting energy from the environment, and it offers a potential solution for powering nanodevices and nanosystems.

Based on the same principle used in nanogenerator, other devices have also been fabricated, such as piezoelectric field-effect transistor[127] (Figure 1.26 a-c) and piezoelectric-gated diode[128](Figure 1.26 d-g).

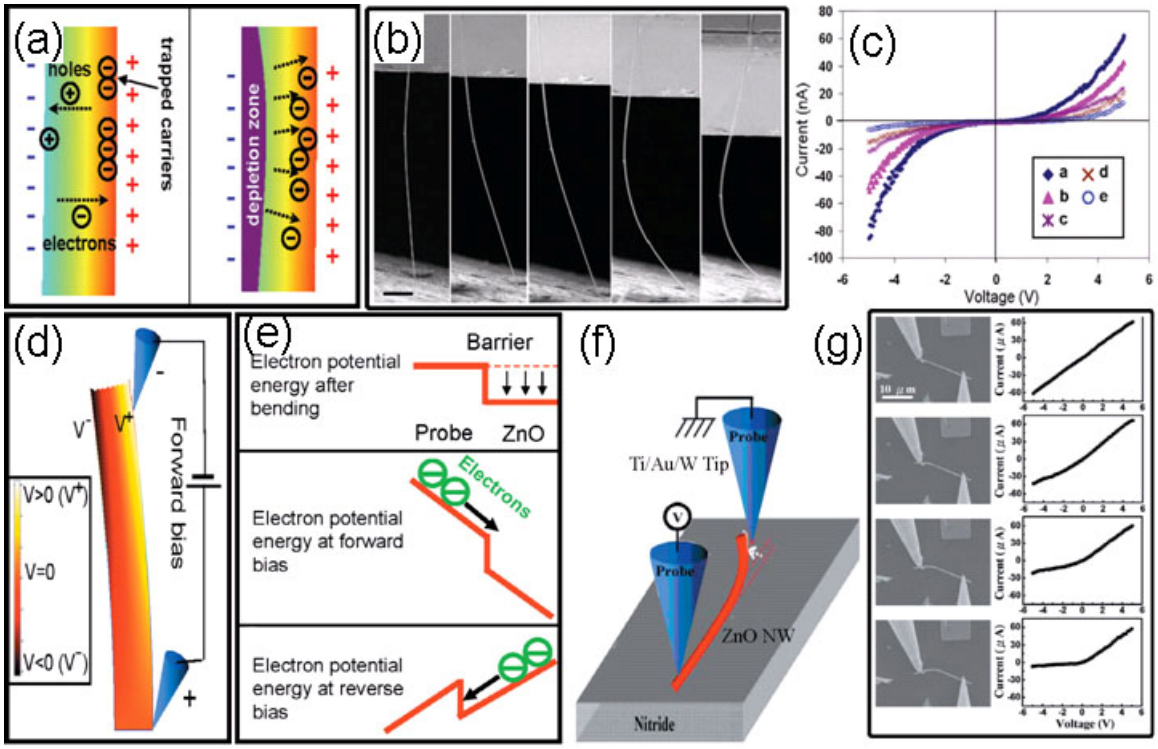

Figure 1.26 (a) The carrier trapping and the creation of a charge depletion zone due the piezoelectric effect in the deformed ZnO nanowire. (b) SEM images showing five bending conditions introduced into a ZnO nanowires. Scale bar=10μm. (c) Corresponding I-V characteristic of the ZnO nanowires for the five different bending cases. (d) Piezoelectric potential distribution in a bent NW. (e) Energy formed at the probe tip-nanowire interfaces as a result of the piezoelectric potential (V^+) at the stretched side, and current flow under forward or reverse bias. (f) Schematic of the nanomanipulation and in situ I-V measurement system. (g) Sequence of SEM images of the ZnO NW at various bending angles and the corresponding I-V characteristics.

Field-effect transistors (FETs) based on NWs and nanotubes are some of the most frequently studied nanodevices, in which the signal from the drain electrode of the NW is controlled by the gate voltage applied between the gate and the NW. By connecting a ZnO NW across two electrodes, and applying a bending force to the NW, the piezoelectric field created across the bent NW serves as the gate for controlling the electric current flowing through the NW (Figure 1.26 a-c). Alternatively, this piezoelectric FET can be considered as a new type of transistor that is turned on/off by applying a mechanical force. In other words, it can act as a force sensor capable of measuring forces in the nanoNewton range and smaller.

A piezoelectric-gated diode has also been demonstrated using a two-probe technique[128](Figure 1.26 d-g), in which one probe holds the NW stationary while the other bends the NW from the tensile side. Due to the strain-induced piezoelectric effect, a piezoelectric electric field will build up along and across the bent ZnO NW. Because of the nonuniform distribution of strain, the energy barrier is not fixed and increases with deflection of the NW. As the probe-induced deflection proceeds, *I-V* measurements in Figure 1.26 g clearly show an asymmetric *I-V* behavior. The rectifying I–V characteristic is similar to a *p-n* junction based diode.

1.4 Summary

This chapter has provided a broad view of the field of nanomaterials and nanotechnology. 1D nanostructures have been discussed, and three typical examples, carbon nanotube, Si nanowire, and ZnO nanobelt, are given in more detail. Hierarchical nanostructures have attracted more and more interest for their functionality and possible integration in nanosystem. Different techniques for characterizing nanostructures have been covered in this chapter, and the applications of nanostructure have also been presented in the last part.

The broad, but concise, review provides sufficient content to grasp and digest the subsequent chapters of this dissertation: controllable growth of the novel and hierarchical piezoelectric ZnO nanostructures, understanding the physical and chemical insights behind the involved growth phenomena by a variety of characterization techniques from structure characterization to chemical analysis, and optoelectronic device fabrications from nanostructures.

CHAPTER 2

FABRICATION METHODOLOGY

All of the synthesis within this dissertation was performed using a solid vapor deposition by way of thermal evaporation technique and pulse laser deposition technique. This chapter will cover the general experimental setup, synthesis procedure, and growth mechanism. As will be shown later in this dissertation, slight changes in the experimental parameters can have a significant impact on the type of the synthesized nanostructure. Accordingly, the specifics of each individual nanostructure synthesis will be reserved for its respective section.

2.1 Synthesis Setup

2.1.1 Furnace System

The furnace system that was used for the synthesis of nanostructures consists of three main components: the tube furnace, the carrier gas module, and the pressure control module. A schematic of the entire system is provided in Figure 2.1 for clarity.

According to the synthesis temperature, two types of furnaces have been used. One is a Thermolyne 79300 single zone split tube furnace for temperatures less than 1200°C, and the other is Thermolyne 54500 high temperature tube furnace for temperatures greater than 1200°C. An alumina tube with a length of 30”, 1.75” outer diameter and 1.50” inner diameter was placed inside the tube furnace. Because the furnace chamber is only 24” in length, the alumina tube protruded six inches on either side of the furnace. Heating elements of the furnace are equally spaced to provide uniform heat within the tube furnace. Cooling water is circulated inside the cover caps, which are sealed tightly to both ends of the tube. As result, a reasonable temperature gradient in the tube can be achieved. One end cap is fitted with a gas inlet connection for introducing carrier gas from the carrier gas module. The other end cap is connected to the

pressure control module, which maintains desired pressure for the synthesis and exhaust the waste gases into a hood. The furnace is equipped with a digital temperature controller, which can set up programs of eight segments each. Each segment of the program consists of three parts: a ramp rate (ranging form 1ºC/min to 60ºC/min), a temperature setpoint (ranging from 100ºC to 1200ºC or 1500°C), and a dwell time (ranging from 0.1 min to 999.9 min).

In this setup, the alumina tube acts as the reaction chamber for evaporation and deposition. High purity source powders were placed in the middle of the furnace, the highest temperature region. The desired nanostructures were deposited on collecting substrates, which is placed at a lower temperature region in the down-stream direction of the carrier gas. Temperature control is one of the most important parameters for the nanostructure synthesis. The furnace has a thermal-couple placed at the center of the furnace, but outside the alumina tube. This thermocouple is used to control the heating progress of an experiment. The temperature gradient along the tube and the local deposition temperature is also critical for controlling the nanostructures. As such, running the furnace at several distinct temperatures, we have measured the temperature distribution, which is served as a guide for synthesis parameters.

Other than the tube furnace, this synthesis setup also contains other two important parts, the carrier gas module and the pressure control module, which are used to control the gas type, flow and vacuum level.

The carrier gas module consists of gas cylinders, regulators, and mass flow controllers. Three types of gas, including N_2, Ar, and O_2, are connected to an Aalborg mass flow controller. The flow rate can be regulated separately and flowing of different gas simultaneously is also possible.

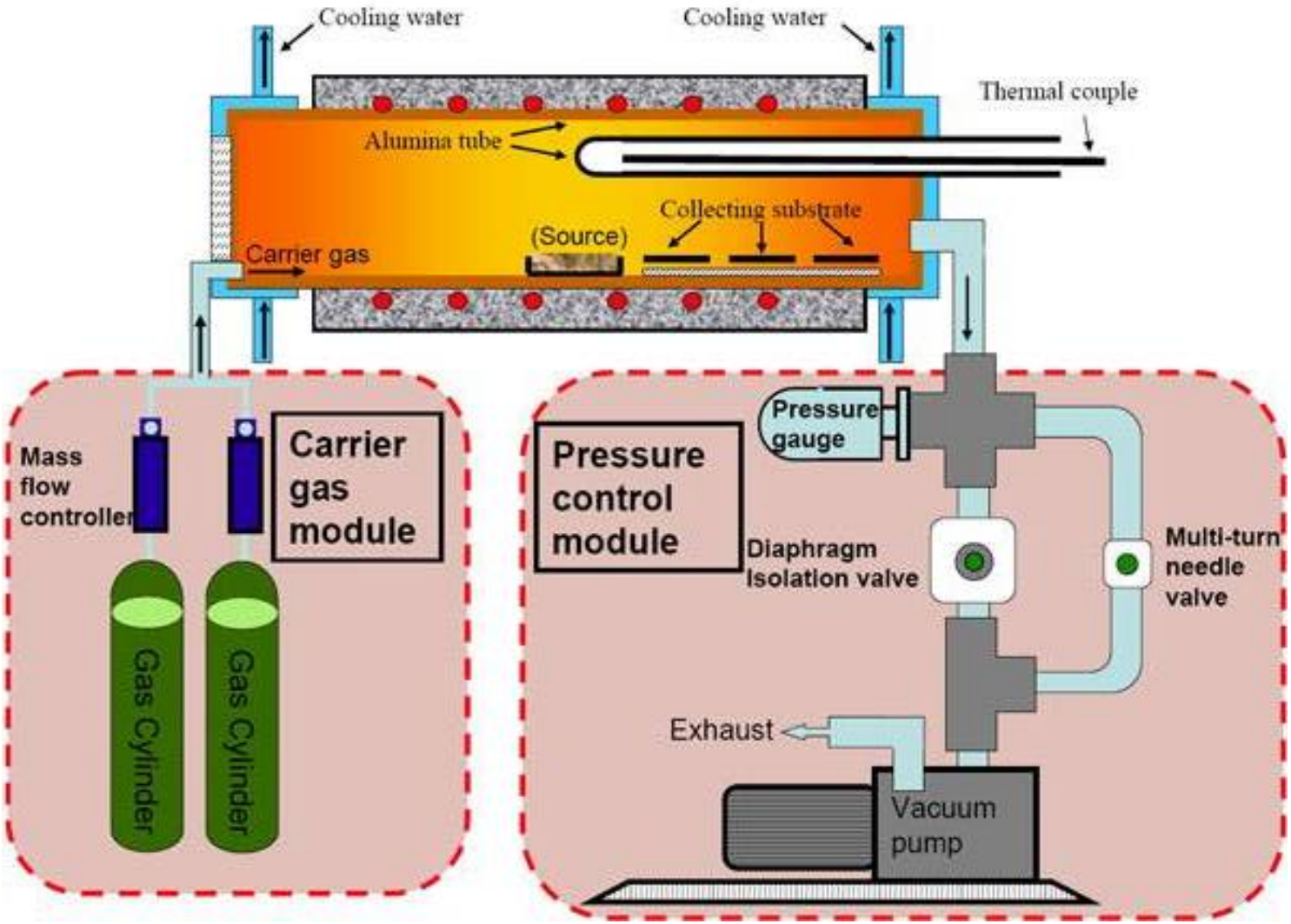

Figure 2.1 Schematic diagram for furnace system, which including furnace, pressure control module, and carrier gas module.

The pressure control module was connected to the outlet of the furnace system. The vacuum level is monitored with two pressure gauges (BOC Edwards analog Pirani vacuum gauge with a working range of 100 to 10^{-3} mbar, and a BOC Edwards analog dial vacuum gauge for low vacuum lever). Two valves are incorporated in order to control the pressure within the synthesis chamber. The valve for coarse adjustment is a BOC Edwards diaphragm isolation valve. In order to maintain a stable reaction chamber pressure, a Cole-Palmer multi-turn needle valve is used for fine adjustment. BOC Edward RV8 Hydrocarbon rotary vacuum pump was used to maintain the vacuum of the system. This pump has pumping rate of 8.0 m^3/h and an ultimate vacuum of $2x10^{-3}$ mbar.

2.1.2 Laser Ablation Setup

Pulsed laser deposition (PLD) is conventionally a thin film deposition technique, where a high power pulsed laser beam is focused inside a vacuum chamber to strike a target of the desired composition. Material is then vaporized from the target and deposited as a thin film on a substrate, such as a silicon wafer facing the target. Inspired by the fast development of nanoscience and nanotechnology, laser ablation technique has been used to fabricate nanostructures from different materials, including carbon nanotubes [129, 130].

Laser ablation is a process of removing materials from a solid surface by irradiating it with a laser beam. The materials are heated by the absorbed laser energy and evaporate or sublime at low laser flux. In contrast, the materials are typically converted to plasma at high laser flux. People usually use pulsed laser for this process, while a continuous wave laser beam can also do the job as long as the laser intensity is high enough.

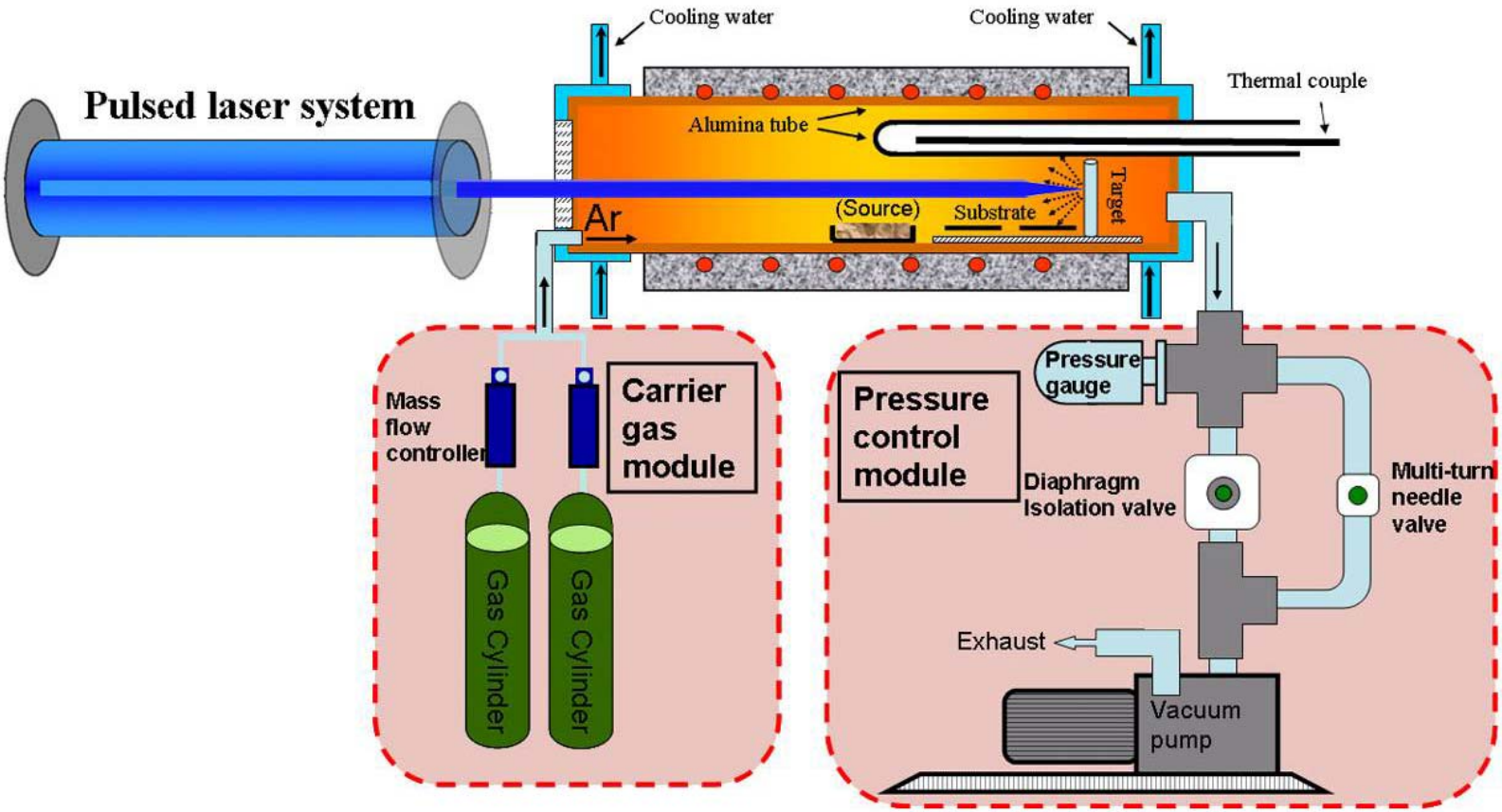

Figure 2.2 Schematic diagram for laser ablation setup

Pulsed laser ablation has many advantages in fabricating nanostructures. First, due to the highly intense energy of the laser spot, almost any material can be ablated for the synthesis purpose. In addition, PLD generally can allow better control over stoichiometry of the deposited materials, which will benefit the growth of complex functional materials.

The work discussed in this dissertation also utilized PLD technique for the nanostructure synthesis. The schematic setup is presented in Figure 2.2. Basically, the reaction chamber, temperature control, carrier gas module, and pressure control in the furnace system and are linked to a pulsed laser system. The integrated system is able to satisfy the requirement for the synthesis of nanostructure with pulsed laser deposition.

The target source was ablated with a KrF (248 nm) excimer laser (Lambda Physik, Compex 102, pulse duration; <20 ns) in air at the ambient temperature. The pulse energy and the repetition rate can be adjusted for the optimum synthesis condition. The pressure, temperature, and carrier gas can also be adjusted with the furnace system, as mentioned in the previous section.

2.2 Experimental Procedure

Pulsed laser deposition (PLD) experiments share a common furnace system with the thermal evaporation experiments. Accordingly, we will discuss the thermal evaporation first and add a few notes for laser ablation.

There are several processing parameters such as temperature, pressure, carrier gas (including gas species and its flow rate), evaporation time period, and collecting substrates, which can be controlled and need to be selected properly before and/or during the thermal vaporization. Other parameters related to laser system also need to be considered when PLD is employed, which will be discussed separately. The source temperature selection mainly depends on volatility of the source material. Usually, it is slightly lower than the melting point of the source when pure source materials are used. When a mixture source, such as ZnO with graphite, is used as source materials, this

temperature can be significantly reduced. The pressure can be determined according to the evaporation rate or vapor pressure of the source material(s).However, the thermodynamic data are not always available for certain materials. In this case, some preliminary testing experiments are necessary to find a reasonable start point. The carrier gases used are either nitrogen (N_2) or argon (Ar), and a small fraction of O_2 is occasionally introduced into the system. The substrates used to grow nanostructures can be classified into two categories: polycrystalline and single-crystalline substrates. The use of a particular type of substrate over another is determined by the experiment design.

The first step in the synthesis process is preparing the alumina tube, source materials, and collecting substrate. The tube is routinely cleaned with ethanol prior to the experiment. The clean tube is placed inside the furnace before loading the source materials and collecting substrates. A designated amount of source material is weighed on a Denver Instrument XE- 3100D mass balance, placed in an alumina crucible, and then transferred into the center of the tube. Collecting substrates, either single-crystal or polycrystalline, are cut and placed in the tube and positioned a certain distance away from the source materials in the middle. Once the substrates and source material are in position, the alumina tube is sealed with two watered-cooling end caps before the next evacuation step.

The thermal evaporation process is very sensitive to the concentration of oxygen in the growth system. Oxygen influences not only the volatility of the source material, and the stoichiometry of the vapor phase, but also the formation of the final products. As such, the second step of the synthesis process involves a simple evacuation process to reduce the initial oxygen content in the system prior to synthesis. The mechanical pump is tuned on and the diaphragm isolation valve, closed at this point, is slowly opened to ensure that the powder source material will not be pulled from center of the tube. The ultimate vacuum for the system was $\sim 5\times10^{-3}$ mbar. The system is held at this pressure for a minimum of 60 minutes, after which the synthesis process will begin.

A designated pressure and temperature set point are already chosen prior to the synthesis process. The carrier gas is introduced into the chamber first. By adjusting the coarse and fine valves on the vacuum system, the rate of evacuation for the chamber can be manipulated and the system pressure can be maintained at a specific set point before evaporation of the source material begin. The pressure set point is always achieved before heating up the furnace. The furnace is heated at a ramp rate of 20 ºC/min to 50°C/min. The system is held at constant pressure and temperature for a designated time. After which the furnace is turned off. A fan is usually directed towards the inside of the furnace to enable a speedy cooling time. Once the cooling process was complete, the flow of the carrier gas into the system is stopped, and the diaphragm valve is fully opened to evacuate any potentially harmful vapor in the chamber.

Pulsed laser ablation experiment also uses the same furnace system and follows the aforementioned procedure of preparation, evacuation, thermal evaporation, and cooling off. However, some modification is also needed due to the characteristic of laser. Laser ablation requires a solid target instead of loose powders. The designed source materials were pressed in a 9.5 mm diameter steel die at 700 kg pressure to form a cylindrical target for laser ablation The alumina tube was replaced with a quartz tube, which allows us to precisely focus the laser onto the target.

The target is placed vertically downstream during the preparation process, and collecting substrates were positioned close to the target and at the upstream side, as shown in the schematic diagram in Figure 2.2. More source materials could also loaded in the middle of the tube. After that, the chamber was evacuated for at least 60 minutes before introducing carrier gas. The valve was carefully adjusted to main the chamber pressure at a constant set point. The top cover was then opened so that the target was visible. The excimer laser was turned on with very low pulse energy and repetition rate for alignment and focusing. Through adjusting the mirrors and lenses, the pulsed laser could impinge directly on the target with a spot about 5 mm in length and 1 mm in width.

The laser was turned off, top coved of furnace was closed, and the furnace began to heat up. When the furnace reaches, or almost reaches, at the designed synthesis temperature, the excimer was turned on again with preset pulse energy and repetition rate. The synthesis would last a preset time. The furnace began to cool off and the laser was turned off in sequence.

2.3 Growth Mechanism

Although a variety of synthesis techniques have been used for the synthesis of nanostructures, physical vapor deposition has proved to be powerful and versatile in synthesizing numerous type of nanostructures. Two primary growth mechanisms, vapor-solid (VS) process, and vapor-liquid-solid process, are widely accepted among the 1D nanostructure synthesis community, while some other mechanism have also been proposed and might play an important role in certain synthesis process. Fundamental understanding of the growth process is critical for the synthesis of nanostructures with a good control of morphology, composition, etc, and will be investigated in this dissertation. As such, the following sections will describe possible mechanisms during the synthesis of nanostructures.

2.3.1 Vapor-Solid Process

During a catalyst-free vapor-solid (VS) growth process, deposition occurs when vapor condenses directly to form a solid without experiencing an intermediate liquid phase. Vapor-solid growth of 1D nanostructures is historically based on whisker formation. Although the whisker was firstly observed as early as in 1946[131], more research is required to develop a predictive model for 1D nanostructure growth.

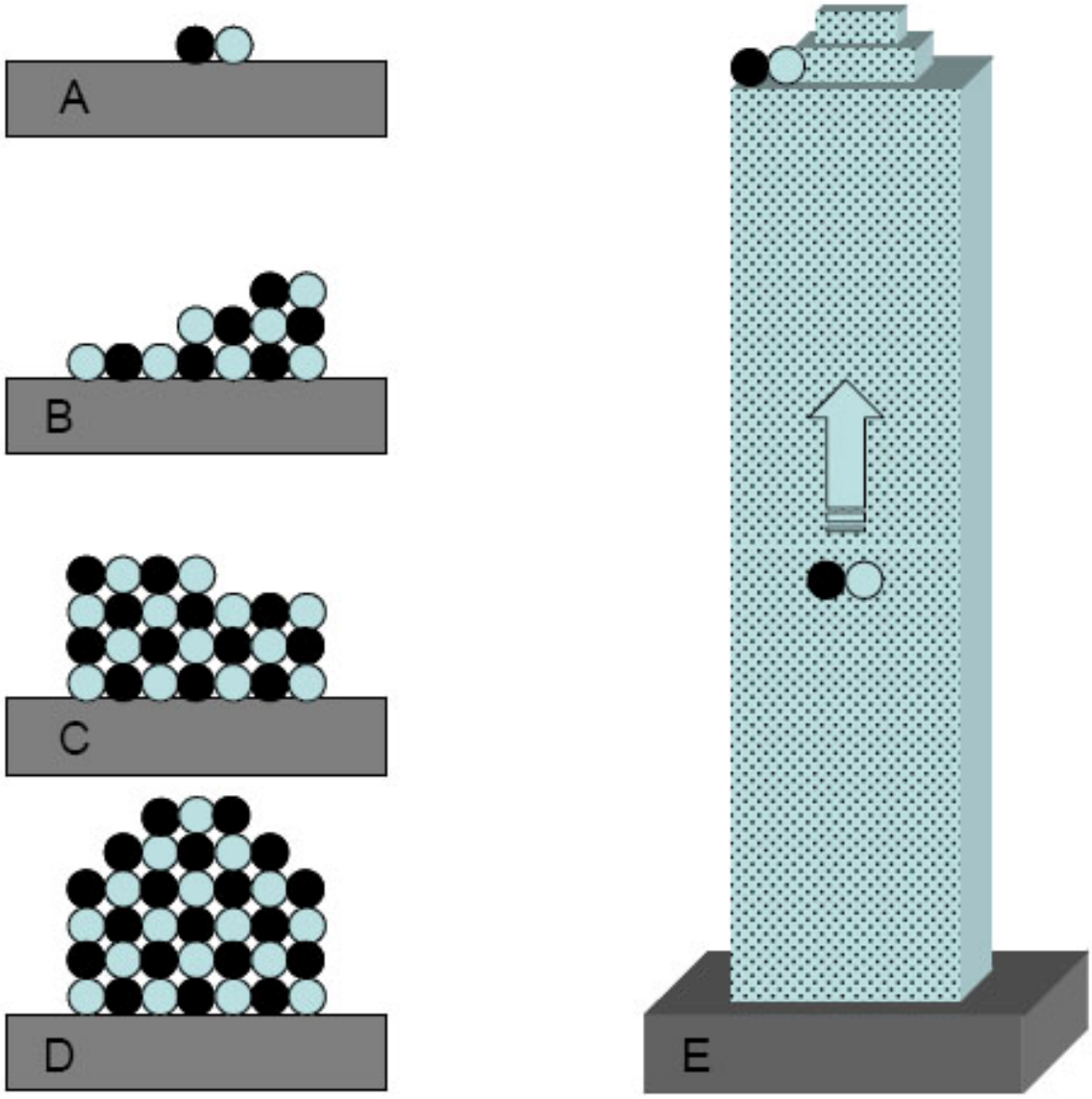

Figure 2.3 A proposed growth mechanism for ZnO nanobelts through a VS process

In a typical VS process, the vapor species is firstly generated by evaporation, chemical reduction, laser ablation, and other gaseous reactions. These species are subsequently transported and condensed on the surface of a solid substrate placed in a zone with lower temperature than that of the source materials. As a consequence of the research on VS process, whiskers, as well as one-dimensional nanostructures, are thought to be kinetically-driven, anisotropic, crystallization processes that are heavily dependent on supersaturation[132]. Fortunately the temperature and the supersaturation ratio are

easily controlled parameters during synthesis. Higher temperature and larger supersaturation ratios facilitate two-dimensional nucleation resulting in the formation of films. In comparison, lower temperatures and smaller supersaturation ratios are preferred for the nucleation and growth of wire-like structures. In summary, temperature and the supersaturation ratio are the two dominant factors during VS growth and provide the ability to control the morphology of deposited product

Various ZnO nanostructures, such as nanobelts from ZnO, SnO_2, In_2O_3, CdO, Ga_2O_3, PbO_2, ZnS, CdSe, [51, 54, 56, 133], have been synthesized in the absence of any catalyst. Taking ZnO nanobelt as an example, Dai, et al [134]have proposed a VS growth process. The source materials is vaporized into molecular species at high temperature and transported downstream by carrier gas. At the low temperature region, the vapor is condensed onto the substrate (Figure 2.3a). During the condensation, the cation-anion molecules arrange in such a way that a proper cation-anion coordination is preserved to balance the local charge and structural symmetry, forming a small nucleus (Figure 2.3b). Newly arriving molecules will continue to deposit on the formed nucleus while the surfaces that have lower energy start to form the side surfaces. Because of the local growth temperature, 800°C-1000°C, the mobility of the atoms/molecules is high enough that the low-energy surfaces tent to be flat, preventing the transverse growth normal to the side surfaces (Figure 2.3c). The side surface expands as more molecule stick onto the rough growth front, leading to the fast growth of a nanobelt (Figure 2.3 d) and formation of long nanobelt (Figure 2.3 e). The size of the nanobelt is determined by the growth temperature and supersaturation ratio in the kinetics of crystal growth.

2.3.2 Vapor-Liquid-Solid Process

The VLS growth mechanism was first proposed by Wagner and Ellis[135] to explain the formation and morphology of Si whiskers. This growth mechanism has been

studied extensively and become the most successful method for generating nanowires and more complex nanostructures with single crystalline structures [20, 93].

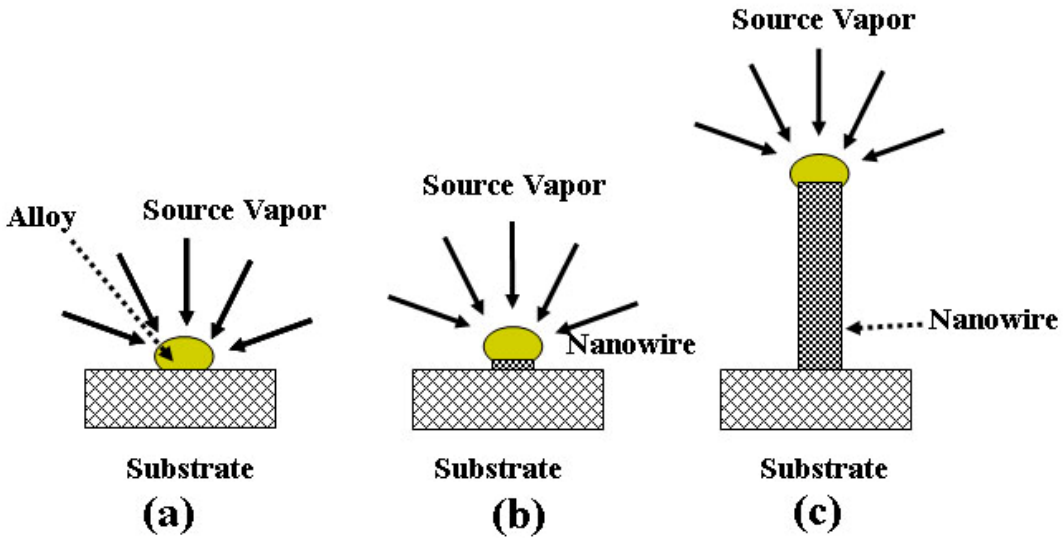

Figure 2.4 Schematic steps of the growth of a nanowire via VLS process.

A typical VLS process starts with the dissolution of gaseous reactant into nano-sized droplets of a catalyst metal, followed by the nucleation and growth of single-crystalline short rods and then longer nanowires. The catalyst droplet absorbs source vapor and forms alloy, ideally in eutectic form (Figure 2.4a). When the alloy becomes supersaturated, the source materials will precipitate out of the droplet and start forming a nanowire (Figure 2.4b). The nanowire will continue to grow with further precipitation until the source vapor is exhausted. The 1D growth is mainly induced, guided and confined by the liquid droplets, which serves as a template in some sense.

Unlike VS growth, in-situ Ge nanowire growth through a VLS process have been observed with TEM by Yang and Wu[136], as shown in Figure 2.5. They have observed three well-defined stages during this process, metal alloying, crystal nucleation, and axial growth. They started the experiment with a mixture and of Ge particle with Au nanoclusters and heated the supporting TEM grid to promote the growth. The real-time observation of the Ge nanowire growth mirrors the VLS process in Figure 2.4. The

growth started with a alloying process (Figure 2.5a-c). Au nanoclusters form an alloy and liquefy in the presence of Ge vapor. The volume of the alloy droplets increases and the elemental contrast decreases due to the absorption of the lighter element Ge vapor. When the alloy becomes supersaturated, the nucleation process begins (Figure 2.5 d, e). Interestingly, two nucleation events on the same droplet have also been observed (Figure 2.5 h, i). Once the Ge nanocrystals nucleate at the liquid/solid interface, further condensation/dissolution of Ge vapor into the system will increase the amount of Ge crystal precipitation form the system. This axial growth process proceeds as long as the catalyst alloy remains active and the source vapor is sufficient.

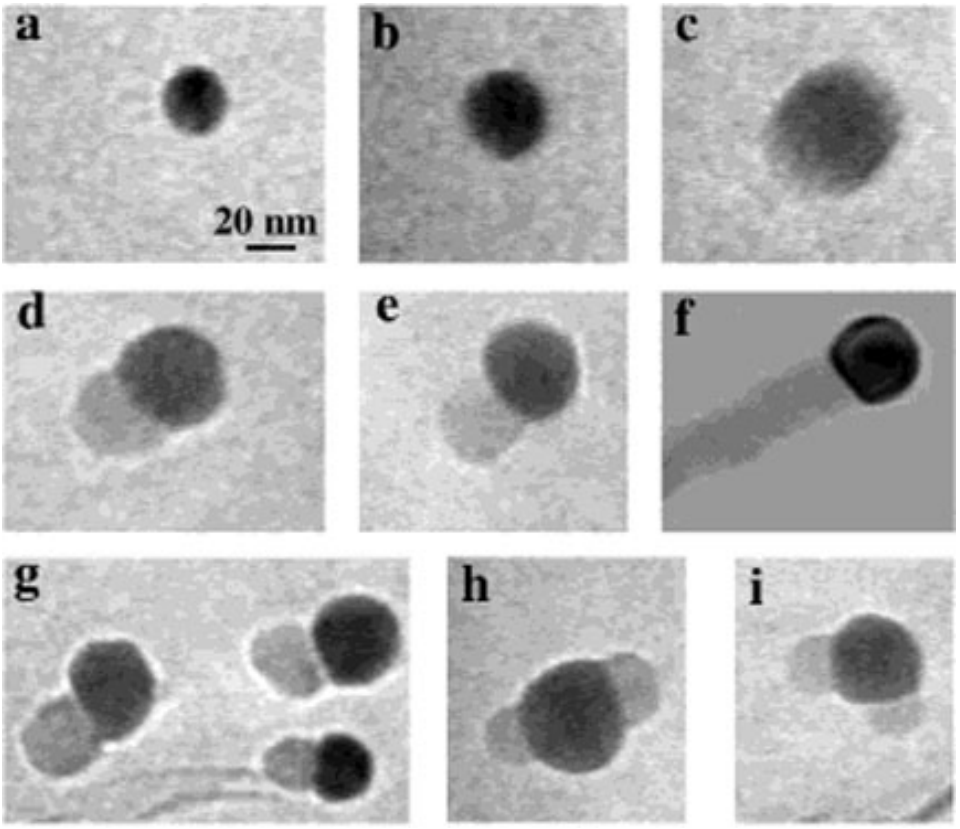

Figure 2.5 A series of TEM images showing the growth of a Ge nanowire from a gold nanoparticle (a-g) and double nucleation from single Au nanoparticle (h-i).

2.3.3 Other Growth Processes

Other than VS and VLS growth mechanism, many other growth processes have also been proposed for the synthesis of nanostructures, such as oxide-assisted growth mechanism [137-139] and vapor-solid-solid (VSS) mechanism [140-143]. The debate over whether Au-catalyzed GaAs nanowire growth should be described by the VSS[144] or the VLS[145] suggests another growth mode, in which the catalyst particle exists in a partly liquid and partly solid state. Such hybrid growth is also supported with the TEM observation of Sn-catalyzed ZnO nanostructures[146]. It's worth to note that a self-catalyzed growth is also possible for the formation of nanostructures[75].

During the growth of nanomaterials with non-centrosymmetric crystal structures, such as wurtzite-structured ZnO and CdSe, polar surfaces play an important role for many novel structures. The polar surface induced growth mechanism is one of the research interests in this dissertation and will be discussed in more detail in the flowing part. Here we will present a ZnO nanostructure as example to show the importance of polar surfaces and self-catalyzed grow process.

ZnO consists of alternating layers of oppositely charged Zn^{2+} and O^{2-} ions stacked parallel to the basal plane. The layer-by-layer structure produces an accumulating normal dipole moment and results in the divergence in surface energy. Crystals with polar surfaces generally have facets or experience massive surface reconstruction to compensate the electrostatic charge on the surface. However, ZnO ± (0001) is stable and without reconstruction, which has inspired extensive theoretical and experimental studies and is ascribed to several possible reasons: the decrease of the surface ZnO concentration, charge transfer from oxygen to Zn, and surface absorbed atoms. The surface polarity has even more significant effect at nanoscale and induced various nanostructures. For example, double-sided "comb-like" structure were synthesized and found to be a result of polar surface induced asymmetric growth[75].

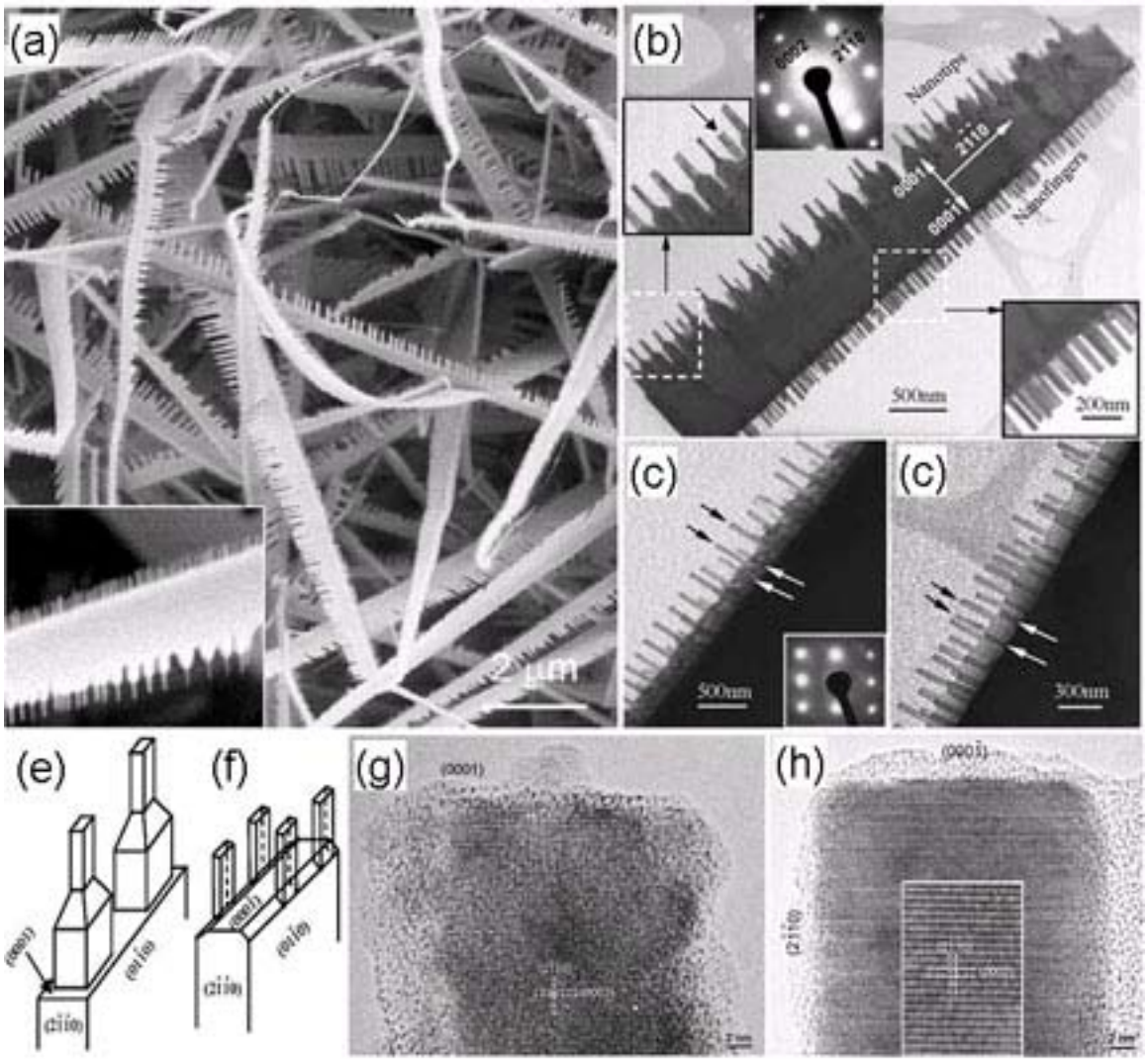

Figure 2.6 (a) SEM image and (b) TEM image of the double-sided "comb-like'' structure grown by a solid-vapor process. (c), (d) TEM images of the nanocantilever oriented at an angle with the incident electron beam so that their origin at the two edges of the main ribbon can be seen. (e), (f) Schematic models of nanotips and nanofingers grown out of the (0001) and (000 $\bar{1}$) sides, respectively. (g), (h) High-resolution TEM image recorded from a nanocantilever growing along [0001] and along [000 $\bar{1}$], respectively.

Figure 2.6a presents SEM images of the comb-like nanostructures, which consist of a thick crystal slab with many parallel longer nanoteeth on one side and shorter ones on the other side. TEM images in Figure 2.6b show that the comb ribbon grows along [2 $\bar{1}$ $\bar{1}$ 0] and nanoteeth arrays on both side grow along ± [0001]. Convergent beam electron diffraction (CBED) patterns indicate that the longer nanoteeth (nanotips) grow

along [0001] and the shorter ones (nanofingers) grow along [000 $\bar{1}$]. A tilted TEM image of the nanostructure in Figure 2.6 (c, d) clearly shows that the nanotips root at the side surface while the nanofingers root at the edges of the ribbon, as illustrated in Figure 2.6 (e, f). High resolution images of the growth front of nanotips and nanofingers give more detail about the asymmetric growth on the polar surfaces. Growing along [0001]-Zn, the nanotip in Figure 2.6g has a rough side and front surfaces, with tiny ZnO nanocrystals being formed at the growth front. In comparison, growing along [000 $\bar{1}$], the nanofinger in Figure 4.6h has a flat and smooth side and top surfaces.

Based on the quantitative structural analysis, the growth features observed for the comb structure with asymmetric structures on the two sides are apparently resulting from a fast nanoribbon growth along [2 $\bar{1}$ $\bar{1}$ 0] followed by a slow nanoteeth growth on its two sides. The (0001)-Zn terminated surface is more catalytically active, while (000 $\bar{1}$)-O terminated surfaces is more inert. The different growth rates on the (0001)-Zn and (000 $\bar{1}$)-O terminated surfaces result in the formation of comb-like nanostructure with asymmetric nanoteeth arrays on the two polar surfaces.

CHAPTER 3

HIERARCHICAL NANOSTRUCTURES

3.1 Motivation

As inspired by the discovery of oxide nanobelts, research on functional oxide-based one-dimensional nanostructures is expanding rapidly coming into the forefront of research in nanotechnology. Field-effect transistors[147], ultra-sensitive nanometer-size gas sensors[148] and humidity sensors[149], nanoresonators[108], nanocantilever[150], and nanogenerators[96, 123, 126] have been fabricated in different laboratories based on individual nanobelt/nanowire. Those novel nanostructures from functional oxide will open many new applications in nanotechnology. However, challenging still exist for any commercial application.

Structure, morphology, dimensionality, and composition control of nanostructures during synthesis is essential for practical applications. For large-scale integration, controlling the surface structure of nanostructures would have the same importance as controlling the helical angle of carbon nanotubes, which determines the semiconductor or metallic behavior of the nanotube. In order to achieve such controllability, fundamental understanding of the growth mechanism and growth kinetics must be investigated in depth. To understand the chemical and physical process involved in the growth is essential for the rational design and control of the synthesis process so as to get desired nanostructures for certain application purpose.

In this chapter, we will focus on the synthesis of oxide nanostructures. A system investigation has been carried out on ZnO and SnO_2 nanostructures. The growth mechanism of novel ZnO nanostructures has been studied carefully. Investigation on ZnO revealed that polar surface is critical for the formation of many hierarchical nanostructures in the absence metal catalyst. Based on the VS, and VLS growth

mechanism of ZnO nanostructures, experiments have been designed and resulted in complex nanoarchitectures. Guided with the growth mechanism of ZnO nanostructures, we have also investigated SnO_2 and achieved similar novel structures as ZnO. The success with SnO_2 indicates the generality of the growth mechanism derived from ZnO.

3.2 ZnO Nanorings[73]

Self-assembly of nanocrystals can be driven by van der Waals forces and hydrogen bonding among the passivating organic molecules on the particle surfaces [151-153]. For inorganic nanostructures that expose charge-polarized surfaces, such as nanobelts of oxides like ZnO[51], electrostatic forces can drive self-assembly, especially in gas-phase environments where these forces are unscreened by solvents. For crystalline nanomaterials grown in a solid-vapor environment, one type of polar charge–induced helical and spiral ZnO structure was previously reported[70]. More research on the effect of polar-charge effect was necessary for a better understanding of the fundamental growth mechanism. The experiments in this section worked towards this goal and resulted in the synthesis of single-crystal nanorings formed by epitaxial self-coiling of polar nanobelts[73].

3.2.1 Fabrication Method

Single-crystal nanorings of ZnO were grown by a solid-vapor process. The raw material was a mixture of high purity commercial ZnO (melting point 1975°C), indium oxide, and lithium carbonate powders at a weight ratio of 20:1:1, and it was placed at the highest temperature zone of a horizontal tube furnace. Before heating to a desired temperature of 1400°C, the tube furnace was evacuated to ~10^{-3} torr to remove the residual oxygen. The source materials were then heated to 1400°C at a heating rate of 20°C/min. ZnO decomposes into Zn^{2+} and O^{2-} at high temperature (1400°C) and low pressure (~10^{-3} torr), and this decomposition process is the key step for controlling the

anisotropic growth of the nanobelts. After a few minutes of evaporation and decomposition, the Ar carrier gas was introduced at a flux of 50 standard cubic centimeters per minute (sccm). The synthesis process was conducted at 1400°C for 30 min. The condensation products were deposited onto a silicon substrate placed in a temperature zone of 200° to 400°C under Ar pressure of 500 torr.

3.2.2 Structure Characterization

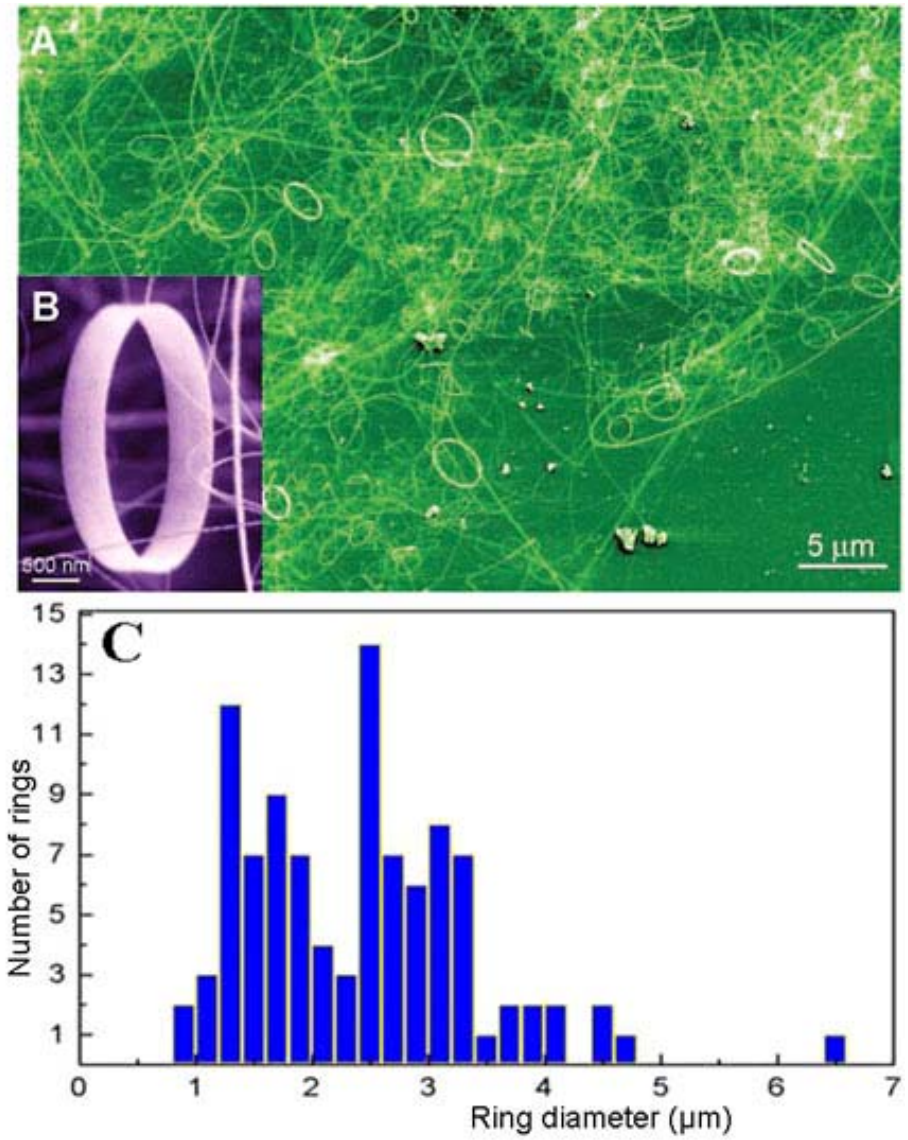

Figure 3.1 (a), (b) SEM image of the as-synthesized ZnO nanorings. (c) Distribution of nanorings as a function of diameter.

The as-synthesized samples were analyzed by scanning electron microscopy (SEM) and high-resolution transmission electron microscopy (HRTEM).The as-synthesized sample was composed of many freestanding nanorings at a significant percentage (~20 to 40%) of the yield (Figure 3.1a) and 70% reproducibility from run to run. The rings had typical diameters of ~1 to 4μm and thin, wide shells that were ~10 to 30 nm thick (Figure 3.1c). SEM images recorded at high magnification clearly show the perfect circular shape of the complete rings, with uniform shapes and flat surfaces (Figure. 3.1b). Energy dispersive x-ray spectroscopy analysis didn't detect any impurity with a resolution limit of 2%, indicating indicated that the nanorings were ZnO.

Two types of nanoring structures were found. The type I structure is presented in Figure 3.2. A TEM image (Figure 3.2a) indicates that the nanoring is a single-crystal entity with nearly perfect circular shape, although there is electron diffraction (ED) contrast caused by non-uniform deformation along the circumference. The single-crystal structure referred to here means a complete nanoring that is made of a single-crystal ribbon bent evenly at the curvature of the nanoring. Tilting the nanoring by ~20° clearly shows the single-crystal circular shape (Figure 3.2b). The corresponding dark-field TEM image (Figure 3.2c) shows the contrast produced by the equally bending lines across the width of the nanoring (Figure 3.2c), which is caused by the tilting of the atomic plane with respect to the electron beam. Deformation in the nanometer-thick ribbon does not necessarily introduce dislocations. An ED pattern recorded from the center of the nanoring (area a1 in Figure 3.2a) shows that the radial direction of the nanoring is $[1\,\bar{2}\,10]$, the tangential direction is $[10\,\bar{1}\,0]$, and the nanoring axis is [0001]. HRTEM images recorded from the three corners of the image in Figure 3.2a (areas d, e, and f in Figure 3.2, d to f, respectively) show the distribution of the equally spaced planar defects nearly parallel to the nanoring plane. The planar defects align from the top of the nanoring to the bottom without interruption (Figure 3.2, d and f).

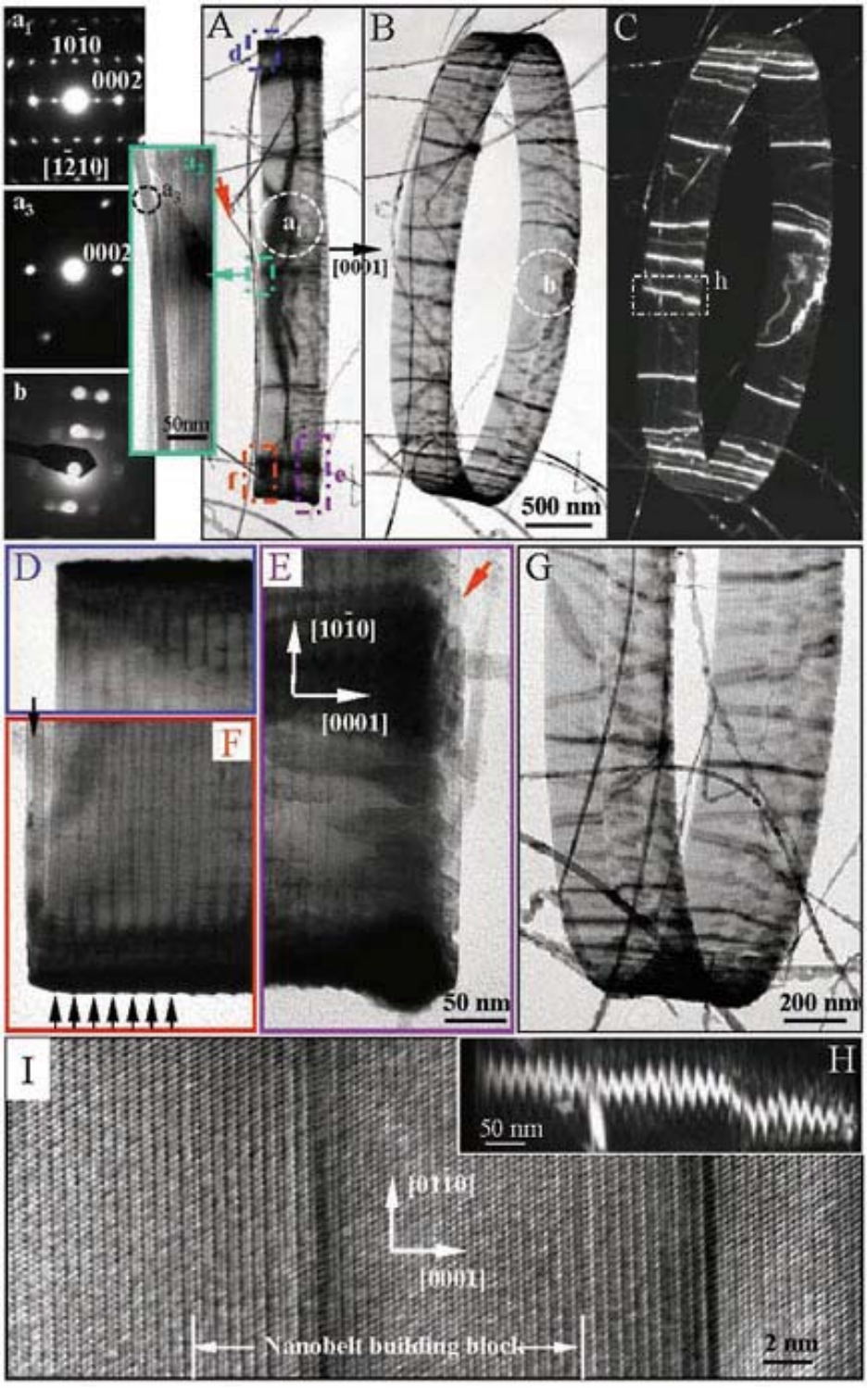

Figure 3.2 Structure of the type I ZnO singlecrystal nanoring. (A) A TEM image of a ZnO nanoring viewed with the electron beam parallel to the plane of the nanoring. (a_1) An ED pattern recorded from area a1 marked in (A). (a_2) Enlargement of area a_2 marked in (A), showing a loose end at the left-hand side. (a_3) An ED pattern recorded from the loose end (area a_3 marked in a_2). (B and C) Bright-field and dark-field TEM images

recorded from the nanoring after it was tilted by ~15°. (b) The ED pattern recorded from area b marked in (B). (D to F) are the larger images from areas d to f, respectively, marked in (A), after the nanoring was slightly tilted. (G) An enlarged TEM image of the nanoring tilted by ~10°. (H) An enlargement of area h indicated in (C), illustrating a uniform distribution of planar defects across the entire width of the nanoring. (I) HRTEM image recorded from the nanoring when the incident electron beam was parallel to the ring plane, showing planar defects inside the nanobelt and at the interface between the coiled loops. The width of the nanobelt is indicated.

The trace of the coiling nanobelt is best seen through the side of the nanoring, as indicated by arrowheads in Figure 3.2f. The entire nanoring is a single crystal, although the quality of the crystallinity varies slightly across the width of the nanoring, as shown in the enlarged TEM image in Figure 3.2g.

The nanoring is made of coaxial, uniradial, epitaxial coiling of a nanobelt. Careful examination of the image in Figure 3.2a shows a loose end of the raveling nanobelt, as indicated by a red arrowhead. The coiling of this nanobelt to form the nanoring is shown in the enlarged image in Figure 3.2f, as marked by an arrowhead at the top. Examination of the other side of the nanoring found the other loose end of the nanobelt (indicated by an arrowhead in Figure 3.2E). The ED pattern recorded from the loose end of the nanobelt, as circled in the enlarged area a_3, indicates that the nanobelt has a growth direction of $[10\bar{1}0]$, side surfaces $\pm(1\bar{2}10)$, and top/bottom surfaces $\pm(0001)$. The nanoring is made of coiling loops of the nanobelt, as in a child's "Slinky" spring, by interfacing its (0001)-Zn and $(000\bar{1})$-O planes at the same crystallographic orientation. The coiling of the nanobelt introduces a small helical angle of ~0.3°; this small rotation is hardly detectable by the ED pattern.

The loose end of the nanobelt in Figure 2F has a (0001) planar defect located close to the middle of its width, which suggests that the planar defect was produced during the nanobelt's growth and is the key for producing the fastest growth of the nanobelt along its axial direction. The reason is that planar defects usually reduce the

energy for the nanostructure and it is easy to form during the growth of one-dimensional oxide nanostructures. Once formed, it leads to the fastest growth along a direction parallel to the defect plane. For a ZnO nanobelt growing along $[10\bar{1}0]$, a single stacking fault is always present[51]. We counted 33 coiling loops in the dark-field TEM image displayed in Figure 3.2H. HRTEM indicates that, besides the planar defect inside the nanobelt, a stacking fault is formed at the interface between the adjacent loops, which is introduced to match the lattices of the Zn-terminated and O-terminated (0001) polar surfaces. Wurtzite structure has four different types of stacking faults[154]. The stacking fault at the nanobelt interface is type I. Type I and type III stacking faults have the lowest energy. The interface between the loops is coherent, epitaxial, and chemically bonded (Figure 3.2I).

The type II nanoring structure is presented in Figure 3.3. Bright-field (Figure 3.3A) and dark-field (Figure 3.3B) TEM images show that the complete nanoring is a single crystal, which again implies that the nanoring shell is a uniformly deformed, single-crystal ribbon around the circumference. Electron diffraction (Figure 3.3C) and the corresponding HRTEM image recorded from the central region (Figure 3.3D) show that the radial direction of the nanoring is $[1\bar{2}1\bar{3}]$, the tangential direction is $[10\bar{1}0]$, and the nanoring plane is $(1\bar{2}12)$ (see the model in Figure 3.4A), and there is no dislocation in the volume. Figure 3.3E displays the enlarged view of the corner indicated in Figure 3.3A, which shows an end of the nanobelt (indicated by an arrowhead) and the screw coiling of the nanobelt. The pitch distance for the coiling is 10 nm, and the total number of loops is 100. The contrast produced by stacking faults parallel to the nanoring plane is visible, but the (0001) stacking fault plane is at an angle of ~28° from the nanoring axis. The nanoring has a thin crystal wall ~15 nm thick, as clearly shown by tilting the nanoring by 15° (Figure 3.3F).

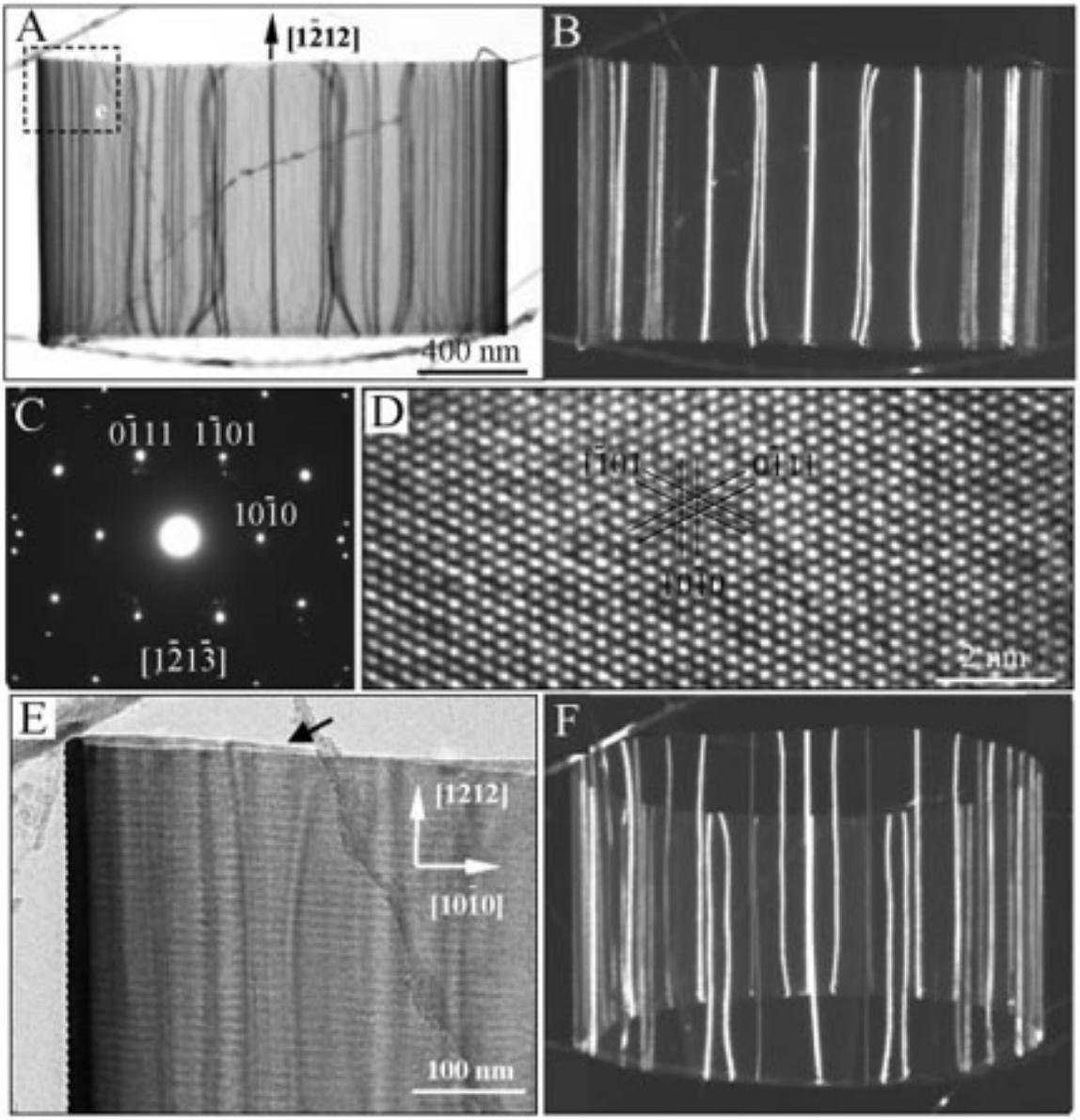

Figure 3.3 Structure of the type II ZnO singlecrystal nanoring. (A and B) Bright-field and dark-field TEM images recorded from the nanoring, with the incident electron beam parallel to the ring plane. (C) ED pattern recorded from the nanoring. The pattern shows vertical mirror symmetry, and the extra diffraction spots at the two sides are from the cylindrical bending of the single-crystal ribbon. (D) HRTEM image recorded from the central symmetric line in (A). (E) Enlarged TEM images from area e marked in (A), showing the coiling layers. The total number of loops forming this nanoring is 100. (F) Dark-field TEM image recorded from the nanoring after it was tilted by 15°.

3.2.3 Growth Mechanism

The growth of the nanoring structures can be understood on the basis of the polar surfaces of the ZnO nanobelt. The wurtzite-structured ZnO crystal is described schematically as a number of alternating planes composed of tetrahedral coordinated O^{2-} and Zn^{2+} ions, stacked alternatively along the c axis (Figure 3.4A). The oppositely charged ions produce positively charged (0001)-Zn and negatively charged $(000\bar{1})$-O polar surfaces. The polar nanobelt, which is the building block of the nanoring, grows along $[10\bar{1}0]$, with side surfaces $\pm(1\bar{2}10)$ and top/bottom surfaces $\pm(0001)$[51], and has a typical width of ~15 nm and thickness of ~10 nm. The planar defect parallel to (0001) lowers the nanobelt energy and is the key to producing the fastest anisotropic growth along $[10\bar{1}0]$, but it does not affect the intrinsic polarity of the nanobelt. Therefore, the nanobelt has polar charges on its top and bottom surfaces (Figure 3.4B). The local deposition temperature is ~200° to 400°C, which is high enough to prevent physical adsorption of molecules on the surface during growth. Thus, the polar charges on the surface are likely uncompensated for and are electrostatically effective for aligning the oppositely charged surfaces of the nanobelt during growth. As a result, the nanobelt may tend to fold itself as it lengthens, in order to minimize the area of the polar surface. One possible way to reduce the electrostatic energy is to interface the positively charged (0001)-Zn plane (top surface) with the negatively charged $(000\bar{1})$-O plane (bottom surface), resulting in neutralization of the local polar charges and in reduced surface area, thus forming a loop with an overlapped end (Figure 3.4B). The radius of the loop may be a result of how the nanobelt folds during its initial growth, but the size of the loop cannot be too small to reduce the elastic deformation energy.

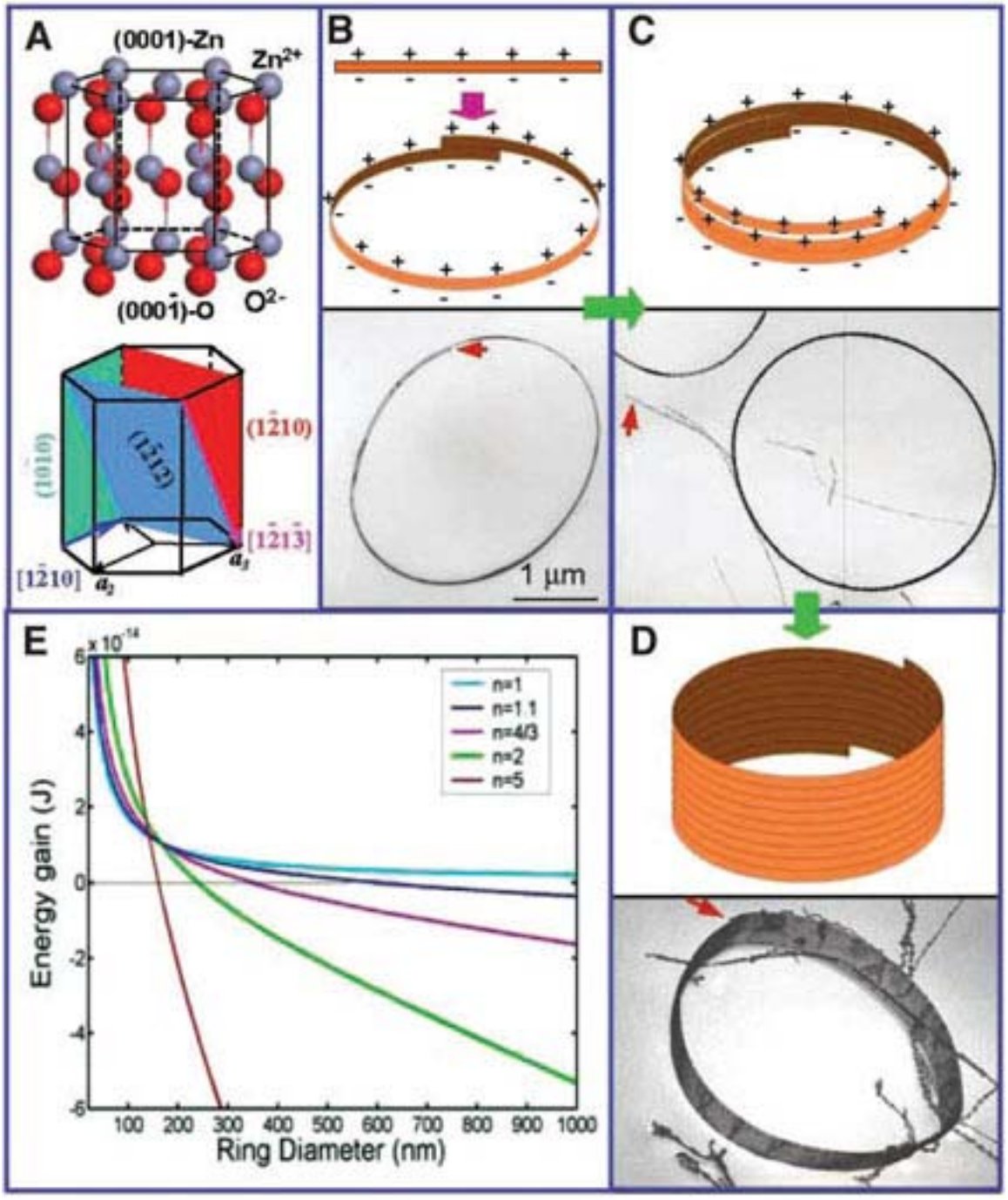

Figure 3.4 (A) Structure model of ZnO and the corresponding crystal planes discussed in the text, showing the ± (0001) polar surfaces. (B to D) Proposed growth process and corresponding experimental results showing the initiation and formation of the single-crystal nanoring via self-coiling of a polar nanobelt. The nanoring is initiated by folding a nanobelt into a loop with overlapped ends driven by long-range electrostatic interactions among the polar charges. Short-range chemical bonding stabilizes the coiled ring structure, and the spontaneous self-coiling of the nanobelt is driven by minimizing the

energy contributed by polar charges, surface area, and elastic deformation. (E) Calculated energy gain ($\Delta E=\Delta E_{Deform}+\Delta E_{Electro}$) before and after folding of a straight polar nanobelt into a loop-structured nanoring as a function of the ring radius and the number of loops. Nanobelt width=20 nm, thickness=16 nm, Young's modulus=50 GPa, and surface charge density $|\sigma|$=0.057 C/m^2. The calculation gives the threshold radius under which initiation of the nanoring structure is energetically unfavorable. The smallest nanoring observed has D=0.8μm.

There are three components of energy involved in the formation of ring structure: electrostatic interaction energy among the polar charges, surface area energy due to the decrease in surface area after chemically bonding the loops, and elastic deformation energy due to bending. The former two are usually called the surface energy, which includes the contribution from surface tension, but we separate them here for the convenience of discussion in the text. Electrostatic and deformation forces are long-range interactions, and chemical bonding is a short-range interaction. Self-coiling is possible if the decreased electrostatic energy surpasses the increased elastic deformation energy, which is the case for a thin and narrow nanobelt. The long-range electrostatic interaction is likely to be the initial driving force for folding the nanobelt to form the first loop on which subsequent growth is based. The initiation of the first few loops is likely due to long-range interactions. Calculations have been made to assess the possibility of balancing the increased elastic deformation energy (ΔE_{Deform}) by the decreased electrostatic energy ($\Delta E_{Electro}$) at the initiation of the nanoring structure (Figure 3.4E).

a) Since the thickness of the nanobelt is much smaller than the ring radius, the radial stress across the nanobelt is negligible because the two sides are free surfaces without external force. The dominant strain is along the φ-direction (tangential direction). The elastic energy is the volume integration of the φ -direction strain energy. For a nanobelt of length L, width W and thickness t, the elastic deformation energy after being coiled into a n-loop ring of radius R and wall thickness W is:

$$\Delta E_{Deform} = \frac{\pi n t Y}{24 R} w^3$$

where Y is the bending modulus, which has been measured for ZnO nanobelts with inclusion of geometrical factor.

b) The change in electrostatic energy $\Delta E_{Electro}$ contributed by the polar charges is calculated by electrostatics. A straight nanobelt is approximated to be a flat planar capacitor (length L, width W, interplane distance t, and uniform surface charge density σ). The total charges on the top and bottom surfaces are $Q_b = \pm LW\sigma$. The ring structure is approximated to be a pair of coaxial oppositely charged rims of radius R ($=L/2\pi n$), rim width W, and inter-rim distance nt ($t << R$). The total charges on the top and bottom rims of the ring are $Q_c = \pm LW\sigma/n$, respectively, much reduced for $n >> 1$.
The solutions for the two cases were received numerically by solving the integrated form of the Poisson equation. The total electrostatic energy is calculated by volume integration.

If a nanobelt is folded to form a single-loop complete ring (n=1), the energy gain ΔE ($\Delta E = \Delta E_{Deform} + \Delta E_{Electro}$) is positive regardless of the size of the loop, suggesting that a single-loop complete ring is energetically unfavorable. For a 10% overlapped nanoring (n=1.1), the nanoring structure is energetically possible if its diameter (D) is larger than 600 nm. It is thus possible to form a single-looped nanoring with overlapped ends at the beginning of the growth caused by fluctuation (Figure 3.4B). For a 33% overlapped nanoring (n=4/3), the nanoring structure is possible if D is larger than 360 nm. The diameters of the experimentally observed nanorings are in the range of 0.8 to 4 μm, and no ring has D<0.8 μm. From the SEM images, we believe that the first step (Figure 4B) occurs before the nanoring lands on the substrate.

The presence of a planar defect within the nanobelt (Figure 3.2F) is likely to be the key to producing the fast growth of the nanobelt along $[10\bar{1}0]$, because it lowers the energy in the wurtzite-structured lattice. The planar defects are mostly due to the

segregation of doping element. With the accumulation of doped indium ions in ZnO *c* planes, head-to-head and tail-to-tail inversion domain boundaries (IDBs) can be formed[155]. As growth continues, the nanobelt may be naturally attracted to the rim of the nanoring by electrostatic interactions and then extend itself parallel to the rim of the nanoring to neutralize the local polar charge and reduce the surface area, resulting in the formation of a self-coiled, coaxial, uniradial, multilooped nanoring structure. The self-assembly is spontaneous, which means that the self-coiling along the rim proceeds as the nanobelt grows. The reduced surface area and the formation of chemical bonds (a short range force) between the loops stabilize the coiled structure. The width of the nanoring increases as more loops wind along the nanoring axis (Figure 3.4C), and all of them remain in the same crystal orientation.

Sintering in ceramics usually involves mass transport and diffusion. The two adjacent loops are chemically bonded epitaxially with the same crystal orientation, and there may be no diffusion involved, which we called “epitaxial sintering” here. As the nanobelt grew along its axial direction as guided by the planar defect, it was being bonded down on the rim of the ring by electrostatic interaction. Because the melting point for a nanostructure can be as low as one-third of its bulk melting point, and the temperature required for sintering is usually one-third of the melting temperature, it is thus possible to chemically join the loops at 200° to 400°C. As a result, “epitaxial sintering” of the adjacent loops forms a single-crystal cylindrical nanoring structure, and the loops of the nanobelt are joined by chemical bonds as a single entity. The loops that were coiled first remained at the growth temperature for a longer time, resulting in higher crystallinity, whereas the ones that wound on later had less time for sintering and thus had relatively poorer crystallinity, forming the structure in Figure 3.2G, with two contrast regions across the width of the nanoring. Finally, as the growth time was extended, the entire nanoring exhibited high-quality crystallinity, as shown by the diffraction contrast in Figure 3.4D. A uniaxial and perfectly aligned coiling is energetically favorable

because of the complete neutralization of the local polar charges inside the nanoring and the reduced surface area. The entire growth process may have no relation to the substrate used for collecting the sample. In principle, the polarity of the surfaces can be determined by convergent beam ED (CBED)[156], but it requires a specimen thickness of 50 nm or more to enhance the dynamic scattering effect. The 20-nm thickness of the rim of the nanoring is insufficient for CBED analysis to determine its polarity.

The coiling process presented in Figure 3.4 unifies the two types of nanoring structures described in Figs. 3.2 and 3.3. If the (0001) polar surface of the ZnO nanobelt is parallel to the ring plane, self-coiling of the nanobelt at a radial direction of [1 2 10] forms the type I structure in Figure 3.2. Alternatively, if the nanobelt is tilted toward the nanoring center so that the radial direction is $[1\,2\,1\,\bar{3}]$. Among the possible glide systems for hexagonal close-packed structure, (0001), [1 2 10]; and (1 2 12), $[1\,2\,1\,\bar{3}]$ are the two possible systems, which correspond to the cases presented in Figure 3.2 and 3.3, respectively[157]. Self-coiling of the nanobelt produces the type II structure in Figure 3. The tilting of the nanobelt may reduce the elastic deformation energy.

The model presented here can also be adopted to explain the helical nanostructure reported previously[70]. If the nanobelt in Figure 3.4B is flipped by 90° so that the radial direction of the nanoring is [0001], which means that the polarization is in the radial direction, a bending of the nanobelt into a circle slightly reduces the electrostatic energy, possibly in favor of forming an in-plane spiral nanoring[70]. Alternatively, as a result of preserved polar charges on the inner and outer arc surfaces, the circular loops of the nanobelt cannot be densely packed into a single-crystal coil structure because of the electrostatic repulsion among them; instead, a helical structure would be formed, with a pitch distance of 200 to 500 nm [much larger than the width (~20 nm) or thickness (~10 nm) of the nanobelt], which is suggested to be a result of balancing the electrostatic repulsive force between the loops and the elastic deformation force.

The polar charge–induced nanorings presented here have potential applications in investigating fundamental physical phenomena, such as the Aharonov-Bohm oscillations in exciton luminescence[158]. The piezoelectric and semiconducting properties of ZnO predict that the nanorings could be used as nanoscale sensors, transducers, and resonators.

3.3 ZnO Nanohelixes

Helical structures are the most fundamental structural configurations for proteins, RNAs, and other biomolecules. One-dimensional nanocoils have been observed for carbon nanotubes[159], Sic[160] and amorphous silicon carbide[161]. The carbon coils are created due to a periodic arrangement of the paired pentagon and heptagon carbon rings in the hexagonal carbon network[162], and the SiC coils are suggested to be formed due to the existence of planar defects and/or dislocations. Recently, spontaneous polarization-induced nanostructures due to the presence of ±(0001) polar surfaces have been reported, such as nanohelixes/nanosprings[70, 163], seamless nanorings[73], and nanobows[164] of single-crystal ZnO nanobelts. The nanosprings have a typical diameter of ~1-2 μm and pitch distance of ~0.3 μm and are made of a uniformly deformed single-crystal nanobelt around the circumference. The side surfaces of the coiling nanobelt are dominated by Zn^{2+}- and O^{2-}-terminated ± (0001) surfaces with positive and negative ionic charges, respectively, creating a spontaneous polarization across the nanobelt thickness. Nanosprings are formed by rolling up single-crystal nanobelts to minimize the electrostatic energy, and their equilibrium shape and dimensions are determined by balancing the electrostatic interaction and the elastic deformation [70, 164].

In this section, a new single-crystal nanohelical structure of ZnO was discussed. Being rigid and free from deformation, the nanohelixes are formed following a hexagonal screw-coiling model, analogous to the charge model of an RNA molecule. It is shown

that the electrostatic interaction between the new polar surfaces of $\pm \{01\bar{1}1\}$ results in the formation of the deformation-free nanohelixes

3.3.1 Fabrication Method

The ZnO nanohelixes were synthesized by thermal evaporation of a mixture of source materials consisting of powders of ZnO (0.6 g) Li_2CO_3 (0.3 g) and Ga_2O_3 (0.1 g), which were placed at the center of an alumina tube that was inserted in a horizontal tube furnace, where the temperature, pressure, and evaporation time were controlled. The tube furnace was heated to 1000 °C at a heating rate of 30 °C/min and held at the peak temperature for 2 h, which is important for controlling the growth kinetics and the formation of helical nanostructure. The tube chamber pressure was kept at 200 Torr with Ar flux at about 25 sccm (standard cubic centimeters per minute). During evaporation, the products were deposited onto an alumina substrate placed at the downstream end of the alumina tube, where the deposition temperature was 250-350 °C, which is located about 23 cm from the source material (the total length of the tube furnace is 75 cm). Our previous study [70, 163] shows that the introduction of Li_2CO_3 and Ga_2O_3 in the source material makes it possible to grow polar-surface dominated nanobelts, but the mechanism needs further investigation.

3.3.2 Structure Characterization

The as-synthesized products were first examined by scanning electron microscopy (SEM). The high yield of the nanohelixes is manifested by the low-magnification SEM image (Figure 3.5a). The high-magnification SEM image (Figure 3.5b) clearly demonstrates the shape of the nanohelixes. Nanohelixes of both right- and left-handed chiralities have been observed at ~50% each. With a detection limit of 1-2 at. %, energy-dispersive X-ray spectroscopy detected mainly Zn and oxygen without the presence of other elements in the sample. The observed helixes here have a typical diameter of 30

nm, which is much smaller than the ZnO nanosprings of typical diameter of 800 nm reported previously[70].

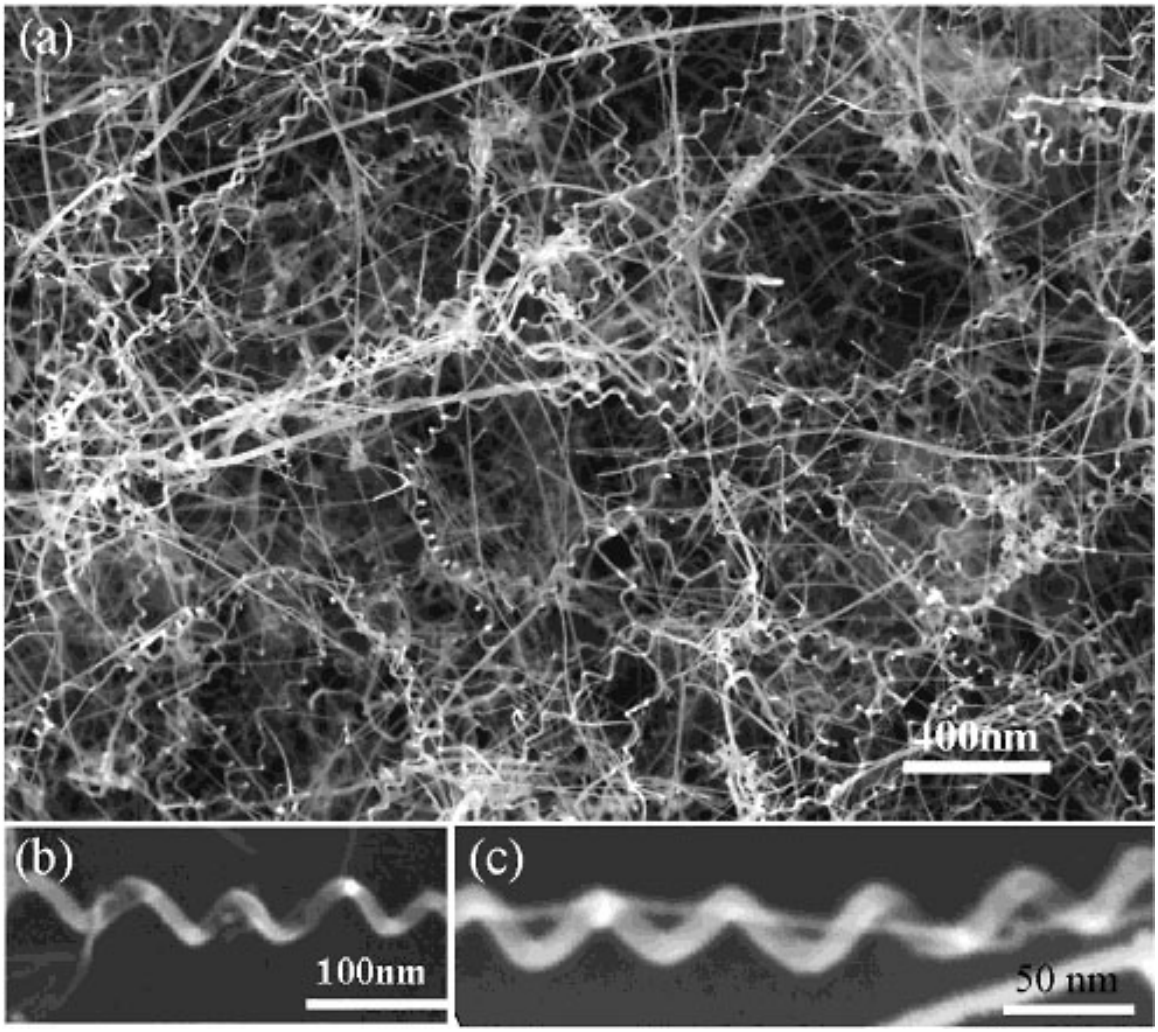

Figure 3.5 (a) Low-magnification SEM image of the as-synthesized nanohelixes of ZnO, showing their uniform sizes and high yield. (b) An enlarged right-handed nanohelix. (c) A small nanohelix with pitch distance of 60 nm and radius 40 nm, which grows around a straight nanowire.

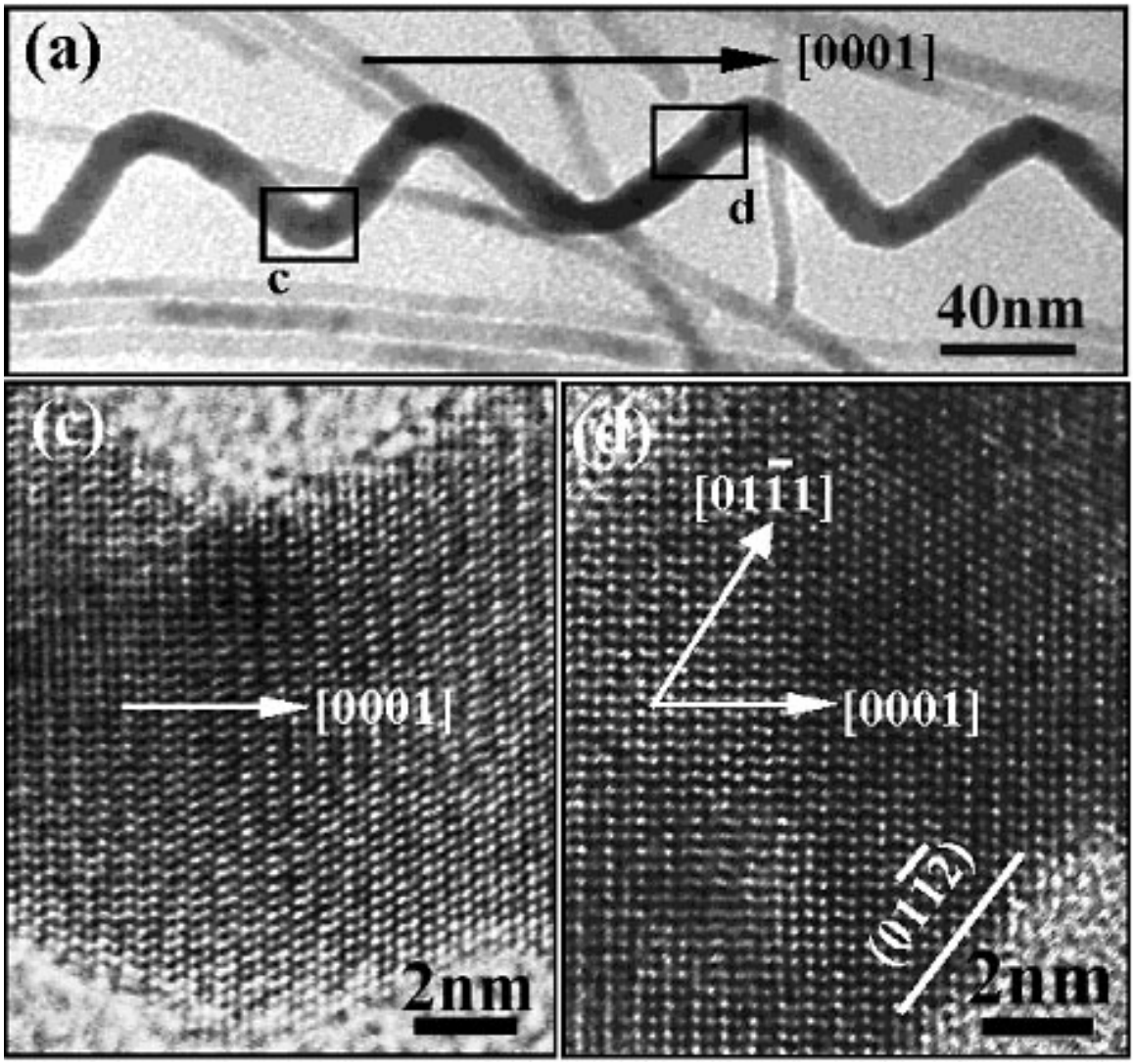

Figure 3.6 (a) A bright-field TEM image of a nanohelix. No significant strain contrast is found (apart from the overlap effect between the nanohelix and nanowires). (c, d) HRTEM images recorded from the c and d areas labeled in (a), respectively, showing the growth direction, side surfaces, and dislocation-free volume.

The intrinsic crystal structure of the nanohelixes has been investigated by transmission electron microscopy (TEM), showing a uniform shape and contrast (Figure 3.6a). High resolution TEM (HRTEM) imaging reveals that the nanohelix has an axial direction of [0001], although the growth direction of the nanowire changes periodically along the length. Detailed HRTEM images from the regions labeled c and d in Figure 3.6a are displayed in Figure 3.6c,d, respectively, which show that the nanowire that

constructs the nanohelix grows along [01 $\bar{1}$ 1]. Because the incident electron beam is parallel to [2 $\bar{1}$ $\bar{1}$ 0], the two side surfaces of the nanowire are ± (01 $\bar{1}$ $\bar{2}$). No dislocations were found in the nanohelixes. It is important to note that the image recorded from the "twist" point of the nanohelix shows no change in crystal lattice (Figure 3.6b), and the traces of the two sides are visible, indicating the non-twisted single-crystal structure of the entire nanohelix.

3.3.3 Growth Mechanism

The nature of the ± {10 $\bar{1}$ $\bar{1}$} and ± (01 $\bar{1}$ $\bar{2}$) planes can be understood from the atomic model of ZnO. By projecting the structure along [1 $\bar{2}$ 10], in addition to the most typical ± (0001) polar surfaces that are terminated with Zn and oxygen, respectively, ± (10 $\bar{1}$ $\bar{1}$) and ± (10 $\bar{1}$ 1) are also polar surfaces (Figure 3.7a). From the structure information provided by Figure 3.6, the structure of the nanowire that self-coils to form the nanohelix can be constructed (Figure 3.7b). The nanowire grows along [01 $\bar{1}$ 1], the two end surfaces being ±(0001), side surfaces being non-polar ±(01 $\bar{1}$ $\bar{2}$) (represented by yellow), Zn^{2+}-terminated (1 $\bar{1}$ 01) and ($\bar{1}$ 011) (represented by red), and O^{2-}-terminated ($\bar{1}$ 10 $\bar{1}$) and (10 $\bar{1}$ $\bar{1}$) (represented by green) surfaces (see Figure 3.7b,c).

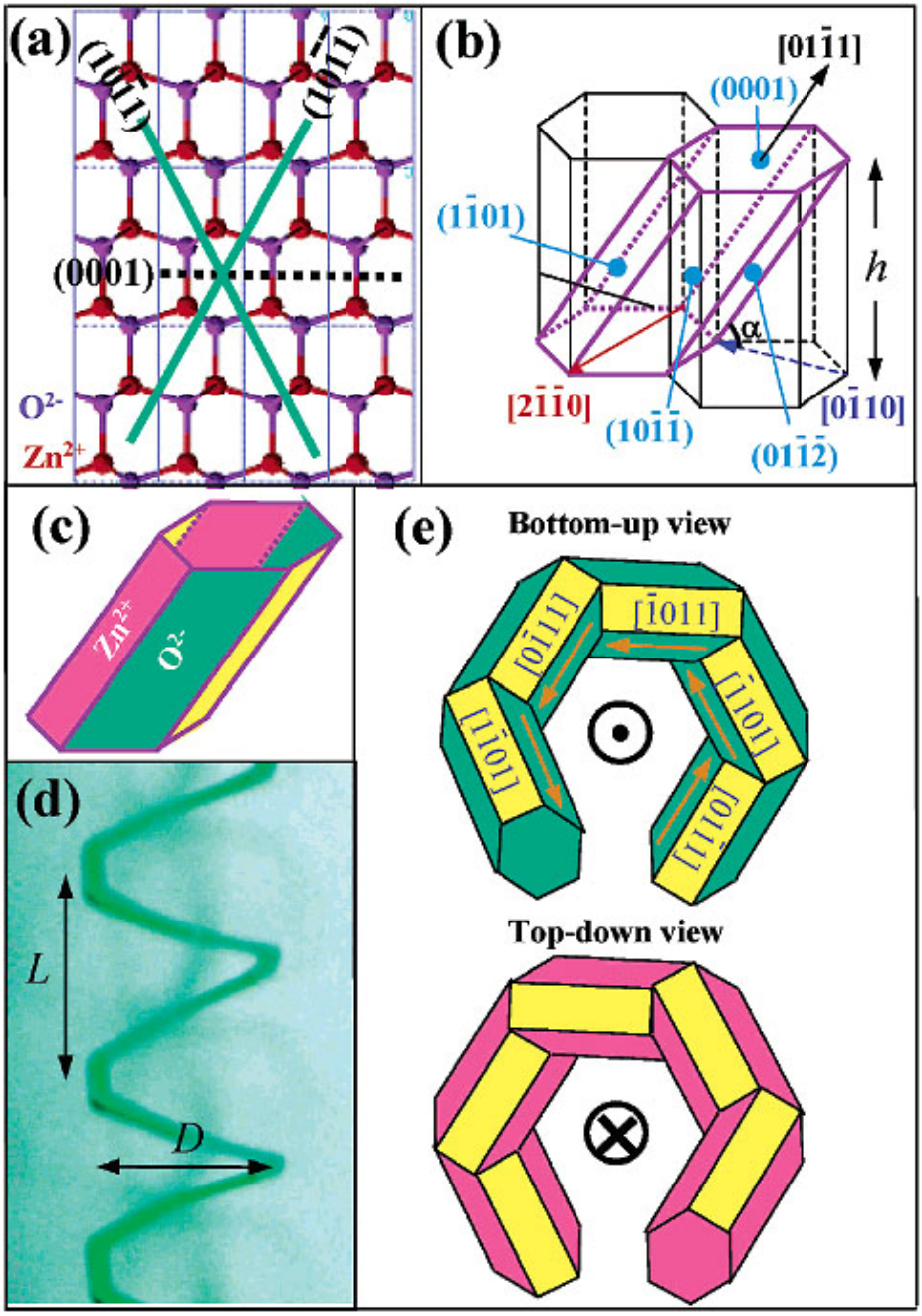

Figure 3.7 (a) Atomic structure of wurtzite ZnO projected along [1 $\bar{2}$ 10], showing $\pm$ (0001), {10 $\bar{1}$ $\bar{1}$} type polar surfaces. (b) The fundamental building block of the nanowire (in purple) for constructing the nanohelixes, and its growth direction and surfaces. (c) The Zn- and O-terminated surfaces for the building block as represented by red and green colors, respectively. (d) A schematic model of the nanohelical structure, where the red and green represents the Zn and oxygen terminated surfaces, respectively. (e) The bottom-up and top-down views of the nanohelical model.

The structure model presented in Figure 3.7c is the basic building block/segment for constructing the nanohelix via a self-coiling process during the growth. Because there are a total of six crystallographically equivalent <0 $\bar{1}$ 11> directions: [01 $\bar{1}$ 1], [$\bar{1}$ 101], [$\bar{1}$ 011], [0 $\bar{1}$ 11], [1 $\bar{1}$ 01], and [10 $\bar{1}$ 1], and there is a 60° rotation between the two adjacent directions, thus, there are six equivalent orientations to stack the building block along the [0001] axial direction without introducing deformation or twist. A realistic three-dimensional model of the nanohelix is presented in Figure 3.7d, which is a stacking of the building blocks around the [0001] axis following the sequences of the six directions described above. The interface between the two building blocks is perfectly coherent and the same piece of crystal, without mismatch, translation, or twist.

The distribution of the polar charges on the surfaces of the polar nanowire is analogous to the charge model of an RNA single helix model, and it is best seen through the top and bottom views of the model (Figure 3.7e). If viewing the nanohelix from bottom-up, the nonpolar (0 $\bar{1}$ 12), Zn^{2+}- terminated (1 $\bar{1}$ 01) and ($\bar{1}$ 011) are seen. The six growth directions of the building blocks are indicated. It is important to point out that there is no deformation introduced in the hexagonal screw-coiling stacking process, thus, no dislocations are needed to accommodate deformation. If viewing the nanohelix from top-down, the nonpolar (0 $\bar{1}$ 12) and the O^{2-}-terminated ($\bar{1}$ 10 $\bar{1}$) and (10 $\bar{1}$ $\bar{1}$) surfaces are seen. The Zn-terminated (0001) leads the nanowire growth due to self catalysis[75].

The geometrical structure parameters calculated from the model shown in Figure 3.7b-e can be directly compared to the experimental data. If the height of the building block is h along [0001] (see Figure 3.7b), the pitch distance would be $L = 6h$; the mean diameter D of the nanohelix, defined as the average of the inner and outer diameters of the nanohelix and is measured between the centers of the nanowire perpendicular to the helical axis, is $D \approx 2h/\tan\alpha$, thus, $\alpha = \arctan(L/3D)$. The ZnO nanowires that coil to form helixes have uniform diameters of ~12 nm; the mean diameter D of the nanohelixes is

~30 nm (Figure 3.8a), but the measured pitch distance varies due to the three-dimensional projected shape in the images. The derived angle from the measured *D/L* is almost a constant: $\alpha \approx 40\pm2°$ (Figure 3.8b) and it matches well to the theoretically expected inclining angle between the nanowire growth direction $[01\bar{1}1]$ and the c-plane (0001), which is $\alpha = 42.77°$ (see Figure 3.7b).

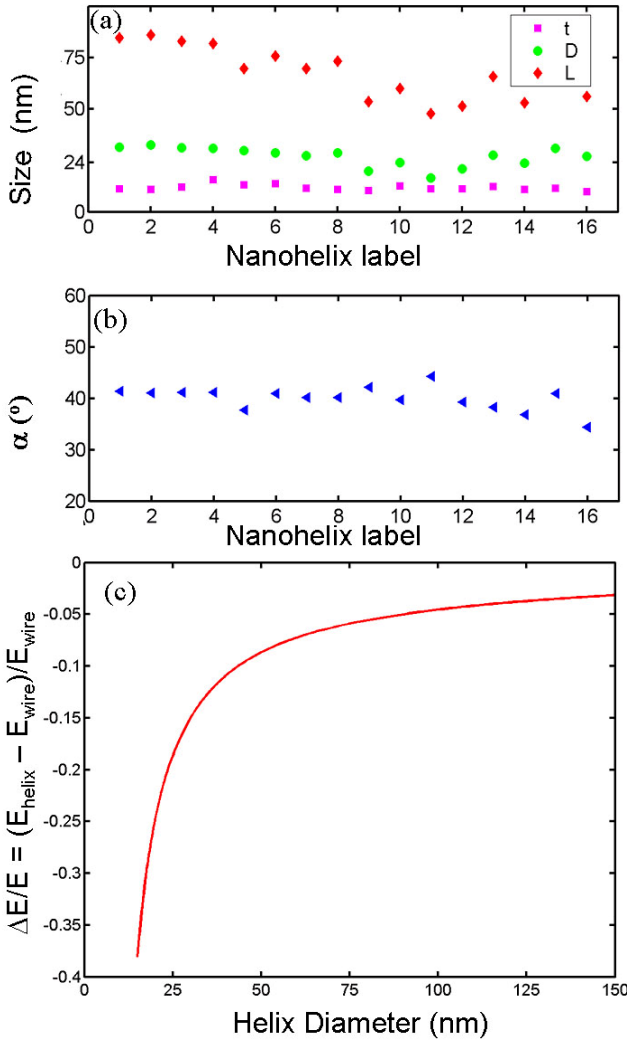

Figure 3.8 (a) Measured diameter (*t*) of the nanowire, mean diameter (*D*), and pitch distance (*L*) for 16 nanohelixes. (b) The angle (see the model in Figure 3.7b) is derived from the experimentally measured *D* and *L* according to $\alpha = \arctan(L/3D)$. (c) Calculated change in relative electrostatic energy ($\Delta E/E$) by folding an infinitely long and straight polar nanowire into a helical structure as a function of the mean diameter, *D*, for *t*) 11.7 nm.

To gain a quantitative understanding about the charge model proposed, we calculated the relative change in electrostatic energy ($\Delta E/E$) by folding a straight polar nanowire into a helical structure as represented by the model in Figure 3.7c,d without introducing deformation (Figure 3.8c). A straight nanowire is approximated to be a capacitor made of two long, parallel and oppositely charged strips (width W, interplanar distance t, and uniform surface charge density ($\pm\sigma$). The shape of the nanohelix is approximated to be a circular screw-coiling of the nanowire with the positively charged plate directly above the negatively charged plate, being separated by a distance of t. The potential was calculated numerically by solving the integrated form of the Poisson equation. The electrostatic energy decreases after forming a nanohelix (Figure 3.8c). However, the magnitude of energy decrease is significant only if the mean diameter $D <$ 75 nm, strongly in favor of forming small-size helixes. For the observed value of $D = 30$ nm in our experiment, $\Delta E/E = -15\%$, indicating the nanohelical structure is energetically favorable.

Switching of chirality occurs for the nanohelix. Nanohelixes that stick together have been found (see the area indicated by an arrowhead in Figure 3.9a). This is possible because the oppositely charged nanohelixes of the same chirality would attract each other to neutralize the interface charge. This is observed at the left-hand side of Figure 3.9b, where the two nanohelixes have the left-handed chirality. On the right-hand side of Figure 3.9b, however, one of the nanohelixes switches its chirality to right-handed. As a result, the two nanohelixes touch at the surface areas that have no polar charge (see the model in Figure 3.7e). The point at which the nanohelix changes its chirality is indicated by an arrowhead in Figure 3.9b. A TEM image of a nanohelix that changes its chirality during the growth is shown in Figure 3.9c. There is a short, straight segment of the nanowire that is along [0001], which bridges the two nanohelixes that were formed by stacking of the building blocks clockwise and counterclockwise, respectively, resulting in a change in chirality. It is important to note that the [0001] c-axis remains as the uniaxial

direction of the entire nanostructure (see the (0002) lattice fringes in Figure 3.9d), and there is no twist. The result shows that the nanohelix has no preference either in left-handed or right-handed chirality. This is because the electrostatic interaction energy remains the same if the signs of the two polar surfaces are switched.

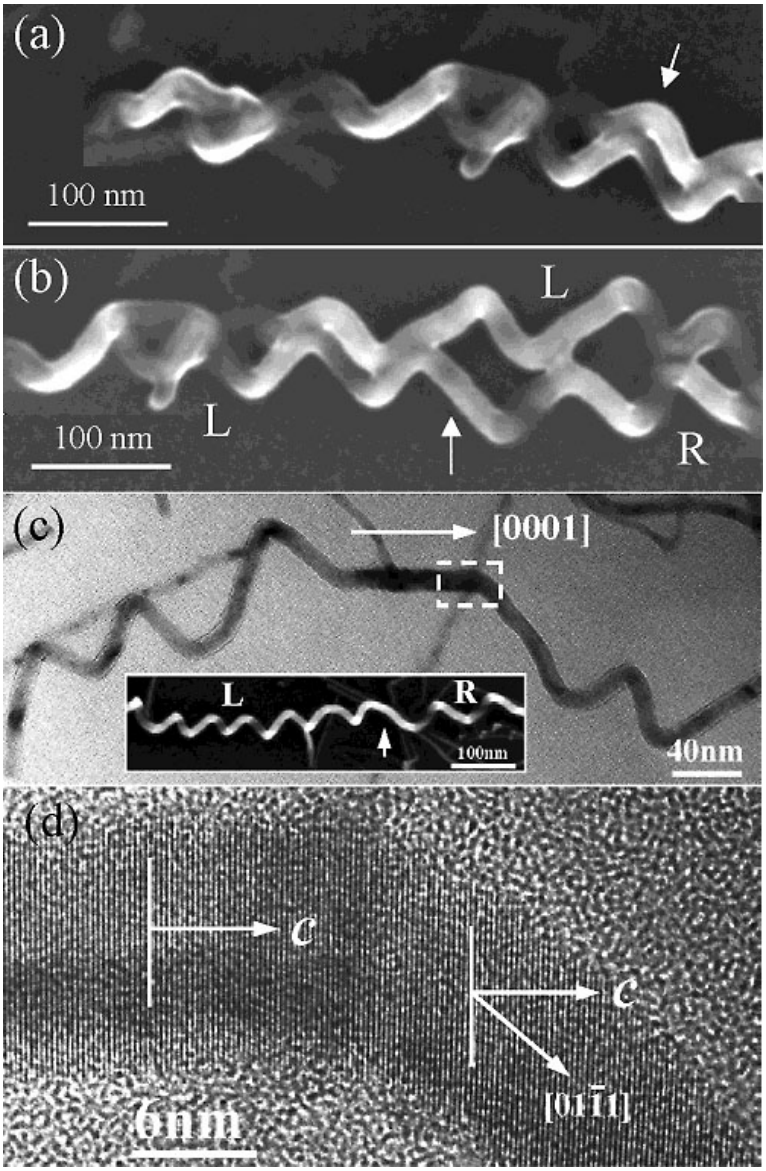

Figure 3.9 (a) SEM image of two nanohelixes that adhere possibly due to electrostatic attraction. (b) Two adhered nanohelixes, one of which changes its chirality from left-handed (L) to right-handed (R) through a straight segment of the nanowire. (c) TEM image of a nanohelix that changes its chirality from left-handed to right-handed, and (d) is a high-magnification TEM image from the boxed region, showing the change of growth direction from [0001] at the straight segment to [01 $\bar{1}$ 1] in the coiled region.

The nanohelixes reported here are distinct from the nanorings and nanosprings reported previously [70, 73, 164]. First, the nanohelixes are single-crystal without elastic deformation, while elastic deformation was induced in forming the nanorings and nanosprings due to the different structural configurations. Second, because no elastic/plastic deformation is introduced in forming the nanohelix, it is the electrostatic energy that dominates the entire formation process, making it possible to form the nanohelixes much smaller than the diameters of the nanorings and nanosprings. Third, the ± (0001) polar surfaces were responsible for forming the nanorings and nanosprings, while the new polar surfaces of ± $\{01\bar{1}1\}$ are responsible for forming the nanohelixes reported here. Finally, the geometrical shape and sizes of the nanohelixes are more uniform.

A deformation-free, single-crystal nanohelical structure of ZnO and its hexagonal screw-coiling growth process is presented in this section. The growth of the nanowire is led by the Zn-terminated (0001) surface due to self-catalysis[75]. A sequential change in growth direction among the six equivalent growth directions of $<0\bar{1}11>$ in an ordered and equal distance results in the formation of the nanohelix. The entire structure is a deformation-free, block-by-block stacking process following hexagonal screw symmetry, without introducing distortion in crystal lattices. The sequential change in growth direction is to reduce the electrostatic interaction energy between the ± $\{01\bar{1}1\}$ polar surfaces. The type of ZnO structure could be a potential object for studying fundamentals of nanoscale piezoelectric effect. They could have potential applications as nanoscale sensors, transducers, and actuators for applications in nanoelectromechanical systems (NEMS) and biosensing.

3.4 ZnO Nanowire Arrays

VS process have resulted in 1D nanobelts or nanowires from various materials, such as ZnO, SnO_2, In_2O_3, CdO, ZnS, CdSe, ZnSe, and CdS[51, 54], in which

longitudinal growth along there length direction are considered to be dominant and the transverse growth across its diameter/width is neglected in most case. In this section, interpenetrative ZnO nanorod arrays are presented and demonstrated that transverse growth play an import role for the formation of this kind nanostructure. In addition, base on careful study of VS and VLS growth process, designed experiments have resulted in the growth of complex nanoarchitectures.

3.4.1 Self-Catalyzed ZnO Nanorods

Growth of 1D nanostructures is mainly attributed to a vertical growth model, in which the nanostructure is believed to grow along its length direction (the longitudinal growth), and there is little growth across its diameter/width (the transverse growth), because most of the 1D nanostructures have uniform structures along their lengths. The size of the nanostructure is believed to be defined at the very beginning of the growth. In this section, distinct from the traditional model, the transverse growth of the nanorods across their width is demonstrated. Using the growth of ZnO nanorods without catalyst as an example, we first illustrate the interpenetrative structures of nanorods at an arbitrary angle. Then, the self-catalyst growth at the Zn-terminated (0001) surface is presented, which is responsible for the formation of "pencil" or “bullet” shaped structure. The formation of interpenetrative tapering nanorods is due to self-catalyzed asymmetrical growth together with the transverse growth. The understanding of this growth mechanism gives some insight about the formation of complex oxide nanostructures.

3.4.1.1 Fabrication Method

The interpenetrative nanorods were synthesized through a thermal evaporation process in a horizontal tube furnace. Commercial grade ZnO powder was place in the center of a single zone tube furnace. The system was pumped down to 10^{-3} torr and evacuated for several hours to purge oxygen in the chamber. Polycrystalline alumina

substrate was used for growing the nanostructures. After the evacuation the temperature of the system was elevated to the synthesis temperature of 1370 °C with Ar running through at the rate of 50 sccm. The pressure was kept at 500 mbar before the temperature reached 800 °C and 200 mbar afterward. The as-synthesized products were analyzed by scanning electron microscopy (SEM) and transmission electron microscopy (TEM)

3.4.1.2 Structure Characterization

ZnO nanorods of uniform size have been synthesized by a solid-vapor phase process directly by vaporizing ZnO powder without using catalyst (Figure 3.10a). Most of the nanorods grow vertically upwards and they are separated from each other. The nanorods with uniform diameter around 800 nm were collected at a temperature region of about 500˚C. But a close examination has found that some of the nanorods are interpenetrative (Figure 3.10b). This is a rather unique feature. The facets at the side and at the front of the nanorods are well defined and flat. The "pencil" or "bullet" shape of the nanorods can be seen through the SEM image displayed in Figure 3.10c, where one end of the nanorod is flat and the other end is a sharp tip.

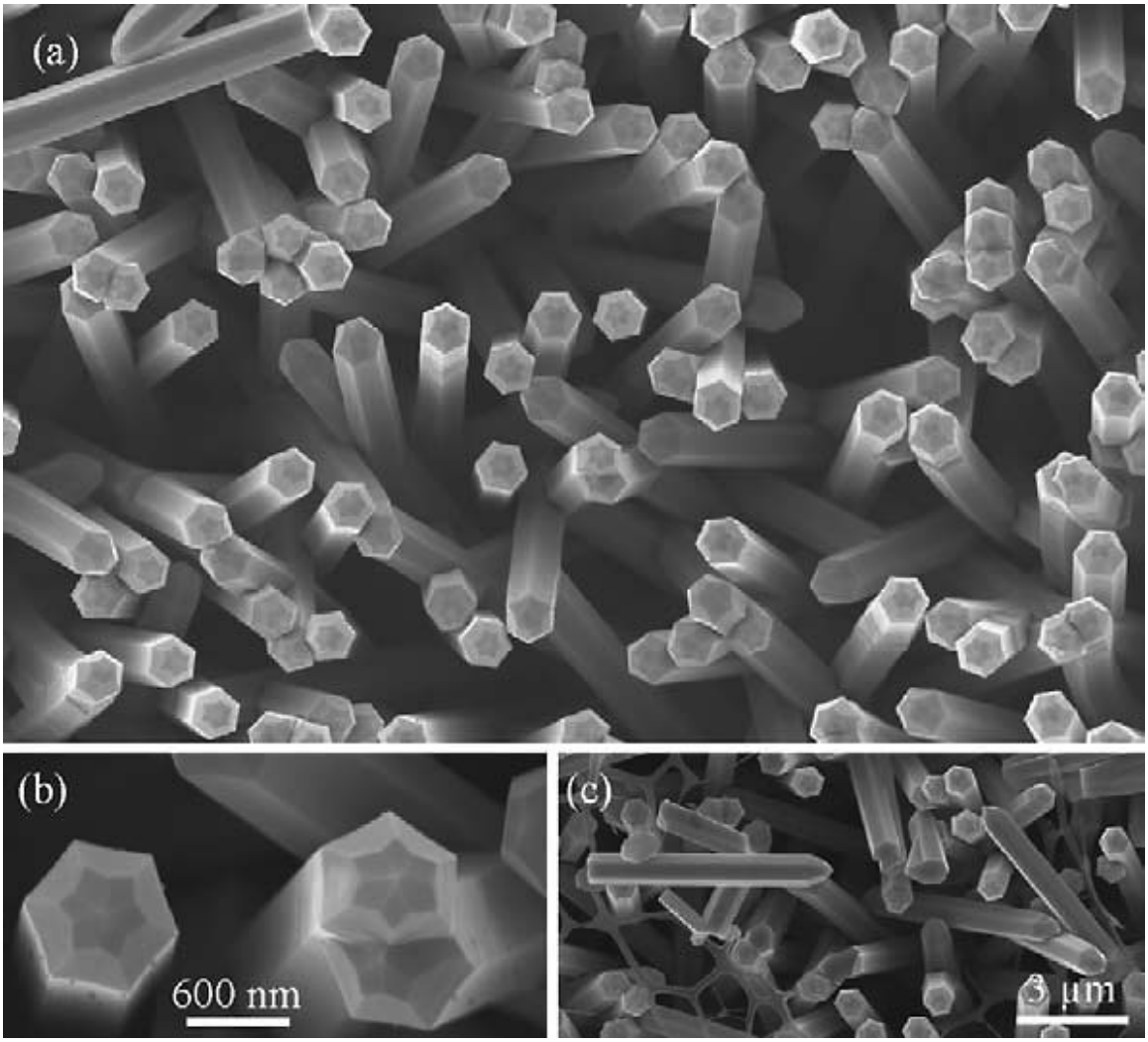

Figure 3.10 (a) SEM image showing a high percentage of interpenetrative nanorods in the sample collected at a local temperature of 500°C. (b) SEM image showing the well-defined facets on the tip. (c) The 'pencil' or 'bullet' shaped morphology of the nanorod.

The nanorods collected in a temperature region of 450˚C are less dense (Figure 3.11a). The diameter of the nanorods is about 600 nm. Compared to the nanorods in Fig 3.10b, the nanorods in Fig 3.11 have small pyramids at the growth fronts. The diamond-shaped facets at the growth front are larger, and the trapezoidal shape facets become triangular shape (Figure 3.11b). In spite of the appearance of pyramids, the nanorods still penetrate each other freely as shown in Figure 3.11c, and there is no specific angle at which the two intercept.

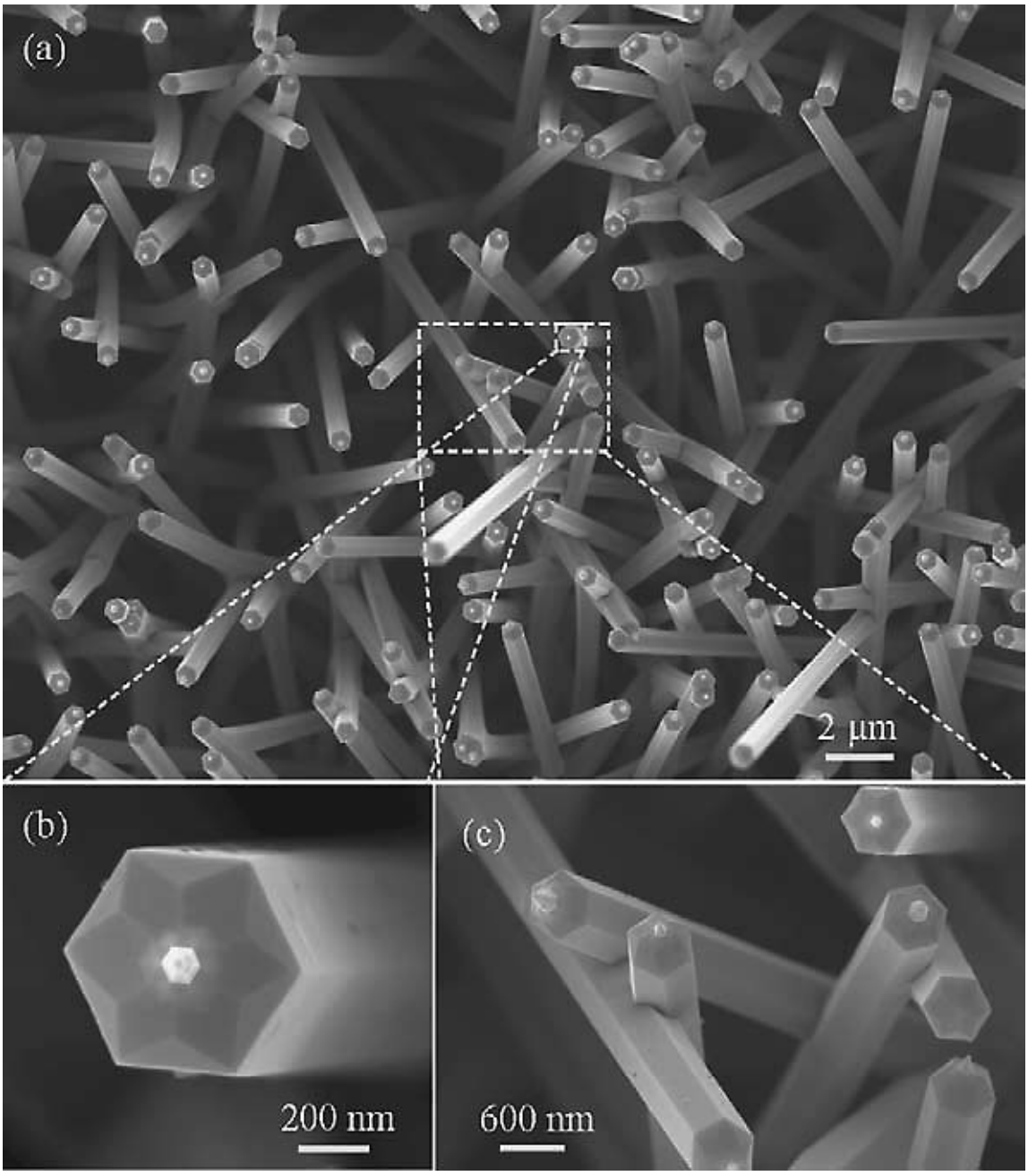

Figure 3.11 (a) SEM image showing interpenetrative nanorods in the sample collected at a local temperature of 450°C. (b) SEM image showing the well-defined facets and a small pyramid at the tip. (c) The interpenetrative structure with small pyramids on the tips.

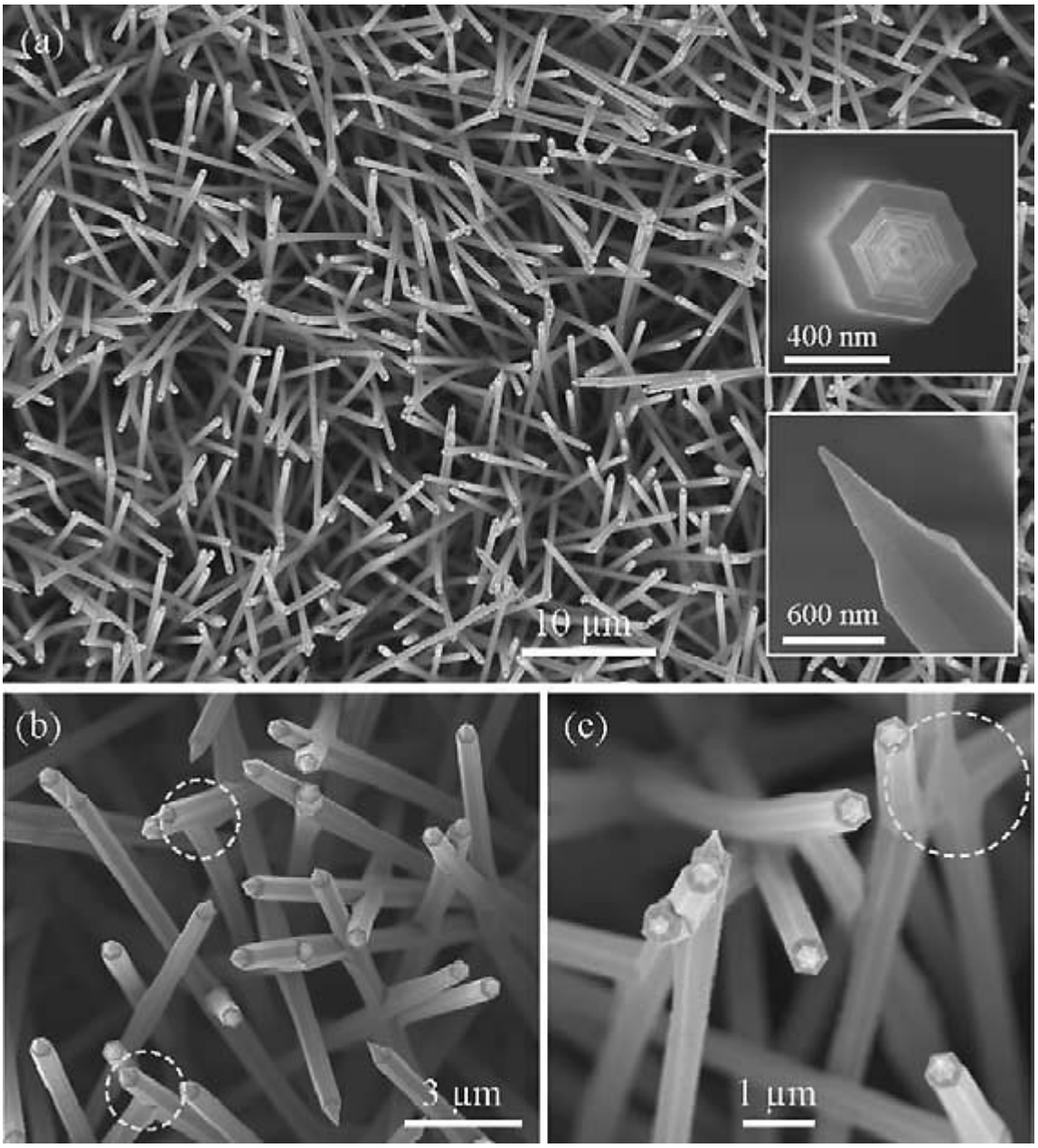

Figure 3.12 (a) SEM image showing interpenetrative nanorods in the sample collected at a local temperature of 400°C. The insets show clearly the evenly spaced stairs on the sharp cone-shaped tip. (b) SEM image showing nanorods that are either interpenetrative or terminated at other nanorods. (c) Swelling and bent at the nanorod intersection.

With a further decrease in local growth temperature to 400˚C, the hexagonal pyramid at the center of the tip is getting larger, while the diameter of the nanorods becomes smaller (Figure 3.12). From the inserts in Fig 3.12a, the side surface of the

pyramid is not a flat facet but evenly spaced stairs. Besides a significant percentage of interpenetrative nanorods, the nanorods terminated at other nanorods are also found, as shown in the circled regions in Figure 3.12b. The interpenetrative nanorods still preserve the hexagonal shape and growth direction after crossing. But the nanorods are slightly swelled at the intersection, as seen inside the circle in Figure 3.12c, which implies that the nanorods can have a transversal growth besides the fast longitudinal growth. These are important features of the interpenetrating nanorods.

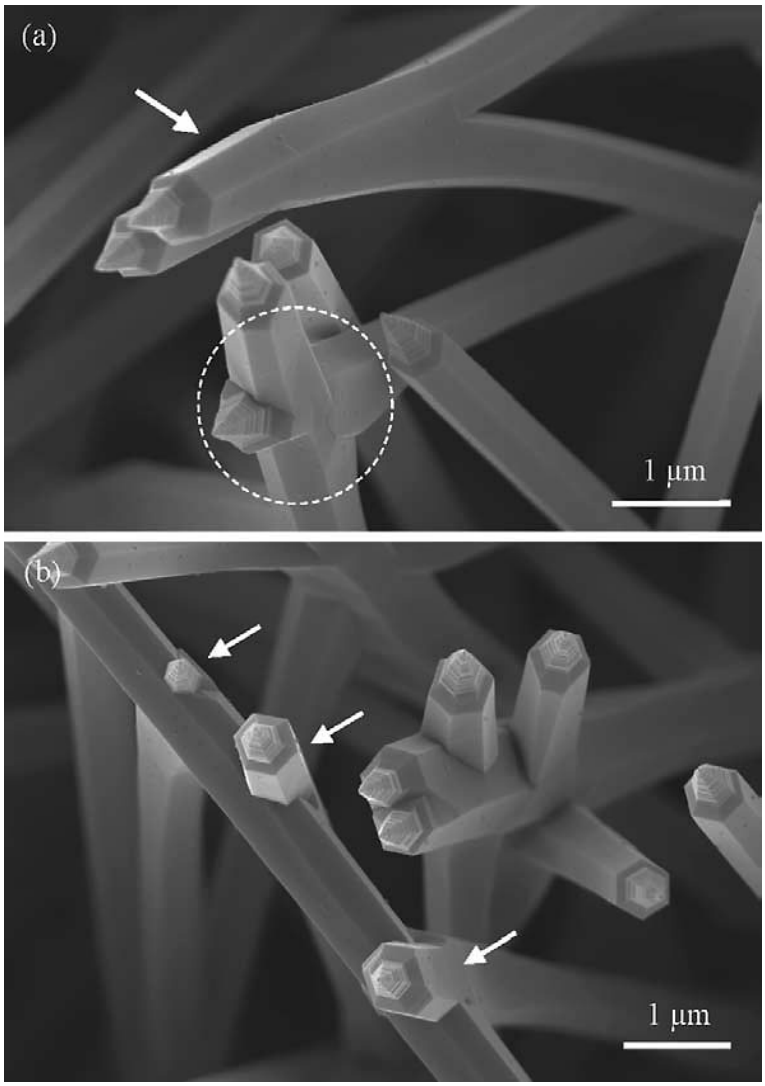

Figure 3.13 (a) SEM image showing the swelled intersection and a tortuous configuration due to the competition growth between the nanorods. (b) A nanorod that was intersected by three nanorods. The right-hand is a complex interpenetrative structure.

The nanorods at the interpenetration site often inflate due to transverse growth, as seen inside the circle in Figure 3.13a, which is a clear indication of joining of one nanorod over the other one after crossing. The nanorods grew longitudinally first, the physical contact and a subsequent transverse growth result in joining. Figure 3.13a also shows another configuration of two nanorods that joint together at the end when the growth fronts meet (as indicated by an arrowhead). The bending of the nanorods is apparent. In the case that a nanorod meets a pre-existing nanorod, the nanorod tends to pass the existing one by taking a by-pass approach but with joint volume, as indicated by arrowheads in Figure 3.13b. The existing nanorod does not change much, while the newly grown nanorod inflates due to the transversal growth, as suggested by the structure displayed in Figure 3.13b. The nanorod still preserves the hexagonal shape after passing the existing nanorod due to the lower energy of the $\{2\bar{1}\,\bar{1}\,0\}$ or $\{01\bar{1}\,0\}$ facets. In addition, one nanorod at the upper right-hand side in Figure 3.13b splits into two nanorods due to the transversal growth after the penetration.

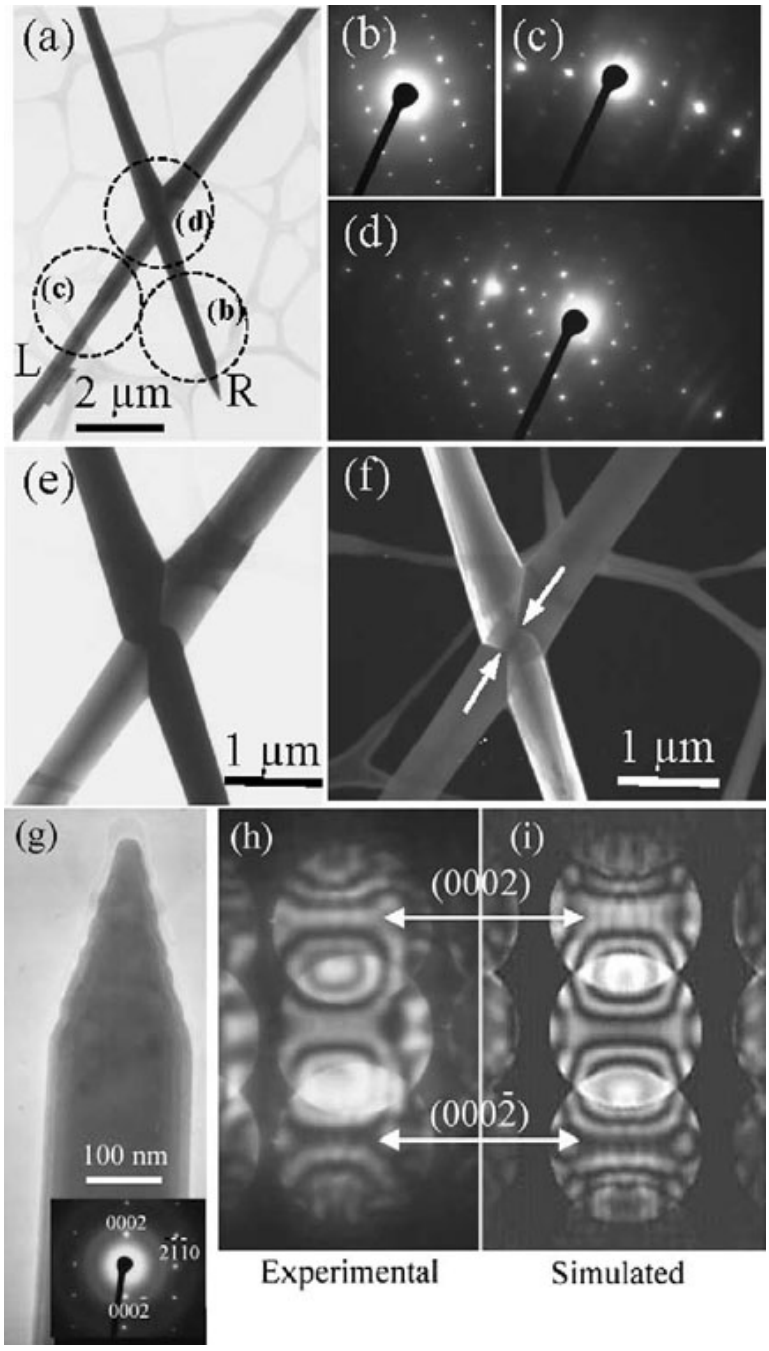

Figure 3.14 (a) TEM image of two interpenetrative nanorods, labeled L and R. (b)–(d) are selected area electron diffraction patterns from R, L and their intersection region, respectively. (e) and (f) Bright-field and dark-field TEM images of the intersection. (g) TEM image of a nanorod and its corresponding selected area electron diffraction pattern. (h) An experimental CBED pattern recorded from the nanorod using an electron beam of 3 nm in diameter. (i) A simulated CBED pattern using dynamic electron diffraction theory.

The joining point of two nanorods has been imaged by TEM. Figure 3.14a is a bright-field TEM image of two interpenetrating nanorods, labeled L and R. Selected area electron diffraction (SAED) patterns were recorded from the areas indicated to be b, c and d without tilting the sample, and the results are shown in Figs. 3.14b, c and d, respectively. The SAED pattern in Figure 3.14b shows that the nanorod R grows along [0001] and the electron beam is $[2\,\bar{1}\,\bar{1}\,0]$. The SAED pattern recorded from the nanorod L (Figure 3.14c) shows the Laue circle, indicating that the nanorod orientation is far from a zone axis. The SAED pattern from the crossing region is an overlap of two patterns (Figure 3.14d), clearly indicating that the two nanorods have no orientation relationship, and the nanorods preserve their own orientation before and after interpenetrating with each other. This is very different from the twin, tetraleg[68] or nanopropeller[69] structures for ZnO, which have specific angles defined by crystallography. To confirm this observation, bright-field and dark field TEM images were recorded from the crossing area, as shown in Figs. 3.14e and f, respectively. The images suggest that the L nanorod was formed first, and then the R nanorod contacted the L nanorod at a width indicated by two arrowheads in Figure 3.14f. The subsequent transverse growth forms the joining of the two nanorods and their observed widths.

3.4.1.3 Growth Mechanism

To understand the formation of the pencil or bullet structure of the [0001] nanorods, we first examine the structure of ZnO. Wurtzite ZnO crystal can be viewed as a number of alternating layers of tetrahedrally coordinated O^{2-} and Zn^{2+} ions, stacked alternatively along the c-axis. The negative charged $(000\,\bar{1})$-O^{2-} layers and the positively charged (0001)-Zn^{2+} layers result in the spontaneous polarization along positive c-axis. To identify the polarity of the nanorod, we have applied the convergent beam electron diffraction (CBED). Due to the strong dynamic diffraction effect of electrons in a crystal, the polarity of ZnO can be determined using CBED by quantifying the electron

diffraction intensity as a function of the incident angle of the electron beam. Figure 3.14g shows a TEM image of a nanorod and its corresponding SAED pattern, which indicates that the nanorod grows along [0001]. Figure 3.14h is a CBED pattern recorded from the nanorod by using a convergent electron beam. Thus, the diffraction spot becomes a disk. The detailed intensity distribution within the disk is related to the crystal structure and sample thickness. The intensity distributions in the (0002) and $(000\,\bar{2})$ disks are non-symmetric due to the polarity of the ZnO structure[156]. Quantitative interpretation of the CBED relies on dynamic electron diffraction simulations, which were performed using an improved version of the Bloch wave program[165] and the structure data from single crystal neutron diffraction[166]. A comparison of the experimental pattern with a theoretically calculated pattern is given in Figs. 3.14h and i, and the excellent agreement between the two indicates that the nanorod grows out of the positively charged (0001)-Zn surface. Therefore, the sharp tip is due to the catalytically active (0001)-Zn surface, while the flat surface at the bottom is the chemically inactive $(000\,\bar{1})$-O surface, forming the pencil or bullet shape structure (Figure 3.10c). The growth is thus due to self-catalysis of Zn-terminated (0001) surface[75].

The information provided by SEM and TEM enables us to propose a growth model, in which both longitudinal growth and transverse growth co-exist, but the former is a lot faster than the latter. Due to the distinct catalytic activities of the Zn- and O-terminated surfaces, the nanorod grow along [0001], possibly forming a growth tip at the front that is terminated with Zn. The transversal growth along either $<2\,\bar{1}\,\bar{1}\,0>$ or $<01\,\bar{1}\,0>$ is negligible in comparison to the longitudinal growth. When the growth front of a nanorod meets a grown nanorod, the grown nanorod behaves like a pre-existing nanorod (Figure 3.15a). If the two nanorods cross at a larger angle, the latter coming one may be partially terminated by the grown nanorod and partially by-pass the nanorod (Figure 3.15b) (see the nanorods indicated by arrowheads in Figure 3.13b), and its

continuous growth leads to the formation of the front tip on the body of the grown nanorod (Figure 3.15c). A continues growth both longitudinally and transversely leads to the joining of the two nanorods (Figure 3.15d) (see Figure 3.13, Figure 3.11c, and Figure 3.12c). Facets are preserved due to the symmetry and lower energy surfaces of the crystal structure. Transversal growth continues when source material is continuously supplied, resulting in the tortuous or bent shape at the intersection. If two crossing nanorods happen to have twin orientation relationship, accomplishment of the penetration can also result in a twin boundary, which has also been observed in our sample.

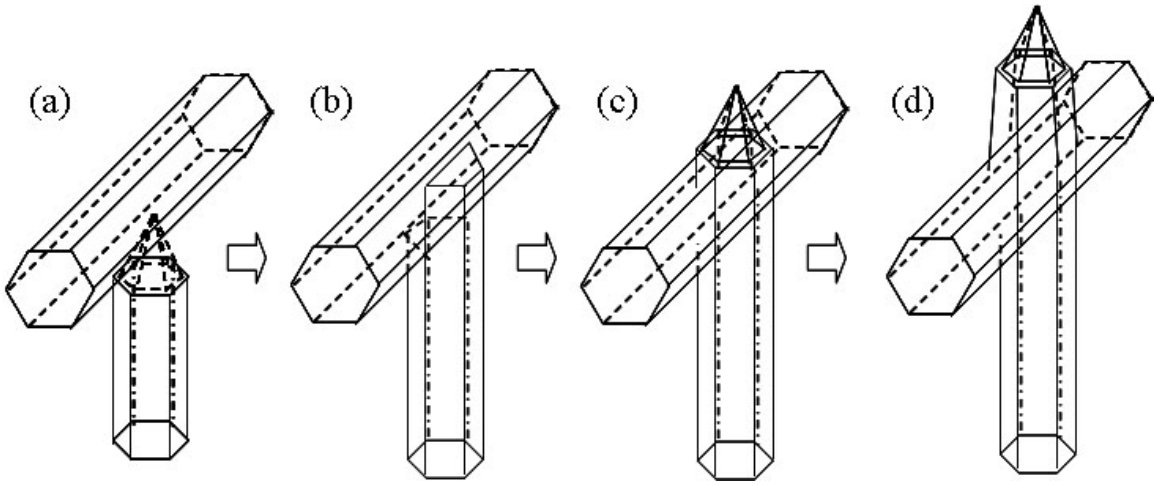

Figure 3.15 Interpenetrative and transversal growth model for the formation of crossed nanorods. (a) The growth forefront of bottom nanorod encounters the top nanorod. (b) Only the unblocked part can still continue with longitudinal growth. (c) The bottom nanorod regains its hexagonal shape through transversal growth. (d) The bottom rod continues with longitudinal growth after the penetration.

In summary, interpenetrative ZnO nanorod arrays show significant transverse growth during growth and penetrating each other. This is a significant progress in understanding the formation of 1D nanostructures, because the transverse growth has been ignored in many cases. The interpenetrative growth of two nanorods at a random angle has been illustrated for ZnO. The Zn-terminated (0001) surface has been shown to be catalytically active, while the oxygen-terminated $(000\bar{1})$ is catalytically inert; the

former is responsible for forming the sharp tip at the growth front. A model is proposed for understanding the formation of the interpenetrative nanorods.

3.4.2 Sn-Catalyzed ZnO Nanowire Arrays[167]

Growth of ZnO nanostructures can be achieved through various techniques, such as chemical vapor deposition (CVD)[168], metalorganic chemical vapor deposition (MOCVD)[169], physical vapor deposition (PVD)[51, 170], hydrothermal process[171], thermal decomposition[172], etc. Among them, PVD can produce various nanostructures with excellent crystallinity and has been adopted widely. Two basic growth modes have been proposed for ZnO nanostructures grown in PVD process, including vapor-solid (VS) and vapor-liquid-solid (VLS) growth. VS can result in the most versatile morphologies via self-catalysis process. However, limited control has been achieved on the location, growth direction or even size of those nanostructures with VS process. In comparison, facilitated with metal catalysts, such as Au[118, 173], Co[174], and NiO[175], VLS can provide a better control over ZnO nanostructures and benefit many applications with well defined nanowire size and growth pattern.

In this section, the growth phenomena of novel ZnO nanostructures catalyzed by metallic tin have been investigated for the specific synthesis system of ZnO-SnO_2-C.

3.4.2.1 Fabrication Method

ZnO nanostructures here were synthesized through a simple vapor-transport deposition process in a single-zone horizontal tube furnace which is equipped with an alumina tube, water-cooled end caps, a rotary pump system, and a gas controlling system. During the synthesis the temperature, pressure, atmosphere, and evaporate time were controlled. Serving as source materials, commercial ZnO, SnO_2 and graphite powders (1.62 gram, 1.51 gram and 0.12 gram, respectively) were mixed, ground and then loaded onto an alumina crucible, which were placed in the middle of the alumina tube. Placed “down

stream" at a lower temperature region in the tube, single crystal (111)-plane silicon wafer served as a substrate for the growth and collecting of ZnO nanostructures. The alumina tube was then sealed with two water-cooled end caps, which can maintain a desirable temperature gradient across the tube from the middle to the end during the synthesis. The alumina tube was placed under vacuum (~ 10^{-3} torr) for several hours before introducing the entrained gas of Ar. The pressure was allowed to increase to and maintained at 150 torr (~20 kPa) through the whole synthesis process. The temperature in the middle of the tube was gradually elevated to 1100°C or 1150°C and maintained at the peak temperature for 20-30 minutes. The sublimated vapor from the source was transported by the flowing Ar towards the Si substrate. The local growth condition near the substrate leads to the formation of various nanostructures. The resultant ZnO nanostructures were characterized by LEO1530 field emission scanning electron microscopy (SEM) and Hitachi HF2000 transmission electron microscopy (TEM).

3.4.2.2 Structure Characterization

In the experiment with a peak temperature of 1100°C highly hierarchical ZnO nanowire arrays and uniaxial fuzzy nanowires were found on the Si substrate, which is in the temperature region of 400-500°C. At relatively lower temperature part of this Si substrate, numerous ZnO nanowire arrays grew from the surface, as shown in Figure 3.16 Many ZnO nanowires were roughly perpendicular to the underneath Si substrate. At the same time, considerable nanowires grew radially from one spot. The inlet of Figure 3.16 indicates that the ZnO nanowire have tapered front tip. Although we introduced SnO_2 in the source materials and Sn is believed to serve as catalyst in similar experiment [76], no Sn catalyst was found on top of those ZnO nanostructures.

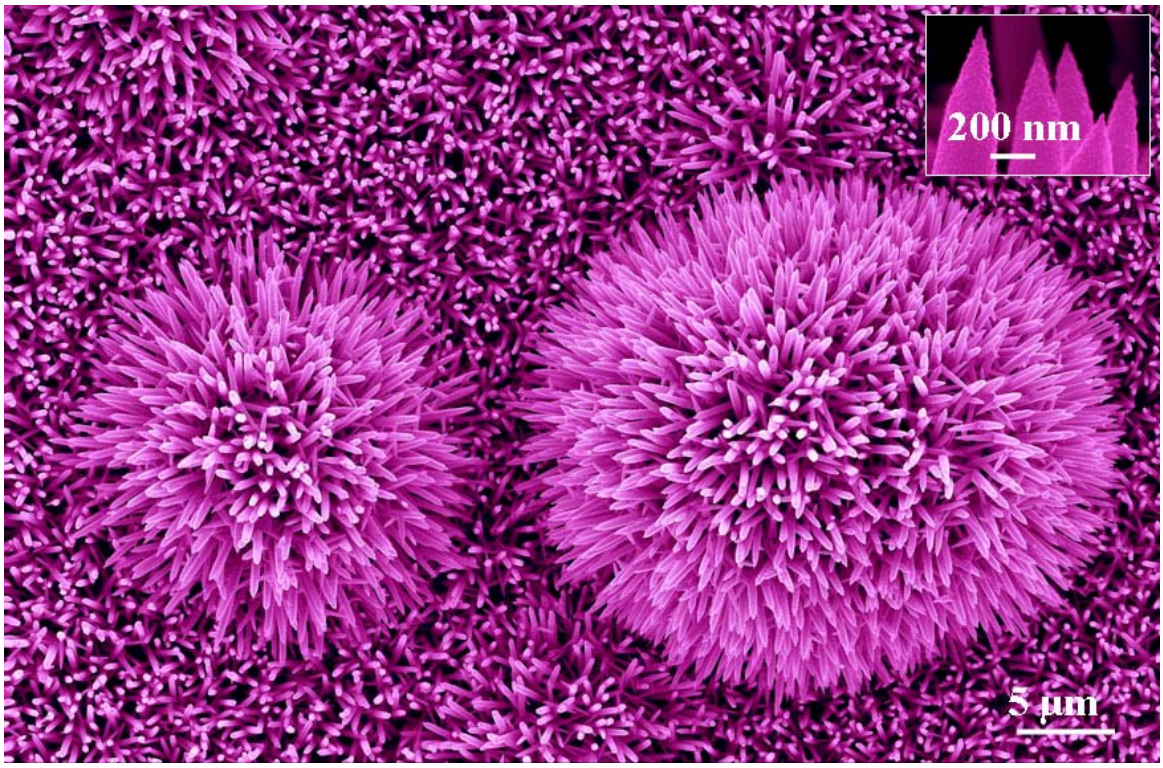

Figure 3.16 ZnO nanowire arrays and radial nanowire clusters with enlarged nanowire tips in the inlet.

In order to further investigate crystallographic structure of ZnO nanowires, we had taken TEM study on those nanowires, which is given in Figure 3.17. Figure 3.17(a) shows a typical ZnO nanowire at this temperature region. The ZnO wire was gradually getting bigger towards the growth front and shrinked rapidly to form a sharp tip. High resolution TEM image in Figure 3.17(b) and electron diffraction pattern in Figure 3.17(c) confirm that the ZnO nanowire has wurtzite structure and the growth direction is along [0001].

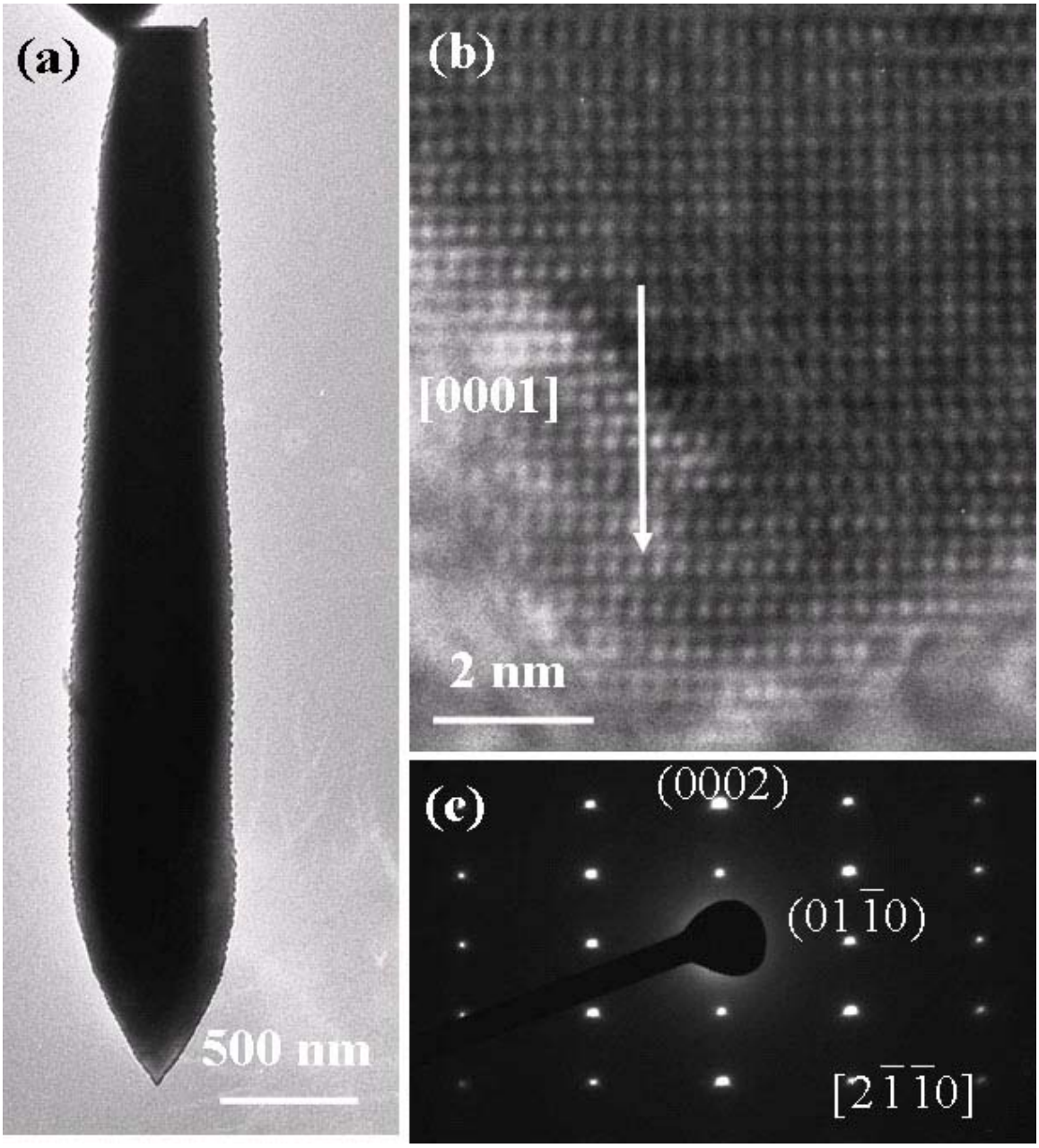

Figure 3.17 (a) TEM image of a nanowire taken from the ZnO nanowire array. (b) HRTEM image taken from the tip of the nanowire in (a). (c) Electron diffraction pattern of the nanowire showing a [0001] growth direction.

Surprisingly, more complex ZnO nanowire assembly was found at a higher temperature region on the same Si substrate. Figure 3.18(a) shows numerous ZnO nanowires grow radially from a common axis. Due to this 3 dimensional structure and ultra dense growth, high yield of ZnO nanowires can be achieved. In addition, a close examination reveals

that ZnO nanowires at the root of this cluster are slightly longer than those at the top. Moreover, the morphology of the tip of the nanowires is also changing from the bottom to the top of the cluster. Taken from the squared areas in Figure 3.18(a), Figure 3.18(b) and Figure 3.18(c) present ZnO nanowires from the top part and from the bottom part respectively. The ZnO nanowires in Figure 3.18(b) have a diameter from 300-400 nm, relatively rough surface and truncated hemispherical tips. In comparison, The ZnO nanowire in Figure 3.18(c) have a diameter of 300 nm or less, smoother surface and flat tips composed of multiple small "fingers". Such difference is also observed in TEM characterization.

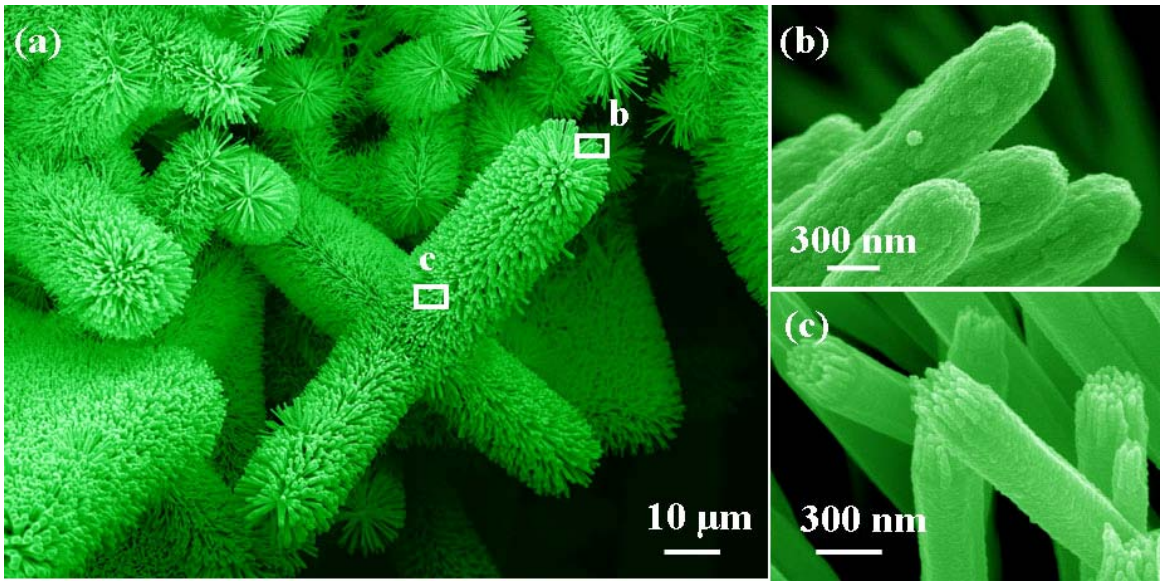

Figure 3.18 (a) Uniaxial fuzzy nanowire clusters from a higher temperature region. (b) and (c) Enlarged images of nanowires from white square area in (a).

Figure 3.19(a) and Figure 3.19(b) present two kinds of ZnO nanowires, which should be dissociated from the bottom of the cluster and the top respectively. Shown in the insets of Figure 3.19 (a) and Figure 3.19(b), the electron diffraction patterns from corresponding nanowires indicate that all ZnO nanowires grow along [0001] direction. The HRTEM in Figure 3.19(c) from a finger in Figure 3.19(b) suggests the single-crystallinity of wurtzite-structured ZnO nanowire and verifies the growth direction being along [0001].

Although the ZnO nanowire has blunt end, the component fingers have a really sharp tapered tip, which could be useful as field emitter[176].

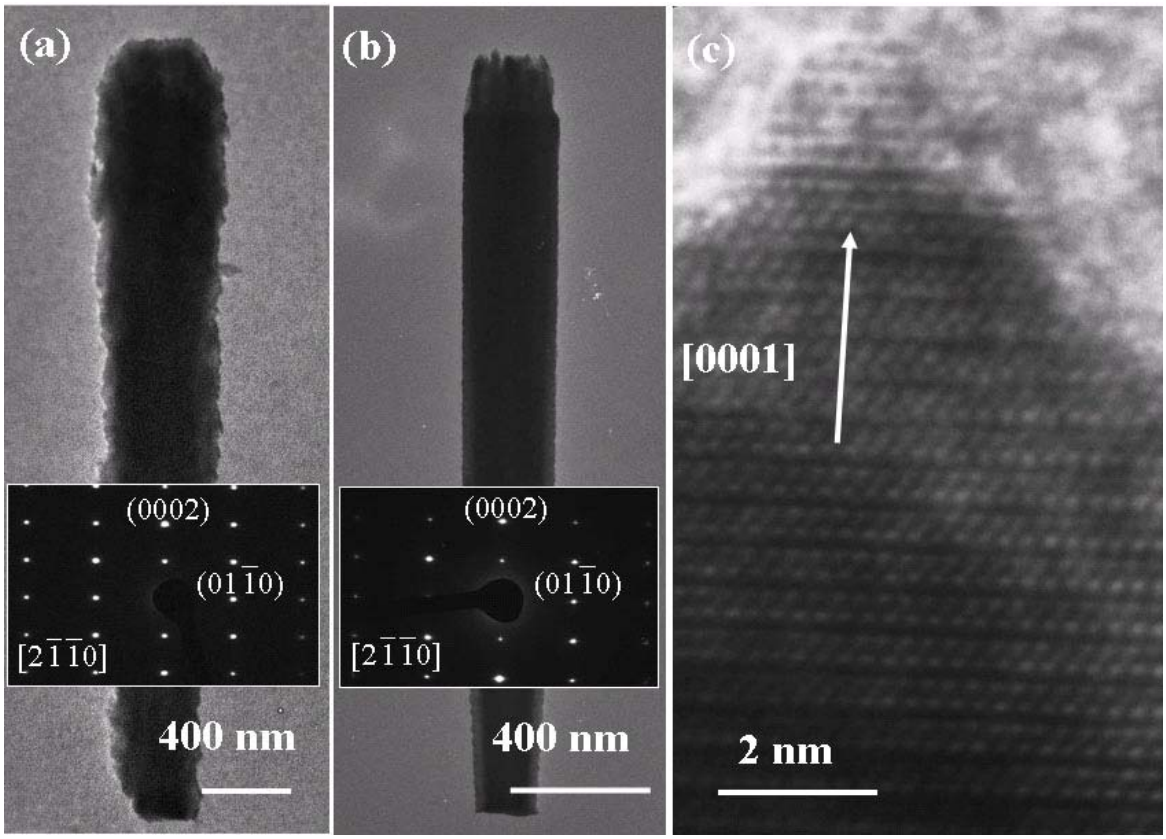

Figure 3.19 (a) and (b) TEM images and corresponding electron diffraction pattern of nanowires from uniaxial fuzzy nanowire cluster. (c) HRTEM image taken from the tip of the nanowire in (b).

To further study the effect of the temperature on the ZnO nanostructures, we performed another experiment with a peak temperature of 1150°C at the center and 550-650°C at the Si substrate. Self-assembled ZnO nanowire-nanobelt arrays were found on the substrates. In addition, a new ZnO nanostructure assembly was discover on the same substrate in a higher temperature region (600-650°C), which is present in Figure 3.20. The backbone of this nanostructure assembly was still the nanowire-nanobelt junction. More important, numerous ZnO radial nanowire clusters grew on the main trunk, mimicking closely the bloom of flowers on the branches. The enlarged image of one cluster in the inlet of Figure 3.20 clearly indicates that all nanowires have very uniform body and a tapered tip.

In addition, some ZnO nanowires have also a much smaller Sn ball at the end of the tip, while some others don't have any Sn ball. In addition, such ZnO nanowire clusters were mainly found on the nanowire-nanobelt junction backbones. Accordingly, a further study of nanowire-nanobelt junction is necessary to understand the reason for those nanowire clusters.

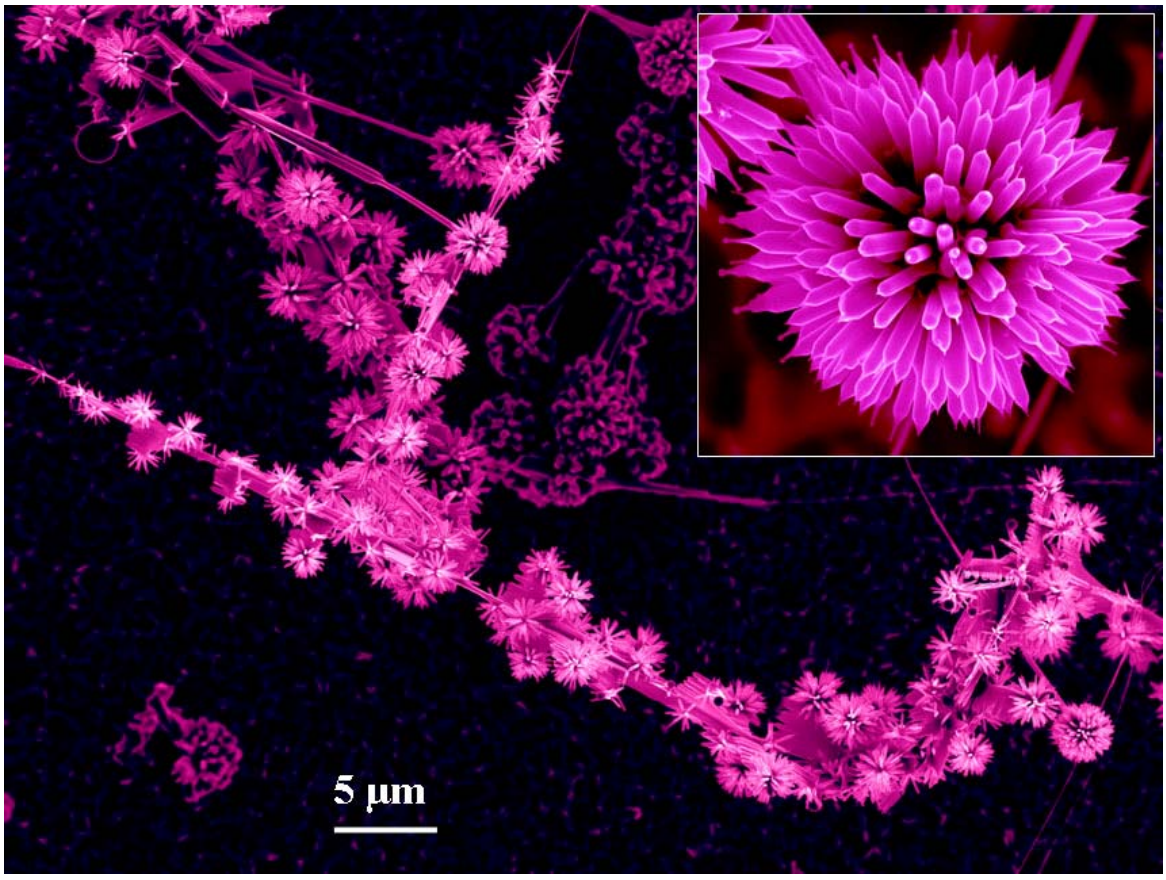

Figure 3.20 Flower-like nanowire clusters on the nanowire-nanobelt junction with an inlet showing an enlarged image of a flower-like nanowire cluster.

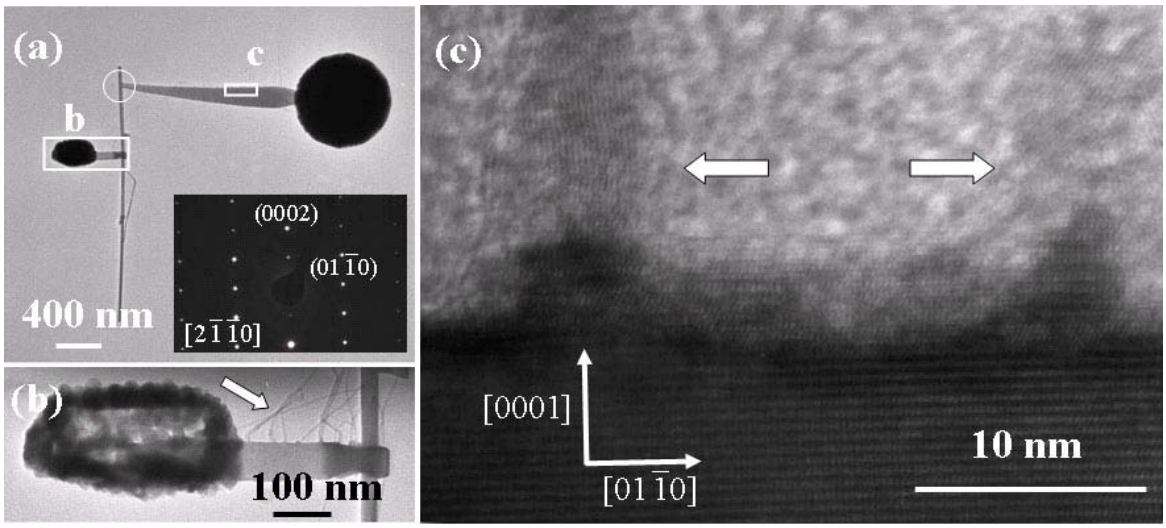

Figure 3.21 (a) TEM image of a nanowire-nanobelt junction structure. Electron diffraction pattern in the inlet is taken from the white circle area. (b) A nanobelt branch showing clearly the asymmetrical growth of secondary ZnO nanowires growth from the upper side surface, as indicated with white arrow. (c) HRTEM image taken from the white square area indicated in (a), showing the single-crystal structure and the growth direction being $[01\bar{1}0]$ and [0001] for the nanobelt and nanowire, respectively. White arrows indicate the secondary nanowires.

Figure 3.21 presents TEM characterization of a typical nanowire-nanobelt junction structure. More interestingly, numerous smaller secondary ZnO nanowires grew from nanobelts. The TEM image and electron diffraction pattern confirms that nanowires and nanobelts are of the same crystal piece and have the wurtzite structure. Sharing the common $\pm (2\bar{1}\bar{1}0)$ plane, ZnO nanowires and ZnO nanobelts grew along [0001] direction and $[01\bar{1}0]$ (and equivalent) direction, respectively. ZnO nanobelts have $\pm$ (0001) planes as side surfaces. In addition, the ZnO nanobelt in Figure 3.21(b) clearly indicates that secondary ZnO nanowires grew only from one side surface and rarely from the opposite side surface. High-resolution TEM image of the ZnO nanobelt and secondary nanowires from the white squared area in Figure 3.21(a) is shown in Figure 3.21(c), which indicates that the ZnO nanowires epitaxially grew from the nanobelt in the direction of [0001]. All secondary ZnO nanowires display a single-crystalline structure with a diameter of about 6 nm.

3.4.2.3 Growth Mechanism

ZnO nanowires can easily grow through the vapor-liquid-solid (VLS) process with Sn catalyst on the tip[69, 177] or sometimes at the root[66]. In the absence of other metal catalysts, ZnO nanowires can grow through a vapor-solid (VS) process and self-catalytic effect can play an important role in forming some nanostructures[75]. The morphology and growth direction of nanostructures are determined by the growth kinetics, which can be controlled though the pressure, growth temperature, etc. In this experiment setup, ZnO and SnO_2 powders give off possibly Zn, ZnO, Sn, and O vapors under the reduction of graphite[69] and those vapors are transported to the substrate under the influence of flowing/carrier gas. Due to the chemical activity difference of Sn and Zn, SnO_2 is dissociated into Sn and O vapor prior to ZnO. Accordingly, at an early stage of synthesis, Sn and O vapor dominate the source vapor with small amount of Zn and ZnO vapor. Sn vapor condenses on the surfaces of the Si substrate to form various liquid Sn balls. At higher temperature region, a few ZnO wires can also form at early stage but are surrounded quickly by liquid Sn layer or balls as a result of incoming abundant Sn vapor. At lower temperature region, much less ZnO wires can form due to the low Zn and ZnO vapor concentrations. Sn vapor decreased quickly as a result of the consumption of SnO_2 source powder. As the Zn and ZnO vapor concentrations increase in the synthesis region, ZnO nanowires start growing from the Sn balls on the Si substrate and from Sn layer or balls on the few early grown ZnO nanowires. Under current growth condition, ZnO growth along [0001] is greatly enhanced and growth along other direction is mainly suppressed, which explains why only ZnO nanowire along [0001] is observed in TEM characterization. The tiny Sn balls on Si substrate can also initiate the growth of ZnO nanowires, which forms nanowire arrays as shown in Figure 3.16. The inevitably formed larger Sn balls due to agglomeration can simultaneously catalyze numerous ZnO nanowires and result in the radial ZnO nanowire cluster in Figure 3.16, which is similar to the growth of highly aligned silica nanowires from molten gallium balls[178]. In

comparison, Sn ball or liquid Sn layer on the ZnO wire at higher temperature region also absorb the incoming Zn vapors and initiate fuzzy growth of ZnO nanowires surround the common axis, resulting in the highly hierarchical ZnO nanostructure assembly in Figure 3.18. A slightly better vapor source at the top of the assembly might bring a faster growth, rougher surface, larger diameter and different tip morphology compared with ZnO nanowires at the lower part of this assembly.

In comparison, the nanostructures in Figure 3.20 and Figure 3.21 follow a slightly different process. In this experiment setup the Si substrate is closer to the center and the peak temperature is also higher. In a similar way as discussed earlier, ZnO nanowires can form first before the furnace reach the peak temperature of 1150°C. Under this different growth condition, other direction growth is also possible and results in the ZnO nanobelt branches along $[01\bar{1}0]$ in Figure 3.21 with ± (0001) as side surfaces. As is well-known that Zn-terminated polar surface is chemically active while the opposite O-terminated polar surface is inert during the growth [75]. The self-catalyzed growth from only (0001) surfaces results in the asymmetrical growth of secondary ZnO nanowires from one side of the ZnO nanobelt. In addition, the Sn balls at the tip of ZnO nanobelts and at other places can also initiate considerable growth of the most favorable ZnO nanowires along [0001] and lead to the flower-like nanowire clusters.

In summary, by evaporating a mix of ZnO, SnO_2, and graphite, highly hierarchical 3-dimentional nanostructures were synthesized. Sn particles from the reduction of SnO_2 serve as catalysts and initiate the growth of ZnO nanowires. Under such growth condition that the growth along [0001] is dominant and others are suppressed, ZnO nanowire arrays, radial nanowire cluster were initiated from a large Sn particle, and fuzzy ZnO nanowire with a common axis were grown. Moreover, manipulating the synthesis kinetics can cause the formation of nanowire-nanobelt junction at an early stage. The consequent fast growth of ZnO nanowires around Sn particles result in the flower-like nanowire clusters. The studying of the nanostructures

revealed the underling growth mechanism, which is important for engineering nanoscale assemblies.

3.5 Springs, Rings, and Spirals Structured SnO_2 Nanobelts[179]

In this section, the discovery of single-crystalline SnO_2 springs, rings and spirals, which have the rutile structure, is discussed. The grown nanostructures are made of tetragonal SnO_2 with the (011) polar surfaces facing towards the center. The formation process has been analyzed based on the polar charge interaction model. The discovery of SnO_2 rings and springs presents another family of polar surface dominated growth phenomena in a non-wurtzite structured material, indicating the possibility of forming similar structures for other materials, such as TiO_2. Considering the important application of SnO_2 in sensors, catalysts, and transparent conducting electrodes, these structures are not only ideal systems for fundamental understanding of the polarization effect on the morphology at nanoscale, but also having potential applications[180] as nanoscale sensors, resonators, and transducers.

3.5.1 Introduction

3.5.1.1 Polar Surface Induced Nanostructures

Synthesis of nanomaterials with well controlled size, morphology and chemical composition may open new opportunities in exploring material's chemical and physical properties. Since the discovery of semiconducting oxide nanobelts [51](ZnO, SnO_2, CdO, Ga_2O_3, PbO_2) in 2001, nanobelts have been found and widely investigated in numerous materials including but not excluded to [52, 181, 182] (Zn, Si, and C), II-IV semiconductors[54, 56, 57, 183, 184] (ZnS, CdSe, ZnSe), and some other compound [51, 185-189](In_2O_3, Ge_3N_4, Bi_2S_3, SiC, GaP, and $Pb_3O_2Cl_2$). Among these materials, wurtzite structured ZnO is the most outstanding member. The uniqueness of the wurtzite structure is non-central symmetry and the surface polar charges due to the cation and anion

terminated surfaces, such as Zn^{2+}-terminated (0001) and O^{2-}-terminated $(000\bar{1})$. As a result, spontaneous polarity is built up within ZnO crystals. To minimize the electrostatic interaction energy among the polar charges, the nanobelt dominated by the ±(0001) polar surfaces tends to fold over, resulting in the formation of single-crystalline nanorings, nanosprings and nanospiral [70, 71, 73, 163]. The reduction in the area of polar surfaces causes a structural transformation of a single crystal ZnO nanobelt into a superlattice-structured, partial-polar surface dominated nanobelt, which eventually forms a rigid nanohelix[72]. Figure 3.22 included some of the ZnO nanostructures, which are greatly affected or determined by spontaneous polarity during their growth[190]. Besides the nanorings observed for wurtzite AlN due to polar surfaces[191], no report has been found about the formation of single-crystalline rings/springs/spirals for a material that has a structure different from wurtzite. Based on the polar surface induced growth mechanism, which is originally proposed for wurtzite-structured ZnO nanostructures, similar nanostructures might also be possible in other materials, which has also polar surfaces according to its crystallographical structure. The generality of this growth mechanism needs to be tested with other materials from other crystal structure system. In this section, novel rutile-structured SnO_2 nanostructures were discussed and proved of the validity of polar surface induced growth mechanism in rutile-structured materials.

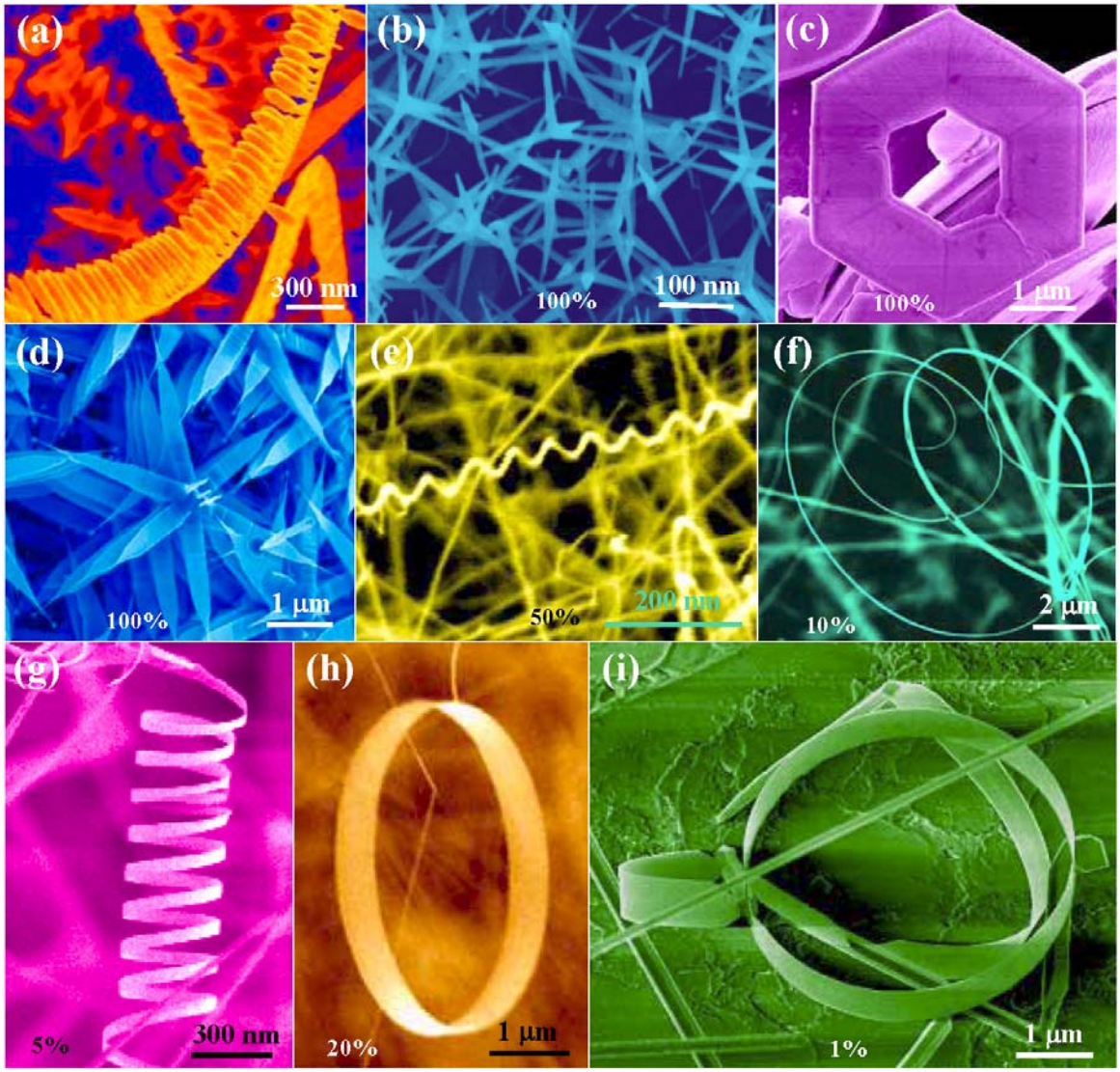

Figure 3.22 A collection of nanostructures of ZnO synthesized under controlled conditions by thermal evaporation of solid powders. The percentage indicates the purity of the as-synthesized sample with the selected structure feature.

3.5.1.2 Properties and Applications of SnO_2

Based on the following three characteristic of SnO_2, we selected SnO_2 for the growth of polar surface induced novel nanostructures, rutile structure, availability of various nanostructure, and promising applications.

First of all, SnO_2 have rutile structure with a tetragonal unit cell, which is non-centrosymmetric and different from wurtzite structure. SnO_2 have also some polar

surfaces according to its crystal structure and might induce novel structures as what has happed to ZnO. A summary of physical properties of SnO_2 and ZnO is given in Table 3.1. The crystal structure and polar surface will be discussed in detail in the later part of section.

Table 3.1 Summary of physical properties of the transparent conducting oxide, ZnO and SnO_2[192].

Property	ZnO	SnO_2
Mineral name	Zincite	Cassiterite
Abundance of the metal in the earth's crust (ppm)	132	40
Crystal structure	Hexagonal, Wurtzite	Tetragonal, rutile
Space group	$P6_3mc$	$P4_2mnm$
Lattice Constant (nm)	a=0.325; b=0.5207	a=0.474; b=0.319
Density ρ (g cm^{-3})	5.67	6.99
Mohs hardness	4	6.5
Thermal expansion coefficient (300K) ($10^{-6}K^{-1}$)	$\parallel c : 2.92;\ \perp c : 4.75$	$\parallel c : 3.7$
Melting point (°C)	2240	>1900[a]
Melting point of metal (°C)	420	232
Vapor pressure of metal at 500 °C	10	5×10^{-9}

Table 3.1 (Continued)

Property	ZnO	SnO_2
Heat of formation (eV)	3.6	6.0
Band gap (eV)	3.4	3.6
Static dielectric constant ε_r	$\parallel c$: 8.75; $\perp c$: 7.8	$\parallel c$: 9.6; $\perp c$: 13.5
Effective electron mass of conduction electron m^*/m_0 (experimental)	-	$\parallel c$: 0.23; $\perp c$: 0.3
Effective electron mass of conduction electron m^*/m_0 (computational)	$\parallel c$: 0.58, 0.59; $\perp c$: 0.6, 0.59	$\parallel c$: 0.20; $\perp c$: 0.26
Common extrinsic n-type dopants	B, Al, Ga, In, Si, Ge, Sn, Y, Sc, Ti, Zr, Hf, F, Cl	Sb, F, Cl
[a] Decomposition into SnO andO_2 at 1500°C		

Second, various SnO_2 nanostructures have been synthesized. The success of those nanostructures from different synthesis technique and conditions can guide the experimental design for novel nanostructures. A variety of self-organized tin oxide materials with two or all three dimensions at the nano- to micro-meter scale have been recently discovered and characterized. The most often utilized approach for synthesis nanomaterials is a simple vapor phase transport method[134], which resulted in the discovery of nanobelt from SnO_2 and other materials[51]. A schematic diagram of the equipment used for such a synthesis is shown in chapter 2. Tin oxide powder is evaporated at the middle of a tube furnace and subsequently transported in a gas flow along the furnace tube. The tin oxide molecules then condense in a colder region of the furnace. The growth mechanism of SnO_2 nanobelts is still not entirely resolved. It is

important to point out that the SnO_2 nanostructures do not require a hetero-metal catalyst to grow, contrary to many other nanostructures via VLS growth process. However, it can not be excluded that the growth is self-catalyzed, i.e. that a thin metallic Sn layer or nanoclusters exists at the end of the nanobelt that catalyzes the growth reaction. It is more likely, though, that the growth of SnO_2 nanobelts proceeds via a VS process only, where SnO_2 molecules arrive at a nucleated nanobelt and attach themselves to the rough growth front.

Finally, the study of tin oxide is also motivated by its applications as a solid state gas sensor material, oxidation catalyst, and transparent conductor[192].

ZnO and SnO_2 are the most commonly used gas sensing materials[192]. The gas sensitivity of oxides is often divided into bulk- and surface-sensitive materials. TiO_2, for example, increases its conductivity due to the formation of bulk oxygen vacancies under reducing conditions and thus is categorized as a bulk sensitive gas sensing material. SnO_2, on the other hand, belongs to the category of surface sensitive materials, although bulk defects affect its conductivity as well. The basic reason of gas sensing is the acceptor or donor like adsorption of molecules that consequently induces a band bending in the Debye layer of the SnO_2 surface region. In addition, the high charge carrier mobility and the strongly dispersing conduction band is also an important ingredient to make it a good gas sensing material

SnO_2 acts as an important support material for dispersed metal catalysts and exhibits good activity towards CO/O_2 and CO/NO reactions. The oxidation reactions are supposed to follow the Mars–van Krevelen mechanism, in which the molecules are oxidized by consuming lattice oxygen of SnO_2 which in turn is re-oxidized by gas-phase oxygen. It is shown that for different oxygen chemical potentials surfaces with Sn^{4+} or Sn^{2+} are stable. This indicates that an easy reduction and reoxidation of SnO_2 surfaces can be expected in catalytic oxidation reactions.

SnO_2 belongs to the important family of oxide materials, which have both low electrical resistance and high optical transparency in the visible range of the electromagnetic spectrum. These properties are sought in a number of applications; notably as electrode materials in solar cells, light emitting diodes, flat panel displays, and other optoelectronic devices where an electric contact needs to be made without obstructing photons from either entering or escaping the optical active area and in transparent electronics such as transparent field effect transistors. In addition, the high reflectivity for infrared light is responsible for today's dominant use of SnO_2 as an energy conserving material.

3.5.2 Fabrication Method

SnO_2 nanostructures are synthesized through a solid-vapor process in a horizontal tube furnace. The experimental apparatus has been described in chapter 2[193]. After the tube had been evacuated to a pressure of 1×10^{-3} Torr, commercial SnO powders (Alfa Aesar) in the middle of the tube was heated to 800 °C, held for 90 minutes, heated again up to 1100°C and held for another 50 minutes to complete the synthesis of the SnO_2 nanostructures. The Ar carrier gas was flowed through the system at a rate 50 sccm (standard cubic centimeters per minute) under a constant pressure of 300 mbar during the entire synthesis process. The grown nanostructures were collected using a polycrystalline Al_2O_3 substrate placed downstream in the tube furnace at a temperature range of 600-700°C.

3.5.3 Structure Characterization

We first examined the as-synthesized product by scanning electron microscope (SEM) in conjunction with energy dispersive x-ray spectroscopy (EDS). We found that SnO_2 nanobelts tend to bend while they grow longitudinally. As a result, numerous SnO_2 spirals formed on the substrate. Figure 3.23a-c shows SnO_2 nanospirals with multiple

loops or only half loop. Those curved nanobelts have different curvatures (Figure 3.23a) or varied curvature even along the same nanobelt (Figure 3.23b-c) for different size of nanobelts or size change during the growth. When the growth front meet the grown part, closed nanorings can also be formed, as shown in Figure 3.23d.

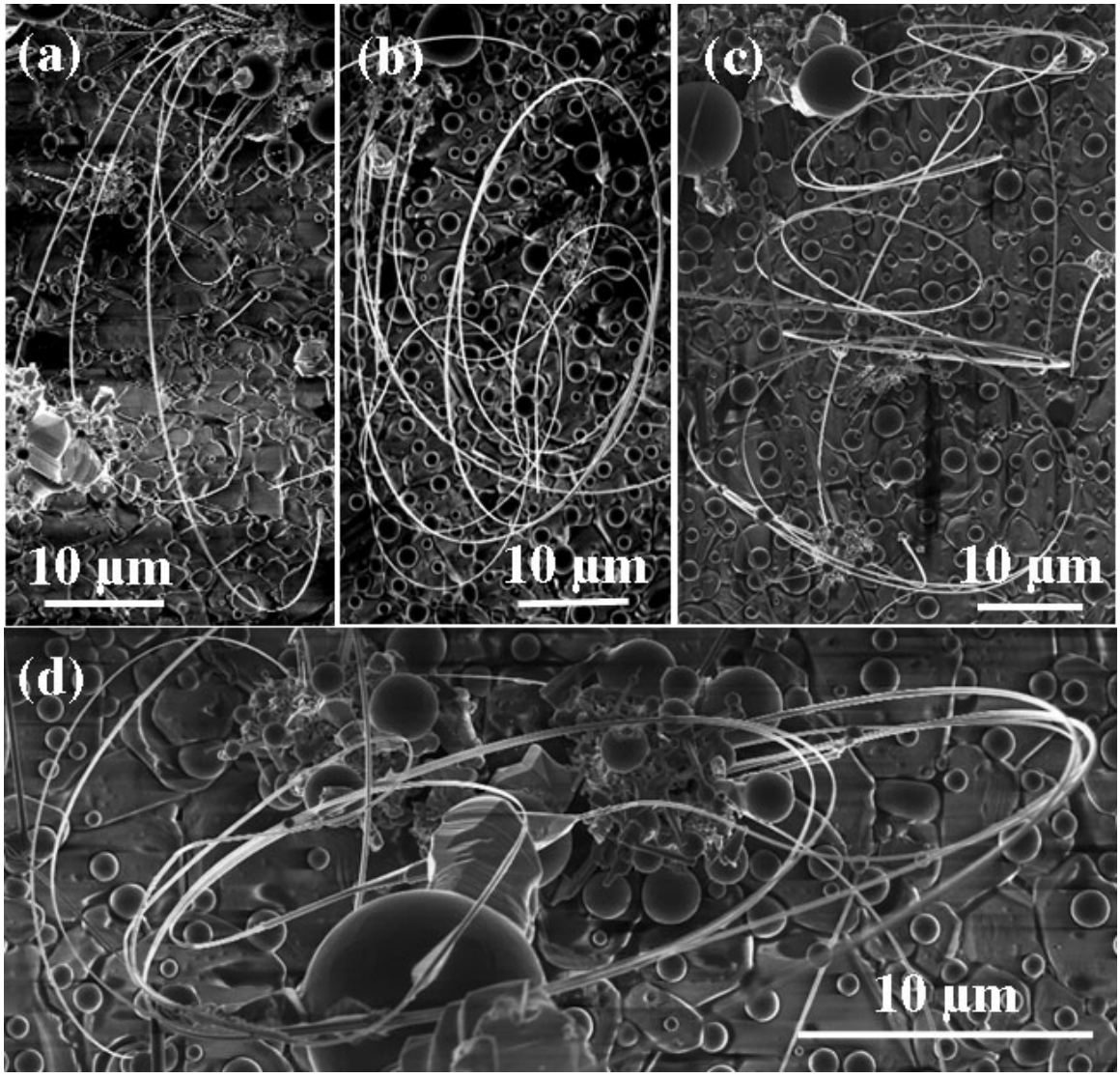

Figure 2.23 (a) half-loop nanospirals. (b) multiple-loop nanospirals. (c) multiple-loop nanospirals stressed along central axis. (c) self-closed nanorings.

In addition, springs were also found in the grown product. Figure 3.24a shows a SnO_2 spring lying on an Al_2O_3 substrate. The helical structure is made of a uniformly curved SnO_2 nanobelt with pitch distance ~20 μm. The most common SnO_2 spirals are

also included in Figure 3.24b, in which the curvature of the SnO_2 nanobelt changed during its growth. Most spirals/rings have diameters of 10-50 μm. A magnified part of the spring from Figure 3.24a is given in Figure 3.24c, showing clearly a belt-like geometry with width of ~300 nm and thickness of several tens nm. In addition, numerous nanoparticles are also formed on the Al_2O_3 substrate.

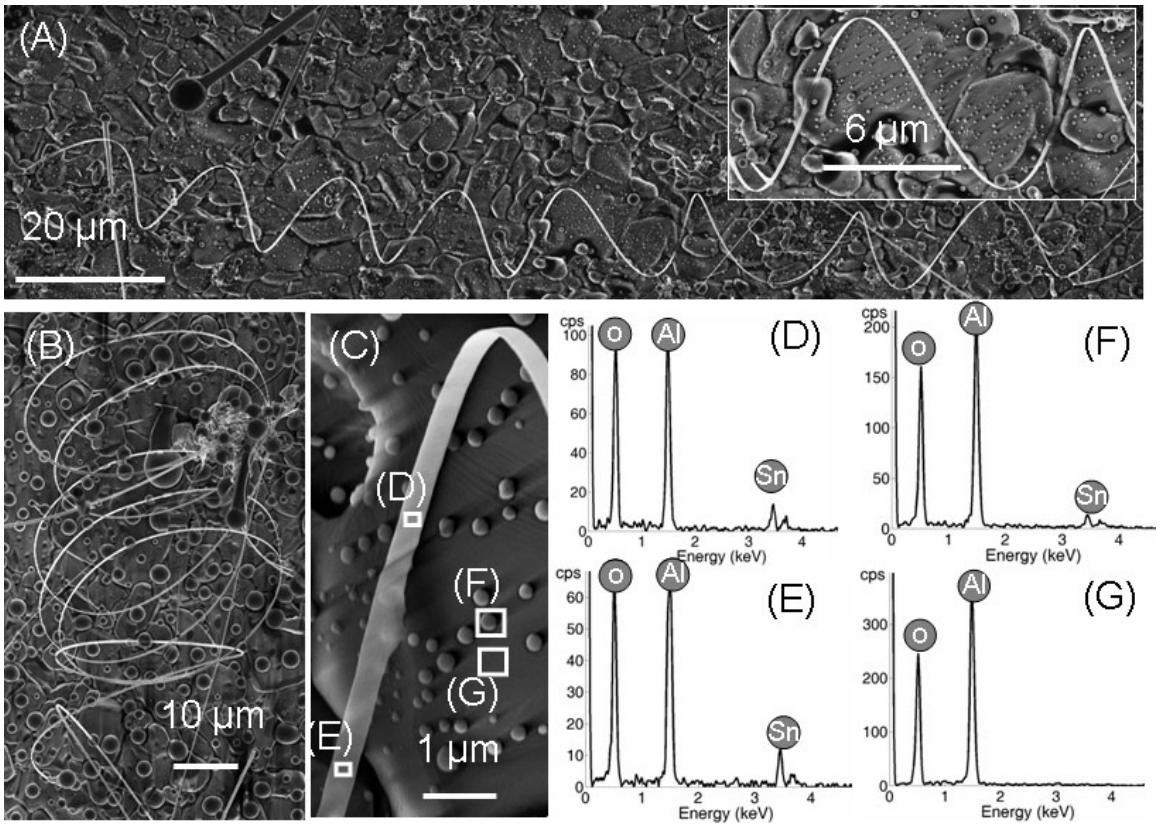

Figure 3.24 Scanning electron microscopy (SEM) and energy dispersive x-ray spectroscopy (EDS) of SnO_2 nanostructures. (a) SEM image of a ZnO nanospring. (Inset) An enlarged image of the nanospring. (b) SEM image of SnO_2 nanospirals. (c) A higher magnification SEM image from the nanospring indicated in (a). (d, e, f, g) EDS spectra acquired from the areas labeled with d, e, f and g in (c), respectively.

In order to investigate the chemical composition of the product, we took EDS spectra from a series of locations along the nanobelt, on the nanoparticles and on the blank substrate as labeled from d-g in Figure 3.24c and the results are displayed in Figs 3.24d-g, respectively. The EDS spectrum in Figure 3.24d shows only Al and O peaks with atomic ratio close to 2:3, which is consistent to the composition of the underneath

Al_2O_3 substrate. The absence of Sn peak or any other peaks excludes a possible layer of SnO_2 or Sn that might be formed on the substrate surface. After deducting the Al_2O_3 component, the EDS spectra in Figs 3.24f-g indicate that the nanobelt is composed of elements Sn and O.

The crystal structure of Sn-O nanobelt was determined with transmission electron microscopy (TEM) and selected area electron diffraction (SAED). Electron diffraction patterns from a partially curved nanobelt (Figure 3.25) show that the surface facing to the center is consistently being the (011) polar surface, as reported in the text, which is the dominant surface of the SnO_2 nanobelt and the driving mechanism for forming the rings, springs and spirals.

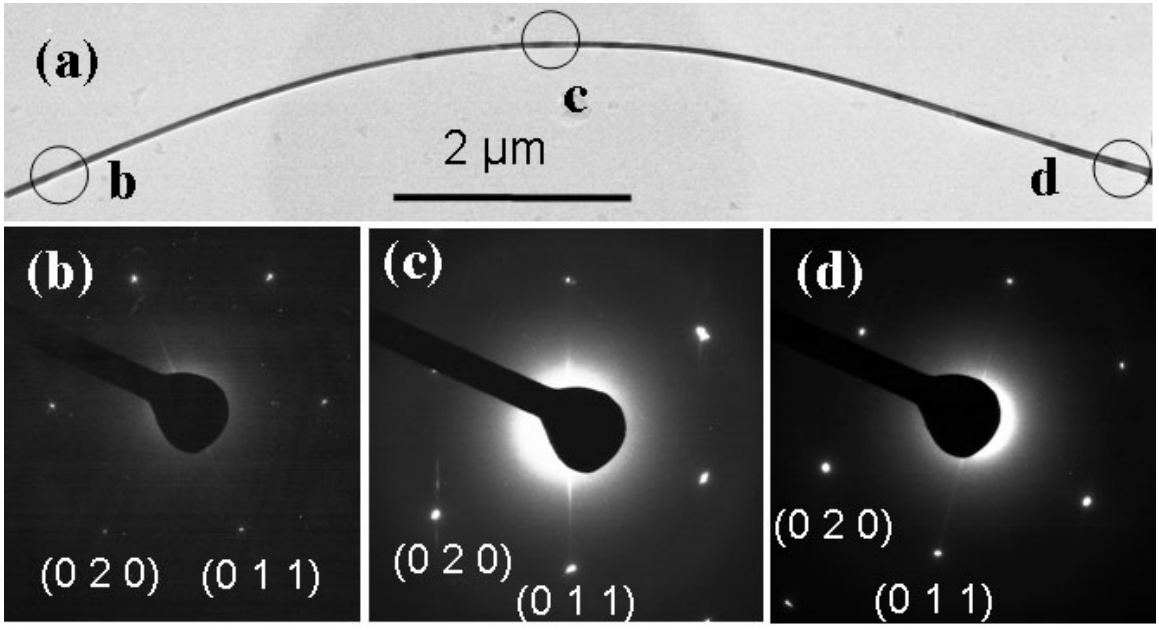

Figure 3.25 (a) low magnification TEM image of a curved nanobelt. (b)-(d) SAED pattern from circled area in (a).

The TEM image in Figure 3.26a presents a full ring formed by a closed nanobelt. The single-crystalline nature is confirmed by the sharp SAED patterns along the constituent nanobelt. The SAED pattern in the inset of Figure 3.26b was taken along the direction normal to the plane of the ring. Analysis of the SAED pattern reveals that the nanobelt has a tetragonal crystal structure with lattice parameters $a = b = 4.75$ Å and $c =$

3.20 Å, which are consistent to the lattice parameters of the rutile SnO_2 ($P4_2/mnm$, $a = b = 4.7382$ Å and $c = 3.1871$Å JPCDS No. 41-1445). It is worth to note that the SnO_2 belt grows along ~[0 $\bar{1}$ 1] with the side surfaces facing the center of the ring being ±(011), and the top and bottom surfaces parallel to the ring plane are ±(100). SAED and TEM examination of several other SnO_2 nanostructures consistently show that the nanobelt is dominated by the ±(011) surfaces.

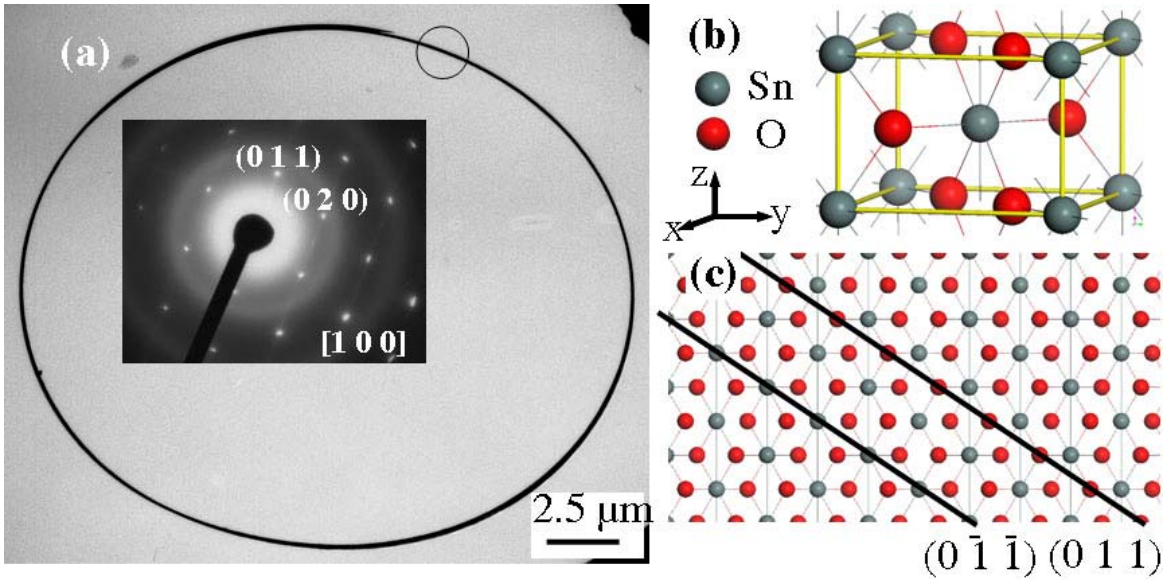

Figure 3.26 (a) Low magnification TEM image of a SnO_2 ring and the corresponding SAED pattern (inset) from the circled region (b) Tetragonal structure model of SnO_2 (c) The structure model of SnO_2 projected along [100], displaying the ±(011) polar surfaces.

3.5.4 Growth Mechanism

The growth of the ring, spring and spirals can be understood on the basis of polar surfaces of the rutile structured SnO_2, the atomic model of which is shown in Figure 2b. By projecting the structure model along [100], as shown in Figure 3.26c, the ±(011) plane can be terminated either solely with Sn^{4+} or solely with O^{2-}, respectively, resulting in a pair of positively and negatively charged polar surfaces on the inner and outer surfaces (or vice versa) of the nanobelt. During the growth at ~ 500-600 ^oC in an argon atmosphere, the probability for foreign molecules being adsorbed on the surfaces was

negligible within the time of the growth. Thus, the polar charges are likely to be preserved. If the charges on the ±(011) side surfaces are not compensated during the growth, the net dipole moment across the side surfaces and the surface energy tend to diverge with the increase of the nanobelt length. On the other hand, the electrostatic energy due to dipole moment can be minimized or neutralized when the nanobelt roll up to form a ring or spiral structure. On the other hand, bending of the nanobelt introduces elastic deformation energy, which increases with the decrease of the ring/spiral radius. The minimization of the total energy contributed by electrostatic polarization energy and elastic deformation energy determines the final morphology of the SnO_2 nanobelt, resulting in the formation of the ring (Figure 3.26a and Figure 3.27a) or multiply looped spiral (Figure 3.23, Figure 3.24b and figure 3.27b). Alternatively, if the bending of the nanobelt proceeds during the growth along the axial direction of the curled nanobelt, a helical structure will form (Figure 3.24a and Figure 3.27b). The spring is formed due to the stretching of the spiral (or multi looped ring) and/or possibly the electrostatic repulsion between the two adjacent rings.

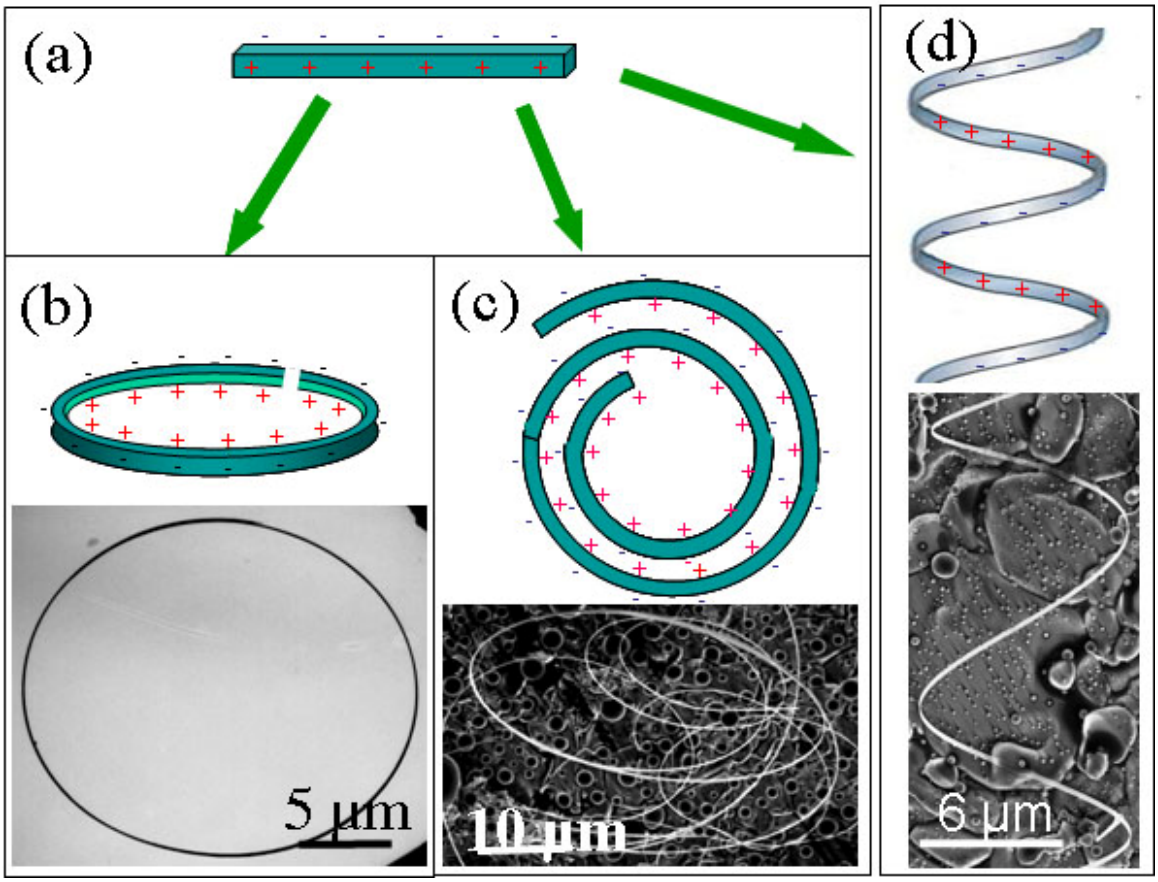

Figure 3.27 Schematic model showing the formation of SnO_2 ring, spiral, and spring.

The above proposed mechanism is consistent to the model established for ZnO [70, 71, 73, 163]. In comparison, the ZnO nanorings/nanosprings reported previously have radii of ~500-800 nm, nanobelt width of 10-60 nm and thickness of 5-20 nm [70, 71, 73, 163]. The radii of the SnO_2 rings and springs reported in this section are 5-50 μm, and the SnO_2 nanobelts have widths of a few hundred nanometers and thickness of a few tens nanometers, which are also larger than those of the ZnO nanobelts. This may be closely related to the charge density on the polar surfaces. The elastic energy increases rapidly with the curvature, width, and thickness of the nanobelt. Accordingly, it is rational to expect much larger helical nanostructures of SnO_2 than ZnO. In addition, the surface energies of Sn- and O- terminated surfaces can also contribute to the formation of rings and springs. A deep insight on the effect of polarization, elasticity, and surface

energy on the nanostructures requires further investigation with first principle computation and more experiments.

In summary, through a vapor-solid process, single crystalline springs, rings and spirals have been discovered for the first time in a rutile structured SnO_2. The crystal structure and growth mechanism investigation indicate that the formation of those nanostructures is mainly due to polar surfaces of tetragonal SnO_2. The research demonstrates that hierarchical nanostructures exclusively in ZnO are also possible in other materials with different crystal structures. The synthesized SnO_2 nanostructures will benefit the studying of the effect of polar surfaces on the morphology of the nanostructures and applications.

3.6 Summary

Seamless nanorings and deformation free helixes of ZnO have been synthesized with a thermal vapor deposition process. A detailed analysis revealed that the polar surface plays a critical role during the formation these nanostructures. When ZnO nanobelts grow with polar surface as side surface ($\{0001\}$ for nanorings, and $\{1\bar{1}01\}$ for nanohelixes), the electrostatic energy due to spontaneous polarity diverges with the growth. Depending on the growth direction, nanobelt dimension, and other factors, the nanobelt might bend and form a nanoring through a self-coiling process. A spiral or a spring can also result in the absence of self-coiling. The final dimension is determined by the competition of the minimization of the electrostatic energy and the increase of elastic energy due to deformation. Alternatively, the nanobelt can also minimize its polarization energy through changing its growth direction without introducing any deformation. In the absence of elastic energy, the electrostatic energy dominates and results in the ultra-small deformation-free ZnO nanohelixes.

The generalization of the growth mechanism is very important for rational control of nanostructures. The discovery and analysis of rings, spirals, and spring of rutile-

structured SnO_2 confirmed that the polar-surface-induced growth mechanism is not limited to specific material or crystal structure. The synthesized SnO_2 nanostructures benefit the study of the effect of polar surfaces on the morphology of the nanostructures and applications of SnO_2 in nanotechnology.

In addition, through manipulation of the synthesis kinetics, highly hierarchical 3-dimensional nanostructures of ZnO were synthesized by evaporating a mix of ZnO, SnO_2, and graphite. Both VLS growth and the self-catalyzed growth from polar surfaces influenced the final morphology of the nanostructures.

The growth of ZnO nanowires shows their versatile characteristic, and they can interpenetrate at a random angle. A detail analysis reveals that the significant transverse growth is responsible for such morphology. This is a significant progress in understanding the formation of 1D nanostructures, because the transverse growth has been ignored in many cases.

CHAPTER 4

BRANCHED NANOSTRUCTURES AND ZNO/ZN_3P_2 PHOTODIODE

4.1 Motivation

Being a smart functional material, ZnO has received much attention recently for its possible application as UV light-emitting diodes (LEDs), spin functional devices, gas transparent electronics, and surface acoustic wave devices. A key requirement for advancing the technological uses of ZnO is improved control of doping, including realization of p-type materials and enhanced conductivity in both n-type and p-type ZnO. However, p-type ZnO is notoriously difficult to get, and detailed knowledge of the intrinsic point defects responsible for native n-type behavior and of acceptor states in the gap of doped p-type materials is still lacking. In addition, p-type doping is mainly performed in ZnO film and little literature has mentioned similar research in the nanoscale.

In nanoscale, dimensional confinement and the surface effect is substantially greater than in the bulk, which will result in a lower threshold for laser excitation, better gas sensitivity, and other enhanced properties. As in bulk materials, achieving p-type ZnO becomes the most significant impediment to the widespread exploitation of ZnO related materials in electronic and photonic applications. Furthermore, nanoscale UV LEDs and other electronic devices also require the realization of high quality p-n nanowire junctions with good breakdown characteristics, which are the basic building blocks.

Currently, the electronic and optoelectronic applications of ZnO suffer from the difficulty of reproducible *p*-type doping of ZnO with high carrier concentration and hole mobility. *P*-type doping of ZnO has been attracting much attention and effort, and a

better understanding the origin of *p*-type doping difficulty in ZnO is necessary for the next step development.

Alternatively, in order to avoid the *p*-type doping problem, heterojunctions of n-type ZnO with other *p*-type semiconductors is another promising direction and has achieved rapid progress. In comparison with ZnO, Zn_3P_2 is another functional material with promising applications for solar cells, photodetector, and many other optoelectronic applications. However, Zn_3P_2 grown by the conventional method exhibits only *p*-type conductivity and *n*-type Zn_3P_2 is very difficulty to achieve. The combination of *p*-type Zn_3P_2 and *n*-type ZnO will bring new opportunities and will be discussed in this chapter of the dissertation.

4.1.1 P-type doping of ZnO

ZnO is a direct band-gap semiconductor with E_g=3.4eV and this band gap can be further turned with divalent substitution on the Zn. The undoped ZnO is an n-type semiconductor, and the negative electron carrier is attributed to intrinsic defects, such as Zn interstitials, oxygen vacancies, or hydrogen. Another important property is that ZnO has an exciton binding energy of 60 meV in bulk materials, and even higher in confined structure[194]. ZnO The intrinsic direct band gap, a strongly bound exciton state and gap states due to point defects are revealed with photoluminescence and photoconductivity.

ZnO, with or without dopant, has been grown through various processes, such as physical vapor deposition (PVD), chemical vapor deposition (CVD), Metal-organic CVD (MOCVD), pulse laser deposition (PLD), molecular beam epitaxy (MBE), MOMBE, ultrasonic spray pyrolysis (USP), and sputtering, both DC and RF. In addition, implant doping has also been employed to grown ZnO. Currently, most groups have focused on dopant from the group-V elements for p-type ZnO or transition metal for ferromagnetic ZnO.

The natural candidates for acceptor dopant are group-I elements (Li, Na, K) and group-V elements (N, P, As). Substitutional Li_{Zn}, Na_{Zn}, and K_{Zn} have acceptor energy levels of 0.09, 0.17, and 0.32 eV, and substitutional N_O, P_O, and As_O, have acceptor energy levels of 0.40, 0.93 and 1.15 eV respectively according to first principle total-energy calculations based on the local density approximation (LDA)[195]. However, Li doped ZnO is actually semi-insulating (SI) due to the formation of Li_I[196]. Na is not good for p-type either because Na_I is more energetically favorable than Na_{Zn}, and K doping has failed to form p-type ZnO due to the formation of V_O donors[196]. On the other hand, doping with group-V elements has made rapid progress, despite difficulties in achieving shallow acceptor states according to theoretical prediction [195, 197].

It seems that the most promising dopant for p-type ZnO is N, which has the smallest mismatch with Zn and shallowest acceptor energy level. Most efforts have been focused on nitrogen doping, as also can be seen from Table 4.1. (Table 4.1 is a summary of p-type ZnO samples reported in the literature, and is modified and updated from reference[194]). Instead doping N as acceptor , Kim et al [198] have successfully produced excellent P-doped p-type ZnO with a resistivity as low as 0.6 Ω-cm, and Ryu et al also achieved As-doped p-type ZnO with an activation energy of about 120 meV. The success with P and As indicates that the either LDA is not accurate, or the acceptor in not simple substitutional dopant.

Table 4.1 Data on p-type ZnO samples reported in the literature.

First Author	Technique	Dopant	Resistivity (Ω cm)	Year of publication
Minegishi[199]	CVD	N	34	1997
Joseph[200]	PLD	N, Ga	4	1999
Ryu[201]	PLD	As	?	2000
Joseph[202]	PLD	N, Ga	0.5	2001
Guo[203, 204]	PLD	N	2	2001,2002
Butkhuzi[205]	Quasi-epi	None	900	2001
Ashrafi[206]	MOMBE	N	?	2002
Xiong[207]	DC Mag. sputt.	None	3	2002
Look[208]	MBE	N	40	2002
X Li[209, 210]	MOCVD	N	20	2003
Bang[211]	RF Mag. sputt.	P	?	2003
B S Li[212]	CVD	N	150	2003
Singh[213]	RF diode sputt.	N, Ga	12	2003
Huang[214]	DC Mag. sputt.	N	31	2003
Ryu[215]	Hybrid beam	As	2	2003
Kim[198]	RF Sputt.	P	0.6	2003
Lu[216]	DC Mag. sputt.	N	31	2003
J Wang[217]	MOCVD	N	100	2003
C Wang[218]	DC Mag. Sputt.	N	83	2003
Rommeluere[219]	MOVPE/diffusion	N	0.6	2003
Lu[220]	CVD	N	20	2003
Ma[221]	MOVPE	None	43	2004

Table 4.1 (continued)

First Author	Technique	Dopant	Resistivity (Ω cm)	Year of publication
Lin[222]	RF Mag. Sputt	N	10	2004
Ye[223]	DC Mag. Sputt.	N, Al	160	2004
Xu[224]	MOCVD	N	3	2004
Look[225]	Evaporation/sputt.	As	0.4	2004
Lu[226]	DC Mag. Sputt.	N, Al	57.3	2004
Suemune[227]	MOMBE	N	?	2004
Heo[228]	PLD	P, Mg	?	2004
Fei[229]	Mag. Sputt.	N, Al	<100	2004
Barnes[230]	CVD	N	?	2005
Liang[231]	MBE	N	9.36	2005
Lu J.G. [232]	DC Mag. Sputt.	N, Al	3.20	2005
Sanmyo[233]	RF Mag. Sputt.	N, Be	45	2005
Tsukazaki[234]	MBE	N	?	2005
Vaithianathan[235]	PLD	As	2.2	2005
Ye[236]	DC Mag. sputt.	N, Al	157	2005
Yuan[237]	DC Mag. Sputt.	N, Al	24.5	2005
Zhuge[238]	DC Mag. Sputt.	N, Al	100	2005
Tsukazaki[234]	MBE	N	?	2005
Vaithianathan[235]	PLD	As	2.2	2005
Ye[236]	DC Mag. sputt.	N, Al	157	2005
Yuan[237]	DC Mag. Sputt.	N, Al	24.5	2005
Zhuge[238]	DC Mag. Sputt.	N, Al	100	2005

Table 4.1 (continued)

First Author	Technique	Dopant	Resistivity (Ω cm)	Year of publication
Tu[239]	RF Mag. Sputt.	N	2.83	2006
Sun[240]	MBE	N	?	2006
Miao[241]	MOCVD	P	11.3	2006
Lu[242]	PLD	N, Li	0.93	2006
Kumar[243]	RF Mag. Sputt.	N, Ga	38	2006
Gangil[244]	MOCVD	N	?	2007
Pan[245]	PLD	Sb	2-4	2007
Zeng[246]	MOCVD	N	1.72	2007
Zhang[247]	USP	N, Al	8.1	2007

Many *p*-type ZnO structures with very low resistivity and high hole concentration and mobility, especially in ZnO thin films on Si substrates [248-251] have been reported. These values, if reliable, are already satisfactory for device application. Unfortunately, such outstanding *p*-type conductivity is questionable accordingly to Zeng[252]. The Hall-effect measurement on a conducting substrate might not be able to reveal the real conductivity of the top ZnO thin layer. First, a longitudinal heterojunction can form at the interface between ZnO and Si and lead to an artificial Hall Effect result. When the magnetic field is applied, not only the carrier above the heterojunction but also that below may contribute to the Hall voltage. The thickness of the effective conducting layer, which is required to determine the bulk carrier concentration and resistivity, will become uncertain when a conducting substrate is introduced. Finally, there is no evidence that a conducting Si substrate will be superior to that of insulating substrates, such as sapphire, glass, and quartz, for p-type doping in ZnO.

Zhang[247] et al have noticed much lower resistivity of ZnO on silicon substrate (0.00011 Ω cm) than ZnO on glass (8.1 Ω cm), and they suggested that the difference might come from the influence of the low resistivity, high mobility silicon substrate. Zhao et al.[248] performed scanning capacitance microscopy investigation on ZnO films on silicon substrate anomalous high p-type conductivity and found no significant *p*-type ZnO grains. They indicated that the highly *p*-type behavior might come from the interface state induced by two-dimensional hole gas.

In addition to the *p*-type doping in ZnO thin films, some effort has also made to ZnO nanostructures[253]. However, much work have to be done in order to get stable *p*-type ZnO with reasonable low resistivity and high hole concentration and mobility.

4.1.2 Properties of Zn_3P_2

In recent years increasing attention has been paid to new materials for solar cell and optoelectronic devices. Among such compounds, Zn_3P_2 is relatively new and promising material.

Zn_3P_2 is a $A_3^{II}B_2^{V}$-type semiconductor with *p*-type conductivity in conventional grown crystal. Its intrinsic *p*-type conductivity is believed to be due to the additional phosphorus atoms in the interstitial positions.

Zn_3P_2 crystallizes in the primitive tetragonal lattice, which belongs to the D_{4h}^{15} space group[254]. As shown in Figure 4.1, the unit cell contains eight molecules, including 16 phosphorus atoms and 24 zinc atoms. The zinc atoms are located on four equally spaced planes perpendicular to the *c*-axis in a unit cell, while the phosphorus atoms lie on parallel planes midway between two adjacent cation planes. Each zinc atom is tetrahedrally coordinated with the phosphorus atoms as the nearest neighbors, while the phosphorus atom is surrounded by cation atoms located at six of the eight corners of the cube, the two ‘‘vacant” sites being at diagonally opposite corners of the cubic face. An

examination of this unit cell shows that there are two kinds of phosphorus layers and four zinc layers. The zinc layers differ in the position of cation "vacancies".

The fundamental absorption measurement for undoped single crystals of Zn_3P_2 presented an exponential edge within 1.4-1.6 eV[255]. Such location of the absorption edge is exactly at the optimum range demanded for solar energy conversion[256]. In addition, the distinct changes in the absorption curve slopes of polarized light denote the energies of allowed direct transition. The difference between the edges of the photoresponse spectra for polarized light implies that Zn_3P_2 can also be used for detecting a particular type of light polarization.

Besides the high absorption coefficient, Zn_3P_2 can also benefit from its large diffusion length for minority carriers (electrons), which is in the range of 10 μm.

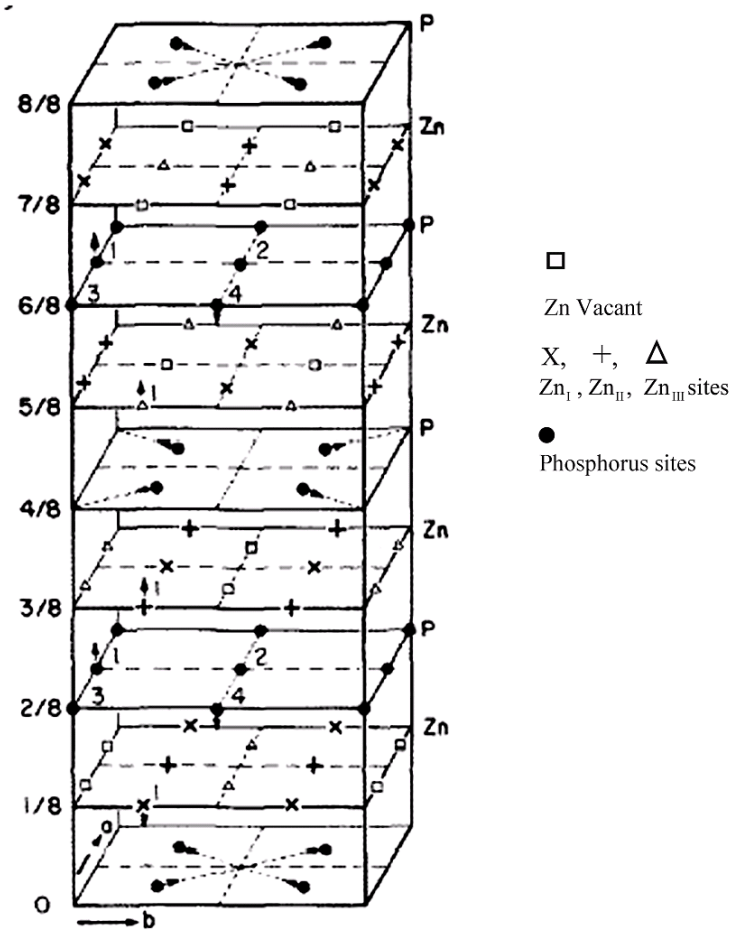

Figure 4.1 Schematic diagram of unit cell of Zn_3P_2.

4.2 Zn_3P_2 Nanostructures

Being a novel optoelectronic material, Zn_3P_2 has many advantages over some other materials. It has a direct band gap in the range of 1.4-1.6 eV, which is the optimum range for solar energy conversion. The large optical absorption coefficient ($>10^4$ cm^{-1}) and a long minority diffusion length (~13 μm) of Zn_3P_2 permit high current collection efficiency [257]. In addition, the constituent materials are abundant and cheap and would allow the large scale deployment of such devices as solar cells, infrared (IR) and ultraviolet (UV) sensors, lasers, and light polarization step indicators [255, 258].

In order to investigate the potential applications of Zn_3P_2, several kinds of heterojunctions have been designed, such as InP/Zn_3P_2 [259], Mg/Zn_3P_2 [260], Zn_3P_2/ZnSe[258, 261], ITO/ Zn_3P_2 [262], and ZnO/Zn_3P_2 [263]. However, the majority of research on Zn_3P_2 has been limited to thin films, and very little work has been done in the nanoscale range except very few reports on the synthesis of Zn_3P_2 nanoparticles [264-266] and on the synthesis of nanotrumpets with an unavoidable ZnO layer coated on the surface[267]. Because of the large excitonic radii, Zn_3P_2 is expected to exhibit pronounced quantum size effect, which has been observed for Zn_3P_2 nanoparticles[265]. To the best of our knowledge, the electric property and photoresponse of Zn_3P_2 nanostructures, and heterojunctions made from Zn_3P_2 nanostructures, have not been reported thus far.

In this section, the synthesis of single crystalline tree-shape Zn_3P_2 structure arrays, nanowires, and nanobelts are presented. The morphology and crystal structure were determined by electron microscopy and analytical techniques. In addition, the optical property of the synthesized nanostructures has been measured through photoluminescence (PL). Furthermore, we also present the crossed heterojunction made using a ZnO nanowire and a Zn_3P_2 nanowire. Optoelectronic measurements of single Zn_3P_2 nanowire and the crossed heterojunction indicate that Zn_3P_2 was very sensitive to

light and the heterojunction exhibits enhanced performance, which implies that the Zn_3P_2 nanostructures have promising applications in optoelectronics.

4.2.1 Fabrication Method

Various nanostructures have been synthesized with thermal evaporation[268] or laser ablation methods[269-271]. Combing the two techniques, Zn_3P_2 structures were synthesized using a thermally assisted pulsed laser ablation (TAPLA) process in a single-zone horizontal tube furnace, which is shown schematically in Fig 4.2 and in Chapter 2 with more detail. The two ends of the tube were closed and water-cooled to ensure a stable synthesis environment inside. A mixture of 0.8 grams ZnO and 0.12 grams graphite powder was placed in the middle of the tube. In order to transport the source vapor and reduce possible oxidization during the synthesis, N_2 was introduced from one end of the tube at a flow rate of 25 sccm during the entire synthesis process. A cylindrical target containing Zn_3P_2, ZnO, and Zn (in ratios of 2:1:1 by weight) was placed downstream. Single crystalline (111) Si wafer was placed in front of the target, serving as a collecting substrate. In order to minimize the residual oxygen, the tube was first evacuated to 10^{-2} mbar and held for 2-3 hours before the introduction of N_2 and maintained at a constant pressure of 200 mbar thereafter. The furnace was then heated up at a rate of 50 ^{o}C per minute to the desired peak temperature of 1100 ^{o}C and held for another 20 minutes before slowly cooling down. Once the temperature exceeded 900 ^{o}C, a Compex Series Excimer 102 Laser (248nm, 10 Hz, 30 kV, ~300 mJ) started to generate pulsed laser energy and kept shining a laser spot, 1 mm wide and 5 mm long, on the target during the synthesis until the furnace was cooled down to 900 ^{o}C.

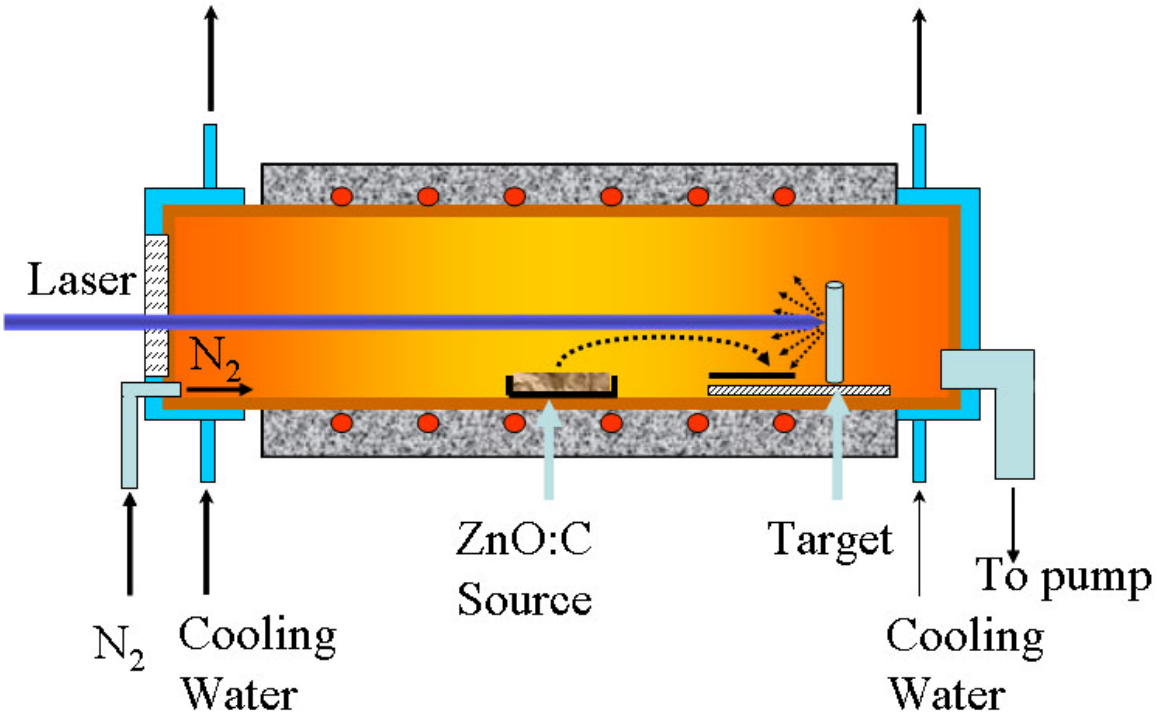

Figure 4.2 Schematic diagram for experiment setup.

When the synthesis process was completed, dark yellowish fuzzy materials were found around the laser ablated pit on the target and on the surface of the substrate. The morphology of the as synthesized materials was examined using a LEO 1530 field emission scanning electron microscope (SEM) and the composition of Zn and P was first confirmed with EDS attached to SEM.

4.2.2 Structure Characterization

Figures 4.3 show typical SEM images of as-synthesized Zn_3P_2 nanostructures. A top view of the as synthesized nanostructures on a Si substrate is present in Figure 4.3(a) and its inset, which shows that those hierarchical nanostructures take a six-fold symmetry. The tree shape is further revealed in the side view of Zn_3P_2 nanostructures in Figure 4.3(b), which is the as-synthesized product from the target lying on conductive carbon tape for SEM imaging. The constituent branches of those tree-shape structures can be as long as several tens of micrometers. The diameter of those branches is in the range

of 10 nm to a few hundreds nm. Generally, the branches at the root of the central trunk are larger than those at the top part of the trunk. A single branch is uniform and gradually gets smaller towards its tip. The tree shaped nanostructure can get very complex with the growth of secondary branches, as shown in Figure 4.3 c and d. (Not matter)?? the large number of branches and the random location, all nanostructures seem to have only four sets of orientations. Among those four orientations, three sets of branches have six-fold symmetry with the four branches in the middle and perpendicular to the aforementioned three sets. Such regularity indicates a direct correlation between the morphology and its crystallographic structures. This correlation is getting more apparent in TEM analysis and will be discussed in more detail later on.

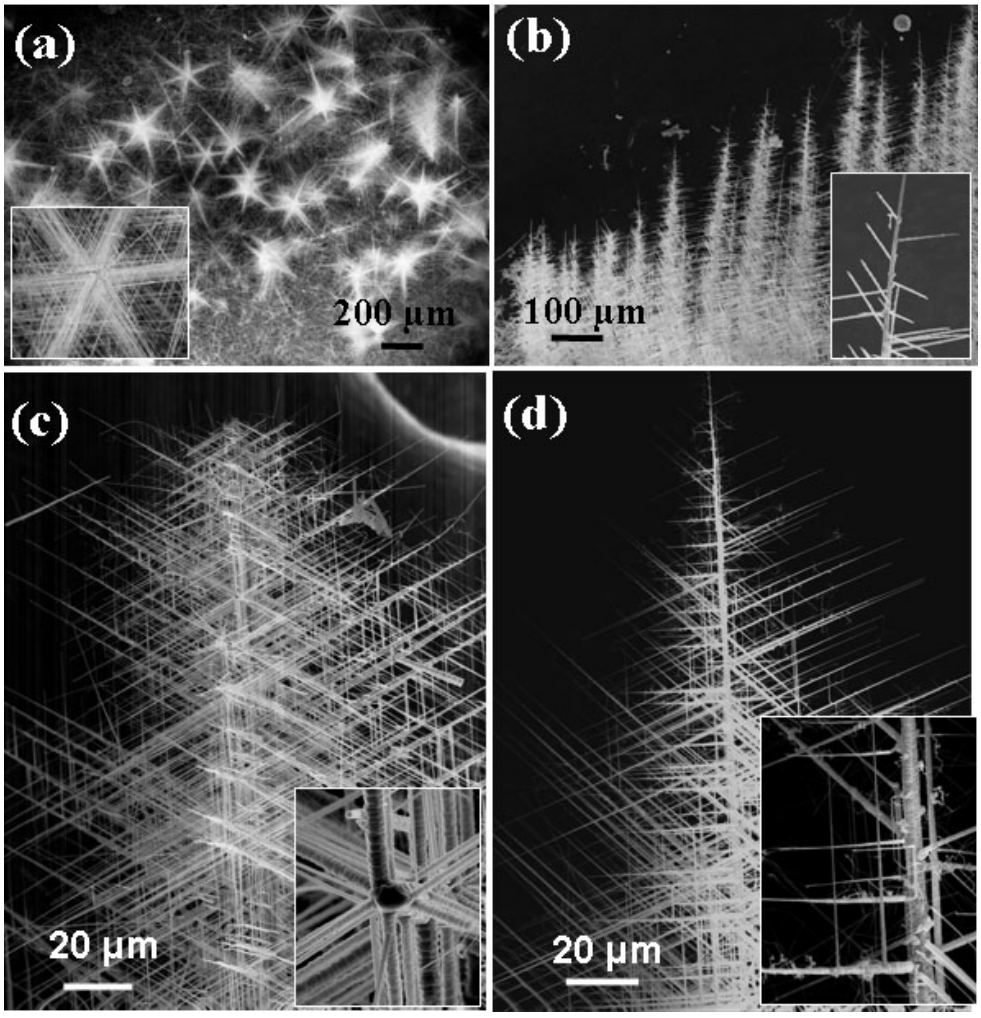

Figure 4.3 SEM images tree-shaped nanostructures of Zn_3P_2.

When the branches grow longer, some Zn_3P_2 nanobelts are also formed, as show in Figure 4.4. The thickness is in the range of 100 nm to several hundred nm, but the same nanobelt has a very uniform thickness throughout the entire belt. In comparison, the widths vary dramatically, even within a single nanobelt. As can be seen from Figure 4.4a, some nanobelts can be as wide as 10 μm at the root and get noticeably narrower towards the tip. Smaller nanobelts have also been observed, as shown in the inset in Figure 4.4b with a width around 100 nm. Some big belts are also frequently observed (Figure 4.4c). No matter how wide the belts is, the thickness are generally well below 100 nm. Considering their super long length, those nanobelts are still overall very uniform. Besides those hierarchical nanostructures and derivative nanobelts, numerous Zn_3P_2 nanowires (NWs) with diameters up to 100 nm have also been found on the surface of the Si substrates.

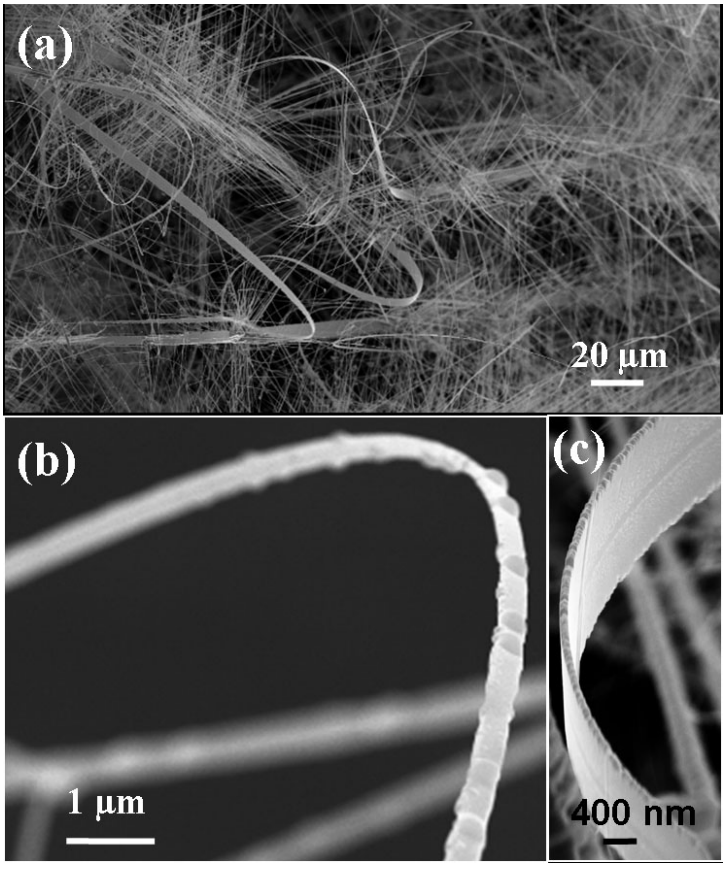

Figure 4.4 SEM images of Zn_3P_2 nanobelts.

EDS analysis in both SEM and TEM modes gave the same result for all nanostructures reported in this paper, including tree-shaped nanostructures, nanowires, and nanobelts. A typical spectrum in Figure 4.5a, which was taken from a Zn_3P_2 branch during TEM analysis, indicates the presence of Zn and P from the nanostructure, with Cu and C peaks originating from the sample grid, and O peaks from contamination during the sample preparation or from partial oxidization of the nanostructure.

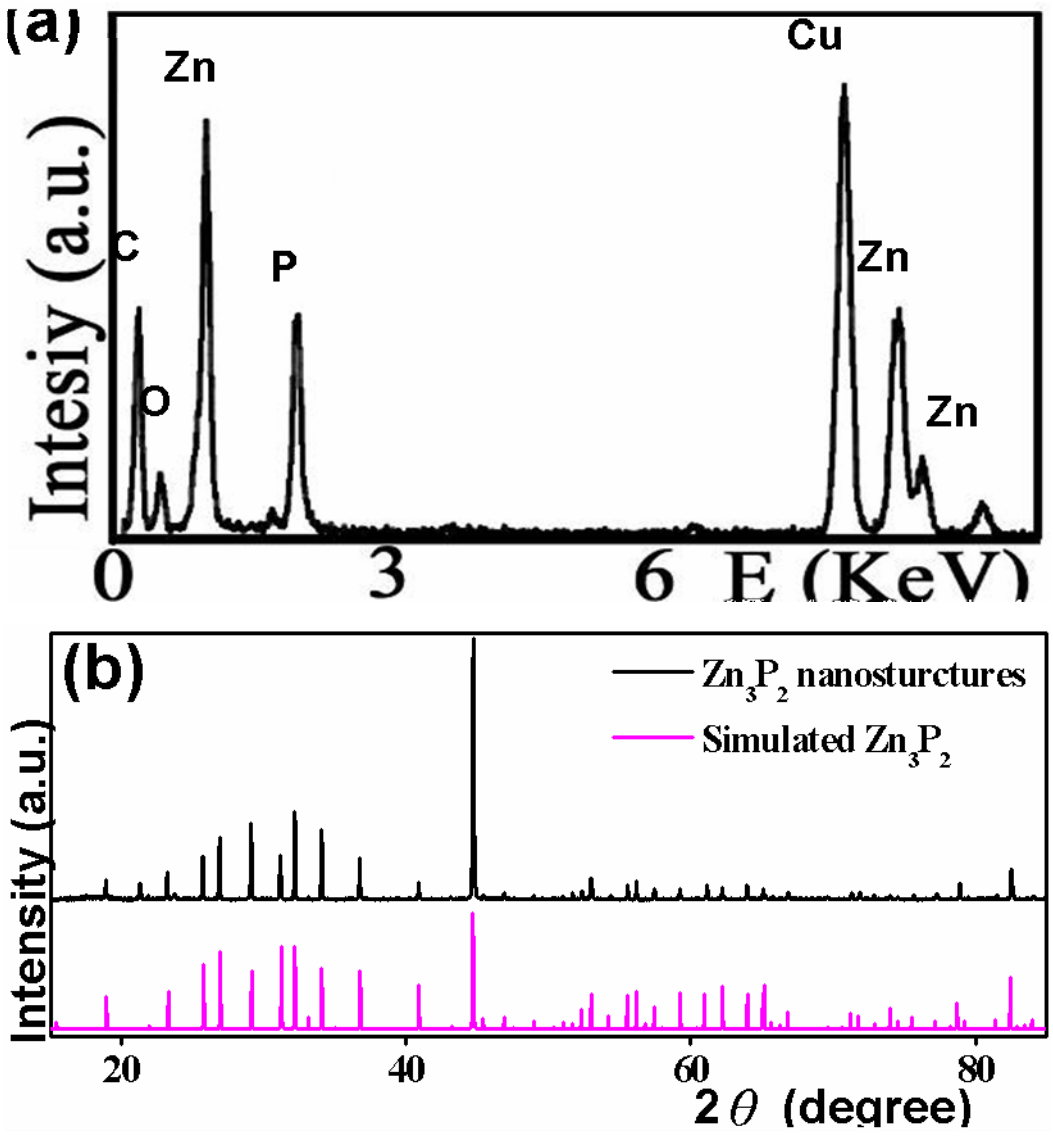

Figure 4.5 EDS and XRD measurement of Zn_3P_2 nanostructures.

X-ray diffraction characterization in Figure 4.5b, performed using a PANalytical X-Pert Pro MRD with Copper K-alpha radiation, confirms that the phase of the nanostructures is tetragonal Zn_3P_2 (JCPDS Card No. 65-2854) with lattice constants a = 8.095 Å and c = 11.47 Å. XRD analysis indicates that the synthesized nanostructures are single phased Zn_3P_2 with very good crystallinity. No Zn, ZnO, or any other phases are detectable.

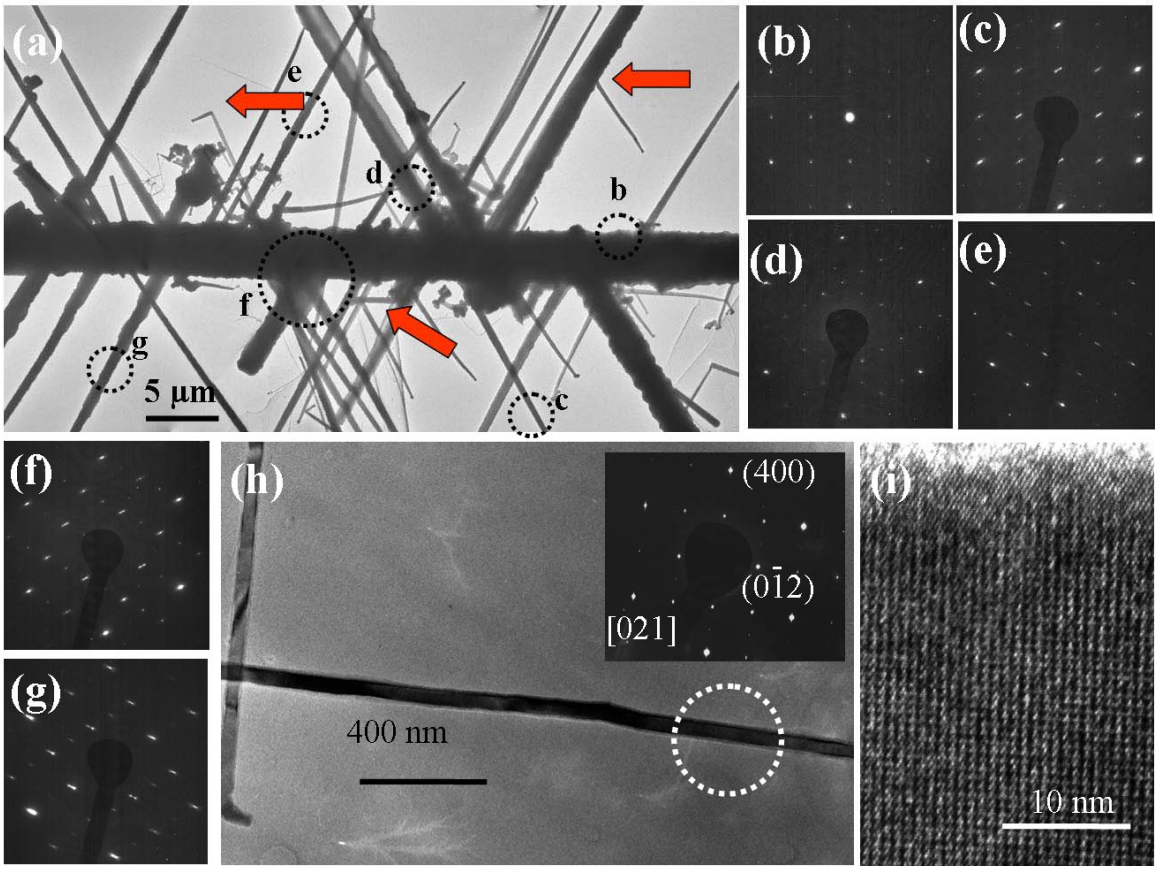

Figure 4.6 A detailed crystal structure analysis with TEM. (a) Low magnification TEM image of Zn3P2 structure with SAED patterns from circled areas labeled b-g and shown in (b-g), respectively. The arrowheads indicate secondary branch growth. (h) TEM image of Zn3P2 nanowires with SAED from the circled area and (i) a high resolution TEM image.

Zn_3P_2 nanostructures were further examined using a Hitachi HF-2000 (FEG) transmission electron microscope, as shown in Figure 4.6. Figure 4.6a presents a TEM image of part of a Zn_3P_2 nanostructure with selected area electron diffraction (SAED)

patterns recorded from the circled areas labeled b-g and shown in Figure 4.6(b-g), respectively. All of the branches in Figure 4.6(a) are in the same plane and the angle between them is about 60 degrees. As expected, all of the SAED patterns from different locations are along the same zone axis, [021]. Additionally, in-plane rotations are found for some of the SAED patterns, indicating the existence of twin structures when forming the branches. More detailed analysis will be reported separately. Figure 4.6(h) presents a TEM image of a Zn_3P_2 nanobelt with the same SAED as that of nanostructures in Figure 4.6(a), which is reasonable because nanobelts always grow from those nanostructures, based on SEM observation. According to those SAED patterns, we conclude that the central wire in Figure 4.6(a) and the nanobelts in Figure 3(h) have a growth front of $(0\bar{1}2)$. The top and bottom branches in Figure 4.6(a) have growth fronts of $(3\bar{1}2)$, $(31\bar{2})$, or the opposite directions. Secondary branches can also grow from grown branches, as indicated by arrowheads in Figure 4.6 (a). The high resolution TEM image in Figure 4.6 (i) taken from the circled area in Figure 4.6 (h) illustrated the nearly perfect single-crystalline arrangement of atoms in the nanowires. Amorphous materials are scarcely seen on the surface. In addition, no ZnO layer has ever been seen on the surface of those Zn_3P_2 nanostructures[267]. Electron microscopy and XRD data demonstrate that perfectly crystalline Zn_3P_2 nanostructures free from an oxidization layer can be obtained.

4.2.3 Growth Mechanism

Because no catalyst was introduced during the synthesis and no catalyst was found at the tip or bottom of the grown nanostructures, the nanostructures must be from a vapor-solid (VS) process. The ZnO and graphite in the middle of the tube follows a carbon-thermal evaporation process as follows[272],

$ZnO(s) + C(s) \leftrightarrow Zn(v) + CO(v)$ (1)

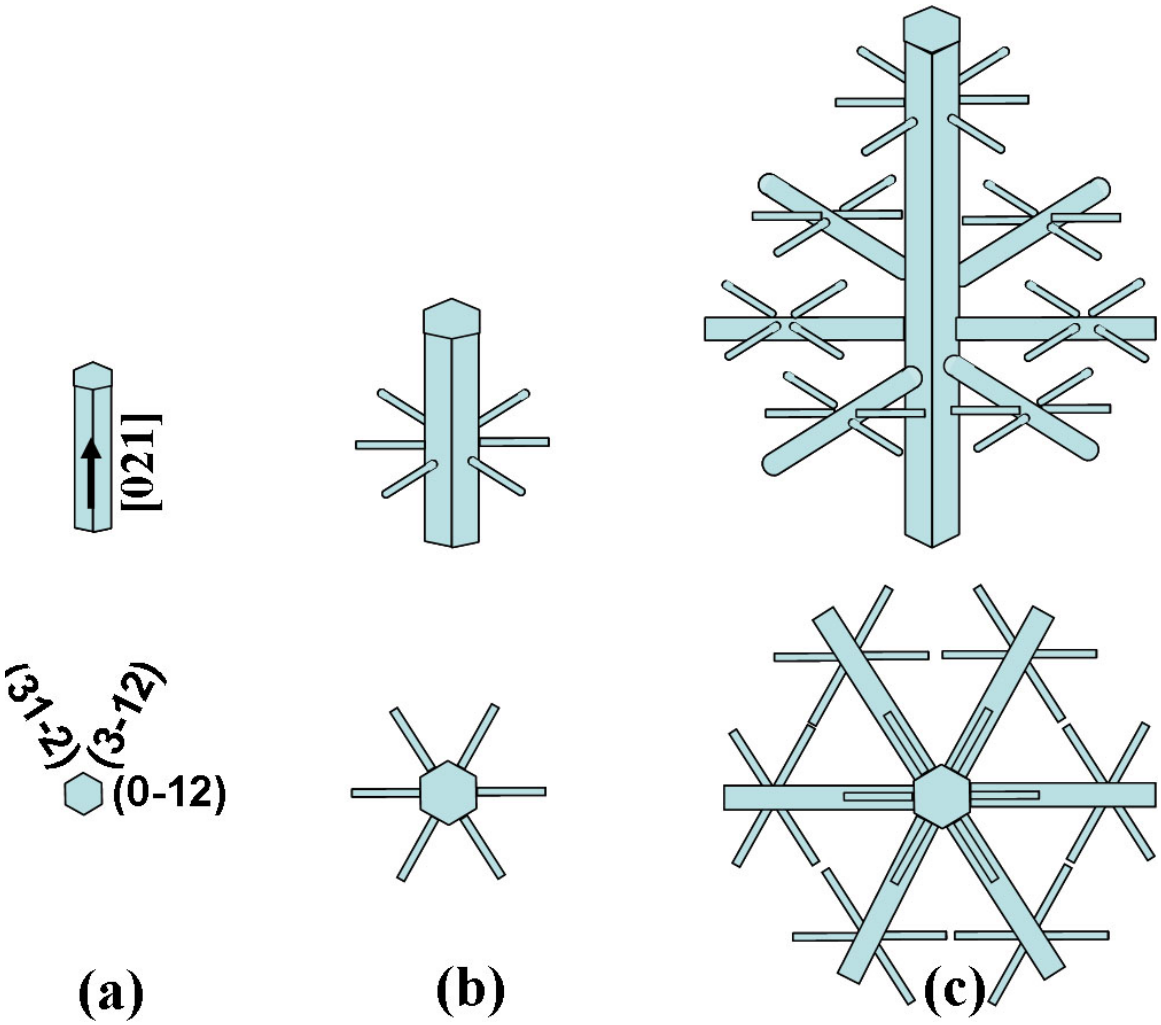

Figure 4.7 (a) Growth of a Zn_3P_2 nanowire along [021]. (b) Branch growth from the central wire (c) Formation of tree-shaped Zn_3P_2 nanostructure as a result of continuous growth of side branches and secondary branches.

Zn vapor was transferred by N_2 carrying gas downwards to the reaction area around the target. Being a mixture of Zn_3P_2, ZnO and Zn, the target releases vapors mainly composed of Zn, P, and O ions under the laser ablation that provides enough energy to break the Zn-P and Zn-O bonds. The O ions were mainly taken by oxidizing the carbon and CO, making it possible for the Zn and P ions to join, resulting in the growth of Zn_3P_2 nanowires. The Zn_3P_2 wires grow along [021], and later are followed by the growth of side branches, as shown schematically in Figure 4.7. Figure 4.7(a) illustrates a Zn_3P_2 wire along [021] with three sets of side surfaces $(0\bar{1}2)$, $(3\bar{1}2)$, and

$(31\bar{2})$. A continuous supply of Zn and P results in the growth of the side branches from the central wire, as shown in Figure 4.7(b). The side growth with six-fold symmetry results from the fact that the angles between the side surfaces in Figure 4.7(a) are 120 degrees. When the central wire and the side branches grow longer, new branches will grow from the central wire and even secondary branches also grow from the side branches, which is illustrated in Figure 4.7(c) and can be found in Figure 4.3.

4.3 Properties and Devices Fabrication

4.3.1 Optical Properties

The optical performance of Zn_3P_2 nanostructures is very interesting. Figure 5 shows reflection spectrum from 1 to 2 eV (left-hand side) and photoluminescence (PL) spectrum under the excitation of 326 nm at room temperature (right-hand side). From the reflectance spectrum it can be seen that energies below 1.4 eV are almost totally reflected by the Zn_3P_2 nanostructures without absorption, while a distinct edge was found at approximately 1.4 eV, indicating a strong absorption of higher energies.[273] The corresponding PL spectrum provides direct evidence of this distinct absorption edge, at which a broad peak of 1.4-1.7 eV can be found. The broad spectrum found in PL likely results from the free exciton emission near the band edge, namely, acceptor-bound excitons [274].

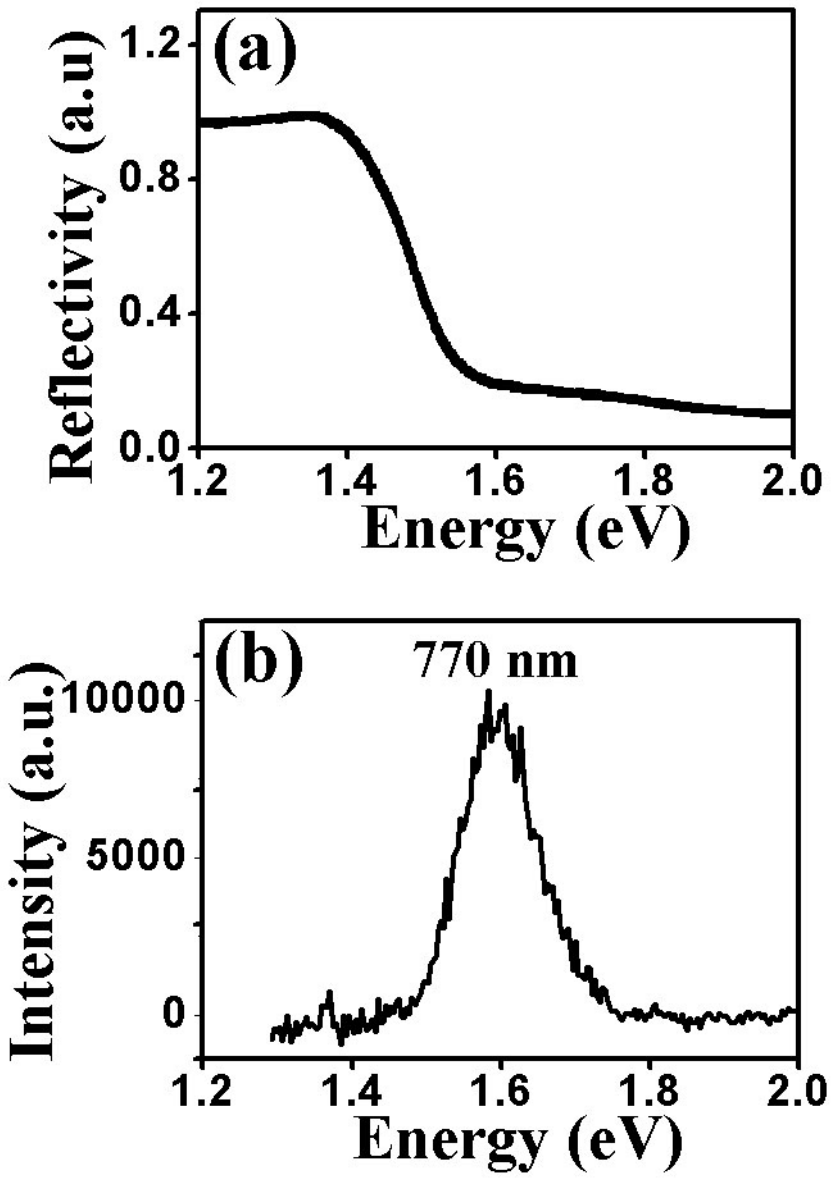

Figure 4.8 (a) Reflection spectrum of Zn_3P_2 nanostructures (b) The corresponding photoluminescence spectrum.

4.3.2 Device Design and Fabrication Techniques

Before we going to the details of device fabrication and characterization based on the Zn_3P_2 nanostructures, the fabrication techniques should be introduced first in order for a good understanding of the process. The whole process includes four steps, which

includes bottom electrodes fabrication, nanostructure manipulation, top electrode deposition, and finally device characterization.

4.3.2.1 Bottom Electrodes Fabrication

We employed photolithography technique to fabricate the bottom electrode patterns for device measurement. Photolithography is an optical means for transferring patterns onto a substrate. It is the primary method used to pattern devices in the manufacture of integrated circuits and has played a key role in the success of CMOS technology as the microelectronics evolves. By using smaller and smaller wavelengths year upon year, the required performance on critical feature sizes has been achieved. Furthermore, a variety of emerging techniques, such as sophisticated mask technology including phase-shift masks and optical proximity corrections, has pushed the physical limits further down to nanoscale range (50-100 nm). A major advantage of photolithography is the ability to fabricate many devices at once (i.e. in parallel), making possible the production of very complex circuit in a relative short time. A fundamental limitation of photolithography is diffraction, which limits the size of the feature that can be made to approximately the wavelength of the light used. Although the smallest feature from photolithography is getting into submicron range, the cost is becoming very high in order to push the limitation a little further.

We used a silicon wafer with an insulating silica top layer as the substrate for the device fabrication. The silicon wafer must be cleaned before any lithography process. A clean surface free from dust, photoresist residue, and films from other sources is required for a successful pattering with photolithography. Figure 4.9 illustrates a typical photolithography process for making the bottom electrodes.

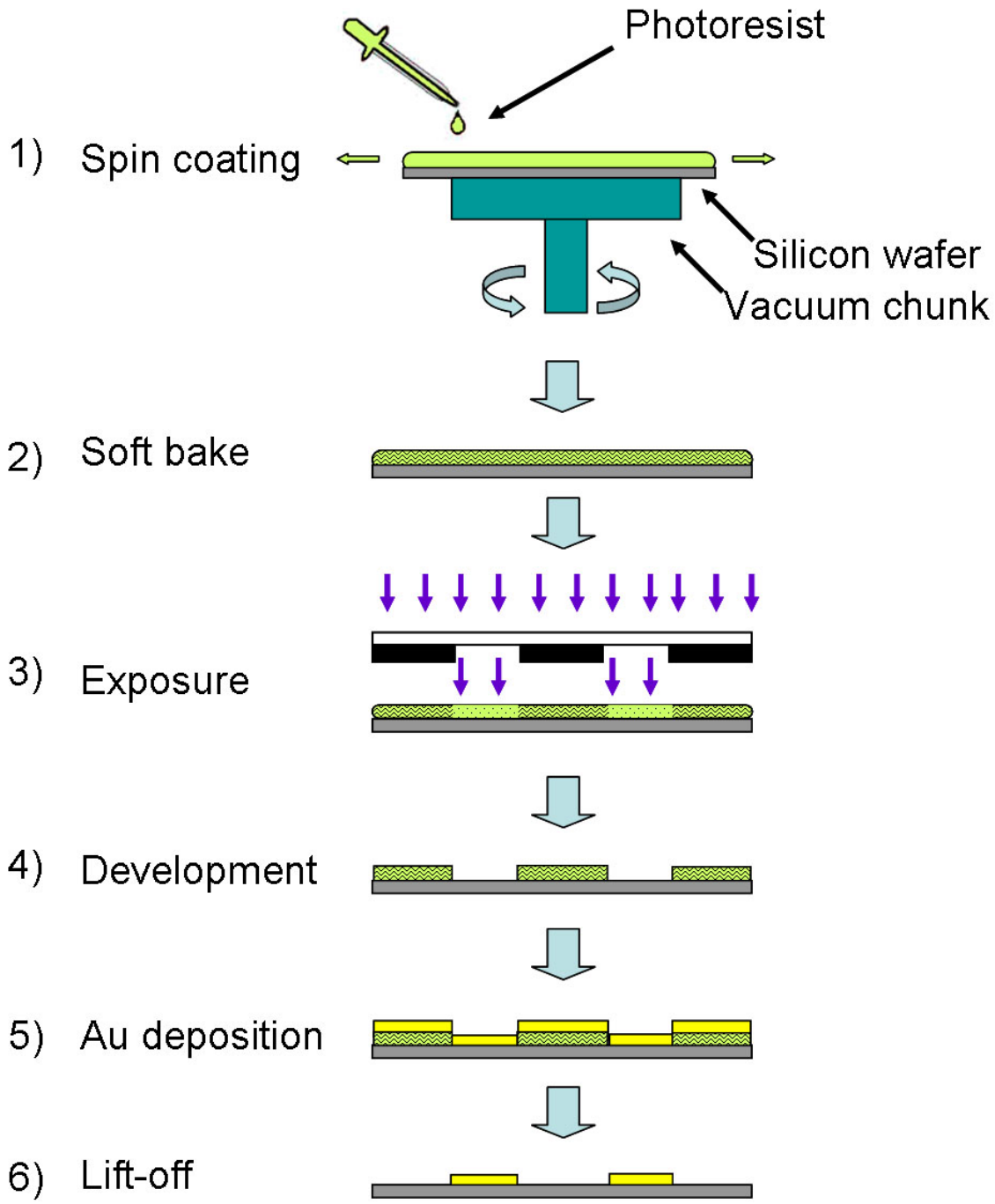

Figure 4.9 Schematic procedure for making electrodes with photolithography technique.

1. A clean wafer is held on a spinner chuck by vacuum and photoresist is coated to uniform thickness by spin coating. The resist thickness is given by $t = \frac{kp^2}{\sqrt{w}}$, where k is

spinner constant, typically 80-100, p is resist solid content in percent, and w is spinner rotational speed in rpm/1000.

2. The wafer with photoresist is baked with a hot plate. This step will evaporate the coating solvent and densify the resist after spin coating.

3. The wafer is aligned with the mask and exposed to UV light for a specific time, which is determined by the type and thickness of photoresist. Exposure to UV light alters the chemistry of the photoresist and changes its solubility relative to unexposed resist. There are two types of resist, “positive” and “negative”. When a positive resist is exposed to UV light, the energetic photons of the light break certain bonds in the long-chain polymers of the resist, causing them to become shorter and thus more soluble. A developer easily washes away the exposed areas, leaving behind a copy of the pattern on the mask. When a negative resist is exposed to UV light it causes cross-linking between the resist polymers making the exposed areas less soluble. The developer removes the exposed resist, leaving behind a negative image of the mask. We use a positive resist in the schematic fabrication process in Figure 4.9.

4. As mentioned in step 3, the silicon wafer was placed in developer to remove exposed resist. Some parts of the Al film are exposed while other regions are protected under a layer of photoresist.

5. Au film is deposited onto the silicon wafer.

6. The silicon wafer is then put into acetone to remove the photoresist, the unwanted Au layer on the resist, and any other residues.

After stripping all unwanted Au film in step 6, the patterned Au layer appears on the silicon wafer. Generally one silicon wafer contains hundreds of the same pattern. We then cut the wafer to small pieces, such that we have one electrodes pattern on each piece for device fabrication.

4.3.2.2 Nanostructure Manipulation

One-dimensional (1D) nanostructures, such as nanowires, nanotubes, nanobelts, and molecular wires are currently being investigated in great detail for their unique electronic and mechanical properties and their potential implementation as devices. Integration of the nanotubes and nanowires into useful devices requires placing them in specific positions with desired configurations. To meet these requirements, well-controllable and reproducible nanoscale assembly techniques are necessary. Many research groups have developed numerous techniques to manipulate nanostructure and fabricate different devices. Dielectrophoresis (DEP) is attractive for inexpensive and massive parallel manipulations of neutral microscale and nanoscale objects using only standard semiconductor fabrication technologies. It has been utilized to align a variety of structures from suspensions, such as NiSi[275], ZnO[276], and carbon nanotubes[277],

If a particle is placed in an inhomogeneous electric field, it will, in general, experience a translational force:

$$\vec{F}_{elec} = q\vec{E} + (\vec{m}\cdot\nabla)\vec{E} + \frac{1}{6}\nabla(\bar{Q}:\nabla\vec{E}) + \cdots$$

Where q is the net charge of the particle, $\vec{E}$ the electric field, $\vec{m}$ is the dipole moment induced by the applied field, and $\bar{Q}$ is the quadrapole tensor induced by the applied field. The first term, $q\vec{E}$, is the well-know coulombic force due to the net charge of the particle and the electric field. This reprent all aspects of electrophoresis and vanishes in an alternating field or the absence of a net charge on the particle. The rest terms to the right of the electrophoretic force arise from the interaction of dielectric polarization in the particle induced by the electric field with spatial inhomogeneities in that field. The polarization forces vanish only if the electric field is spatially homogeneous or if the particle has dielectric properties that are identical to its surroundings. The two DEP forces components, electrophoresis force and polarization force, act independently and can be exploited along or combination. Accordingly, applying appropriate electrical

signals to electrode arrays can create the required electric condition for different applications.

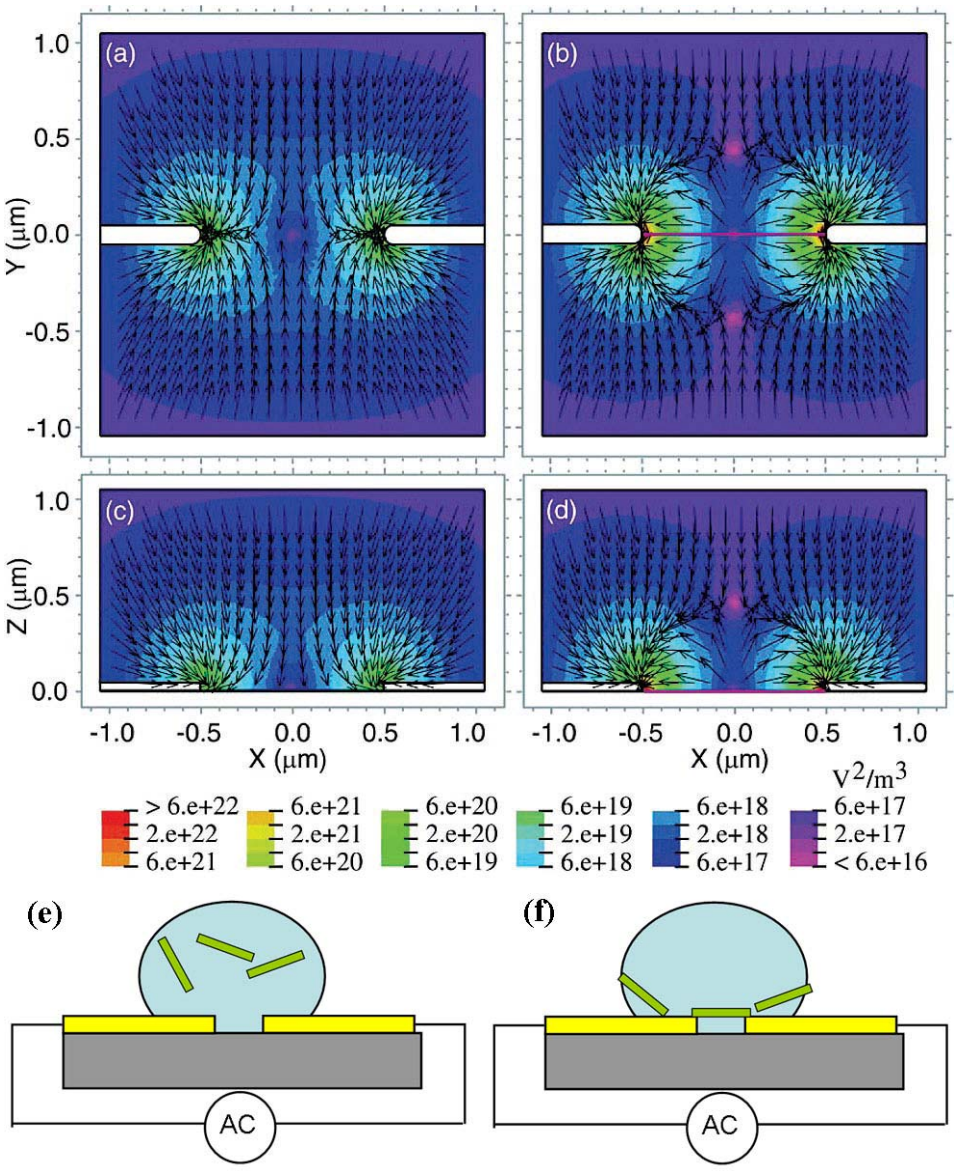

Figure 4.10 Simulation of dielectrophoretic force fields in a volume around the electrodes for two orthogonal cross sections and schematic diagram for the nanowire alignment with dielectrophoresis. (a, b) ∇E^2 at the surface of the substrate (X-Y plane at Z) 0). (c, d) ∇E^2 perpendicular to the substrate (X-Z plane at Y). The arrows indicate the direction of the force and the background color is the magnitude of ∇E^2. (e) Electrodes are emerged in nanowire-dispersed solution. (f) Nanowire is attracted to and trapped between two electrodes.

Figure 4.10 presents the simulated DEP force field in the vicinity of the electrodes[278] and the schematic diagram showing the nanowire alignment under the influence DEP force. As can be seen from Figure 4.10 a-d, the nanowires attractive forces toward the gap at all points, directing a nanowire to deposit between the electrodes. As a result, a nanowire might bridge the two electrodes for device fabrication and property measurement.

4.3.2.3 Top electrodes Deposition

In order to achieve good enough contact between the electrodes and the nanobelts, we chose to deposit another layer of metal layer on top of the nanowire, such that the nanowire was sandwiched in between two electrodes. This step was done with focused ion beam lithography (FIBL), which is a technology called “direct writing” for nanofabrication. FIBL can transfers patterns by direct impingement of a small spot of the FIB onto a substrate without mask. Direct writing is comprised of several major approaches, including milling, implantation, ion-induced deposition, and ion-assisted etching, which respectively perform material removal from, property change on, material addition on, and material removal from the substrates with or without chemical assistance. The FIBL could be controlled in a variety of parameters, such as the beam size, current density, and energy density to remove or add a required amount of material with or without chemical reactions from a predefined location. In this way, high-precision and complex two-dimensional (2D) or even three-dimensional (3D) nanostructures can be created. The basic device structure is shown in Figure 4.11.

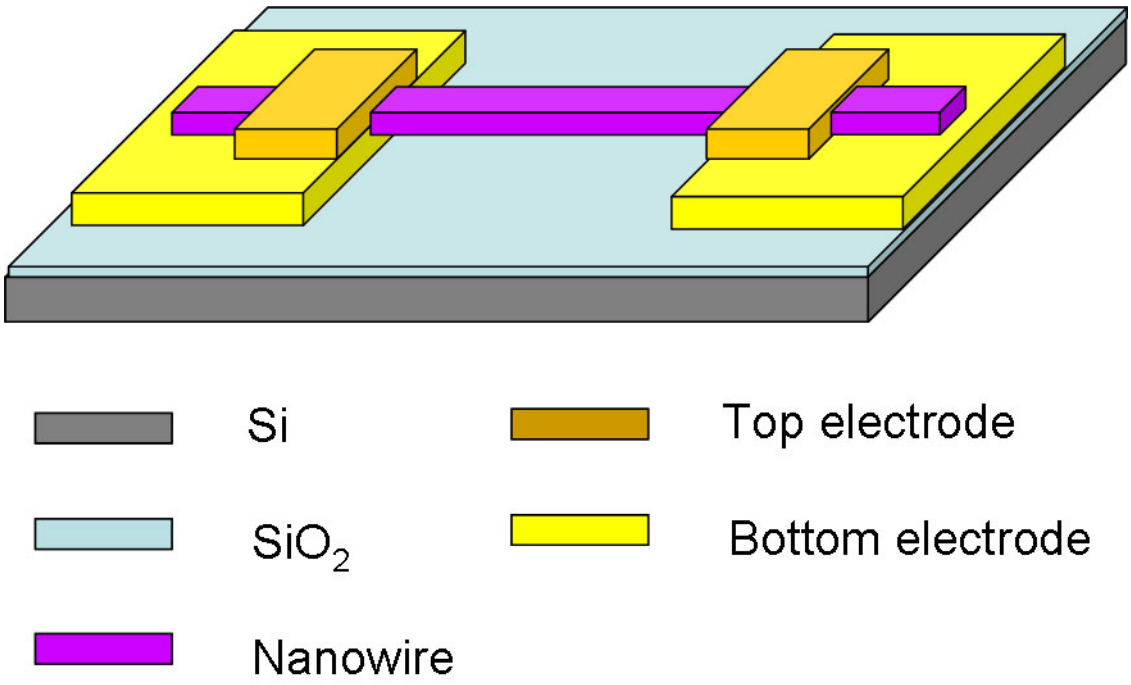

Figure 4.11 A simplified schematic diagram of the device structure.

4.3.2.4 Photoconductivity Measurement

The experiment setup for photoconductivity measurement consists of two components, the light source in the top part in Figure 4.12, and the electrical measurement in the bottom part.

We used LED as light source, green (532 nm, <5 mW), red (680 nm, <5mW), and white lamp (continuous wavelength). Measurement in the dark verified the Ohmic contact between the nanowire and the electrode and revealed the intrinsic property of the tested device. Utilization of different light source revealed the response of tested device to different wavelength.

Electrical characterization was carried out through a volt-amperometric technique at certain bias with current change measured by picoamperometer. Two-probe electrical measurement method was used for measuring the current-voltage characteristics in terms of different light illumination condition.

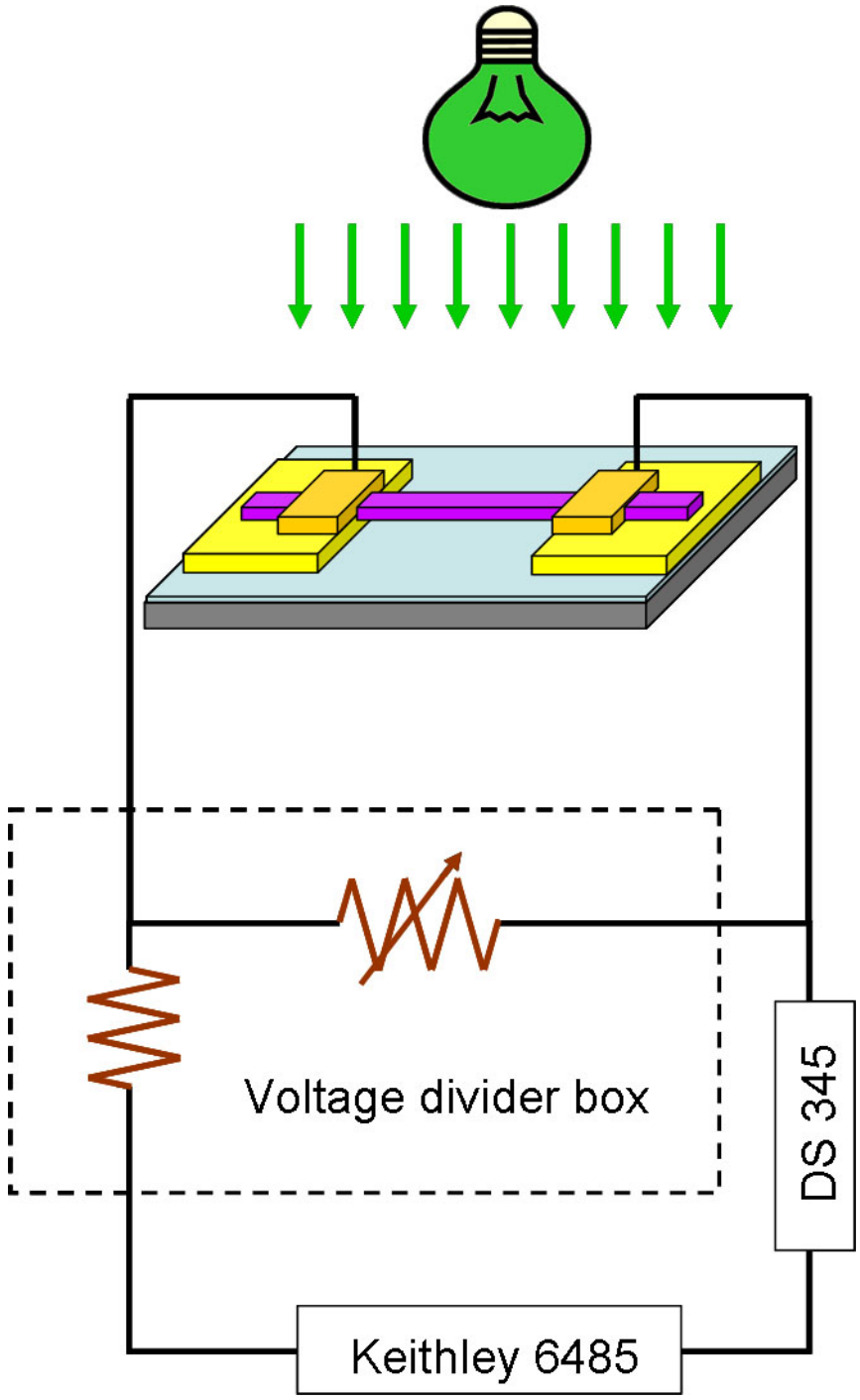

Figure 4.12 A schematic diagram of the photoconductivity measurement setup.

During the measurement, an alternating bias voltage with certain frequency (typically 0.001Hz -30MHz in triangle waveform or sine waveform) was applied across the two Au/Pt terminals. The voltage range was 0-5Vp-p. A SRS DS345 synthesized

functional generator is used as the voltage source. The picoammeter we used is the Keithley 6485 5-1/2 digit Picoammeter with 10 fA resolution. A voltage divider box is used for providing the protection and voltage bias for the device under test. LabView 7.0 software is used for a computer to acquire digital data via PCI data acquisition board with separate ports respectively connected with the analogue outputs of current and voltage.

4.3.3 Photoconductivity of Zn_3P_2 Nanowire

Single Zn_3P_2 nanostructures were prepared for the investigation of photoconductivity under the illumination of different wavelengths of light or a white LED lamp, as shown in Figure 4.13a. To characterize the I-V characteristics of single NW, we placed a Zn_3P_2 NW between two Au electrodes via a dielectrophoresis (DEP) technique (Figure 3.10) and deposited Pt by focused ion beam (FIB) microscopy as the top electrode to improve the contact (Figure 3.11). An ohmic contact can be obtained between Au and Zn_3P_2.[279] In addition, Pt/Zn_3P_2 also forms an Ohmic contact because Pt has a greater work function (5.7 eV) than p-type Zn_3P_2 (5.06eV) despite the possible presence of Ga dopants during the Pt deposition process. The ohmic contact was also proved by the linear behavior in later I-V measurement of the device. The representative nanodevice is schematically illustrated in upper inset of Figure 4.13a and the corresponding SEM image of the nanodevice is inset in Figure 4.13a. A LabView program was used to control the two-terminal I-V testing process. The linear I-V characteristic without illumination of light (blue line) confirms the ohmic contact between the electrodes and Zn_3P_2 NW and a resistance about 3.63×10^9 Ω is derived. The resistivity of Zn_3P_2 NW was calculated about 5.6×10^2 Ω-cm with the length and the diameter as 35 μm and 232 nm, respectively, based on the SEM characterization. The dark resistance here is higher than that of its thin film counterpart ($2\text{-}3\times 10^2$) [280] possibly due to the contact resistance.

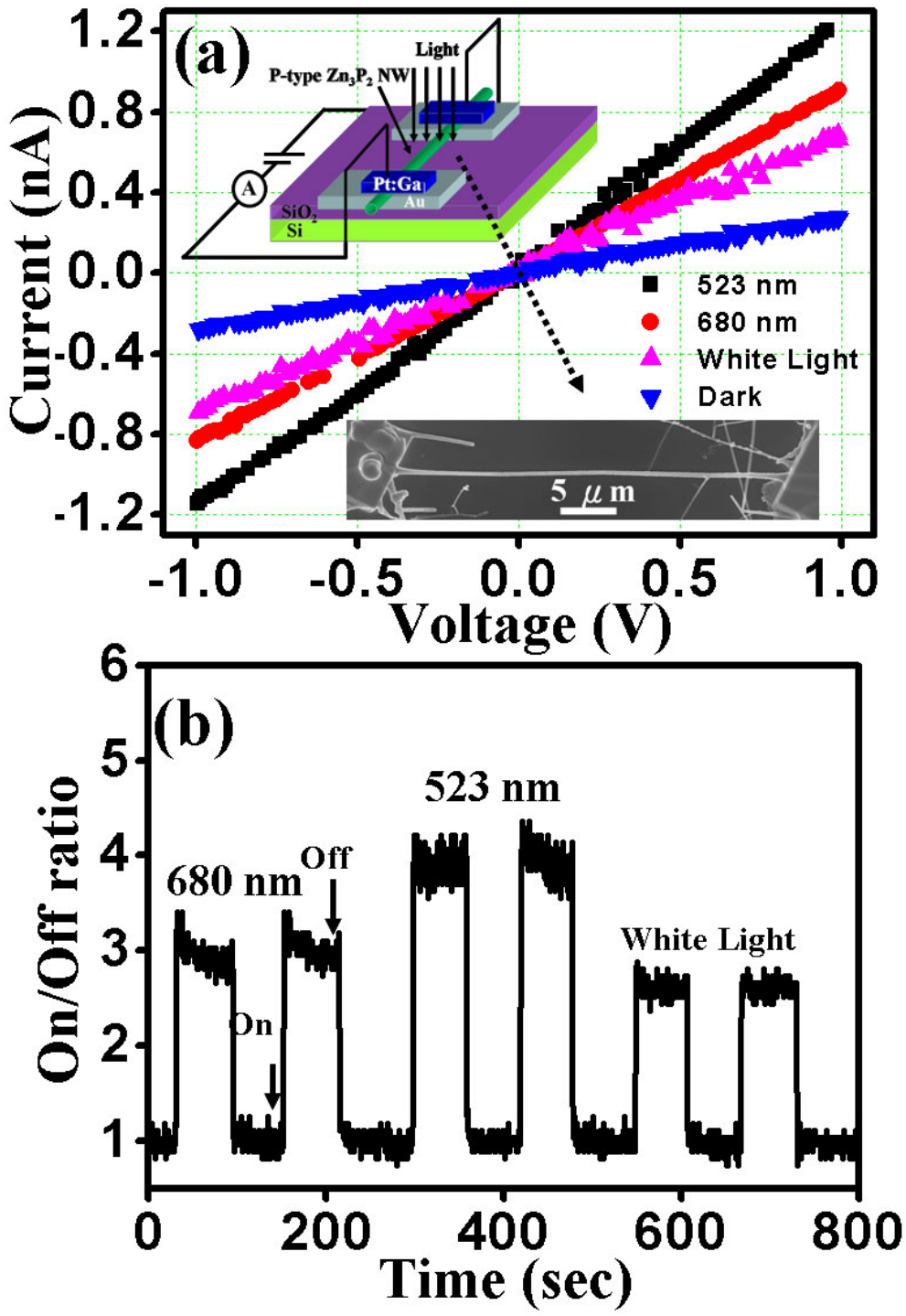

Figure 4.13 (a) I-V curve for single Zn_3P_2 NW in dark or under the illumination of different wavelength light. Upper inset shows the device configuration under the illumination of light. Bottom inset shows the corresponding SEM image of the Zn3P2 NW based nanodevice. (b) On/off ratio as a function of the time under red (680nm), green (523 nm), or white light illumination, respectively.

On the other hand, under the illumination of light at a wavelength of 532 nm (green color with power <5 mW), 680 nm (red color with power <5 mW), or continuous wavelength from a white LED lamp, the resistance decreased significantly due to excess electron-hole pairs (EHPs) excited by the illuminating light, which has an energy larger than the bandgap of Zn_3P_2. In addition, the desorption of the contaminants from the surface due to the illumination increased the conductivity as well. It is reasonable to expect that the shorter wavelength results in higher photoconductivity because the light with higher energy can create more electron-hole pairs inside the NW. In addition, the excess energy (hv-Eg) created phonons in the lattice and raised the temperature, resulting in larger electron and hole mobility and contributing a higher conductivity. The on/off ratio, which is defined as the current under the illumination over the dark current, is presented in Figure 4.13(b) as a function of the illuminated time, indicating high sensitivity of Zn_3P_2 NW to the illumination of different wavelength of light. The response time for all of the light is considerably less than 1 sec with the on/off ratio being about 3 for red light (680 nm), 4-5 for green light (532 nm), and 2-3 for white light from a LED lamp.

4.3.4 ZnO/Zn_3P_2 Nanoscale Photodiode

Having shorter response time and higher on/off ratio than that of single NW [281], the p-n photodiode is an alternative form of photoconductor and can be constructed with crossed nanowires[282, 283]. By combining with wide bandgap materials, such as ZnO, SnO_2, and ZnS, the whole range of light from ultraviolet to the near infrared can be effectively absorbed by this kind of photodiode, which is beneficial for terrestrial application of solar cell. This section focuses on the performance of a prototype nanoscale photodiode based on the crossed structure of a p-type Zn_3P_2 NW with an n-type ZnO NW. In order to form the required nano heterojunction, we aligned a Zn_3P_2 NW between two Au electrodes via the DEP technique (Figure 4.10) and fixed it with Pt metal

via a FIB (Figure 4.11), which can improve the contact. After that, a ZnO NW was aligned perpendicular to Zn_3P_2 NW by DEP technique and connected to another pair of Au electrodes via Pt deposition by FIB microscopy. The final structure and schematic diagram are illustrated in Figure 4.14 and insets of Figure 4.17(a).

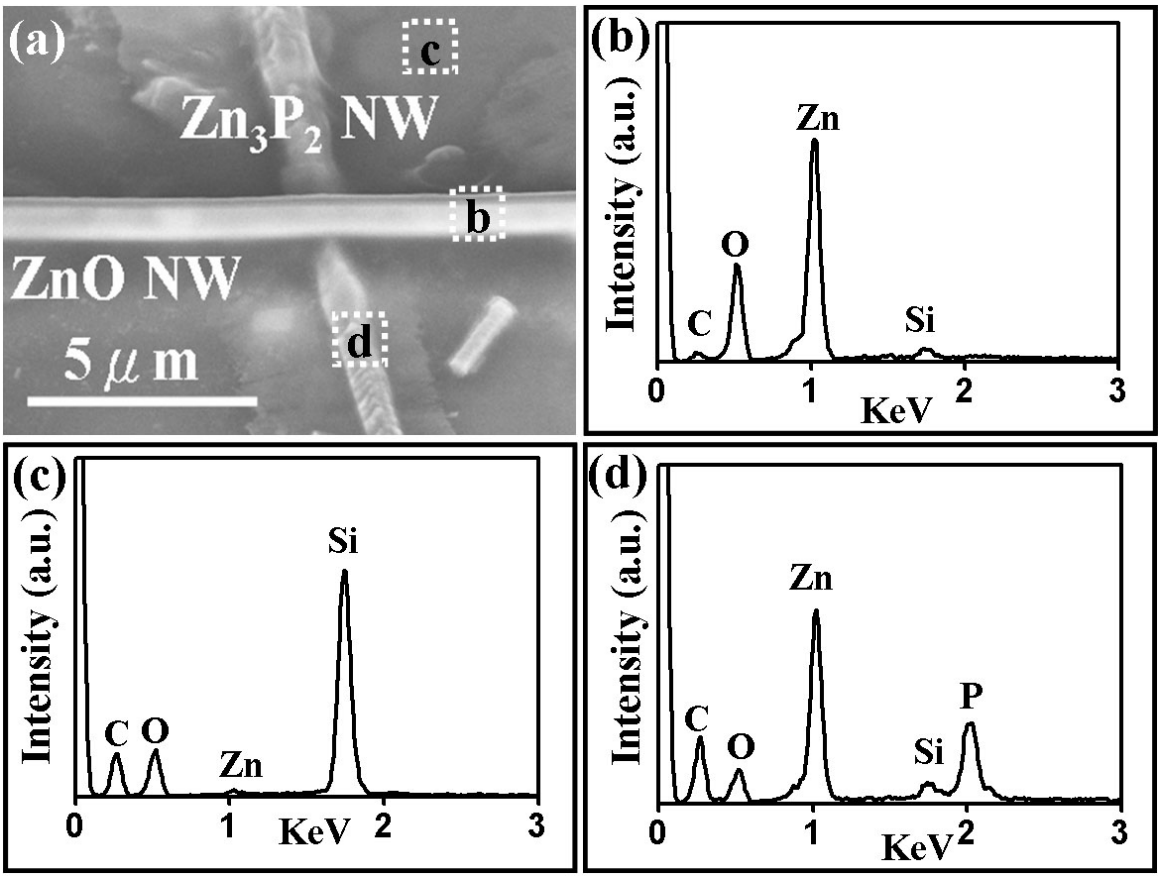

Figure 4.14 EDS analysis showing the crossed-nanowire structure.

We did microanalysis with energy dispersive x-ray spectroscopy during SEM examination, Figure 4.14. Figure 4.14a clearly indicates that the two nanowires crossed each other. All EDS contains C, O, Si peaks. O and Si mainly come from the underneath substrate and C should comes from contamination during the alignment with DEP. EDS from the top nanowire shows only Zn and O peaks, indicating the top nanowire is ZnO nanowire. In comparison, EDS from the bottom nanowire shows Zn and P signal, indicating the bottom one is Zn_3P_2 nanowire.

In order to investigate the intrinsic property of this photodiode with crossed nanowires, we first performed current-voltage characteristic measurement while the device is dark. The I-V measurement across two ends Zn_3P_2 nanowire shows linear behavior, indicating that the contact between Zn_3P_2 nanowire and the electrodes is Ohmic contact (Figure 4.15a). The Ohmic contact between ZnO and electrodes is also proved with linear behavior of I-V measurement across two ends of ZnO nanowires (Figure 4.15b).

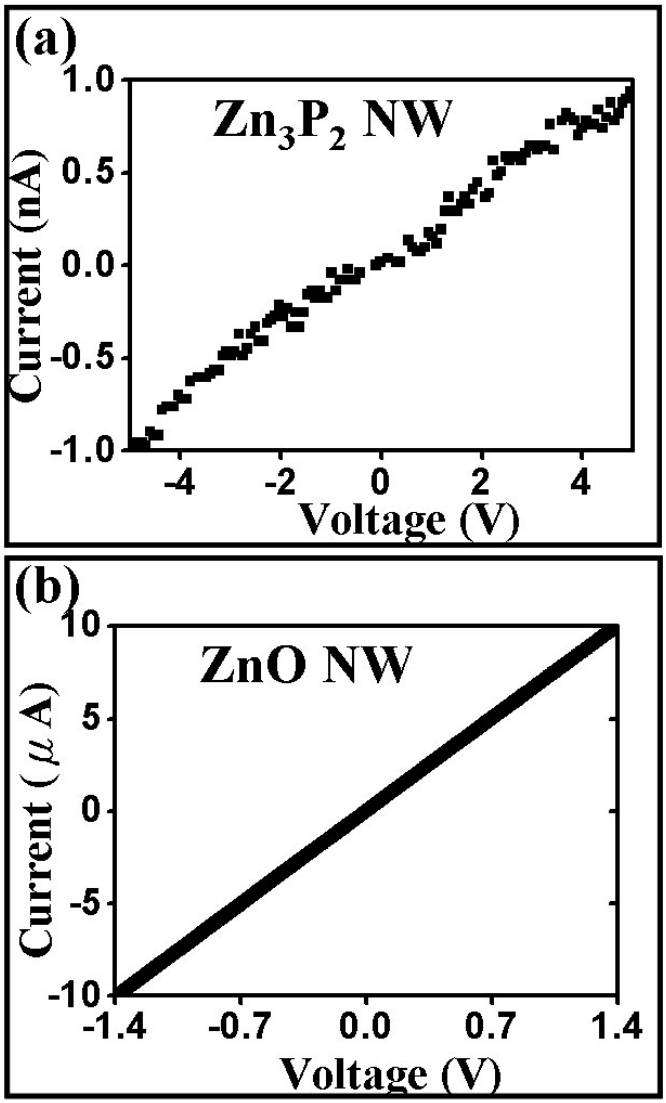

Figure 4.15 Linear I-V characteristic of Zn_3P_2 nanowire and ZnO nanowire indicating Ohmic contact between nanowire and electrodes.

In order to further understand the detailed issue of this nano heterojunction, an ideal energy diagram of this heterojunction is constructed in Figure 4.16a on the basis of the experimental data. According to the bandgap E_g (3.3 eV for ZnO and 1.5 eV for Zn_3P_2) and electron affinity X (4.35 eV for ZnO and 3.8 eV for Zn_3P_2), the ZnO/Zn_3P_2 heterojunction exhibits a type II (staggered) alignment. The energy barrier for electrons, ΔE_c, is found about 0.55 eV via $\Delta E_c = X_{ZnO} - X_{Zn3P2}$. Meanwhile, the energy barrier for holes, ΔE_V, is found 2.35 eV via $\Delta E_V = E_{g,ZnO} + \Delta E_c - E_{g,Zn3P2}$. Accordingly, ΔE_c is smaller than ΔE_v, causing electron injection from n-type ZnO to p-type Zn_3P_2 to be more favorable than hole injection from p-type Zn_3P_2 to n-type ZnO. The resultant neutral p-region, neutral n-region, and the depletion region in the absence of applied bias are shown in Figure 4.16b with the length of the depletion region and built-in voltage defined as W_{bi} and V_{bi}, respectively. In addition, it is well known that the carrier concentration of ZnO NW is found in the range of ~10^{17}-10^{18} cm^{-3} [284], which is consistent with the bulk counterpart. In contrast, the carrier concentration of Zn_3P_2 NW has not been reported in the literature. If we make the hypothesis that the carrier concentration of Zn_3P_2 NW is the same order as that for thin films and on the order of ~10^{15} cm^{-3}, the ZnO/Zn_3P_2 nano heterojunction can be considered as an abrupt N^+P junction, in which the depletion region is almost located at the Zn_3P_2 side, which have been calculated for the thin film case.[263]

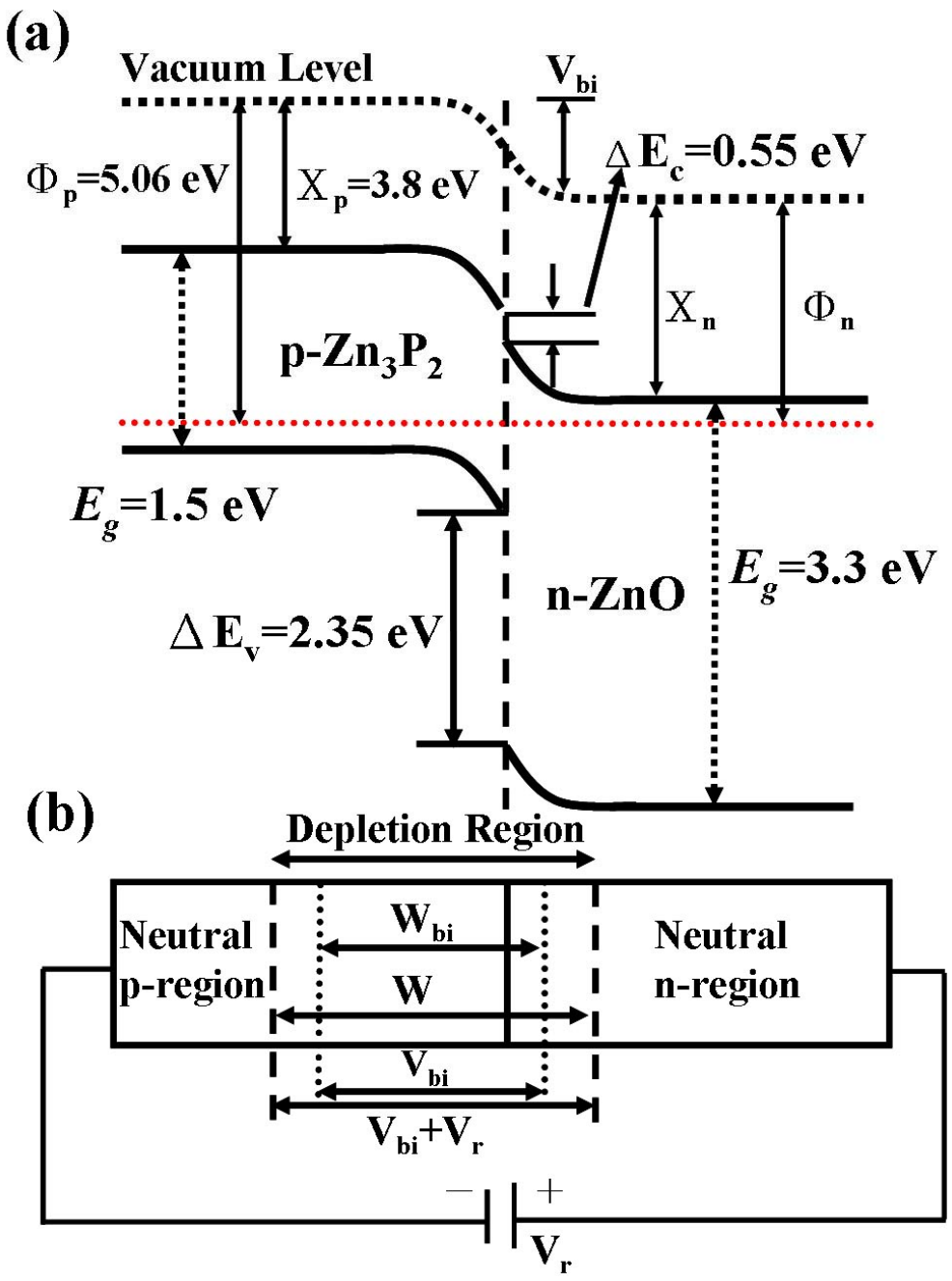

Figure 4.16 (a) The ideal energy diagram for ZnO/Zn_3P_2 heterojunction. (b) The individual position and length for neutral n- and p-regions as well as the depletion region without applied bias and under reverse bias, respectively.

The N^+P junction characteristic is revealed by the rectification behavior of the I-V measurement in Figure 4.17a. At high forward bias, some of the minority carriers can diffuse and recombine in the depletion region, resulting in the recombination current.

Considering the contribution of diffusion and recombination currents under forward bias, a simple I-V behavior can be empirically given by:[285, 286]

$$J \approx J_0 \exp\left(\frac{eV}{nkT}\right)$$

where J_0 is the saturated current, n is an ideality factor, k is Boltzmann's constant, and T is the absolute temperature, respectively. When the I-V curve is dominated by an ideal diffusion current, n = 1; whereas when the I-V curve is dominated by a recombination current, n = 2. Otherwise, when n has a value between 1 and 2, both mechanisms are at play. However, the ideality factor n > 2 found in the present study may be explained by fitting the plot of $\ln(J/J_0)$ as a function of forward bias, which likely results from the high contact resistance at both the interfaces of (Pt, Au)/ZnO NW and (Au, Pt)/Zn_3P_2 NW and is consistent with previous reports[286].

In order to distinctly display the I-V behavior of the photodiode under the illumination of different wavelength lights, we reversed the polarity of the input voltage compared with the one in Figure 4.17a. The I-V curves for the photodiode under reverse bias and in the dark and under the illumination of light with wavelength of 532 or 680 nm are presented in Figure 4.17b, showing apparent current enhancement by the light. The increase of the current results from the generation of electron-hole pairs inside the depletion region and nearby under the excitation of the light and can be given by:

$I_{ph} = I_n + I_p = q\Delta n \upsilon_n + q\Delta p \upsilon_p$

where I_{ph} is the total photocurrent density, I_n and I_p are the photocurrent caused by electrons and holes. q, Δn, Δp, υ_n, and υ_p represent electronic charge, the concentration of generated electrons and holes, average drift velocities of electrons and holes within the specific depletion field, respectively.

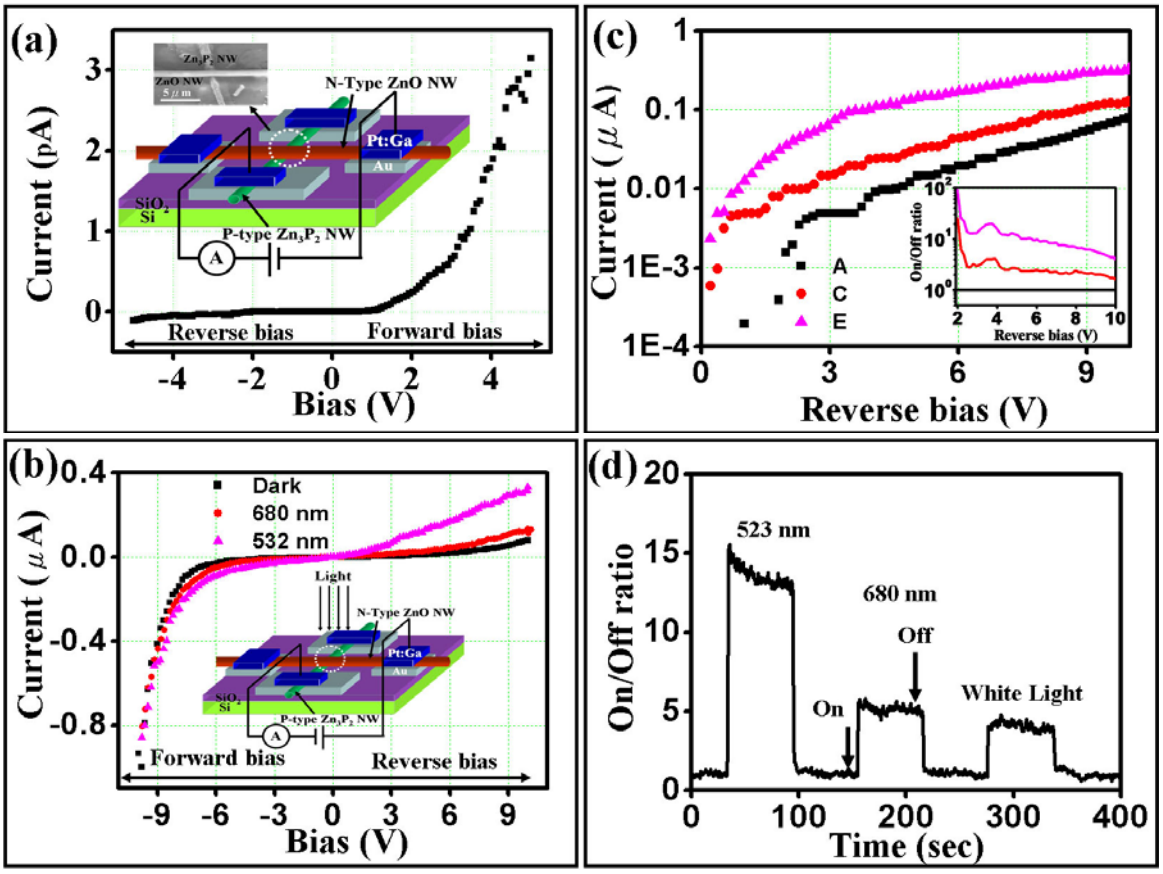

Figure 4.17 (a) I-V curve for ZnO/Zn_3P_2 nanoscale heterojunction at reverse and forward bias. Inset shows the prototype of the nanodevice, in which a ZnO NW was placed on top of a Zn_3P_2 NW. (b) I-V curve of ZnO/Zn_3P_2 heterojunction under illumination of different wavelengths as displayed in logarithmic scale under reverse bias. (c) The on/off ratio as a function of the time under red (680nm), green (523 nm), or white light illumination, respectively. The inset is the schematic of the device.

The concentration of the generated electron-hole pairs and the resultant current as well increase with the increase of the energy and intensity of incoming light, which explains why red light causes less current enhancement than green light while the dim white light produces the least enhancement. In addition, the lights have greater effect on reverse biased photodiode than forward biased photodiode, which is consistent with the fact that the photoexcited electron-hole pairs can significantly influence the concentration of minority carriers, which dominate the current through a reverse biased diode. The influence of the lights on the reverse biased photodiode is illustrated explicitly in Figure

4.17b with logarithmic scale and with the on/off ratio plot shown inset. Interestingly, all of the current from the illumination of light shows a similar trend: significantly greater than dark current under low reverse bias and more and more comparable to dark current under higher reverse bias.

In general, the reverse current is composed of the diffusion current in neutral regions and the generation current in the depletion regions. The reverse current, or reverse saturation current, comes from minority carriers in the neutral region, which diffuse towards and subsequent drift through the depletion region. On the other hand, the generation current comes from electron-hole pairs which are generated in the depletion region and drift towards neutral regions under the internal field. Thermal generated minority carriers and electron-hole pairs contribute to the dark current. In contrast, the impinging photon can generate substantial electron-hole pairs in both the depletion region and neutral region on the Zn_3P_2 side and considerably enhance the reverse current. At low reverse bias, photon generated carriers are overwhelming over thermal generated carriers and result in a surprisingly high on/off ratio ($\sim 10^2$) in the inset of Figure 8(b). However, thermal generated electron-hole pairs increase with increased bias and contribute more and more to the reverse current, as can also been seen in the dark current curve in Figure 8(a). Accordingly, the on/off ratio should decrease with increased reverse bias, which confidently agrees with our result in the inset of Figure 4.17b. Despite of the decrease at high reverse bias, the on/off ratio can still reach 9-10, which is superior to other single NW as photoconductors[287-290].

Additionally, the photon response of the photodiode to different lights is shown in Figure 4.17c in which we applied a fixed reverse bias of 5 V and turned on and off green light (523 nm), red light (680 nm), and the white light lamp serially. Green light produces the highest (~13) on/off ratio as expected. Interestingly, the dim white light also produces an on/off ratio (~5) which is significantly greater than one, indicating the high sensitivity of the photodiode to visible lights. Furthermore, the response time for all tested lights is

below one second. The very nice performance of the diode may result from the following advantages. First of all, the top ZnO NW has a wide band gap and the light from infrared to violet can penetrate easily with minimum energy loss [291, 292]. Second, the depletion region is mostly located at Zn_3P_2 NW side so that electron-hole pairs can be generated by a wide light range from 380-800 nm, and significant generation current enhancement is observed. Finally, the large minority diffusion length of Zn_3P_2 enables more photon generated minority carriers in the neutral region to diffuse into the depletion region and results in a large on/off ratio and high sensitivity as well. The high sensitivity, quick response and nanoscale size can benefit the ZnO/Zn_3P_2 nanoscale heterojunction as a candidate for a high efficient and spatial resolved photon detector.[278]

4.4 Summary

In summary, tree-shaped Zn_3P_2 nanostructures, nanobelts, and nanowire were synthesized in a thermally assisted laser ablation process, and a possible growth process of those nanostructures was also proposed. The photoluminescence spectrum of Zn_3P_2 nanostructures shows a broad emission centered at 770 nm with a slight blue shift with regard to that of the bulk Zn_3P_2. A strong absorption from ultraviolet to near infrared is apparent from the reflectivity measurement of those nanostructures. Taking advantage of the direct band gap of 1.5 eV, high absorption coefficient, large minority diffusion length, and high crystallinity free from oxidization, those nanostructures have potential applications in solar cells, broad range photodetectors, lasers, etc. Preliminary investigation on their application has been performed on the optoelectric measurement of a single Zn_3P_2 nanowire and a nanoscale photodiode.

The conductance of a single Zn_3P_2 nanowire shows high sensitivity to green light (523 nm), red light (680 nm) and white light and is very suitable as a photoconductor. Furthermore, we also constructed a nanoscale photodiode with crossed ZnO/Zn_3P_2 nanowires. The linear behavior of individual nanowires and the rectification behavior

between ZnO and Zn_3P_2 revealed the formation of p-n heterojunction. Despite the absence of an anti reflection coating or any other optimization, the photon diode gives rapid response and very high on/off ratio upon the illumination of light. Considering their small size, we expect Zn_3P_2 nanostructures and corresponding heterojunctions will play an important role in nano-optoelectronics.

CHAPTER 5

CONCLUSION

This thesis work comprehensively and systematically studied semiconducting materials, ZnO, SnO_2, and Zn_3P_2, and their related structures at the nano/micro scale. It encompasses the synthesis, characterization, and device fabrication, and the following goals have been achieved: 1) Improved understanding of polar-surface-induced growth mechanism in wurtzite-structured ZnO, and generalization of this growth mechanism with the discovery and analysis of rutile –structured SnO_2, 2) observation of the significance of the transversal growth, which is usually ignored, in interpenetrative ZnO nanowires, 3) rational design and growth control over versatile nanostructures of ZnO and Zn_3P_2, and 4) conjunction of *p*-type Zn_3P_2 and *n*-type ZnO semiconducting nanostructures for device fabrications.

Seamless nanorings and deformation free helixes of ZnO have been synthesized with a thermal vapor deposition process. A detailed analysis revealed that the polar surface plays a critical role during the formation these nanostructures. When ZnO nanobelts grow with polar surface as side surface ($\{0001\}$ for nanorings, and $\{1\bar{1}01\}$ for nanohelixes), the electrostatic energy due to spontaneous polarity diverges with the growth. Depending on the growth direction, nanobelt dimension, and other factors, the nanobelt might bend and form a nanoring through a self-coiling process. A spiral or a spring can also result in the absence of self-coiling. The final dimension determined by the competition of the minimization of the electrostatic energy and the increase of elastic energy due to deformation. Alternatively, the nanobelt can also minimize its polarization energy through changing its growth direction without introducing any deformation. In the absence of elastic energy, the electrostatic energy dominates and results in the ultra-small deformation-free ZnO nanohelixes.

The generalization of the growth mechanism is very important for rational control of nanostructures. The discovery and analysis of rings, spirals, and spring of rutile-structured SnO_2 confirmed polar-surface-induced growth mechanism is not limited to specific material or crystal structure. The synthesized SnO_2 nanostructures benefit from studying the effect of polar surfaces on the morphology of the nanostructures and applications of SnO_2 in nanotechnology.

The growth of ZnO nanowires shows their versatile characteristics, and they can interpenetrate at a random angle. A detailed analysis reveals that the significant transverse growth is responsible for such morphology. This is a significant progress in understanding the formation of 1D nanostructures, because the transverse growth has been ignored in many cases.

In addition, highly hierarchical 3-dimensional nanostructures from ZnO and Zn_3P_2 have also been fabricated from rational designed experiment, which will provide more insight into the nanoscience and more candidates for nanotechnology.

The lack of the *n*-type or *p*-type materials hinders the applications of many materials. For example, ZnO is an intrinsic *n*-type semiconductor and good *p*-type doping is notoriously difficult to achieve. In comparison, Zn_3P_2 is intrinsically *p*-type and *n*-type doping is very difficult to get. A new strategy has been successfully probed and developed for fabrications of a versatile group of nanostructure building blocks for nanoelectronics and optoelectronics.

Electrode patterns were fabricated with microfabrication techniques and the intrinsic *n*-type ZnO nanowires and intrinsic *p*-type Zn_3P_2 nanowires were synthesized separately. Through a dielectrophoresis (DEP) technique those nanowires could be manipulated and aligned between the electrodes one after the other. The resulting crossed nanowire structure formed nanoscale heterojunction at the interface and has been successfully demonstrated for nano-optoelectronic applications.

REFERENCES

1. Murr, L.E., et al., Carbon nanotubes and other fullerene-related nanocrystals in the environment: A TEM study. Jom, 2004. **56**(6): p. 28-31.

2. Murr, L.E., et al., Carbon nanotubes, nanocrystal forms, and complex nanoparticle aggregates in common fuel-gas combustion sources and the ambient air. Journal of Nanoparticle Research, 2004. **6**(2-3): p. 241-251.

3. Hughes, T.V. and C. C.R., U. Patent, Editor. 1889.

4. Monthioux, M. and V.L. Kuznetsov, Who should be given the credit for the discovery of carbon nanotubes? Carbon, 2006. **44**(9): p. 1621-1623.

5. L.V., R. and L. V.M., O Strukture ugleroda, obrazujucegosja pri termiceskom razlozenii okisi ugleroda na zeleznom kontakte. Zurn Fisic Chim, 1952. **26**: p. 88-95.

6. Oberlin, A., M. Endo, and T. Koyama, Filamentous Growth of Carbon through Benzene Decomposition. Journal of Crystal Growth, 1976. **32**(3): p. 335-349.

7. Iijima, S., Helical Microtubules of Graphitic Carbon. Nature, 1991. **354**(6348): p. 56-58.

8. Bethune, D.S., et al., Cobalt-Catalyzed Growth of Carbon Nanotubes with Single-Atomic-Layerwalls. Nature, 1993. **363**(6430): p. 605-607.

9. Iijima, S. and T. Ichihashi, Single-Shell Carbon Nanotubes of 1-Nm Diameter. Nature, 1993. **363**(6430): p. 603-605.

10. Hamada, N., S. Sawada, and A. Oshiyama, New One-Dimensional Conductors - Graphitic Microtubules. Physical Review Letters, 1992. **68**(10): p. 1579-1581.

11. Krupke, R., et al., Separation of metallic from semiconducting single-walled carbon nanotubes. Science, 2003. **301**(5631): p. 344-347.

12. Arnold, M.S., et al., Sorting carbon nanotubes by electronic structure using density differentiation. Nature Nanotechnology, 2006. **1**(1): p. 60-65.

13. Chopra, N.G., et al., Boron-Nitride Nanotubes. Science, 1995. **269**(5226): p. 966-967.

14. Wengsieh, Z., et al., Synthesis of Bxcynz Nanotubules. Physical Review B, 1995. **51**(16): p. 11229-11232.

15. Tenne, R., et al., Polyhedral and Cylindrical Structures of Tungsten Disulfide. Nature, 1992. **360**(6403): p. 444-446.

16. Remskar, M., et al., Self-assembly of subnanometer-diameter single-wall MoS2 nanotubes. Science, 2001. **292**(5516): p. 479-481.

17. Ajayan, P.M., et al., Carbon Nanotubes as Removable Templates for Metal-Oxide Nanocomposites and Nanostructures. Nature, 1995. **375**(6532): p. 564-567.

18. Goldberger, J., et al., Single-crystal gallium nitride nanotubes. Nature, 2003. **422**(6932): p. 599-602.

19. Yu, D.P., et al., Nanoscale silicon wires synthesized using simple physical evaporation. Applied Physics Letters, 1998. **72**(26): p. 3458-3460.

20. Morales, A.M. and C.M. Lieber, A laser ablation method for the synthesis of crystalline semiconductor nanowires. Science, 1998. **279**(5348): p. 208-211.

21. Otten, C.J., et al., Crystalline boron nanowires. Journal of the American Chemical Society, 2002. **124**(17): p. 4564-4565.

22. Busbee, B.D., S.O. Obare, and C.J. Murphy, An improved synthesis of high-aspect-ratio gold nanorods. Advanced Materials, 2003. **15**(5): p. 414-+.

23. Yu, D.P., et al., Amorphous silica nanowires: Intensive blue light emitters. Applied Physics Letters, 1998. **73**(21): p. 3076-3078.

24. Gundiah, G., A. Govindaraj, and C.N.R. Rao, Nanowires, nanobelts and related nanostructures of Ga2O3. Chemical Physics Letters, 2002. **351**(3-4): p. 189-194.

25. Yin, Y.D., G.T. Zhang, and Y.N. Xia, Synthesis and characterization of MgO nanowires through a vapor-phase precursor method. Advanced Functional Materials, 2002. **12**(4): p. 293-298.

26. Zhang, Y.X., et al., Hydrothermal synthesis and photoluminescence of TiO2 nanowires. Chemical Physics Letters, 2002. **365**(3-4): p. 300-304.

27. Duan, X.F. and C.M. Lieber, Laser-assisted catalytic growth of single crystal GaN nanowires. Journal of the American Chemical Society, 2000. **122**(1): p. 188-189.

28. Zhou, S.M., Y.S. Feng, and L.D. Zhang, A physical evaporation synthetic route to large-scale GaN nanowires and their dielectric properties. Chemical Physics Letters, 2003. **369**(5-6): p. 610-614.

29. Liu, J., et al., Novel synthesis of AlN nanowires with controlled diameters. Journal of Materials Research, 2001. **16**(11): p. 3133-3138.

30. Sardar, K., et al., InN nanocrystats, nanowires, and nanotubes. Small, 2005. **1**(1): p. 91-94.

31. Zhang, H., et al., Single-crystal line CeB6 nanowires. Journal of the American Chemical Society, 2005. **127**(22): p. 8002-8003.

32. Zhang, H., et al., Single-crystalline LaB6 nanowires. Journal of the American Chemical Society, 2005. **127**(9): p. 2862-2863.

33. Dai, H.J., et al., Synthesis and Characterization of Carbide Nanorods. Nature, 1995. **375**(6534): p. 769-772.

34. Xu, D.S., et al., Preparation of CdS single-crystal nanowires by electrochemically induced deposition. Advanced Materials, 2000. **12**(7): p. 520-+.

35. Pena, D.J., et al., Template growth of photoconductive metal-CdSe-metal nanowires. Journal of Physical Chemistry B, 2002. **106**(30): p. 7458-7462.

36. Yang, Q., et al., PVA-assisted synthesis,and characterization of CdSe and CdTe nanowires. Journal of Physical Chemistry B, 2002. **106**(36): p. 9227-9230.

37. Urban, J.J., et al., Synthesis of single-crystalline perovskite nanorods composed of barium titanate and strontium titanate. Journal of the American Chemical Society, 2002. **124**(7): p. 1186-1187.

38. Du, G.H., et al., Potassium titanate nanowires: Structure, growth, and optical properties. Physical Review B, 2003. **67**(3): p. -.

39. Wang, N., et al., Si nanowires grown from silicon oxide. Chemical Physics Letters, 1999. **299**(2): p. 237-242.

40. Cui, Y., et al., Diameter-controlled synthesis of single-crystal silicon nanowires. Applied Physics Letters, 2001. **78**(15): p. 2214-2216.

41. Westwater, J., et al., Growth of silicon nanowires via gold/silane vapor-liquid-solid reaction. Journal of Vacuum Science & Technology B, 1997. **15**(3): p. 554-557.

42. Sunkara, M.K., et al., Bulk synthesis of silicon nanowires using a low-temperature vapor-liquid-solid method. Applied Physics Letters, 2001. **79**(10): p. 1546-1548.

43. Zhang, Y.F., et al., Bulk-quantity Si nanowires synthesized by SiO sublimation. Journal of Crystal Growth, 2000. **212**(1-2): p. 115-118.

44. Ma, D.D.D., et al., Small-diameter silicon nanowire surfaces. Science, 2003. **299**(5614): p. 1874-1877.

45. Duan, X.F. and C.M. Lieber, General synthesis of compound semiconductor nanowires. Advanced Materials, 2000. **12**(4): p. 298-302.

46. Duan, X.F., J.F. Wang, and C.M. Lieber, Synthesis and optical properties of gallium arsenide nanowires. Applied Physics Letters, 2000. **76**(9): p. 1116-1118.

47. Gudiksen, M.S. and C.M. Lieber, Diameter-selective synthesis of semiconductor nanowires. Journal of the American Chemical Society, 2000. **122**(36): p. 8801-8802.

48. Gordon, R.G., Criteria for Choosing Transparent Conductors. Materials Research Society Bulletin, 2000. **25**(8): p. 52-57.

49. Lewis, B.G. and D.C. Paine, Applications and Processing of Transparent Conducting Oxides. Materials Research Society Bulletin, 2000. **25**(8): p. 22-27.

50. Ginley, D.S. and C. Bright, Transparent Conducting Oxides. Materials Research Society Bulletin, 2000. **25**(8): p. 15-18.

51. Pan, Z.W., Z.R. Dai, and Z.L. Wang, Nanobelts of semiconducting oxides. Science, 2001. **291**(5510): p. 1947-1949.

52. Wang, Y.W., et al., Zn nanobelts: a new quasi one-dimensional metal nanostructure. Chemical Communications, 2001(24): p. 2632-2633.

53. Zhang, J., et al., Synthesis of metal Sn nanobelts from SnO2 nanopowders by a substitution reaction. Nanotechnology, 2005. **16**(12): p. 2887-2891.

54. Ma, C., et al., Nanobelts, nanocombs, and nanowindmills of wurtzite ZnS. Advanced Materials, 2003. **15**(3): p. 228-+.

55. Dong, L.F., et al., Catalytic growth of CdS nanobelts and nanowires on tungsten substrates. Chemical Physics Letters, 2003. **376**(5-6): p. 653-658.

56. Ma, C., et al., Single-crystal CdSe nanosaws. Journal of the American Chemical Society, 2004. **126**(3): p. 708-709.

57. Jiang, Y., et al., Zinc selenide nanoribbons and nanowires. Journal of Physical Chemistry B, 2004. **108**(9): p. 2784-2787.

58. Cui, H.M., et al., Sonochemical synthesis of bismuth selenide nanobelts at room temperature. Journal of Crystal Growth, 2004. **271**(3-4): p. 456-461.

59. Bae, S.Y., et al., Single-crystalline gallium nitride nanobelts. Applied Physics Letters, 2002. **81**(1): p. 126-128.

60. Wu, Q., et al., Synthesis and optical characterization of aluminum nitride nanobelts. Journal of Physical Chemistry B, 2003. **107**(36): p. 9726-9729.

61. Yin, L.W., et al., Synthesis, structure, and photoluminescence of very thin and wide alpha silicon nitride (alpha-Si3N4) single-crystalline nanobelts. Applied Physics Letters, 2003. **83**(17): p. 3584-3586.

62. Luo, S.D., et al., Bulk-quantity synthesis of single-crystalline indium nitride nanobelts. Chemical Physics Letters, 2005. **411**(4-6): p. 361-365.

63. Wang, J.W. and Y.D. Li, Synthesis of single-crystalline nanobelts of ternary bismuth oxide bromide with different compositions. Chemical Communications, 2003(18): p. 2320-2321.

64. Shi, H.T., et al., Synthesis of hierarchical superstructures consisting of BaCrO4 nanobelts in catanionic reverse micelles. Advanced Materials, 2003. **15**(19): p. 1647-+.

65. Liu, H., C.G. Hu, and Z.L. Wang, Composite-hydroxide-mediated approach for the synthesis of nanostructures of complex functional-oxides. Nano Letters, 2006. **6**(7): p. 1535-1540.

66. Wang, X.D., et al., Large-scale synthesis of six-nanometer-wide ZnO nanobelts. Journal of Physical Chemistry B, 2004. **108**(26): p. 8773-8777.

67. Lao, C.S., et al., Formation of double-side teethed nanocombs of ZnO and self-catalysis of Zn-terminated polar surface. Chemical Physics Letters, 2006. **417**(4-6): p. 358-362.

68. Dai, Y., et al., Synthesis and optical properties of tetrapod-like zinc oxide nanorods. Chemical Physics Letters, 2002. **358**(1-2): p. 83-86.

69. Gao, P.X. and Z.L. Wang, Nanopropeller arrays of zinc oxide. Applied Physics Letters, 2004. **84**(15): p. 2883-2885.

70. Kong, X.Y. and Z.L. Wang, Spontaneous polarization-induced nanohelixes, nanosprings, and nanorings of piezoelectric nanobelts. Nano Letters, 2003. **3**(12): p. 1625-1631.

71. Yang, R.S., Y. Ding, and Z.L. Wang, Deformation-free single-crystal nanohelixes of polar nanowires. Nano Letters, 2004. **4**(7): p. 1309-1312.

72. Gao, P.M., et al., Conversion of zinc oxide nanobelts into superlattice-structured nanohelices. Science, 2005. **309**(5741): p. 1700-1704.

73. Kong, X.Y., et al., Single-crystal nanorings formed by epitaxial self-coiling of polar nanobelts. Science, 2004. **303**(5662): p. 1348-1351.

74. Hughes, W.L. and Z.L. Wang, Controlled synthesis and manipulation of ZnO nanorings and nanobows. Applied Physics Letters, 2005. **86**(4): p. -.

75. Wang, Z.L., X.Y. Kong, and J.M. Zuo, Induced growth of asymmetric nanocantilever arrays on polar surfaces. Physical Review Letters, 2003. **91**(18): p. 185502.

76. Gao, P.X., Y. Ding, and I.L. Wang, Crystallographic orientation-aligned ZnO nanorods grown by a tin catalyst. Nano Letters, 2003. **3**(9): p. 1315-1320.

77. Velev, O.D., et al., Materials - A class of porous metallic nanostructures. Nature, 1999. **401**(6753): p. 548-548.

78. Zhu, J., et al., Hyperbranched lead selenide nanowire networks. Nano Letters, 2007. **7**(4): p. 1095-1099.

79. Magdas, D.A., A. Cremades, and J. Piqueras, Three dimensional nanowire networks and complex nanostructures of indium oxide. Journal of Applied Physics, 2006. **100**(9): p. 094320.

80. Lao, J.Y., et al., Self-assembled In2O3 nanocrystal chains and nanowire networks. Advanced Materials, 2004. **16**(1): p. 65-+.

81. Zhao, Y.M., et al., Two-dimensional tungsten oxide nanowire networks. Applied Physics Letters, 2006. **89**(13): 133116.

82. Zhou, J., et al., Three-dimensional tungsten oxide nanowire networks. Advanced Materials, 2005. **17**(17): p. 2107-2110.

83. Cao, X.B., Y. Xie, and L.Y. Li, Spontaneous organization of three-dimensionally packed trigonal selenium microspheres into large-area nanowire networks. Advanced Materials, 2003. **15**(22): p. 1914-1918.

84. Gao, P.M., et al., Three-dimensional interconnected nanowire networks of ZnO. Chemical Physics Letters, 2005. **408**(1-3): p. 174-178.

85. Sra, A.K., T.D. Ewers, and R.E. Schaak, Direct solution synthesis of intermetallic AuCu and AuCu3 nanocrystals and nanowire networks. Chemistry of Materials, 2005. **17**(4): p. 758-766.

86. Ramanath, G., et al., Templateless room-temperature assembly of nanowire networks from nanoparticles. Langmuir, 2004. **20**(13): p. 5583-5587.

87. Wang, D.H., et al., A general route to macroscopic hierarchical 3D nanowire networks. Angewandte Chemie-International Edition, 2004. **43**(45): p. 6169-6173.

88. Adelung, R., et al., Self-assembled nanowire networks by deposition of copper onto layered-crystal surfaces. Advanced Materials, 2002. **14**(15): p. 1056-+.

89. Li, H.J., et al., SiC nanowire networks. Journal of Alloys and Compounds, 2003. **352**(1-2): p. 279-282.

90. Paulose, M., et al., Self-assembled fabrication of aluminum-silicon nanowire networks. Applied Physics Letters, 2002. **81**(1): p. 153-155.

91. Adelung, R., et al., Nanowire networks on perfectly flat surfaces. Applied Physics Letters, 1999. **74**(20): p. 3053-3055.

92. Li, Y.B., Y. Bando, and D. Golberg, Quasi-aligned single-crystalline W18O49 nanotubes and nanowires. Advanced Materials, 2003. **15**(15): p. 1294-+.

93. Wang, D., et al., Rational growth of branched and hyperbranched nanowire structures. Nano Letters, 2004. **4**(5): p. 871-874.

94. Haynes, C.L., et al., Angle-resolved nanosphere lithography: Manipulation of nanoparticle size, shape, and interparticle spacing. Journal of Physical Chemistry B, 2002. **106**(8): p. 1898-1902.

95. Wang, X.D., C.J. Summers, and Z.L. Wang, Large-scale hexagonal-patterned growth of aligned ZnO nanorods for nano-optoelectronics and nanosensor arrays. Nano Letters, 2004. **4**(3): p. 423-426.

96. Wang, X.D., et al., Direct-current nanogenerator driven by ultrasonic waves. Science, 2007. **316**(5821): p. 102-105.

97. Huang, Z.P., et al., Growth of large periodic arrays of carbon nanotubes. Applied Physics Letters, 2003. **82**(3): p. 460-462.

98. Dick, K.A., et al., Position-controlled interconnected InAs nanowire networks. Nano Letters, 2006. **6**(12): p. 2842-2847.

99. Dick, K.A., et al., Synthesis of branched 'nanotrees' by controlled seeding of multiple branching events. Nature Materials, 2004. **3**(6): p. 380-384.

100. Xiao, Y., et al., An X-ray nanodiffraction technique for structural characterization of individual. Journal of Synchrotron Radiation, 2005. **12**: p. 124-128.

101. Wang, Z.L., New developments in transmission electron microscopy for nanotechnology. Advanced Materials, 2003. **15**(18): p. 1497-1514.

102. Wang, Z.L., P. Poncharal, and W.A. de Heer, Nanomeasurements in transmission electron microscopy. Microscopy and Microanalysis, 2000. **6**(3): p. 224-230.

103. Wang, Z.L., P. Poncharal, and W.A. de Heer, Measuring physical and mechanical properties of individual carbon nanotubes by in situ TEM. Journal of Physics and Chemistry of Solids, 2000. **61**(7): p. 1025-1030.

104. Frank, S., et al., Carbon nanotube quantum resistors. Science, 1998. **280**(5370): p. 1744-1746.

105. Wang, Z.L., et al., In situ imaging of field emission from individual carbon nanotubes and their structural damage. Applied Physics Letters, 2002. **80**(5): p. 856-858.

106. Wang, Z.L., et al., Measuring the Young's modulus of solid nanowires by in situ TEM. Journal of Electron Microscopy, 2002. **51**: p. S79-S85.

107. Bai, X.D., et al., Measuring the work function at a nanobelt tip and at a nanoparticle surface. Nano Letters, 2003. **3**(8): p. 1147-1150.

108. Bai, X.D., et al., Dual-mode mechanical resonance of individual ZnO nanobelts. Applied Physics Letters, 2003. **82**(26): p. 4806-4808.

109. Carlotti, G., et al., Acoustic Investigation of the Elastic Properties of Zno Films. Applied Physics Letters, 1987. **51**(23): p. 1889-1891.

110. Mao, S.X., M.H. Zhao, and Z.L. Wang, Nanoscale mechanical behavior of individual semiconducting nanobelts. Applied Physics Letters, 2003. **83**(5): p. 993-995.

111. Lucas, M., et al., Aspect Ratio Dependence of the Elastic Properties of ZnO Nanobelts. Nano Letters, 2007. **7**(5): p. 1314-1317.

112. Oliver, W.C. and G.M. Pharr, An Improved Technique for Determining Hardness and Elastic-Modulus Using Load and Displacement Sensing Indentation Experiments. Journal of Materials Research, 1992. **7**(6): p. 1564-1583.

113. Zhao, M.H., Z.L. Wang, and S.X. Mao, Piezoelectric characterization of individual zinc oxide nanobelt probed by piezoresponse force microscope. Nano Letters, 2004. **4**(4): p. 587-590.

114. Christman, J.A., et al., Piezoelectric measurements with atomic force microscopy. Applied Physics Letters, 1998. **73**(26): p. 3851-3853.

115. Dunn, S., Determination of cross sectional variation of ferroelectric properties for thin film (Ca. 500 nm) PZT (30/70) via PFM. Integrated Ferroelectrics, 2003. **59**: p. 1505-1512.

116. Shi, L., et al., Thermal conductivities of individual tin dioxide nanobelts. Applied Physics Letters, 2004. **84**(14): p. 2638-2640.

117. Turkes, P., C. Pluntke, and R. Helbig, Thermal-Conductivity of Sno2 Single-Crystals. Journal of Physics C-Solid State Physics, 1980. **13**(26): p. 4941-4951.

118. Huang, M.H., et al., Room-temperature ultraviolet nanowire nanolasers. Science, 2001. **292**(5523): p. 1897-1899.

119. Poncharal, P., et al., Electrostatic deflections and electromechanical resonances of carbon nanotubes. Science, 1999. **283**(5407): p. 1513-1516.

120. Nishio, M., et al., Carbon nanotube oscillators toward zeptogram detection. Applied Physics Letters, 2005. **86**(13): p. 133111.

121. Ilic, B., et al., Enumeration of DNA molecules bound to a nanomechanical oscillator. Nano Letters, 2005. **5**(5): p. 925-929.

122. Zhou, J., et al., Nanowire as pico-gram balance at workplace atmosphere. Solid State Communications, 2006. **139**(5): p. 222-226.

123. Wang, Z.L. and J.H. Song, Piezoelectric nanogenerators based on zinc oxide nanowire arrays. Science, 2006. **312**(5771): p. 242-246.

124. Wang, Z.L., The new field of nanopiezotronics. Materials Today, 2007. **10**(5): p. 20-28.

125. Wang, Z.L., Nanopiezotronics. Advanced Materials, 2007. **19**(6): p. 889-892.

126. Song, J.H., J. Zhou, and Z.L. Wang, Piezoelectric and semiconducting coupled power generating process of a single ZnO belt/wire. A technology for harvesting electricity from the environment. Nano Letters, 2006. **6**(8): p. 1656-1662.

127. Wang, X.D., et al., Piezoelectric field effect transistor and nanoforce sensor based on a single ZnO nanowire. Nano Letters, 2006. **6**(12): p. 2768-2772.

128. He, H., et al., Piezoelectric gated diode of a single ZnO nanowire. Advanced Materials, 2007. **19**(6): p. 781-+.

129. Guo, T., et al., Catalytic Growth of Single-Walled Nanotubes by Laser Vaporization. Chemical Physics Letters, 1995. **243**(1-2): p. 49-54.

130. Guo, T., et al., Self-Assembly of Tubular Fullerenes. Journal of Physical Chemistry, 1995. **99**(27): p. 10694-10697.

131. Cobb, H.L., Camium Whiskers. Monthly Review of the American Electroplaters Society,, 1946. **33**: p. 28-30.

132. Xia, Y.N., et al., One-dimensional nanostructures: Synthesis, characterization, and applications. Advanced Materials, 2003. **15**(5): p. 353-389.

133. Pan, Z.W., Z.R. Dai, and Z.L. Wang, Lead oxide nanobelts and phase transformation induced by electron beam irradiation. Applied Physics Letters, 2002. **80**(2): p. 309-311.

134. Dai, Z.R., Z.W. Pan, and Z.L. Wang, Novel nanostructures of functional oxides synthesized by thermal evaporation. Advanced Functional Materials, 2003. **13**(1): p. 9-24.

135. Wagner, R.S. and W.C. Ellis, Vapor-Liquid-Solid Mechanism of Single Crystal Growth (New Method Growth Catalysis from Impurity Whisker Epitaxial + Large Crystals Si E). Applied Physics Letters, 1964. **4**(5): p. 89-90.

136. Wu, Y.Y. and P.D. Yang, Direct observation of vapor-liquid-solid nanowire growth. Journal of the American Chemical Society, 2001. **123**(13): p. 3165-3166.

137. Wang, N., et al., SiO2-enhanced synthesis of Si nanowires by laser ablation. Applied Physics Letters, 1998. **73**(26): p. 3902-3904.

138. Wang, N., et al., Nucleation and growth of Si nanowires from silicon oxide. Physical Review B, 1998. **58**(24): p. 16024-16026.

139. Prokes, S.M. and K.L. Wang, Novel methods of nanoscale wire formation. Mrs Bulletin, 1999. **24**(8): p. 13-19.

140. Kamins, T.I., et al., Chemical vapor deposition of Si nanowires nucleated by TiSi2 islands on Si. Applied Physics Letters, 2000. **76**(5): p. 562-564.

141. Mandl, B., et al., Au-free epitaxial growth of InAs nanowires. Nano Letters, 2006. **6**(8): p. 1817-1821.

142. Dick, K.A., et al., Failure of the vapor-liquid-solid mechanism in Au-assisted MOVPE growth of InAs nanowires. Nano Letters, 2005. **5**(4): p. 761-764.

143. Wang, Y.W., et al., Epitaxial growth of silicon nanowires using an aluminium catalyst. Nature Nanotechnology, 2006. **1**(3): p. 186-189.

144. Persson, A.I., et al., Solid-phase diffusion mechanism for GaAs nanowire growth. Nature Materials, 2004. **3**(10): p. 677-681.

145. Harmand, J.C., et al., Analysis of vapor-liquid-solid mechanism in Au-assisted GaAs nanowire growth. Applied Physics Letters, 2005. **87**(20): 203101.

146. Ding, Y., P.X. Gao, and Z.L. Wang, Catalyst-nanostructure interfacial lattice mismatch in determining the shape of VLS grown nanowires and nanobelts: A case of Sn/ZnO. Journal of the American Chemical Society, 2004. **126**(7): p. 2066-2072.

147. Arnold, M.S., et al., Field-effect transistors based on single semiconducting oxide nanobelts. Journal of Physical Chemistry B, 2003. **107**(3): p. 659-663.

148. Comini, E., et al., Stable and highly sensitive gas sensors based on semiconducting oxide nanobelts. Applied Physics Letters, 2002. **81**(10): p. 1869-1871.

149. Kuang, Q., et al., High-Sensitivity Humidity Sensor Based on a Single SnO2 Nanowire. Journal of the American Chemical Society, 2007. **129**: p. 6070-6071.

150. Hughes, W.L. and Z.L. Wang, Nanobelts as nanocantilevers. Applied Physics Letters, 2003. **82**(17): p. 2886-2888.

151. Murray, C.B., C.R. Kagan, and M.G. Bawendi, Self-Organization of Cdse Nanocrystallites into 3-Dimensional Quantum-Dot Superlattices. Science, 1995. **270**(5240): p. 1335-1338.

152. Whetten, R.L., et al., Nanocrystal gold molecules. Advanced Materials, 1996. **8**(5): p. 428-433.

153. Banfield, J.F., et al., Aggregation-based crystal growth and microstructure development in natural iron oxyhydroxide biomineralization products. Science, 2000. **289**(5480): p. 751-754.

154. Stampfl, C. and C.G. Van de Walle, Energetics and electronic structure of stacking faults in AlN, GaN, and InN. Physical Review B, 1998. **57**(24): p. R15052-R15055.

155. Ding, Y., X.Y. Kong, and Z.L. Wang, Doping and planar defects in the formation of single-crystal ZnO nanorings. Physical Review B, 2004. **70**(23): p. 235408.

156. Vigue, F., et al., Defect characterization in ZnO layers grown by plasma-enhanced molecular-beam epitaxy on (0001) sapphire substrates. Applied Physics Letters, 2001. **79**(2): p. 194-196.

157. Shuvalov, L.A., Modern Crystallography IV Solid-State Science 37, ed. L.A. Shuvalov. 1988, New York: Springer-Verlag. 109.

158. Romer, R.A. and M.E. Raikh, Aharonov-Bohm oscillations in the exciton luminescence from a semiconductor nanoring. Physica Status Solidi B-Basic Research, 2000. **221**(1): p. 535-539.

159. Amelinckx, S., et al., A Formation Mechanism for Catalytically Grown Helix-Shaped Graphite Nanotubes. Science, 1994. **265**(5172): p. 635-639.

160. Zhang, H.F., C.M. Wang, and L.S. Wang, Helical crystalline SiC/SiO2 core-shell nanowires. Nano Letters, 2002. **2**(9): p. 941-944.

161. Zhang, D.Q., et al., Silicon carbide nanosprings. Nano Letters, 2003. **3**(7): p. 983-987.

162. Gao, R.P., Z.L. Wang, and S.S. Fan, Kinetically controlled growth of helical and zigzag shapes of carbon nanotubes. Journal of Physical Chemistry B, 2000. **104**(6): p. 1227-1234.

163. Kong, X.Y. and Z.L. Wang, Polar-surface dominated ZnO nanobelts and the electrostatic energy induced nanohelixes, nanosprings, and nanospirals. Applied Physics Letters, 2004. **84**(6): p. 975-977.

164. Hughes, W.L. and Z.L. Wang, Formation of piezoelectric single-crystal nanorings and nanobows. Journal of the American Chemical Society, 2004. **126**(21): p. 6703-6709.

165. Spence, J.C. and J.M. Zuo, Electron Microdiffraction. 1992, New York: Plenum.

166. Sabine, T.M. and S. Hogg, Wurtzite Z Parameter for Beryllium Oxide and Zinc Oxide. Acta Crystallographica Section B-Structural Crystallography and Crystal Chemistry, 1969. **B 25**: p. 2254-2256.

167. Yang, R.S. and Z.L. Wang, Growth of Self-assembled ZnO Nanowire Arrays. Philosophical Magazine, 2007: p. in press.

168. Chang, P.C., et al., ZnO nanowires synthesized by vapor trapping CVD method. Chemistry of Materials, 2004. **16**(24): p. 5133-5137.

169. Park, W.I., et al., Metalorganic vapor-phase epitaxial growth of vertically well-aligned ZnO nanorods. Applied Physics Letters, 2002. **80**(22): p. 4232-4234.

170. Kong, Y.C., et al., Ultraviolet-emitting ZnO nanowires synthesized by a physical vapor deposition approach. Applied Physics Letters, 2001. **78**(4): p. 407-409.

171. Cross, R.B.M., M.M. De Souza, and E.M.S. Narayanan, A low temperature combination method for the production of ZnO nanowires. Nanotechnology, 2005. **16**(10): p. 2188-2192.

172. Xu, C.K., et al., A simple and novel route for the preparation of ZnO nanorods. Solid State Communications, 2002. **122**(3-4): p. 175-179.

173. Ng, H.T., et al., Growth of epitaxial nanowires at the junctions of nanowalls. Science, 2003. **300**(5623): p. 1249-1249.

174. Lee, C.J., et al., Field emission from well-aligned zinc oxide nanowires grown at low temperature. Applied Physics Letters, 2002. **81**(19): p. 3648-3650.

175. Lyu, S.C., et al., Low temperature growth and photoluminescence of well-aligned zinc oxide nanowires. Chemical Physics Letters, 2002. **363**(1-2): p. 134-138.

176. Li, Y.B., Y. Bando, and D. Golberg, ZnO nanoneedles with tip surface perturbations: Excellent field emitters. Applied Physics Letters, 2004. **84**(18): p. 3603-3605.

177. Gao, P.X. and Z.L. Wang, Self-assembled nanowire-nanoribbon junction arrays of ZnO. Journal of Physical Chemistry B, 2002. **106**(49): p. 12653-12658.

178. Pan, Z.W., et al., Molten gallium as a catalyst for the large-scale growth of highly aligned silica nanowires. Journal of the American Chemical Society, 2002. **124**(8): p. 1817-1822.

179. Yang, R.S. and Z.L. Wang, Springs, rings, and spirals of rutile-structured tin oxide nanobelts. Journal of the American Chemical Society, 2006. **128**(5): p. 1466-1467.

180. Maiti, A., et al., SnO2 nanoribbons as NO2 sensors: Insights from first principles calculations. Nano Letters, 2003. **3**(8): p. 1025-1028.

181. Shi, W.S., et al., Free-standing single crystal silicon nanoribbons. Journal of the American Chemical Society, 2001. **123**(44): p. 11095-11096.

182. Kang, Z.H., et al., Controllable fabrication of carbon nanotube and nanobelt with a polyoxometalate-assisted mild hydrothermal process. Journal of the American Chemical Society, 2005. **127**(18): p. 6534-6535.

183. Jiang, Y., et al., Hydrogen-assisted thermal evaporation synthesis of ZnS nanoribbons on a large scale. Advanced Materials, 2003. **15**(4): p. 323-327.

184. Johnson, J.C., et al., Ultrafast carrier dynamics in single ZnO nanowire and nanoribbon lasers. Nano Letters, 2004. **4**(2): p. 197-204.

185. Gao, Y.H., Y. Bando, and T. Sato, Nanobelts of the dielectric material Ge3N4. Applied Physics Letters, 2001. **79**(27): p. 4565-4567.

186. Liu, Z.P., et al., Large-scale synthesis of ultralong Bi2S3 nanoribbons via a solvothermal process. Advanced Materials, 2003. **15**(11): p. 936-+.

187. Xi, G.C., et al., Lithium-assisted synthesis and characterization of crystalline 3C-SiC nanobelts. Journal of Physical Chemistry B, 2004. **108**(52): p. 20102-20104.

188. Tsai, J.S., et al., Observation of vacancy ordering structure in GaP nanobelts. Journal of Applied Physics, 2004. **95**(4): p. 2015-2019.

189. Sigman, M.B. and B.A. Korgel, Strongly birefringent Pb3O2Cl2 nanobelts. Journal of the American Chemical Society, 2005. **127**(28): p. 10089-10095.

190. Wang, Z.L., et al., Semiconducting and piezoelectric oxide nanostructures induced by polar surfaces. Advanced Functional Materials, 2004. **14**(10): p. 943-956.

191. Duan, J.H., et al., AlN nanorings. Journal of Crystal Growth, 2005. **283**(3-4): p. 291-296.

192. Batzill, M. and U. Diebold, The surface and materials science of tin oxide. Progress in Surface Science, 2005. **79**(2-4): p. 47-154.

193. Dai, Z.R., Z.W. Pan, and Z.L. Wang, Growth and structure evolution of novel tin oxide diskettes. Journal of the American Chemical Society, 2002. **124**(29): p. 8673-8680.

194. Look, D.C., Electrical and optical properties of p-type ZnO. Semiconductor Science and Technology, 2005. **20**(4): p. S55-S61.

195. Park, C.H., S.B. Zhang, and S.H. Wei, Origin of p-type doping difficulty in ZnO: The impurity perspective. Physical Review B, 2002. **66**(7): p. -.

196. Park, C.H., S.B. Zhang, and S.H. Wei, Origin of p-type doping difficulty in ZnO: The impurity perspective. Physical Review B, 2002. **66**(7): p. -3202.

197. Yamamoto, T. and H. Katayama-Yoshida, Solution using a codoping method to unipolarity for the fabrication of p-type ZnO. Japanese Journal of Applied Physics Part 2-Letters, 1999. **38**(2B): p. L166-L169.

198. Kim, K.K., et al., Realization of p-type ZnO thin films via phosphorus doping and thermal activation of the dopant. Applied Physics Letters, 2003. **83**(1): p. 63-65.

199. Minegishi, K., et al., Growth of p-type zinc oxide films by chemical vapor deposition. Japanese Journal of Applied Physics Part 2-Letters, 1997. **36**(11A): p. L1453-L1455.

200. Joseph, M., H. Tabata, and T. Kawai, p-type electrical conduction in ZnO thin films by Ga and N codoping. Japanese Journal of Applied Physics Part 2-Letters, 1999. **38**(11A): p. L1205-L1207.

201. Ryu, Y.R., et al., Synthesis of p-type ZnO films. Journal of Crystal Growth, 2000. **216**(1-4): p. 330-334.

202. Joseph, M., et al., Fabrication of the low-resistive p-type ZnO by codoping method. Physica B, 2001. **302**: p. 140-148.

203. Guo, X.L., H. Tabata, and T. Kawai, Pulsed laser reactive deposition of p-type ZnO film enhanced by an electron cyclotron resonance source. Journal of Crystal Growth, 2001. **223**(1-2): p. 135-139.

204. Guo, X.L., H. Tabata, and T. Kawai, p-type conduction in transparent semiconductor ZnO thin films induced by electron cyclotron resonance N2O plasma. Optical Materials, 2002. **19**(1): p. 229-233.

205. Butkhuzi, T.V., et al., The regulation of defect concentrations by means of separation layer in wide-band II-VI compounds. Semiconductor Science and Technology, 2001. **16**(7): p. 575-580.

206. Ashrafi, A.B.M.A., et al., Nitrogen-doped p-type ZnO layers prepared with H2O vapor-assisted metalorganic molecular-beam epitaxy. Japanese Journal of Applied Physics Part 2-Letters, 2002. **41**(11B): p. L1281-L1284.

207. Xiong, G., et al., Control of p- and n-type conductivity in sputter deposition of undoped ZnO. Applied Physics Letters, 2002. **80**(7): p. 1195-1197.

208. Look, D.C., et al., Characterization of homoepitaxial p-type ZnO grown by molecular beam epitaxy. Applied Physics Letters, 2002. **81**(10): p. 1830-1832.

209. Li, X., et al., Chemical vapor deposition-formed p-type ZnO thin films. Journal of Vacuum Science & Technology A, 2003. **21**(4): p. 1342-1346.

210. Li, X., et al., p-type ZnO thin films formed by CVD reaction of diethylzinc and NO gas. Electrochemical and Solid State Letters, 2003. **6**(4): p. C56-C58.

211. Bang, K.H., et al., Formation of p-type ZnO film on InP substrate by phosphor doping. Applied Surface Science, 2003. **210**(3-4): p. 177-182.

212. Li, B.S., et al., Optical properties and electrical characterization of p-type ZnO thin films prepared by thermally oxiding Zn3N2 thin films. Journal of Materials Research, 2003. **18**(1): p. 8-13.

213. Singh, A.V., et al., p-type conduction in codoped ZnO thin films. Journal of Applied Physics, 2003. **93**(1): p. 396-399.

214. Huang, J.Y., et al., Growth of N-doped p-type ZnO films using ammonia as dopant source gas. Journal of Materials Science Letters, 2002. **22**(4): p. 249-251.

215. Ryu, Y.R., T.S. Lee, and H.W. White, Properties of arsenic-doped p-type ZnO grown by hybrid beam deposition. Applied Physics Letters, 2003. **83**(1): p. 87-89.

216. Lu, H.G., et al., p-type ZnO films deposited by DC reactive magnetron sputtering at different ammonia concentrations. Materials Letters, 2003. **57**(22-23): p. 3311-3314.

217. Wang, J.Z., et al., Epitaxial growth of NH3-doped ZnO thin films on < 02(2)over-bar-4 > oriented sapphire substrates. Journal of Crystal Growth, 2003. **255**(3-4): p. 293-297.

218. Wang, C., et al., p-type ZnO thin films prepared by oxidation of Zn3N2 thin films deposited by DC magnetron sputtering. Journal of Crystal Growth, 2003. **259**(3): p. 279-281.

219. Rommeluere, J.F., et al., Electrical activity of nitrogen acceptors in ZnO films grown by metalorganic vapor phase epitaxy. Applied Physics Letters, 2003. **83**(2): p. 287-289.

220. Lu, J.G., et al., Structural, electrical and optical properties of N-doped ZnO films synthesized by SS-CVD. Materials Science in Semiconductor Processing, 2003. **5**(6): p. 491-496.

221. Ma, Y., et al., Control of conductivity type in undoped ZnO thin films grown by metalorganic vapor phase epitaxy. Journal of Applied Physics, 2004. **95**(11): p. 6268-6272.

222. Lin, C.C., et al., Properties of nitrogen-implanted p-type ZnO films grown on Si3N4/Si by radio-frequency magnetron sputtering. Applied Physics Letters, 2004. **84**(24): p. 5040-5042.

223. Ye, Z.Z., et al., Preparation of p-type ZnO films by Al plus N-codoping method. Journal of Crystal Growth, 2004. **265**(1-2): p. 127-132.

224. Xu, W.Z., et al., Low-pressure MOCVD growth of p-type ZnO thin films by using NO as the dopant source. Journal of Crystal Growth, 2004. **265**(1-2): p. 133-136.

225. Look, D.C., et al., As-doped p-type ZnO produced by an evaporation/sputtering process. Applied Physics Letters, 2004. **85**(22): p. 5269-5271.

226. Lu, J.G., et al., p-type conduction in N-Al co-doped ZnO thin films. Applied Physics Letters, 2004. **85**(15): p. 3134-3135.

227. Suemune, I., et al., Epitaxial ZnO growth and p-type doping with MOMBE. Physica Status Solidi B-Basic Research, 2004. **241**(3): p. 640-647.

228. Heo, Y.W., et al., p-type behavior in phosphorus-doped (Zn,Mg)O device structures. Applied Physics Letters, 2004. **84**(18): p. 3474-3476.

229. Fei, Z.G., et al., Electrical and optical properties of Al-N co-doped p-type zinc oxide films. Journal of Crystal Growth, 2004. **268**(1-2): p. 163-168.

230. Barnes, T.M., K. Olson, and C.A. Wolden, On the formation and stability of p-type conductivity in nitrogen-doped zinc oxide. Applied Physics Letters, 2005. **86**(11): p. 112113.

231. Liang, H.W., et al., P-type ZnO thin films prepared by plasma molecular beam epitaxy using radical NO. Physica Status Solidi a-Applications and Materials Science, 2005. **202**(6): p. 1060-1065.

232. Lu, J.G., et al., Improved N-Al codoped p-type ZnO thin films by introduction of a homo-buffer layer. Journal of Crystal Growth, 2005. **274**(3-4): p. 425-429.

233. Sanmyo, M., Y. Tomita, and K. Kobayashi, Preparation of zinc oxide films containing Be and N atoms by radio frequency magnetron sputtering. Thin Solid Films, 2005. **472**(1-2): p. 189-194.

234. Tsukazaki, A., et al., Repeated temperature modulation epitaxy for p-type doping and light-emitting diode based on ZnO. Nature Materials, 2005. **4**(1): p. 42-46.

235. Vaithianathan, V., B.T. Lee, and S.S. Kim, Preparation of As-doped p-type ZnO films using a Zn3As2/ZnO target with pulsed laser deposition. Applied Physics Letters, 2005. **86**(6): p. -.

236. Ye, Z.Z., et al., Effect of oxygen partial pressure ratios on the properties of Al-N co-doped ZnO thin films. Journal of Crystal Growth, 2005. **274**(1-2): p. 178-182.

237. Yuan, G.D., et al., P-type Zno thin films fabricated by Al-N co-doping method at different substrate temperature. Journal of Crystal Growth, 2005. **273**(3-4): p. 451-457.

238. Zhuge, F., et al., Effects of growth ambient on electrical properties of Al-N co-doped p-type ZnO films. Thin Solid Films, 2005. **476**(2): p. 272-275.

239. Tu, M.L., Y.K. Su, and C.Y. Ma, Nitrogen-doped p-type ZnO films prepared from nitrogen gas radio-frequency magnetron sputtering. Journal of Applied Physics, 2006. **100**(5): p. -.

240. Sun, J.W., et al., Hole transport in p-type ZnO films grown by plasma-assisted molecular beam epitaxy. Applied Physics Letters, 2006. **89**(23): p. -.

241. Miao, Y., et al., p-Type conduction in phosphorus-doped ZnO thin films by MOCVD and thermal activation of the dopant. Applied Surface Science, 2006. **252**(22): p. 7953-7956.

242. Lu, J.G., et al., Low-resistivity, stable p-type ZnO thin films realized using a Li-N dual-acceptor doping method. Applied Physics Letters, 2006. **88**(22): p. -.

243. Kumar, M., et al., Growth of epitaxial p-type ZnO thin films by codoping of Ga and N. Applied Physics Letters, 2006. **89**(11): p. 112103.

244. Gangil, S., et al., P-type nitrogen-doped ZnO thin films on sapphire (1 1 (2)over-bar-0) substrates by remote-plasma-enhanced metalorganic chemical vapor deposition. Journal of Crystal Growth, 2007. **298**: p. 486-490.

245. Pan, X.H., et al., Fabrication of Sb-doped p-type ZnO thin films by pulsed laser deposition. Applied Surface Science, 2007. **253**(11): p. 5067-5069.

246. Zeng, Y.J., et al., Study on the Hall-effect and photoluminescence of N-doped p-type ZnO thin films. Materials Letters, 2007. **61**(1): p. 41-44.

247. Zhang, X.D., et al., Fabrication of high hole-carrier density p-type ZnO thin films by N-Al co-doping. Applied Surface Science, 2007. **253**(8): p. 3825-3827.

248. Zhao, J.L., et al., Study on anomalous high p-type conductivity in ZnO films on silicon substrate prepared by ultrasonic spray pyrolysis. Applied Physics Letters, 2007. **90**(6): p. -.

249. Xiu, F.X., et al., High-mobility Sb-doped p-type ZnO by molecular-beam epitaxy. Applied Physics Letters, 2005. **87**(15): p. -.

250. Bian, J.M., et al., p-type ZnO films by monodoping of nitrogen and ZnO-based p-n homojunctions. Applied Physics Letters, 2004. **85**(18): p. 4070-4072.

251. Bian, J.M., et al., Deposition and electrical properties of N-In codoped p-type ZnO films by ultrasonic spray pyrolysis. Applied Physics Letters, 2004. **84**(4): p. 541-543.

252. Zeng, Y.J. and Z.Z. Ye, Comment on "Photoluminescence study of Sb-doped p-type ZnO films by molecular-beam epitaxy" [Appl. Phys. Lett. 87, 252102 (2005)]. Applied Physics Letters, 2007. **90**(11): p. 116102.

253. Xiang, B., et al., Rational synthesis of p-type zinc oxide nanowire arrays using simple chemical vapor deposition. Nano Letters, 2007. **7**(2): p. 323-328.

254. Sieranski, K., J. Szatkowski, and J. Misiewicz, Semiempirical Tight-Binding Band-Structure of Ii3v2 Semiconductors - Cd3p2, Zn3p2, Cd3as2, and Zn3as2. Physical Review B, 1994. **50**(11): p. 7331-7337.

255. Misiewicz, J., et al., Zn3P2 - a New Material for Optoelectronic Devices. Microelectronics Journal, 1994. **25**(5): p. R23-R28.

256. Loferski, J.J., Theoretical Considerations Governing the Choice of the Optimum Semiconductor for Photovoltaic Solar Energy Conversion. Journal of Applied Physics, 1956. **27**(7): p. 777-784.

257. Fessenden, R.W., J. Sobhanadri, and V. Subramanian, Minority-Carrier Lifetime in Thin-Films of Zn3P2 Using Microwave and Optical Transient Measurements. Thin Solid Films, 1995. **266**(2): p. 176-181.

258. Kakishita, K., K. Aihara, and T. Suda, Zinc Phosphide Epitaxial-Growth by Photo-Mocvd. Applied Surface Science, 1994. **80**: p. 281-286.

259. Park, M.H., et al., Low resistance Zn3P2/InP heterostructure ohmic contact to p-InP. Applied Physics Letters, 1996. **68**(7): p. 952-954.

260. Hava, S., Polycrystalline Zn3P2 Schottky Photodiode - Vacuum Surface Effects. Journal of Applied Physics, 1995. **78**(4): p. 2808-2810.

261. Kakishita, K., K. Aihara, and T. Suda, Zn3P2 Photovoltaic Film Growth for Zn3P2/Znse Solar-Cell. Solar Energy Materials and Solar Cells, 1994. **35**(1-4): p. 333-340.

262. Suda, T., Zinc Phosphide Thin-Films Grown by Plasma Assisted Vapor-Phase Deposition. Journal of Crystal Growth, 1990. **99**(1-4): p. 625-629.

263. Nayar, P.S., Properties of Zinc Phosphide Zinc-Oxide Heterojunctions. Journal of Applied Physics, 1982. **53**(2): p. 1069-1075.

264. Weller, H., A. Fojtik, and A. Henglein, Photochemistry of Semiconductor Colloids - Properties of Extremely Small Particles of Cd3P2 and Zn3P2. Chemical Physics Letters, 1985. **117**(5): p. 485-488.

265. Green, M. and P. O'Brien, A novel metalorganic route to nanocrystallites of zinc phosphide. Chemistry of Materials, 2001. **13**(12): p. 4500-4505.

266. Buhro, W.E., Metalloorganic Routes to Phosphide Semiconductors. Polyhedron, 1994. **13**(8): p. 1131-1148.

267. Shen, G.Z., et al., Single-crystalline trumpetlike zinc phosphide nanostructures. Applied Physics Letters, 2006. **88**(14): p. 143105.

268. Wang, Z.L., Zinc oxide nanostructures: growth, properties and applications. Journal of Physics-Condensed Matter, 2004. **16**(25): p. R829-R858.

269. Ganesan, P.G., et al., ZnO nanowires by pulsed laser vaporization: Synthesis and properties. Journal of Nanoscience and Nanotechnology, 2005. **5**(7): p. 1125-1129.

270. Liu, Z.Q., et al., Laser ablation synthesis and electron transport studies of tin oxide nanowires. Advanced Materials, 2003. **15**(20): p. 1754-1757.

271. Morber, J.R., et al., PLD-assisted VLS growth of aligned ferrite nanorods, nanowires, and nanobelts-synthesis, and properties. Journal of Physical Chemistry B, 2006. **110**(43): p. 21672-21679.

272. Song, J.H., et al., Systematic study on experimental conditions for large-scale growth of aligned ZnO nanwires on nitrides. Journal of Physical Chemistry B, 2005. **109**(20): p. 9869-9872.

273. Bryja, L., K. Jezierski, and J. Misiewicz, Optical-Properties of Zn3P2 Thin-Films. Thin Solid Films, 1993. **229**(1): p. 11-13.

274. Fuke, S., et al., Some Properties of Zn3P2 Polycrystalline Films Prepared by Hot-Wall Deposition. Journal of Applied Physics, 1986. **60**(7): p. 2368-2371.

275. Dong, L.F., et al., Dielectrophoretically controlled fabrication of single-crystal nickel silicide nanowire interconnects. Nano Letters, 2005. **5**(10): p. 2112-2115.

276. Lao, C.S., et al., ZnO nanobelt/nanowire Schottky diodes formed by dielectrophoresis alignment across Au electrodes. Nano Letters, 2006. **6**(2): p. 263-266.

277. Krupke, R., et al., Simultaneous deposition of metallic bundles of single-walled carbon nanotubes using ac-dielectrophoresis. Nano Letters, 2003. **3**(8): p. 1019-1023.

278. Vijayaraghavan, A., et al., Ultra-Large-scale Directed Assembly of Single-Walled Carbon Nanotube Devices. Nano Letters, 2007: p. ASAP Online.

279. Babu, V.S., P.R. Vaya, and J. Sobhanadri, Doping of Zn3P2 Thin-Films during Growth Using the Hot Wall Deposition Technique and Some Properties of the Grown Films. Semiconductor Science and Technology, 1989. **4**(7): p. 521-525.

280. Kakishita, K., S. Ikeda, and T. Suda, Zn3P2 Epitaxial-Growth by Mocvd. Journal of Crystal Growth, 1991. **115**(1-4): p. 793-797.

281. Sze, S.M., Physics of Semiconductor Devices. 1981, New York: Wiley.

282. Duan, X.F., et al., Indium phosphide nanowires as building blocks for nanoscale electronic and optoelectronic devices. Nature, 2001. **409**(6816): p. 66-69.

283. Zhong, Z.H., et al., Synthesis of p-type gallium nitride nanowires for electronic and photonic nanodevices. Nano Letters, 2003. **3**(3): p. 343-346.

284. Fan, Z.Y., et al., ZnO nanowire field-effect transistor and oxygen sensing property. Applied Physics Letters, 2004. **85**(24): p. 5923-5925.

285. Kasap, S.O., Principles of Electronic Materials and Devices. Second ed, ed. C.F. Shultz. 2002, USA: McGraw-Hill.

286. Wang, C.X., et al., Experimental analysis and theoretical model for anomalously high ideality factors in ZnO/diamond p-n junction diode. Applied Physics Letters, 2004. **84**(13): p. 2427-2429.

287. Philipose, U., et al., Conductivity and photoconductivity in undoped ZnSe nanowire array. Journal of Applied Physics, 2006. **99**(6): p. 066106.

288. Law, J.B.K. and J.T.L. Thong, Simple fabrication of a ZnO nanowire photodetector with a fast photoresponse time. Applied Physics Letters, 2006. **88**(13): p. 133114.

289. Mathur, S., et al., Size-dependent photoconductance in SnO2 nanowires. Small, 2005. **1**(7): p. 713-717.

290. Kim, K., et al., Photoconductivity of single-bilayer nanotubes consisting of poly(p-phenylenevinylene) (PPV) and carbonized-PPV layers. Advanced Materials, 2005. **17**(4): p. 464-+.

291. Park, C.H., et al., Spectral responsivity and quantum efficiency of n-ZnO/p-Si photodiode fully isolated by ion-beam treatment. Applied Physics Letters, 2003. **82**(22): p. 3973-3975.

292. Ma, J., et al., Electrical and optical properties of ZnO:Al films prepared by an evaporation method. Thin Solid Films, 1996. **279**(1-2): p. 213-215.